

THE UNIVERSITY OF TOKYO

博士論文

Microstructure-sensitive modeling for the
prediction of fatigue performances in
structural steels

(構造用鋼の疲労性能予測のための微細構造を
考慮したモデリング)

Author:

Briffod Fabien Roger Lucien
ブリフォ ファビャン ロジェ
ルシアン

Supervisor:

Pr. Manabu Enoki
榎学

Reliable Materials Engineering
Department of Materials Engineering

2017



Acknowledgments

Completion of the work presented in this thesis could not have been possible without the support of several people. First, I would like to express my sincere gratitude to my advisor, Pr. Manabu Enoki, who trusted me to work on such an interesting topic. His advice and questions helped me progressing and keeping my motivation intact throughout these years. I am very grateful to Ms. Keiko Hara for here kindness and help for all the administrative requirements I had to fulfill during these years. I have to apologize for the poor improvements in my Japanese which limited our conversations to simple but nonetheless pleasant moments. I would like to thank my committee members, Pr. Koseki, Pr. Inoue, Pr. Sato and Pr. Sakai for reviewing, questioning and offering criticisms of this work which helped me progressing.

Particular thanks should be given to specific members of the Enoki laboratory. First of all, I would like to thank Dr. Takayuki Shiraiwa, my *senpai*, for his invaluable help during my numerous experiment misfortunes as well as for the time he always spent to translate for me the questions or remarks made by other researchers during project meetings. I am also greatly indebted to Dr. Kaita Ito without who most of the work presented in this thesis could not have been done. His computer skills helped me in countless number of time. Finally, I wish to thank Dr. Pornthep Chivavibul for the time he took to conduct the numerous EBSD analyses presented in this dissertation. I am grateful of the nice discussions we also had about restaurants and life in Japan and also the nice baguettes he gave me several times.

I have deeply enjoyed the atmosphere of the laboratory, especially the morning conversations with Ms. Kanae Oguchi while the lab was empty. I wish to thank my lab neighbor and friend, Mr. Kaigu Wu for all the great time we spent inside and outside the office. The last year witnessed the arrival of another french student in the laboratory, Mr. Alexandre Bleuset. I am extremely thankful to him for our deep (and not so deep) conversations. Having a comrade in the laboratory greatly decreased the feeling of loneliness arising from living far from his home. I would like to thank him also for proof-reading the manuscript. I would like to also thank Dr. Vidit Gaur who helped me understanding some of my experimental results and with who I shared fruitful discussions. Life in the laboratory was paced by the departure and arrival of new students with who I had the pleasure to spend time. I wish to thank Dr. Tomoki Takata, especially for accepting to be my tutor upon my arrival in Japan. I also wish to mention former and new students, Mr. Wang, Mr. Muto, Mr. Sasaki, Mr. Hijikata, Mr. Yoneda, Mr. Miyazawa, Mr. Tamura, Mr. Takahashi, Mr. Sakaguchi and Mr. Yang. I wish to apologize to the new bachelor students for my lack of communication in the last months.

Finally, this great adventure would not have been possible without the support of my former head of department, Pr. Alain Ehrlicher and Mr. Sato who encouraged me to go to Japan and surely without who the stable relationship we share between the University of Tokyo and Ecole des Ponts would not even exist. I would like to thank some of the friends I made in Japan, particularly Ms. Kim Minju and Ms. Yao Lu with who I shared great moments. Finally I would like to thank my parents, my sister and especially my not-so-little brother Sylvain for our weekly talk. Last but certainly not least, I owe a great deal to my second half, Ms. Kim Eunyoung. Thank you for loving me, supporting me, and making me a better person.



Contents

Introduction	1
I Literature review	5
1 Statistical and probabilistic aspects of fatigue	6
1.1 General overview, definitions and notations	6
1.2 Scattering of fatigue life	9
1.3 Reliability and Confidence Levels	11
1.4 Generalized Extreme Value Theory	13
2 Mechanisms and models of fatigue crack formation	15
2.1 Cyclic hardening/softening	15
2.2 Fatigue crack initiation	18
2.3 Microstructurally small crack growth	22
2.4 Long crack growth	25
3 Microstructure-sensitive approach for fatigue modeling	27
3.1 Introduction to microstructural mechanics	27
3.2 Modeling of polycrystalline aggregates	28
3.3 Micro-mechanical modeling of the elasto-plastic behavior	31
3.4 Fatigue criteria and their applications	35
4 Summary and objectives of the research	40
II Microstructural characterization and modeling of synthetic polycrystalline aggregates	41
1 Introduction	42
2 Microstructural characterization of the materials	42
2.1 Chemical compositions and thermal treatments	42
2.2 Morphological and crystallographic analyses	47
3 Spatial tessellations for the generation of synthetic microstructures	58
3.1 Seed definition and sampling	58
3.2 Spatial tessellations	59
3.3 Reconstruction of grain boundaries	64
4 Analysis and reproduction of crystallographic texture	66
4.1 Descriptions of crystalline orientation	66
4.2 Orientation distribution function	67
4.3 Discretization of unweighted orientations	69
4.4 Discretization of weighted orientations	69
4.5 Discretization of orientations for martensite packets and blocks	70
5 Validation of the approaches	72
5.1 Comparison of synthetic and reconstructed grain boundaries	72
5.2 Comparisons between synthetic and real microstructures	73
5.3 Generation of martensitic microstructures	75
6 Summary	77

III Characterization and modeling of the mechanical behavior of the materials under cyclic loadings	79
1 Introduction	80
2 Constitutive models and identification strategies	80
2.1 J_2 -plasticity model	80
2.2 Phenomenological crystal plasticity model	81
2.3 Microstructure-based modeling of the pearlite behavior	82
2.4 Identification strategies	83
3 Experimental methods	86
3.1 Strain-controlled fatigue experiments	86
3.2 Load-controlled fatigue experiments	87
4 Results and Discussion	91
4.1 Strain-controlled fatigue experiments	91
4.2 Parameters identification	98
4.3 Load-controlled fatigue experiments	104
5 Summary	118
IV Numerical simulations of polycrystalline aggregates under cyclic conditions	121
1 Introduction	122
2 Description of the models for the evaluation of initiation and early growth of fatigue cracks	122
2.1 Fatigue crack initiation	122
2.2 Microstructurally short crack (MSC) growth	125
2.3 Grain boundary retardation	126
3 Investigation of the influence of grain morphology and texture on fatigue crack initiation	129
3.1 Introduction	129
3.2 Description of the numerical models	129
3.3 Results and discussion	133
3.4 Conclusions	140
4 Simulations of stage I fatigue cracks in notched polycrystalline aggregates	141
4.1 Introduction	141
4.2 Description of the numerical models	141
4.3 Results and discussion	145
4.4 Conclusions	167
5 Investigation of the strain localization in martensitic microstructure under fatigue conditions	168
5.1 Introduction	168
5.2 Description of the numerical models	168
5.3 Results and discussion	170
5.4 Conclusions	173
Conclusions and Recommendations	175
Bibliography	181

List of Figures

1	Three-link chain model of the paradigm of materials science and engineering as described by Obson [1].	1
I.1	Scheme of the Wöhler diagram including the fatigue limit.	6
I.2	Scheme defining the different parameters of a stress-controlled cyclic loading.	7
I.3	Scheme of the different domains of fatigue, based on [2].	8
I.4	Schematic diagram of the different fatigue stages represented with (a) the crack length against the number of cycles and (b) a Wöhler diagram showing stage I and II.	9
I.5	(a) S-N curves of Al 2024 at stress ratio $R=0.1$ exhibiting two modes of failure [5]. (b) Fatigue variability observed in $\alpha + \beta$ Ti alloy [6].	10
I.6	Scheme of the probabilistic Whöler diagram.	12
I.7	(a) Representation of the three types of extreme value probability distribution and (b) cumulative probability.	14
I.8	(a) Schematic diagram of Schmid law, (b) $\{101\}\langle 11\bar{1}\rangle$, $\{112\}\langle 11\bar{1}\rangle$ and $\{123\}\langle 11\bar{1}\rangle$ slip systems in a BCC lattice.	15
I.9	Isovalues of the Schmid factor for (a) the $(110)[\bar{1}11]$, (b) the $\{112\}\langle 11\bar{1}\rangle$ and (c) the $\{123\}\langle 11\bar{1}\rangle$ slip system in a BCC lattice.	16
I.10	(a) Cyclic stress-strain curve of FCC crystal exhibiting three regions characterized by different dislocation structures [16]: (b) Veins [17], (c) Persistent slip band [18] and (d) labyrinths [19].	17
I.11	(a) Different dislocation structures in function of the stacking fault energy γ_{SFE} [21]. Comparison between monotonic and cyclic stress-strain curves for a material with (b) a high stacking fault energy and (c) a low stacking fault energy [22, 23].	18
I.12	Scheme of the crack types at the surface of a material according to Miller [25].	19
I.13	(a) Fatigue cracks in copper at the intrusions of PSB cycled at a strain amplitude of 0.2% for 60,000 cycles [27]. (b) Scheme of the preferential sites for crack initiation in a strain amplitude vs. number of cycles graph [29].	19
I.14	Schematic diagram of the Tanaka-Mura model, based on [33].	20
I.15	Variation of the irreversibility fraction p_{irr} as a function of the number of cycles for different plastic strain amplitudes [36].	21
I.16	(a) Scheme of MSC growth rate, da/dN against ΔK compared to long crack growth rate. (b) Example of small crack growth rate in aluminium alloys in moist air [39].	23
I.17	Schematic diagram of the crystallographic mechanism of crack propagation at the grain boundary, from [47].	24
I.18	Schematic diagram of the twist and tilt angles.	25
I.19	Modified Kitagawa-Takahashi diagram, based on [50].	26
I.20	Scheme of microstructural mechanics applied to homogenization and localization problems.	27
I.21	3D reconstruction of IN100 Ni-based superalloy [56].	28

I.22	(a) Regular geometry used by Musinski and McDowell [58]. (b) Extruded hexagons used by Osterstock <i>et al.</i> [61].	29
I.23	Synthetic dual-phase microstructure models based on MW-Voronoi tessellation compared with the microstructure analyzed by EBSD [79].	30
I.24	Voronoi tessellation: (a) regular mesh and (b) free mesh [82].	31
I.25	Schematic representation of the multiplicative decomposition of the deformation gradient \mathbf{F}	31
I.26	Schematic representation of the methods to represent a crack in FEM: (a) seam crack, (b) XFEM and (c) degraded stiffness.	37
I.27	Representation of the grain boundary resistance against the twist angle Ψ for 6 different values of tilt angle θ , based on [116].	38
II.1	Dimensions of the blocks cut in the 15mm hot-rolled sheet for the localized heat-treatment.	43
II.2	Scheme of the two treatment patterns with a peak temperature of (a) 1400°C and (b) 1000°C.	43
II.3	Lattice correspondence between austenite and martensite crystals.	45
II.4	CCT diagram of the B material subjected to the first thermal treatment pattern	46
II.5	(a) IQ map of the α -iron with and ellipse fitted to each grain. (b) EBSD map with IPF color coding.	48
II.6	Histograms and empirical and fitted cumulative distribution functions of the grain major axis a , aspect ratio b/a and orientation θ for the α -iron.	49
II.7	$\{100\}$, $\{110\}$ and $\{111\}$ pole figures reconstructed from the ODF of the α -iron.	50
II.8	(a) IQ map of FP steel with and ellipse fitted to each grain. Blue ellipses correspond to ferrite grains, red ellipses to pearlite grains. (b) KAM map discretized with 5 levels. Ferrite grains appear in blue. (c) EBSD map with IPF color coding, pearlite grains appear in black.	51
II.9	Histograms and empirical and fitted cumulative distribution functions of the grain major axis a , aspect ratio b/a and orientation θ for the ferrite of the FP steel.	52
II.10	Histograms and empirical and fitted cumulative distribution functions of the grain major axis a , aspect ratio b/a and orientation θ for the pearlite of the FP steel.	53
II.11	$\{100\}$, $\{110\}$ and $\{111\}$ pole figures reconstructed from the ODF of the FP steel.	54
II.12	(a) Schematic diagram of the hierarchical decomposition of martensite [120]. (b) $\{110\}$ pole figure of the 24 variants (in red) of a $[100]$ prior austenite crystal orientation (in blue).	55
II.13	(a) Optical micrograph of the B14-10 material. (b) $500 \times 500 \mu\text{m}$ EBSD maps with IPF color coding.	55
II.14	(a) Initial EBSD map. (b) Isolated grain. (c) Identification of the four packets based on the orientations in the pole figure. (d) Analysis of one packet using an ellipse fitting process.	57
II.15	Probability densities of the major axis, aspect ratio and orientation of the block in the four packets of the isolated grain in Fig. II.14.	57
II.16	Example of a final configuration of the seed sampling process.	59

II.17	Representation of the unit circle for different values of p	60
II.18	Voronoi, multiplicatively weighted Voronoi and anisotropic tessellations of the final configuration of the seed sampling in Fig. II.16.	62
II.19	Comparison of the area of the cells of the three tessellations in Fig. II.18 with the area of the ellipses in Fig II.16.	62
II.20	(a) Example of a replicated seeds by translation in the two orthogonal directions. (b) Anisotropic tessellation of the domain composed of 9 similar sub-domains. The sub-domain in the center is fully periodic.	63
II.21	Example of a multi-scale tessellation. (a) Prior austenite grain boundaries. (b) Tessellation inside each grain for the packet boundaries. (c) Tessellation inside each packet for the block boundaries.	64
II.22	Schematic representation of the steps for the grain boundary reconstruction.	65
II.23	Example of grain boundary reconstruction with (a) 0 element tolerance, (b) 1 element tolerance and (c) 2 elements tolerance.	65
II.24	Representation of the Euler angles.	66
II.25	ODF calculated from the EBSD of the α -iron.	68
II.26	ODF calculated from the EBSD of the FP steel.	68
II.27	Scheme of the Euler space with a path drawn and corresponding cumulative ODF.	69
II.28	Pole figures of the Kurdjumov-Sachs orientation relations for a [100] prior austenite crystal.	70
II.29	IQ map of (a) α -iron ($450 \times 600 \mu\text{m}$) and (b) FP steel ($200 \times 400 \mu\text{m}$) with reconstructed grain boundaries (in blue) and generated grain boundaries by anisotropic tessellation of the ellipses in Fig. II.5 and II.8.	72
II.30	IPF map of synthetic (a) α -iron ($450 \times 600 \mu\text{m}$) and (b) FP steel ($200 \times 400 \mu\text{m}$) generated from the data evaluated in Section 2.	74
II.31	{100}, {110} and {111} pole figures synthetic (a) α -iron ($450 \times 600 \mu\text{m}$) and (b) FP steel ($200 \times 400 \mu\text{m}$) generated from the microstructures in Fig. II.30.	74
II.32	(a) Multi-scale tessellation representing a martensitic microstructure on a $2000 \times 2000 \mu\text{m}$ window. (b) Corresponding IPF color map.	76
III.1	Flow stress of pearlite.	83
III.2	(a) Single hexahedron elements used for the Taylor model. (b) 3D RVE composed of 400 grains.	85
III.3	Geometry of smooth specimens used for low-cycle fatigue tests (dimensions in mm).	86
III.4	Smooth specimen with the extensometer attached.	87
III.5	(a) Geometry of the specimen used for load-controlled fatigue tests. (b) Geometry of the elliptical notch in the center of the specimen (dimensions in mm).	87
III.6	(a) Distribution of the tensile stress calculated for an elastic behavior. (b) Stress concentration factor near the notch.	88
III.7	(a) Small notch. (b) Large notch.	89
III.8	Procedure of the fatigue test.	90
III.9	(a) Stress amplitude against the number of cycles and (b) hystereses and CSS curves of α -iron.	94

III.10	(a) Stress amplitude against the number of cycles and (b) hystereses and CSS curves of FP steel.	94
III.11	(a) Stress amplitude against the number of cycles and (b) hystereses and CSS curves of C10-30 steel.	94
III.12	(a) Stress amplitude against the number of cycles and (b) hystereses and CSS curves of B10-01 steel.	95
III.13	(a) Stress amplitude against the number of cycles and (b) hystereses and CSS curves of B10-30 steel.	95
III.14	(a) Stress amplitude against the number of cycles and (b) hystereses and CSS curves of B14-10 steel.	95
III.15	(a) Stress amplitude against the number of cycles and (b) hystereses and CSS curves of E14-10 steel.	96
III.16	(a) Stress amplitude against the number of cycles and (b) hystereses and CSS curves of 57-14-10 steel.	96
III.17	(a) Stress amplitude against the number of cycles and (b) hystereses and CSS curves of 57-10-50 steel.	96
III.18	Coffin-Manson curves for the different steels.	97
III.19	SEM observation of fracture surface of (a) B10-01, (b) B10-30 and (c) B14-10 steels subjected to 0.2% strain amplitude.	97
III.20	Comparison between the experimental and the simulated hysteresis curves based on the J_2 model for α -iron.	101
III.21	Comparison between the experimental and the simulated hysteresis curves based on the J_2 model for FP steel.	101
III.22	Comparison between the experimental and the simulated hysteresis curves based on the CP model for α -iron.	102
III.23	Comparison between the experimental and the simulated hysteresis curves based on the CP model for FP steel.	102
III.24	Comparison between the experimental and the simulated hysteresis curves based on the CP model for B14-10 steel.	103
III.25	Results of the fatigue experiments for (a) α -iron, (b) FP steel, (c) B10-01, (d) C10-30, (e) B10-30 and (f) 57-10-50 steels. Arrow indicates a test conducted without failure.	105
III.26	Results of the fatigue experiments for (a) B14-10, (b) E14-10, (c) 57-14-10 steels. Arrow indicates a test conducted without failure.	106
III.27	Example of crack patterns around the elliptic notch for (a) an α -iron (290 MPa), (b) FP steel (200 MPa), (c) B10-01 (260 MPa), (d) B14-10 (300 MPa), (e) E14-10 (288 MPa) and (f) 57-14-10 (300MPa).	107
III.28	(a) Fracture surface of the 57-10-50 steels subjected to $\sigma_a=320$ MPa with R=-1. (b) Close-up observation near the notch. (c) Striations about 100 μm from the notch.	108
III.29	(a) Fracture surface of the E14-10 steels subjected to $\sigma_a=300$ MPa with R=-1. (b) Close-up observation near the notch. (c) Striations about 4 mm from the notch.	109
III.30	Schematic representation of a semi-elliptical surface crack in finite-thickness plate.	110
III.31	Crack length versus the number of cycles and crack growth rate versus the crack length for three different small notch specimens.	112

III.32	Crack length versus the number of cycles and crack growth rate versus the crack length for three different large notch specimens.	113
III.33	(a) Optical microscope picture and (b) EBSD map of the right crack of the FP steel subjected to a stress amplitude of 200 MPa.	116
III.34	(a) Optical microscope picture and (b) EBSD map of the left crack of the FP steel subjected to a stress amplitude of 200 MPa.	116
IV.1	Scheme of the definition of a potential crack path.	123
IV.2	Example of the PCPs evaluated in a grain.	125
IV.3	Representation of the Hobson model of MSC growth for different values of the parameter β	126
IV.4	Representation of the grain boundary resistance against the twist angle Ψ for 6 different values of tilt angle θ , based on [116].	127
IV.5	Example of the PCPs evaluated in a grain adjacent to an existing crack. The grain boundary resistances are also reported.	128
IV.6	Log-normal distribution functions of the grain size for the three microstructure cases.	130
IV.7	$\varphi_2 = 45^\circ$ section of the ODF of a cold rolling texture in the Euler space.	131
IV.8	Pole figures of (a) a uniform texture and (b) a rolled BCC texture in the y -direction.	132
IV.9	Illustration of the different microstructures studied.	132
IV.10	Effective Schmid factor maps computed in the last simulated cycle for one microstructure per case.	134
IV.11	Cumulative distribution functions of the Tanaka-Mura FIP for the different cases studied.	135
IV.12	Inverse pole figures from the loading axis (x or y) including iso-surfaces of highest Schmid factor. Dots represent all the grains and black filled circles refer to the grains with the highest FIP.	136
IV.13	Distributions of the average plastic strain amplitude against the length of the PCP. The color indicates the value of the FIP.	137
IV.14	Distribution of the extreme inverse FIPs for each case. Horizontal lines represent the mean value.	138
IV.15	Cumulative distribution functions of the twist and tilt angles for the different cases.	139
IV.16	Geometry of the global model used to simulate the boundary conditions for the sub-models.	142
IV.17	Macroscopic stress-strain curves of the global model for (a) the α -iron and (b) the FP steel.	143
IV.18	Geometry of the notched polycrystalline aggregates of (a) α -iron and (b) FP steel. Pearlite grains appear in black.	143
IV.19	Procedure for the introduction of a seam crack with non-overlapping faces.	144
IV.20	Von Mises stress fields at the peak tensile stress of the last cycle for the global isotropic model and three different α -iron microstructures subjected to a stress amplitude of 260 MPa.	146
IV.21	Von Mises stress fields at the peak tensile stress of the last cycle for the global isotropic model and three different FP steel microstructures subjected to a stress amplitude of 200 MPa.	146

IV.22	Distribution of the stress concentration factor K_t along the line $y = 0$ for all the simulations of (a) α -iron and (b) FP steel.	146
IV.23	Maximum plastic strain amplitude $\max_{\alpha}(\Delta\gamma^{\alpha}/2)$ accumulated in the last cycle among the 12 available slip systems for eight α -iron microstructures.	147
IV.24	Maximum plastic strain amplitude $\max_{\alpha}(\Delta\gamma^{\alpha}/2)$ accumulated in the last cycle among the 12 available slip systems for eight FP steel microstructures.	148
IV.25	Inverse pole figure from the loading axis (y -direction) including surfaces with similar Schmid factor for (a) α -iron and (b) FP steel. Filled circles represent the crystal orientation of the five highest FIPs per microstructure.	149
IV.26	Cumulative probability of the Schmid factor of all the grains in the microstructures and of the five highest FIPs per microstructure for (a) α -iron and (b) FP steel.	151
IV.27	Distribution of the maximum FIP per grain for all the microstructures against the orientation of the potential crack path for (a) α -iron and (b) FP steel.	151
IV.28	Distribution of the maximum FIP per grain for all the microstructures against the orientation of the potential crack path for (a) α -iron and (b) FP steel.	151
IV.29	Cumulative distribution of the maximum FIP per grain for all the microstructures for (a) α -iron and (b) FP steel.	152
IV.30	(a) Distribution of the inverse extreme FIP for the two materials and different stress amplitudes. (b) Mean and standard deviation of these distributions.	153
IV.31	Cumulative distribution of the maximum FIP per grain for all the microstructures for (a) α -iron and (b) FP steel.	155
IV.32	(a) Likelihoods defined in Eq. IV.27 based on the experimental data of the two materials. (b) Experimental and fitted crack initiation lives for the two materials.	156
IV.33	Maximum plastic strain amplitude $\max_{\alpha}(\Delta\gamma^{\alpha}/2)$ accumulated in the last cycle among the 12 available slip systems for eight α -iron microstructures including cracks.	158
IV.34	Maximum plastic strain amplitude $\max_{\alpha}(\Delta\gamma^{\alpha}/2)$ accumulated in the last cycle among the 12 available slip systems for eight FP steel microstructures including cracks.	158
IV.35	Cumulative probability of the twist angle for all the slip systems, the highest FIP and the lowest resistance slip planes for (a) α -iron and (b) FP steel.	160
IV.36	Cumulative probability of the grain boundary resistance for all the slip systems, the highest FIP and the lowest resistance slip planes for (a) α -iron and (b) FP steel.	160
IV.37	Cumulative probability of the plastic strain amplitude $\frac{\Delta\gamma^{\alpha}}{2}$ for all the slip systems, the highest FIP and the lowest resistance slip planes for (a) α -iron and (b) FP steel.	161
IV.38	Cumulative probability of the inverse FIP for (a) α -iron and (b) FP steel.	162
IV.39	Fatigue lives after a propagation across two grains.	164
IV.40	Fatigue crack growth rates against the crack length for the eight α -iron microstructures in Fig. IV.33 subjected to a stress amplitude of 300MPa.	165

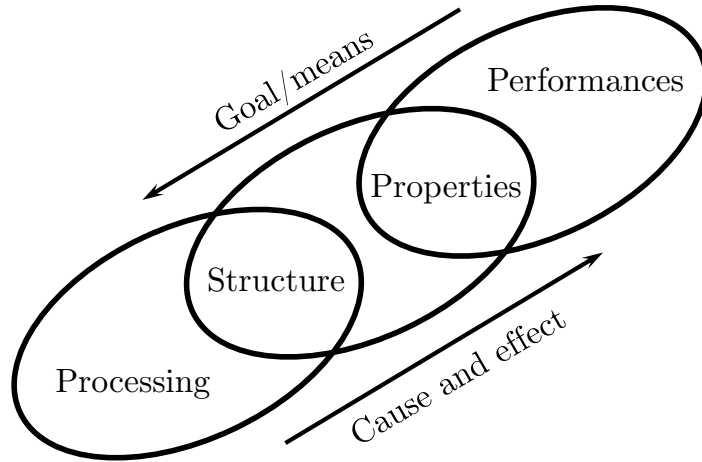
IV.41	Fatigue crack growth rates against the crack length for the eight FP steel microstructures in Fig. IV.34 subjected to a stress amplitude of 200MPa.	166
IV.42	Martensitic microstructure considering (a) prior austenite and packet boundaries,(b) prior austenite, packet and block boundaries.	169
IV.43	Maximum plastic strain amplitude $\max_{\alpha}(\Delta\gamma^{\alpha}/2)$ accumulated in the last cycle among the 12 available slip systems for eight P microstructures. . .	170
IV.44	Maximum plastic strain amplitude $\max_{\alpha}(\Delta\gamma^{\alpha}/2)$ accumulated in the last cycle among the 12 available slip systems for eight B microstructures. . .	171
IV.45	Schmid factor map for the eight B microstructures represented in Fig. IV.44.	172
IV.46	Cumulative probability of the Tanaka-Mura FIP for the two models. . . .	173
V.1	Scheme of the microstructure-sensitive procedure for the evaluation of the fatigue responses for different materials.	178

List of Tables

I.1	Interaction matrix in BCC crystal [93].	34
II.1	Chemical composition of the different low-carbon steels (in mass%, in ppm for B,N,O)	42
II.2	Materials studied in this research.	46
II.3	Parameters of the fitted distribution for the FP-steel.	51
II.4	Twenty-four variants of the Kurdjumov-Sachs relationship.	71
II.5	Phase fraction and log-normal parameters of the fitted grain size distribution for the experimental and synthetic α -iron and FP steel.	73
III.1	Experimental conditions for the LCF experiments	87
III.2	Cyclic properties of the different steels.	92
III.3	Parameters of the J_2 model for the different materials.	99
III.4	Parameters of the CP model for the different materials.	100
III.5	Evaluation of the Schmid factor and slip trace angles of the grains in right crack from Fig. III.33	117
III.6	Evaluation of the Schmid factor and slip trace angles of the grains in left crack from Fig. III.34	117
IV.1	Index of the slip systems in the DAMASK library.	124
IV.2	Parameters of the PDF for the three microstructures.	130
IV.3	Statistical data of the fatigue criterion.	135
IV.4	Statistical data of the extreme value inverse FIP.	139
IV.5	Simulation conditions of the global model.	142
IV.6	Statistical data of the FIP distribution for the two materials and the different stress conditions.	152
IV.7	Statistical data of the extreme inverse FIP and fitted parameters of the generalized extreme value distribution for the two materials and the different stress conditions.	155
IV.8	Statistical data of the extreme inverse FIP for crack initiation, retardation and the sum of both for the two materials and the different stress conditions.	162
IV.9	Statistical data for the fatigue lives after a propagation across two grains.	164

Introduction

The development of structural materials with improved properties and performances is a never-ending quest. Such development is a tedious process requiring significant time and expenses to achieve desired performances and ensure their reliability. Especially long-term performances such as creep or fatigue require exhaustive experiments to be fully characterized due to their intrinsic dependencies on their structure and processing history. With the improvement of computer capacities and the deeper empirical and theoretical understanding of damage mechanisms, a material-oriented design approach based on the prediction of the performance through the modeling of the material at a certain scale is a promising method to lower the development cost and time. Indeed, the design of new materials through the virtual modeling of polycrystalline aggregates based on the knowledge of key microstructural components could open the door towards the optimization of materials for specific applications. Such background is the starting point of the Materials Integration (MI) project which aim is to predict the performances of structural materials by merging theoretical and empirical models, experimental data, etc into a numerical system. Among the key performances to be predicted, particular emphasis is addressed towards fatigue performances which evaluation requires tremendous time and is one of the main causes of failure nowadays.



Three-link chain model of the paradigm of materials science and engineering as described by Obson [1].

Traditionally, predictions of fatigue lives are based on the evaluation of macroscopic mechanical fields and on the application of empirical rules fitted experimentally (Basquin law, Coffin-Manson law, Miner's rule, Goodman diagram). However, these structure-oriented methods are material-specific and do not account for the stochastic nature of fatigue phenomena due to the variability of the material at a lower scale than the structure. Consequently, extensive experimentation is required to characterize the statistical parameters of failure probability and assess the safety of a component with high reliability. Recently, microstructure-sensitive approaches are developed to evaluate the randomness of fatigue performances by considering the variability of the material itself at a certain microstructural scale. The main purpose of this modeling approach is to link the sensitivity of fatigue performances to certain microstructure variations thus lowering the number

of experiments and accelerating the development process of new materials. While the different mechanisms associated with fatigue failure are well identified experimentally (initiation, short cracks, etc), relatively few models and methods have been proposed and developed to numerically account for such mechanisms.

Research objectives

The principal objective of this research is to develop a framework centered around the microstructure for the evaluation of early damage mechanisms under fatigue conditions and the quantification of microstructural attributes affecting the performance and its variability. Specifically, we seek to:

1. Propose a methodology for the quantification and generation of synthetic microstructures based on the material characterization by electron back-scattered diffraction (EBSD) analysis.
2. Characterize from a mechanical point of view the materials in order to calibrate constitutive models used in the numerical simulations. In this regard, an inverse analysis based on the homogenization method is used.
3. Identify physical models for the early stages of fatigue and propose methodologies for their application in finite element software. Experimentally evaluate the different fatigue stages to inform and calibrate these models.

While this framework is intended to be generic, the research focuses on low-carbon steels used for structural applications as well as on an α -iron of high purity. The reason to also study an α -iron is that most of the carbon-steels present a very complex microstructure. Therefore it seemed necessary to start with a *simple* single phase material.

Thesis structure

The thesis is organized in four chapters.

In Chapter I, a literature review is conducted on the mechanisms associated with fatigue failure. The problem of fatigue from a statistical point of view and the source of scattering are described. Theoretical and empirical models for the nucleation and propagation of micro-cracks are then presented. Finally, the microstructure-sensitive approach in the field of fatigue is described. Specific fatigue criteria and their applications are reviewed, and the current limitations of this method are discussed.

Chapter II presents the different materials studied in this work, their characterization by EBSD analysis and the developed methodology for the generation of statistically similar synthetic microstructures. Comparisons are made with common generation methods and experimental EBSD.

Chapter III is focused on experimental methods to characterize the different materials under cyclic conditions. At first, low-cycle fatigue experiments under strain control are presented and constitutive models used in simulations are calibrated. Then load-controlled fatigue experiments are conducted with notched specimens in order to evaluate the different fatigue stages of the materials. Particular focus is aimed towards the nucleation and early growth of micro-cracks.

Finally, in Chapter [IV](#), the numerical models and methods considered for the evaluation of damage mechanisms under fatigue conditions are presented. The predictive capabilities of the parameters are first demonstrated with a parametric study. Then, simulations of notched microstructures similar to the fatigue specimens in Chapter [III](#) are conducted and a calibration of the models is attempted based on experimental results. Finally simulations of martensitic steels are performed to evaluate the importance of considering the various scales of heterogeneity present in such material.

Chapter I

Literature review

Contents

1	Statistical and probabilistic aspects of fatigue	6
1.1	General overview, definitions and notations	6
1.2	Scattering of fatigue life	9
1.3	Reliability and Confidence Levels	11
1.4	Generalized Extreme Value Theory	13
2	Mechanisms and models of fatigue crack formation	15
2.1	Cyclic hardening/softening	15
2.2	Fatigue crack initiation	18
2.3	Microstructurally small crack growth	22
2.4	Long crack growth	25
3	Microstructure-sensitive approach for fatigue modeling . . .	27
3.1	Introduction to microstructural mechanics	27
3.2	Modeling of polycrystalline aggregates	28
3.3	Micro-mechanical modeling of the elasto-plastic behavior . . .	31
3.4	Fatigue criteria and their applications	35
4	Summary and objectives of the research	40

1 Statistical and probabilistic aspects of fatigue

In this section, a general overview of the fatigue problem in metals is given. The statistical aspect of fatigue and the sources of scattering and uncertainties are reviewed.

1.1 General overview, definitions and notations

1.1.1 Introduction

Failure in mechanical parts under fatigue conditions has been under significant investigation since its first definition in the 1850s where it was observed in the railway industry. A. Wöhler was the first to perform a systematic investigation of fatigue failure and showed that the stress range was a more significant factor than the maximum stress for cyclic conditions. Since then, fatigue results are often depicted with the so-called Wöhler diagram or S-N diagram which represents the relation between the applied stress amplitude and the number of cycles to failure N_f , Fig. I.1. The notion of fatigue limit was then developed as the stress amplitude threshold below which no failure occurs.

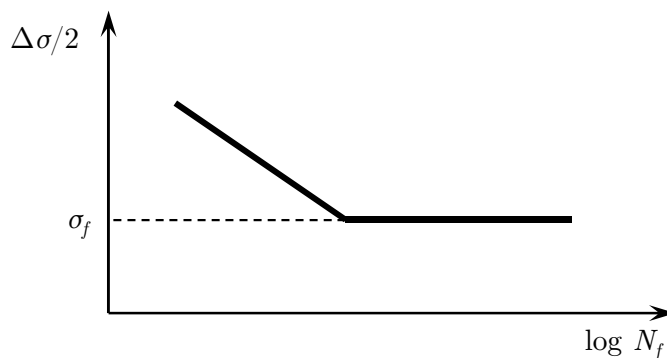


Figure I.1 – Scheme of the Wöhler diagram including the fatigue limit.

The American Society of the International Association for Testing and Materials (ASTM) gives the following definition of fatigue: "*The process of **progressive localized permanent** structural change occurring in a material subjected to conditions which produce **fluctuating** stresses and strains at some point or points and which may culminate in **cracks** or complete **fracture** after a sufficient number of fluctuations.*"

The following precision can be given:

- **Progressive** suggests that fatigue is a gradual process occurring over a certain period of time. While final failure is a sudden event, the damage processes may have started since the early usage of the structure.
- **Localized** as opposed with distributed implies that damage mechanisms are unequally positioned and mainly correspond to rare extreme events.
- **Permanent** implies a certain irreversibility in the fatigue process due to structural and topological changes of the material/component.
- **Fluctuating** suggests that fatigue damage is based on cyclic stress or strain conditions rather than constant or monotonic.
- The process of fatigue involve the formation and growth of one or several **cracks** to a length beyond which the structure can no longer sustain the load conditions leading to final **fracture**.

1.1.2 Notations and definitions

Considering in-phase cyclic conditions, the applied stress $\sigma(t)$ is generally described as a function of the stress amplitude σ_a and the mean stress σ_m :

$$\sigma_{ij}(t) = \sigma_{a,ij} \sin(\omega t) + \sigma_{m,ij} \quad (\text{I.1})$$

where $\omega = 2\pi f$ is the pulsation and f the frequency. The stress amplitude and the mean stress are respectively defined by:

$$\sigma_{a,ij}(t) = \frac{1}{2} \{ \sigma_{max,ij}(t) - \sigma_{min,ij}(t) \} \quad (\text{I.2})$$

$$\sigma_{m,ij}(t) = \frac{1}{2} \{ \sigma_{max,ij}(t) + \sigma_{min,ij}(t) \} \quad (\text{I.3})$$

Similarly, the strain amplitude $\Delta\varepsilon$ can be decomposed into elastic and plastic components:

$$\frac{\Delta\varepsilon}{2} = \frac{\Delta\varepsilon^e}{2} + \frac{\Delta\varepsilon^p}{2} \quad (\text{I.4})$$

$$\frac{\Delta\varepsilon^e}{2} = \frac{\Delta\sigma}{2E} \quad (\text{I.5})$$

where E is the Young modulus. The parameters are represented in Fig. I.2.

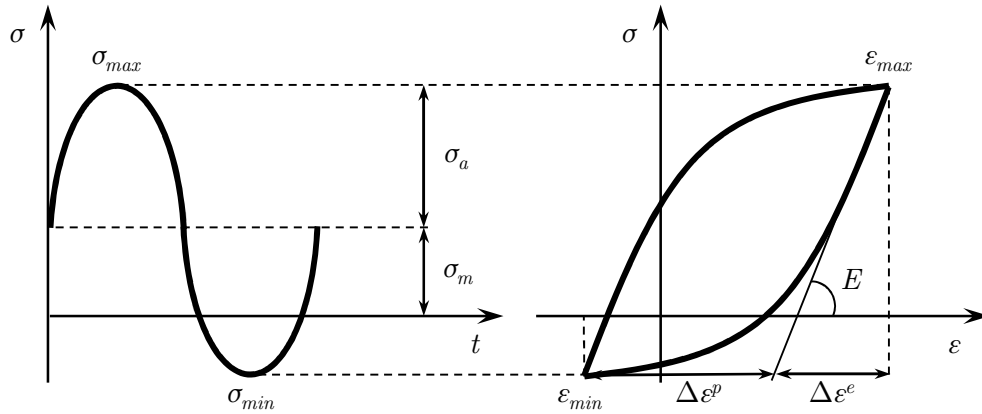


Figure I.2 – Scheme defining the different parameters of a stress-controlled cyclic loading.

1.1.3 Fatigue domains and lifetime models

The observation of Wöhler curves led to the conventional division of the S-N diagram into several domains based on the number of cycles to failure N_f . Fig I.3 illustrates the three domains of fatigue.

The low-cycle fatigue domain (LCF) generally corresponds to the region where the number of cycle for failure is lower than 10^5 . In this regime, the imposed load is high enough to generate macroscopic plastic deformation. The lifetime is relatively low and mainly controlled by the propagation and coalescence of cracks. The LCF fatigue domain is often described with a relation independently proposed by Coffin and Manson in 1954 that links the macroscopic plastic strain amplitude to the number of reversal cycles $2N_f$:

$$\frac{\Delta\varepsilon^p}{2} = \epsilon'_f (2N_f)^c \quad (\text{I.6})$$

where ϵ'_f is the ductility coefficient and c the ductility exponent. This relation is often used in strain-life approach of notched components.

The high-cycle fatigue domain (HCF) includes fatigue life between 10^5 and 10^7 . In this region, the macroscopic behavior of the material is considered elastic. The crack initiation mainly occurs on the surface and with the short crack propagation represent most of the material lifetime. Since no apparent plastic deformation can be easily observed, the HCF regime is mainly described by a Basquin law that relates the macroscopic stress amplitude to the number of reversal cycles $2N_f$.

$$\frac{\Delta\sigma}{2} = \sigma'_f(2N_f)^b \quad (\text{I.7})$$

where σ'_f is the stress for static failure and b the Basquin exponent.

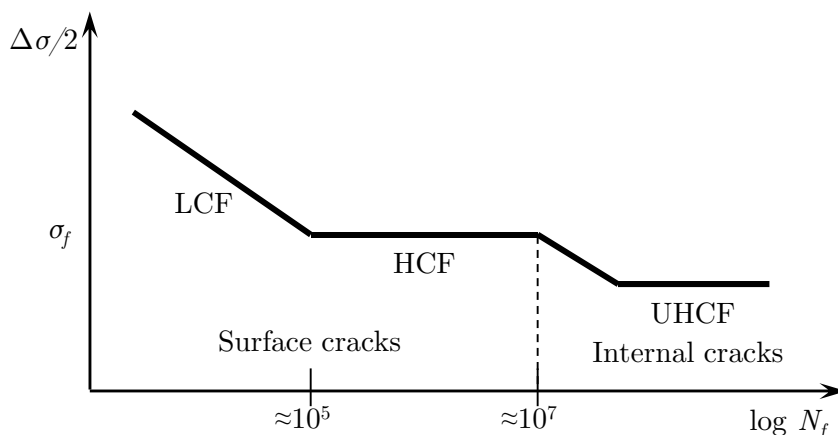


Figure I.3 – Scheme of the different domains of fatigue, based on [2].

Since the total strain amplitude $\Delta\varepsilon$ can be divided into an elastic and a plastic component, Eq. I.6 and I.7 can be combined to form the so-called strain-life approach

$$\frac{\Delta\varepsilon}{2} = \frac{\Delta\sigma}{2E} + \frac{\Delta\varepsilon^p}{2} = \frac{\sigma'_f}{E}(2N_f)^b + \epsilon'_f(2N_f)^c. \quad (\text{I.8})$$

This type of relation is not predictive by nature as it requires the fitting to experimental data. It is rather a way to describe and compare fatigue performances such as the yield and ultimate tensile strength are parameters that describe the monotonic behavior of a material.

Recent studies have shown the possible existence of a failure domain known as very high cycle fatigue (VHCF) or ultra high cycle fatigue (UHCF) above 10^8 cycles where cracks initiate inside the material as opposed to on the surface, due to local stress concentration caused by internal defects, lattice misorientations. . . . According to Mughrabi [2], another fatigue limit is defined around 10^{10} cycles and called "internal fatigue limit" as opposed to the classic "surface fatigue limit". With the development of piezoelectric fatigue machine where experiments can be run at several kHz, Bathias [3] argued the non-existence of any fatigue limit in metallic materials.

1.1.4 Fatigue stages

Fatigue damage in metallic materials is manifested by several complex and permanent microstructural changes related to local irreversibilities of plastic strain. Overall, the fatigue process can be decomposed into several stages [4]:

- **Cyclic hardening / softening** which mainly depends on the initial metallurgical state of the material and on the stress or strain amplitude. This stage is characterized by the appearance of substructures of dislocations, such as veins, persistent slip band and cell structures.
- **Crack initiation** which mainly takes place at the surface of the material in the absence of stress concentration or internal defects.
- **Microstructurally short crack propagation** where the growth rate is strongly influenced by microstructural barrier such as grain or twin boundaries.
- **Long crack propagation** also known as Paris' regime where the crack stably grows under mode I opening. It is often characterized by the appearance of striation due to double-slip growth mechanisms.
- **Final failure** where the crack has reached a sufficient length for the growth to become unstable.

The first three steps can be regrouped as stage I of fatigue life. It corresponds to the stage where the microstructure plays a significant role. In general, the last step represents a negligible portion of the total life of the structure and is often omitted (Eq. I.9). Fig. I.4 is a representation of the fatigue stages in term of crack length versus the number of cycles to failure and on a S-N diagram. A more in-depth description of each phase is given in Section 2.

$$N_f = N_I + N_{II} + N_{III} \approx N_I + N_{II} \quad (\text{I.9})$$

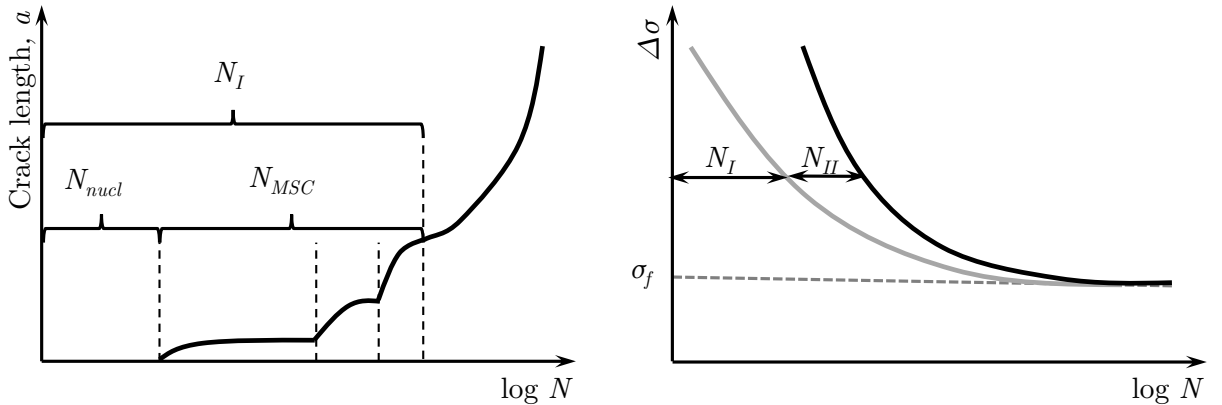


Figure I.4 – Schematic diagram of the different fatigue stages represented with (a) the crack length against the number of cycles and (b) a Wöhler diagram showing stage I and II.

1.2 Scattering of fatigue life

Experimentally, scattering is observed when representing a Wöhler curve, especially in the HCF regime. This scattering highlights the stochastic nature of fatigue failure. For a given stress amplitude, the ratio between the highest and lowest number of cycles for failure can exceed one order of magnitude. It seems therefore necessary to review the possible sources of scattering in fatigue. They can be gathered in different groups.

1.2.1 Metallurgical factors

These parameters are intrinsic to the material itself, its chemical constituents and process history. At first, the grain size is known to significantly affect the fatigue performances as fine grains tend to provide a better resistance against fatigue than larger grains. Thermal treatments may therefore affect the fatigue properties by changing the grain size.

The presence of metallurgical defects such as pores, interstitial defects, precipitates and inclusions can also be the origin of fatigue damage. Indeed, the incompatibility of deformations in their vicinity may provoke stress concentrations. For instance Marines *et al.* [5] observed competing mechanisms in fatigue failure of aluminum alloys. Below 10^6 cycles, cracks were observed to initiate from persistent slip bands while for higher lives, micro-cracks mainly formed at broken inclusions (Fig. I.5 (a)). Jha *et al.* [6] also observed competing mechanisms in $\alpha + \beta$ titanium and nickel-based superalloys (Fig. I.5 (b)). It was found in the case of Ti-alloys that shorter lives originated from the presence of α clusters at the surface of the material. In the case of Ni-alloys, competitions were found between surface/sub-surface and pores/inclusions failures.

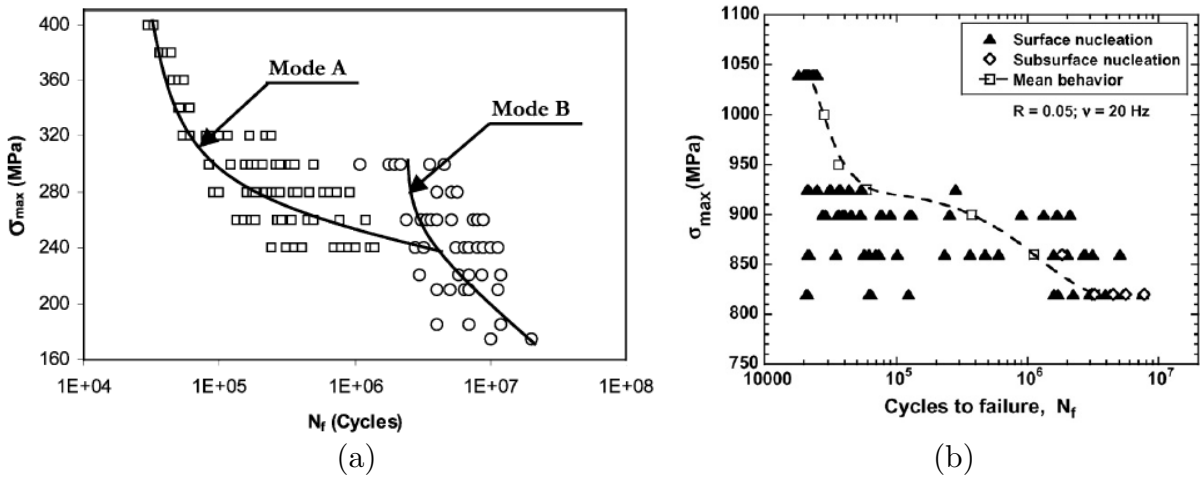


Figure I.5 – (a) S-N curves of Al 2024 at stress ratio $R=0.1$ exhibiting two modes of failure [5]. (b) Fatigue variability observed in $\alpha + \beta$ Ti alloy [6].

Among other intrinsic sources of scattering, the texture of the material which provides a more or less anisotropic behavior, is known to play a major role.

1.2.2 Mechanical and geometrical factors

Murakami and Endo [7–9] extensively studied the effect of small defects on fatigue strength in low and medium carbon steels. They showed that the fatigue limit was not affected by the presence of a small artificial defect when the size of the defect was below a certain threshold. The fatigue limit was emphasized as the threshold for non-propagating crack and not the threshold for crack formation. However, higher stress at the edge of the defect accelerates the degradation of the structure and therefore reduces the fatigue strength. Scattering tends to increase in presence of a defect due to the lack of representativity of the microstructure in its vicinity.

As micro-cracks mainly initiate at the surface of the specimen, the initial state of the surface plays a major role in fatigue strength. The quality of the surface roughness strongly

affects the local stress at the surface and micro-cracks tend to form in valley (of the surface) [10]. Residual stresses may be introduced during the forming process. Residual tensile stresses superposed to the load may accelerate the failure of the material. On the other hand, initial compressive stresses such as those induced by shot peening process are beneficial as they may prevent the propagation of cracks. However, as compared to monotonic performances, these effects are lower due to stress relaxation under cyclic conditions.

The type of loading is also known to affect the fatigue life. We can distinguish two types of loading: monotonic and variable (or even random). Considering a monotonic signal, the main parameters are:

- the shape of the signal: a square signal has a worse effect than a sinusoidal one as it introduces a holding time and might generate local creep.
- the stress ratio R : for same stress amplitude a higher stress ratio is known to reduce the fatigue life. Inversely, for fixed maximum stress, a higher stress ratio improves the fatigue life.
- the frequency of the signal: a high frequency may generate a self-heating effect. Also, the frequency has significant effect when the fatigue is combined with other mechanisms such as creep or corrosion.

Considering a variable signal, the main parameters are:

- overloads: the periodic repetition of overload can delay crack propagation by generating a wider plastic region ahead of the crack tip.
- the order of the signal: low amplitude followed by high amplitude has a different effect than the opposite order [11].

Finally, a last important factor is the scale effect. For equivalent stress conditions, specimens with same geometry but different dimensions will have different fatigue performances: the larger the specimen the lower the life. This can be explained by the fact that the larger the volume of material, the higher the probability to have a local defect. It was phenomenologically explained by Weibull with the weakest link theory.

1.2.3 Environmental factors

An aggressive environment such as high temperature, corrosive environment introduces other mechanisms (creep, corrosion) that reduces the life of the material under fatigue conditions. Such factors are not studied in this work.

1.3 Reliability and Confidence Levels

As a consequence of numerous sources of scattering, fatigue phenomenon should be treated statistically. Instead of representing a single S-N curve which would correspond to the 50% probability of failure, it is necessary to build equiprobability curves often referred as Probabilistic S-N (P-S-N) curves that associate for each stress condition or number of cycle a probability of failure p (Fig. I.6).

The parameters of a given probability distribution are assessed based on extensive experimentation. As it is impossible to investigate all the individuals of a given population,

the parameters are generally estimated based on a finite number of sample n . The key eigenvalues of the observed data are the mean \bar{x} and standard deviation s :

$$\bar{x} = \frac{1}{n} \sum_{i=1}^n x_i \quad (\text{I.10})$$

$$s = \sqrt{\frac{\sum_{i=1}^n (x_i - \bar{x})^2}{n - 1}}. \quad (\text{I.11})$$

The standard deviation is a key index to quantify the dispersion of data around the mean value. The coefficient of variation, which corresponds to the ratio of the standard deviation and the mean, gives a dimensionless indication of the dataset dispersion.

Among the distribution used to characterize the probability of failure, the Weibull distribution has been widely used. The general form of the Weibull distribution is given by:

$$P_f = 1 - \exp\left[-\left(\frac{\sigma_f}{\sigma_0}\right)^{m_w}\right] \quad (\text{I.12})$$

where P_f is the failure probability, σ_f the fatigue limit, σ_0 the normalization parameter and m_w the Weibull parameter also known as shape parameter.

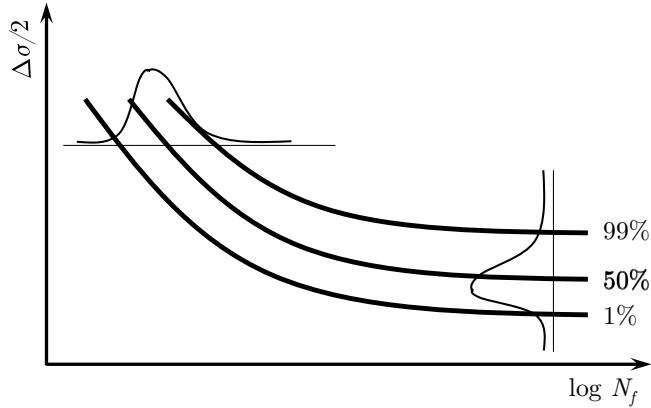


Figure I.6 – Scheme of the probabilistic Whöler diagram.

An other way to describe the scattering related to fatigue is to consider that locally (at the scale of the microstructure), the damage processes are deterministic and that scattering observed macroscopically are linked to the extreme response of the microstructure due to local heterogeneity. Thus, an introduction to the extreme value theory is given in the next section.

1.4 Generalized Extreme Value Theory

Fatigue resistance in HCF domain is governed by the initiation and early growth of a crack. Such phenomenon can be regarded as an extremely rare occurrence of a particular event. Based on this observation Przybyla and McDowell [12–14] proposed the application of the extreme value theory to the fatigue problems in HCF regime. They assumed that fatigue failure can be associated to the tail of a certain probability distribution of a material attribute or a particular damage criterion. They showed that the distribution of these extreme values could be well fitted to the Gumbel distribution. A brief description of the extreme value theory is given in this section.

Let X be a random variable with cumulative probability function $F_X(x)$. The extreme value (*max* or *min*) of n samples of X is given as follows:

$$Y_n = \max(X_1, X_2, \dots, X_n). \quad (\text{I.13})$$

The cumulative distribution function of the Y_n is then defined by:

$$F_{Y_n}(x) \equiv P(Y_n \leq x) = P(X_1 \leq x, X_2 \leq x, \dots, X_n \leq x). \quad (\text{I.14})$$

Assuming that X_1, X_2, \dots, X_n are independent and identically distributed random variables:

$$F_{X_1}(x) = F_{X_2}(x) = \dots = F_{X_n}(x) = F_X(x) \quad (\text{I.15})$$

then, Eq. I.14 can be rewritten as:

$$F_{Y_n}(x) = [F_X(x)]^n. \quad (\text{I.16})$$

The Fisher-Tippett theorem states: if a sequence of pairs of real numbers (a_n, b_n) exists such as:

$$P\left(\frac{Y_n - b_n}{a_n} \leq x\right) \xrightarrow{n \rightarrow \infty} F(x) \quad (\text{I.17})$$

where F is non degenerate, then the distribution F belongs to one of the three types:

- Gumbel or Type I:

$$F(x) = e^{-\exp(-x)}, \forall x \in \mathbb{R}$$

- Fréchet or Type II:

$$F(x) = \begin{cases} 0 & \text{if } x \leq 0 \\ e^{(-x^{-k})} & \text{if } x > 0 \end{cases}$$

- Weibull or Type III:

$$F(x) = \begin{cases} e^{(-(-x^{-k}))} & \text{if } x \leq 0 \\ 1 & \text{if } x > 0 \end{cases}$$

with $k > 0$. The variable $x = \frac{Y_n - b_n}{a_n}$ is called the normalized maximum of the random variable X and a_n and b_n are the scale and location parameters, respectively.

These three functions can be regrouped in the so-called generalized extreme value (GEV) distribution as proposed by Jenkinson [15]. It is defined by:

$$F(x) = \begin{cases} e^{-(1+\xi x)^{-\frac{1}{\xi}}} & \text{if } \xi \neq 0, \forall x/1 + \xi x > 0 \\ e^{(-e^{-x})} & \text{if } \xi = 0. \end{cases} \quad (\text{I.18})$$

The parameter ξ is called the shape parameter. Its sign determines the type of distribution: $\xi = 0$ is the Gumbel distribution, $\xi > 0$ the Fréchet distribution and $\xi < 0$ the Weibull distribution. Fig. I.7 shows the three types of the GEV probability and cumulative distribution function with $a_n = 1$ and $b_n = 0$. An interesting feature of the Fréchet and Weibull distributions is the existence of a tail, upper or lower, beyond which the probability is zero.

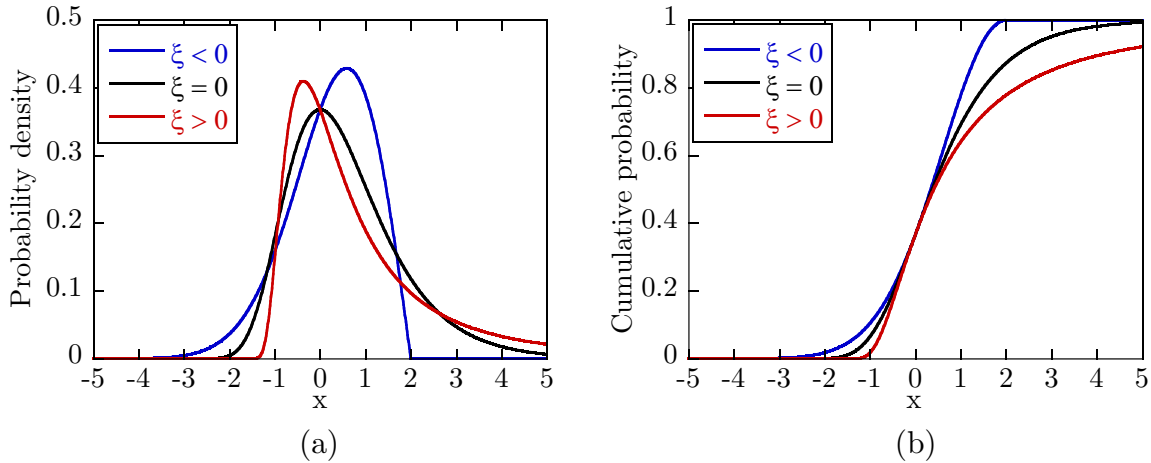


Figure I.7 – (a) Representation of the three types of extreme value probability distribution and (b) cumulative probability.

2 Mechanisms and models of fatigue crack formation

The first section has discussed the fatigue problem from an engineering and statistical point of view. It was shown that the scattering in fatigue life in the HCF regime was strongly affected by local microstructural heterogeneities. Accordingly, the different mechanisms related to the formation and growth of fatigue cracks are presented in this section. Relevant theoretical and empirical models for each mechanism are also described.

2.1 Cyclic hardening/softening

2.1.1 Deformation of a single crystal

A single crystal deforms plastically when the resolved shear stress (RSS) τ acting on a given slip system of normal \mathbf{n} along the direction \mathbf{m} reaches the critical resolved shear stress (CRSS) τ_c . The Schmid law for the evaluation of the RSS is illustrated in Fig. I.8 and defined as follows:

$$\tau = \frac{F \cdot \cos\alpha_m}{\frac{S_0}{\cos\alpha_n}} = \frac{F}{S_0} \cos\alpha_n \cdot \cos\alpha_m \quad (\text{I.19})$$

$$M = (\mathbf{t} \cdot \mathbf{n}) \times (\mathbf{t} \cdot \mathbf{m}) = \cos\alpha_n \cdot \cos\alpha_m \quad (\text{I.20})$$

where F , S_0 are the load and the surface of the specimen normal to the load direction, respectively. The Schmid factor M depends on the orientation of the slip system relative to the load direction \mathbf{t} .

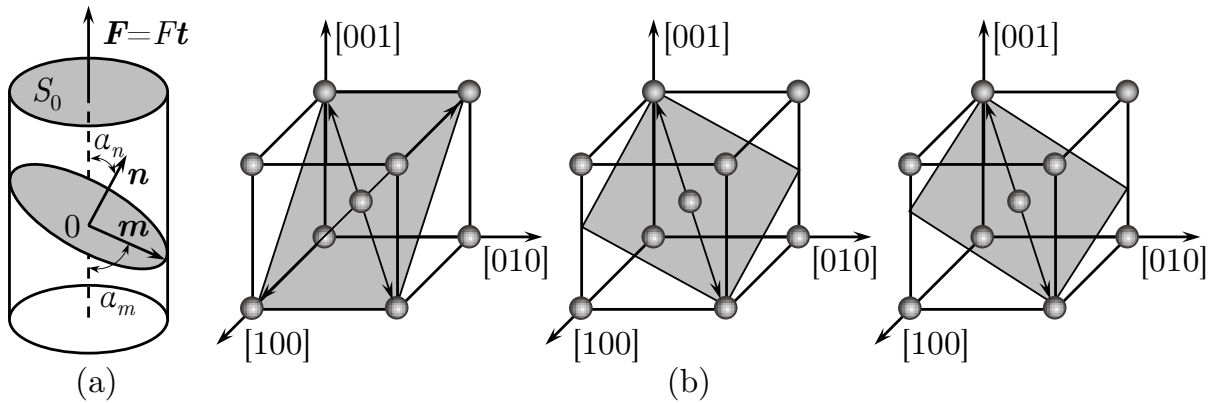


Figure I.8 – (a) Schematic diagram of Schmid law, (b) $\{101\}\langle 111 \rangle$, $\{112\}\langle 111 \rangle$ and $\{123\}\langle 111 \rangle$ slip systems in a BCC lattice.

Considering a BCC lattice, three different slip systems are available: $\{110\}\langle \bar{1}11 \rangle$, $\{112\}\langle 11\bar{1} \rangle$ and $\{123\}\langle 11\bar{1} \rangle$ which correspond to the planes and directions of the densest atom packing. These slip systems are represented in Fig. I.8. Plastic flow will take place on the slip system showing the highest Schmid factor. The maximum value of the Schmid factor is 0.5 and corresponds to a case where the slip plane and the slip direction are oriented 45° from the load direction. The isovalues of the Schmid factor for the three slip systems are represented on a standard triangle on Fig. I.9.

The plastic flow in a single crystal generally exhibits three hardening stages depending on the applied shear strain γ .

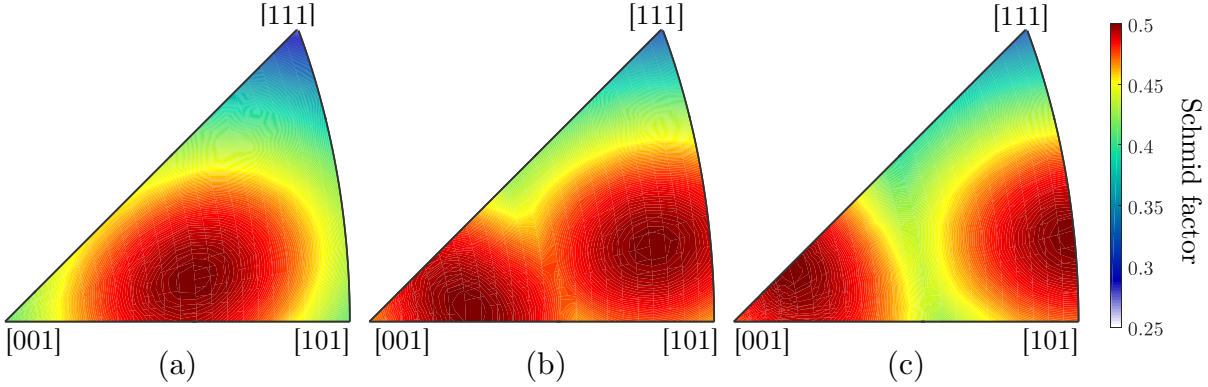


Figure I.9 – Isovalues of the Schmid factor for (a) the $(110)[\bar{1}11]$, (b) the $\{112\}\langle 11\bar{1}\rangle$ and (c) the $\{123\}\langle 11\bar{1}\rangle$ slip system in a BCC lattice.

- 'Easy glide' region characterized by single slip mechanism with a relatively low hardening rate.
- Activation of a secondary slip system due to the rotation of the crystal lattice. The interaction between the dislocations of primary and secondary slip systems involves an increase in the rate of work hardening.
- Further increase in applied strain promotes the formation of dislocation cell structures. Dislocations more easily cross slip which tends to reduce the work hardening.

2.1.2 Formation of dislocation structures and appearance of Intrusion/Extrusion

Under cyclic conditions, single crystals generally harden for the first few cycles until reaching a stabilized state where the hysteresis curve remains constant. The stable cycle is described with the saturated resolved shear strain range $\Delta\tau_{sat}$. Under imposed plastic strain range $\Delta\gamma^p$, the stabilized cyclic stress-strain curve exhibits three stages in the case of FCC crystal as shown in Fig. 1.10, characterized by the appearance of dislocations substructures observable by Scanning Electron Microscope (SEM).

- **Stage A:** the plastic strain range is low enough for single slip deformation which leads to the formation of veins of high dislocation dipole density embedded in a "soft" matrix.
- **Stage B:** the saturation stage corresponds to the formation of persistent slip bands (PSB) which do not produce subsequent hardening due to the stabilized competition between generation and annihilation of dislocation dipoles. The proportion of PSB increases with the plastic strain amplitude.
- **Stage C:** when the plastic strain exceeds a certain threshold γ_B^p , the resolved shear stress increases again due to cross slip and labyrinth structures appear.

These observations are slightly different in BCC metals due to the different dislocation behavior [20]. Indeed, at room temperature, screw dislocations are mainly immobile and under forward and reverse loading, glide on different planes leading to the so-called "slip plane asymmetry". Therefore, plastic deformation mainly occurs by glide of edge dislocations. As a consequence, PSB structures are not observed in pure BCC metals such as α -iron. Nonetheless, ill-defined slip bands still appear at the surface of the material.

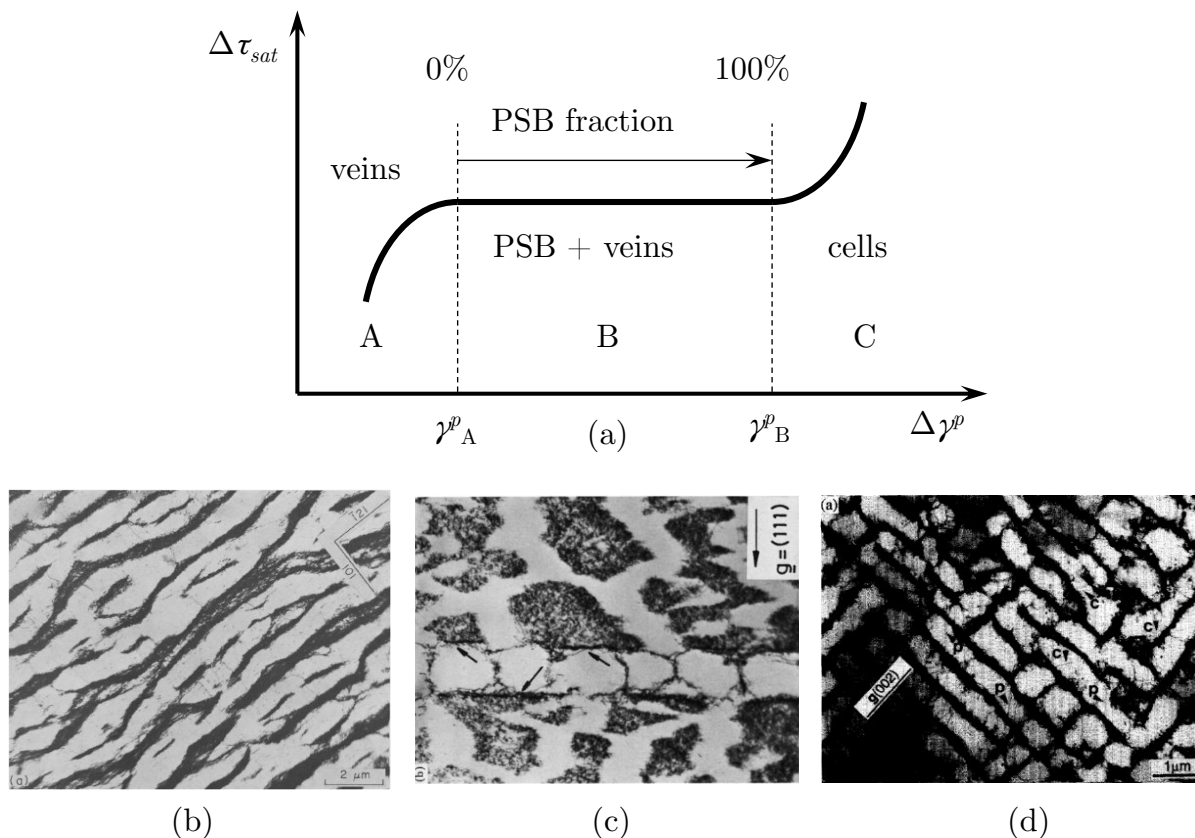


Figure I.10 – (a) Cyclic stress-strain curve of FCC crystal exhibiting three regions characterized by different dislocation structures [16]: (b) Veins [17], (c) Persistent slip band [18] and (d) labyrinths [19].

2.1.3 Deformation of polycrystals

A polycrystal is an heterogeneous structure composed of a grain aggregate. Each grain is equivalent to a single crystal characterized by its phase and the crystal lattice orientation. The macroscopic behavior of a polycrystal is generally isotropic but may show some anisotropy if a certain texture is present. The main difference between a polycrystal and a single crystal is the presence of grain boundaries (GB). The crystal misorientation of neighbor grains, the geometry of the grain boundary and orientation relative to the loading direction, and the difference between surface and interior grains are significant differences between a single crystal and a polycrystal.

Under cyclic conditions, polycrystals also exhibit a stress-strain hysteresis curve that stabilizes after a certain number of cycles due to similar mechanisms to a single crystal with the appearance of dislocation substructures that accommodate the deformation. The type of structure appearing is dependent on the stacking fault energy (SFE) of the material and on the strain amplitude as shown by Lukáš and Klesnil [21] and displayed in Fig. I.11. As a consequence, materials may exhibit a memory effect based on their stacking fault energy as shown in Fig. I.11. Indeed, for materials with high SFE such as pure aluminum or pure iron, under certain cyclic strain conditions, the screw dislocation may cross slip so that screw dislocations of opposite signs annihilate when belonging to the same plane. At equilibrium, the material is mainly composed of edge dislocations in the form of dislocation dipoles. Therefore, a prehardened material will exhibit significant softening due to its high initial dislocation density, while an annealed material will harden

through the formation of dislocation dipoles. Consequently, their stabilized cyclic stress-strain will be very close. On the other hand, screw dislocations in low SFE materials cannot cross slip such that hardened materials will show a lower softening and the cyclic stress-strain curve will be different than from the annealed case. This effect is called the memory effect as the material keeps memory of its initial state.

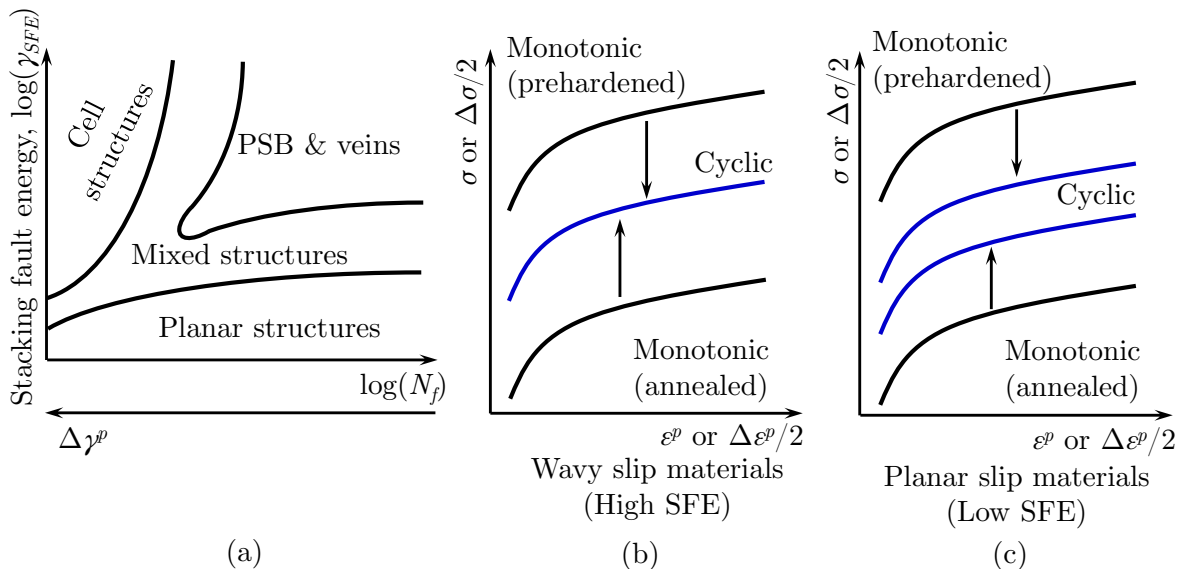


Figure I.11 – (a) Different dislocation structures in function of the stacking fault energy γ_{SFE} [21]. Comparison between monotonic and cyclic stress-strain curves for a material with (b) a high stacking fault energy and (c) a low stacking fault energy [22, 23].

2.2 Fatigue crack initiation

The definition of crack initiation is intimately related to the scale of observation. Several competitive mechanisms may exist in a material that contribute to the formation of a crack [24]:

- Surface roughening mechanisms.
- Local defects (pores, inclusions).
- Stress concentration area.

In this study, fatigue cracks will only be considered to occur at the surface of the material due to roughening mechanisms. According to Miller [25], two types of facets may be observed at the surface as shown in Fig. I.12. The main difference lies in the slip direction which in type B leads to the appearance of extrusions/intrusions and the propagation of the micro-crack through the depth of the material. Under uniaxial tension-compression, type A and B are found in the same proportion, while under torsion conditions, type A cracks are mostly observed. Surface roughening mainly originates from the irreversible shear deformation on slip bands on different slip planes between forward and reverse loadings.

2.2.1 Transgranular crack initiation

Basinski *et al.* [26] have conducted fatigue experiments on copper single crystals. They measured the plastic deformation inside PSBs and showed that it was 30 times higher than

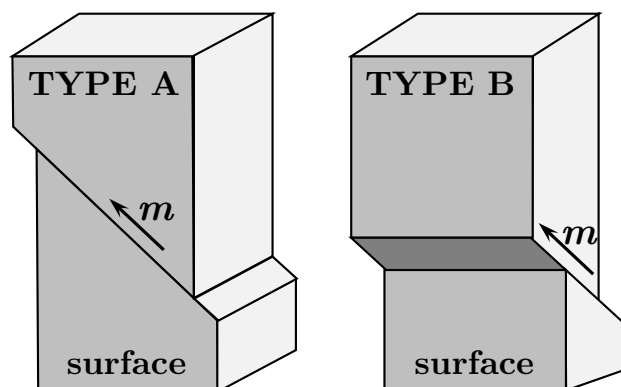


Figure I.12 – Scheme of the crack types at the surface of a material according to Miller [25].

the average plastic deformation which highlights the significant strain localization under fatigue conditions. Polishing the surface to remove these extrusions revealed to increase the life of the specimen. Ma and Laird [27, 28] directly observed the crack initiation in the depth of intrusions on the surface of copper single crystal specimens (Fig. I.13). Huang and Ho [29] showed, for the same material, that crack initiation in PSBs is mostly found under HCF conditions while intergranular crack initiation at grain boundary may be found under higher strain amplitude due to the activation of several slip systems.

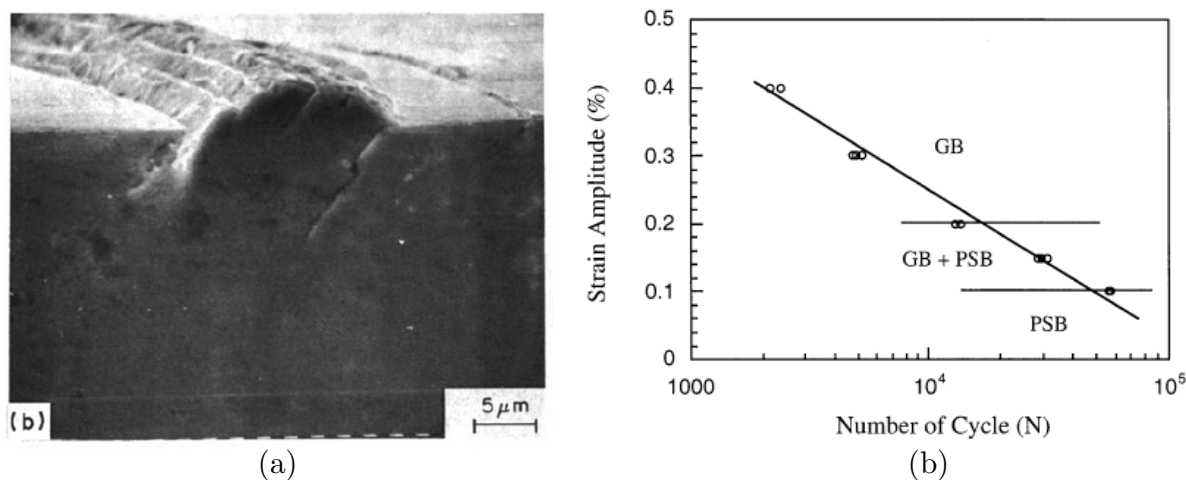


Figure I.13 – (a) Fatigue cracks in copper at the intrusions of PSB cycled at a strain amplitude of 0.2% for 60,000 cycles [27]. (b) Scheme of the preferential sites for crack initiation in a strain amplitude vs. number of cycles graph [29].

2.2.2 Intergranular crack initiation

Intergranular crack initiation mainly occurs in grain boundaries between grains exhibiting high misorientation angles. Indeed, dislocation motions across grain boundaries are strongly related to the misorientation between crystal lattices. High-angle GBs will tend to block dislocations which will therefore accumulate at the GB [30, 31]. In the case of the BCC lattice, the slip plane asymmetry also gives rise to shape incompatibility of neighboring grains and promotes intergranular cracking [32].

2.2.3 The Tanaka-Mura model

Theoretical models have been proposed in the past to predict the number of cycles for crack initiation. A large part of simulations are based on the model proposed by Tanaka and Mura [33, 34] in 1981. This model is described in this section as it will be applied in our study. Fig. I.14 shows a schematic diagram of the Tanaka-Mura model.

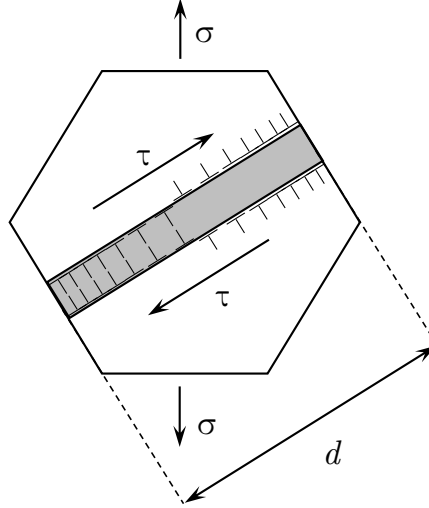


Figure I.14 – Schematic diagram of the Tanaka-Mura model, based on [33].

The model is an energy criterion based on dislocation theory. It is assumed that a slip band is already present in a grain where dislocations accumulate irreversibly on different but close and parallel slip planes under forward and reverse loading. The grain is favorably oriented for a single slip mechanism with a uniform RSS τ along the slip line of length d . The stored energy ΔU per thickness unit in one cycle is explicitly calculated based on the integral of dislocation density and given by:

$$\Delta U = \Delta\gamma_{pl}(\Delta\tau - 2\tau_c)/2 \quad (\text{I.21})$$

where τ_c is the frictional stress (CRSS). A crack is assumed to initiate when the total energy accumulated overcomes the surface energy to form two free surfaces.

$$2N_i\Delta U = 4dW_c \quad (\text{I.22})$$

$$N_i = \frac{8GW_c}{\pi(1-\nu)d(\Delta\tau - 2\tau_c)^2} \quad (\text{I.23})$$

$$N_i = \frac{A}{d} \left(\frac{\Delta\gamma_{pl}}{2} \right)^{-2} \quad (\text{I.24})$$

where W_c is the specific fracture energy for a unit area (kJ/m^2), G the shear modulus, and ν the Poisson's ratio.

This model presents the advantage to consider the influence of the grain size on the number of cycles for crack initiation. Under similar stress conditions, a crack will form earlier in a large grain than in a small grain as more plastic strain will accumulate during one cycle. While this model assumes transgranular crack initiation, Tanaka and Mura argued that it could also be applied to predict intergranular crack initiation due to the stacking of several slip bands on the same grain boundary. However, the size of the

nucleated crack was not predicted. Chan [35] attempted to formulate the crack size $2c$ based on the slip band width h :

$$c = 0.005 \left(\frac{d}{h} \right)^2 \left(\frac{W_c}{G} \right) \quad (\text{I.25})$$

However, the numerical application of the formula predicted a crack size five orders of magnitude lower than those observed experimentally. Such error was attributed to the difficulty to estimate the fracture surface energy W_c and to the fact that the Tanaka-Mura model does not account for the reversibility of the plastic deformation as observed experimentally. Indeed Risbet *et al.* [36, 37] measured the extrusion height of slip bands in nickel-base superalloys using atomic force microscopy. They defined the irreversible plastic strain as:

$$\gamma_{irr,pl} = \frac{h}{d} \quad (\text{I.26})$$

The plastic strain irreversibility fraction p_{irr} was then given by:

$$p_{irr} = \frac{\gamma_{irr,pl}}{\gamma_{pl}} \quad (\text{I.27})$$

Fig. I.15 shows the irreversibility fraction as a function of the number of cycles for different plastic strain amplitudes. Overall, p_{irr} tends to decrease with the applied plastic strain. Considering such plastic strain irreversibility is without a doubt necessary for a precise estimation of crack initiation.

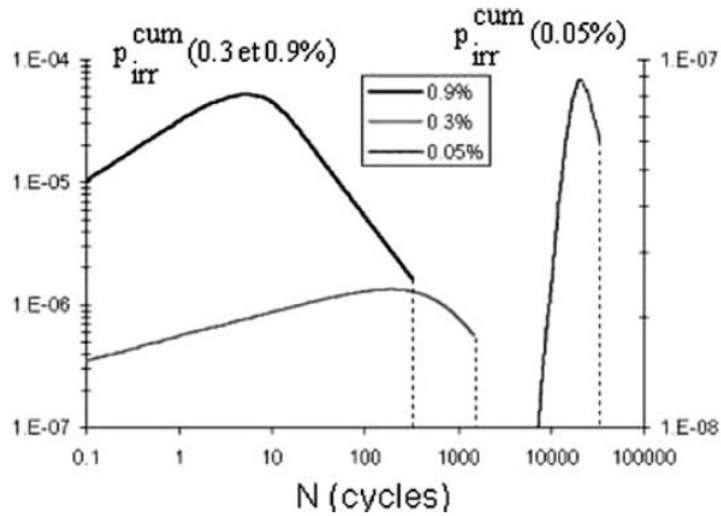


Figure I.15 – Variation of the irreversibility fraction p_{irr} as a function of the number of cycles for different plastic strain amplitudes [36].

2.3 Microstructurally small crack growth

2.3.1 First observations

Once a crack has initiated, it starts propagating. When the crack is small compared to microstructural features (grain, defect), it is referred as microstructurally small crack (MSC) due to the strong influence of the microstructure on its growth. Traditionally, the crack growth rate da/dN is represented against the far field stress intensity factor range ΔK . Pearson [38] was first to report, in the case of aluminium alloys, that MSCs propagate for stress intensity factors lower than the threshold ΔK_{th} and at a higher rate than that predicted by fracture mechanics models of long cracks (Fig. I.16). Lankford [39, 40] also investigated the influence of microstructure and environment on the growth of small cracks for several types of materials including aluminium alloys, titanium alloys and steels. The oscillatory character of the growth rate was well related to material grain size as crack propagation was found to decrease when reaching a length equivalent to the grain size. Such observations revealed the conservative character of long crack growth model such as the Paris' law and the breakdown of the concept of similitude. Indeed, this concept implies that cracks of different length a subjected to the same ΔK will propagate at the same rate as the plastic zone ahead of the crack will be of equal size and shape [41]:

$$\Delta a = da/dN = f(K_{max}, K_{min}) = f(\Delta K, R) \quad (\text{I.28})$$

As opposed to long cracks which mainly propagate under mode I opening, MSCs are considered to propagate under mode II sliding through the accumulation of dislocation at the crack tip. The key parameters controlling the propagation of MSC are:

- The elastic anisotropy due to the type of crystal lattice.
- The available slip system and deformation mechanisms (characterized by the stacking fault energy).
- The size and shape of grains.
- The micro-texture characterized by the local disorientation.

2.3.2 MSC growth models

Several models have been proposed to reproduce MSC growth and can be mainly divided into two categories: phenomenological models that consider microstructural attributes as primary variables and micromechanical models based on the crack tip sliding displacement (CTSD). Hobson [42] proposed an empirical empirical based on the size of the grain d and the position of the length of the crack a inside the grain:

$$\frac{da}{dN} = C(d - a)^{1-\beta} a^\beta \quad (\text{I.29})$$

where $(d - a)$ represents the uncracked portion of the grain and C and β are material parameters. In his model, β was arbitrarily set to 0.4. This model assumes that the crack will stop when it reaches the grain boundary. Miller [25] modified this model to account for the shear strain range $\Delta\gamma$ ahead of the crack tip:

$$\frac{da}{dN} = A(\Delta\gamma)^n (d - a) \quad (\text{I.30})$$

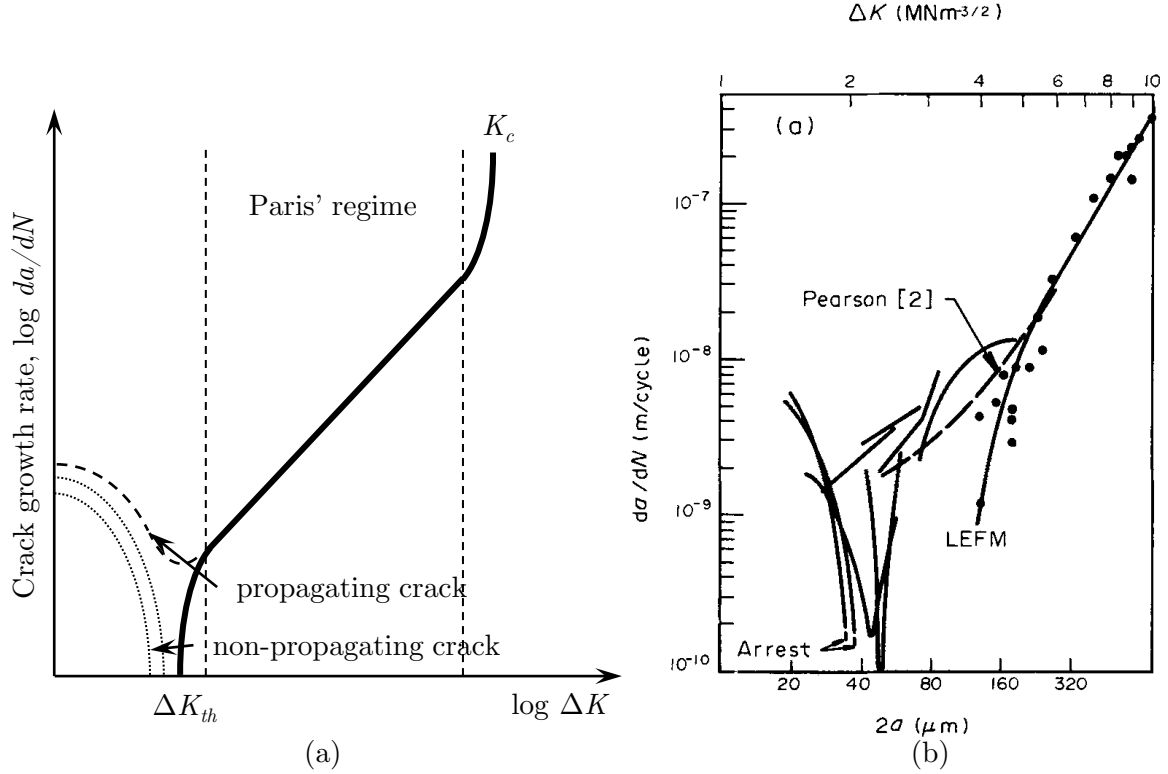


Figure I.16 – (a) Scheme of MSC growth rate, da/dN against ΔK compared to long crack growth rate. (b) Example of small crack growth rate in aluminium alloys in moist air [39].

where A and n are material parameters. It is worth mentioning that these equations are purely empirical and not based on any particular theory.

Alternatively, micromechanical models are based on the measurement of the CTSD whether experimentally or numerically. Crack growth rate is often formulated in Paris' type relation:

$$\frac{da}{dN} = B(\Delta CTSD)^m \quad (\text{I.31})$$

where B and m are parameters to be fitted. For instance, Tanaka *et al.* [43] proposed a slip band model to predict the CTSD based on the size of the slip band and on the shear stress acting on it using dislocation density theory.

2.3.3 Influence of the grain boundary

Upon reaching a grain boundary, a crack generally deviates from its original direction. Blochwitz *et al.* [44, 45] studied the influence of the local disorientation between grains on crack propagation in FCC pure nickel and stainless steel 316L. They tried to correlate the crack direction to the plane of the slip systems based on EBSD observations. They showed that in most cases the crack propagates on an activated slip system due to shear mechanism. Also they emphasized the influence of plastic strain amplitude on the competition mechanism between intergranular and transgranular crack propagation. At low plastic strain amplitude, crack propagation is mainly crystallographic and transgranular while at high plastic strain amplitude, crack propagation is intergranular. When crack

propagation is trangranular, the grain boundary remains undamaged and will constitute a physical barrier for crack propagation.

A grain boundary requires five independent parameters to be fully characterized: three crystal rotation angles to define the misorientation between the slip systems in two neighbor crystals and 2 spherical angles describing the direction of the grain boundary plane [46].

Zhai *et al.* [47] studied the deflection of cracks at grain boundaries in aluminium alloys. They proposed a crystallographic model for the prediction of the crack propagation direction at the grain boundary based on the definition of twist Ψ and tilt angles θ (Fig. I.17). They showed that cracks tend to propagate on the slip system having the lowest twist angle. As opposed to the disorientation which only considers the difference of orientation between two crystals, the twist and tilt angles explicitly account for the geometrical aspect of the grain boundary as shown in Fig. I.18. The twist and tilt angles are defined by:

$$\Psi = \cos^{-1}[(\mathbf{n}_{GB} \times \mathbf{n}_1) \cdot (\mathbf{n}_{GB} \times \mathbf{n}_2)] = |\Psi_1 - \Psi_2| \quad (\text{I.32})$$

$$\theta = \cos^{-1}[(\mathbf{u}_{GB} \times \mathbf{n}_1) \cdot (\mathbf{u}_{GB} \times \mathbf{n}_2)] = |\theta_1 - \theta_2| \quad (\text{I.33})$$

where \mathbf{n}_{GB} , \mathbf{u}_{GB} , \mathbf{n}_1 and \mathbf{n}_2 are the unit normal vector of the grain boundary, unit direction vector of the grain boundary, unit normal vector of the slip system in grain 1 and unit normal vector of the slip system in grain 2, respectively.

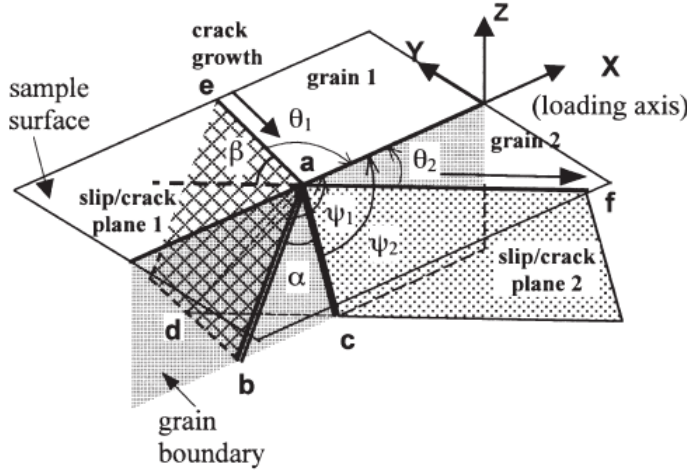


Figure I.17 – Schematic diagram of the crystallographic mechanism of crack propagation at the grain boundary, from [47].

In addition to the deflection observed at a grain boundary, the crack is generally delayed or even blocked for a certain amount of time. The crossing of the grain boundary is often modeled as a coalescence of a newly nucleated crack with the blocked crack in the neighbor grain. A few existing models based on physical mechanisms try to evaluate the blocking time of a crack at grain boundary. Among them, Morris *et al.* [48] proposed a dislocation based model for the incubation and coalescence of a crack in an initially undeformed neighbor grain. In their model, the unblocking of the crack is done by the accumulation of strain energy ahead of the crack tip in the grain where the crack tries to propagate. The number of cycles N_d for incubating a crack was:

$$\int_{N_s}^{N_s+N_d} D\sqrt{2c(N)}(\tau_{eff} - \tau_0)^2 dN = \beta \quad (\text{I.34})$$

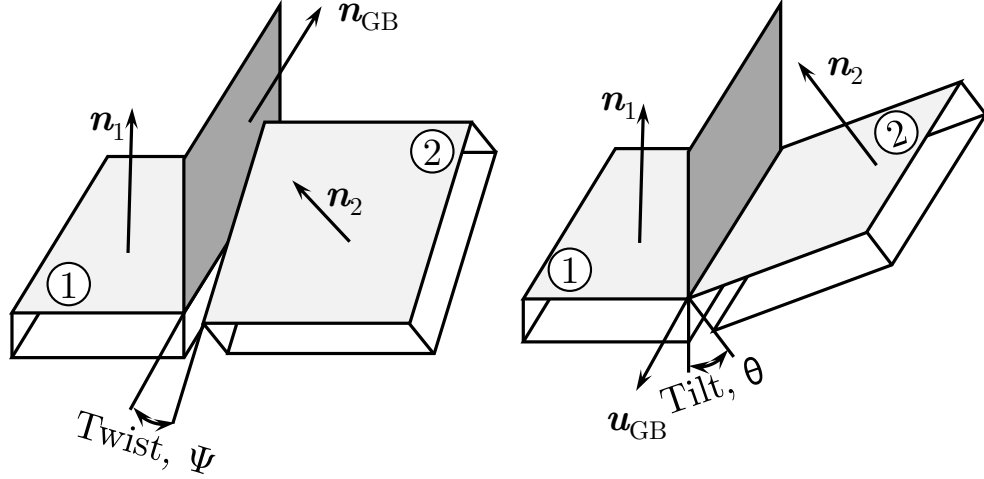


Figure I.18 – Schematic diagram of the twist and tilt angles.

$$N_d = \frac{C}{D\sqrt{c}(\tau_{eff} - \tau_0)^2} \quad (\text{I.35})$$

where N_s is the number of cycles when the crack reaches the grain boundary, $c(N)$ is the crack length at N cycles, D is the slip band length from the crack tip to the next grain boundary, β is a material parameter, τ_{eff} is an effective surface shear stress and τ_0 is the critical resolved shear stress for dislocation motion.

In this current form, the Eq. I.35 is very similar to the Eq. I.23 of the Tanaka-Mura model. One limitation of this model is that it does not explicitly account for the crystallographic discontinuity at the grain boundary.

2.4 Long crack growth

The non-propagating character of MSCs was described by Kitagawa and Takahashi [49] in 1976 using a diagram representing the stress amplitude against the crack length. According to them, a MSC cannot propagate if the stress amplitude is below the fatigue limit σ_f . Beyond a certain length a_0 (generally a few grains), the crack transitions from mode II sliding to mode I opening. Brown [50] modified the diagram due to experimental evidences that cracks may initiate below the fatigue limit. The threshold for MSC growth then increases until reaching the long crack regime (Fig. I.19).

The transition from MSC growth to long crack (LC) growth is often referred as physically short crack (PSC). PSCs are long enough to easily overcome microstructural barriers. However, the transition from mode II to mode I generates some plastic deformation ahead of the crack tip which in return may induce crack closure effect [51]. Accordingly elasto-plastic fracture mechanics (EPFM) models should be used in this stage to account for such effect. Experimentally, crack closure effect is accounted through the introduction of the effective stress intensity factor:

$$\Delta K_{eff} = K_{max} - K_{op} \quad (\text{I.36})$$

where K_{op} is the stress intensity factor when the crack opens. Longer cracks are often modeled using linear elastic fracture mechanics and models based on the Paris' law as

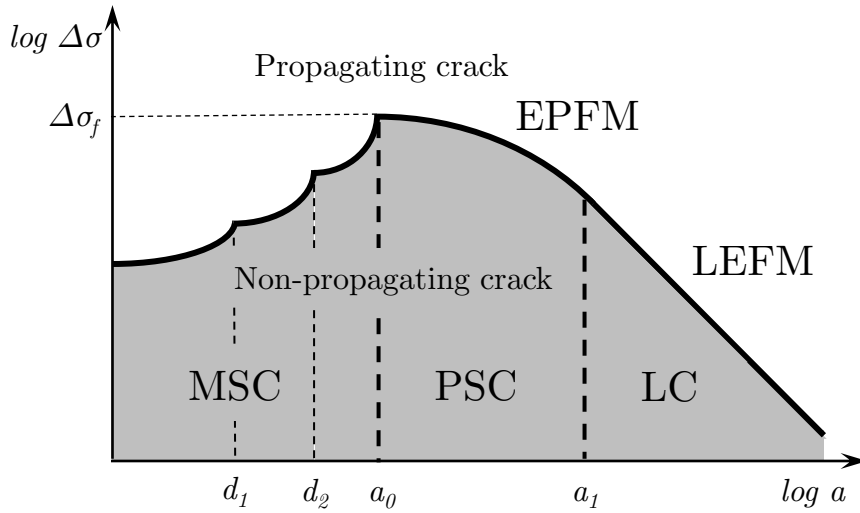


Figure I.19 – Modified Kitagawa-Takahashi diagram, based on [50].

represented in Fig. I.16 and defined by:

$$\frac{da}{dN} = A\Delta K^m \quad (\text{I.37})$$

where A and m are material parameters.

3 Microstructure-sensitive approach for fatigue modeling

The two previous sections have dealt with the experimental and statistical point of view of the fatigue problem in metallic materials. This section presents the recent trends and advances in simulating and evaluating damage mechanisms and how the influence of the microstructure and its attributes can be quantified.

3.1 Introduction to microstructural mechanics

From the observation that the initiation and early growth of fatigue cracks are not controlled by the average response of the material but by the extreme variation of local fields at the grain scale, the recent trends in the evaluation of damage mechanisms is based on microstructural mechanics [52]. This field combines the numerical methods of structural mechanics such as the Finite Element Method (FEM) to evaluate the mechanical fields, and the observation and characterization tools of materials science (SEM, DCT). It has been extensively applied in homogenization problems in order to predict the macroscopic response of an homogeneous material/structure based on local microstructural heterogeneities and constitutive models. Such problem led to the notion of representative volume element (RVE) which first definition was given by Hill [53] in 1963. According to Hill, a RVE is "*entirely typical of the whole mixture on average*" such that the overall moduli are "*independent of the surface values of traction and displacement, so long as these values are macroscopically uniform*". This definition implies that the size of the RVE is not straightforward but mainly depends on the material and the sensitivity of its components. As a consequence, two RVEs of a similar material should exhibit similar properties.

In the field of damage mechanics, the notion of statistical volume element (SVE) is preferred as it takes into account the variability of the microstructure as the source of variability of a certain damage mechanism (Fig. I.20). As opposed to RVEs, the macroscopic response from one SVE to another is allowed to vary slightly. The model description is often smaller and more refined such that the local response is accurate enough to capture the field of interests in the evaluation of a certain damage criterion.

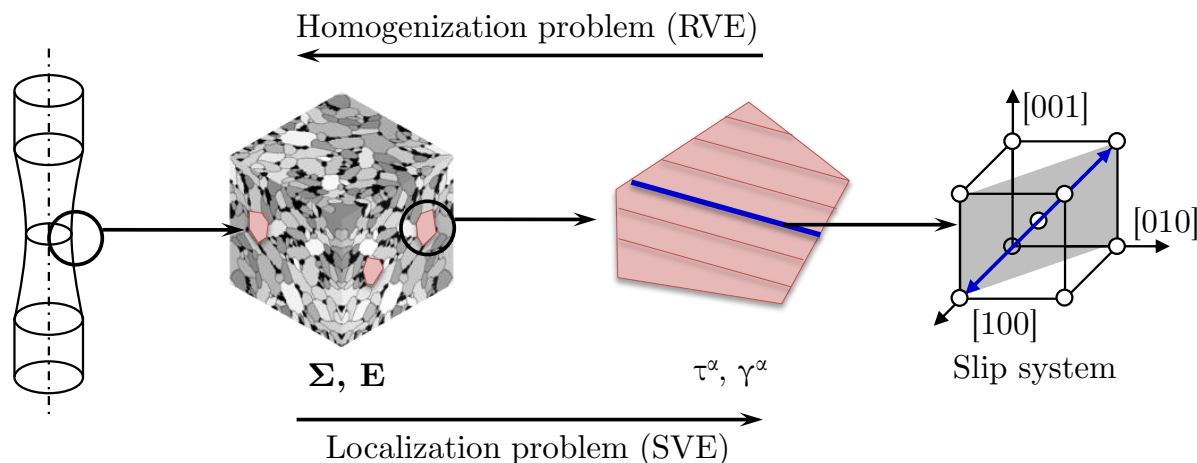


Figure I.20 – Scheme of microstructural mechanics applied to homogenization and localization problems.

As a general framework, microstructural mechanics studies proceed in three steps: the description of the geometric model, the description of the constitutive model and finally the evaluation of a certain field or damage criterion. These three steps will be presented next in regard to the fatigue problem.

3.2 Modeling of polycrystalline aggregates

There exists a wide variety of methods to model polycrystalline aggregates that can be divided into two groups based on the type of study undergone:

- Empirical reconstruction for the direct comparison of simulated mechanical fields with the appearance of damage.
- Synthetic generation in order to capture the variability of a given field based on the variability of certain microstructural parameters.

3.2.1 Empirical reconstruction

Empirical reconstructions are mainly based on two characterization techniques: the diffraction contrast tomography (DCT) and the electron backscatter diffraction (EBSD). Unlike the EBSD method which is destructive, the observation by DCT allows to undertake experiments with interruptions to analyze the microstructure *in situ*. Indeed, EBSD analysis in the depth of the material can be performed through serial sectioning of the surface by mechanical polishing or focus ion beam (FIB) for instance [11, 54, 55]. The different EBSD maps then require to be cleaned to fill the missing points, smoothed and correctly re-positioned to inform each pixel/voxel of the reconstruction [56] (Fig. I.21). The software DREAM.3D [57] was developed with the objective to ease the management and treatment of EBSD data.

While the direct reconstruction ensures a realistic modeling of the microstructure it is maladjusted for fatigue problems that require the computations of several SVEs and would therefore necessitate a large database of similar microstructures.

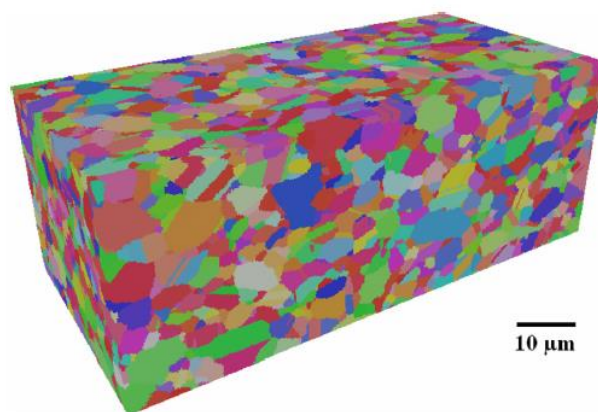


Figure I.21 – 3D reconstruction of IN100 Ni-based superalloy [56].

3.2.2 Synthetic generation

Alternatively, synthetic generations can be used to circumvent this difficulty. Several grain geometries can be found in literature.

The simplest models are often based on regular polygons. For instance, Musinski and McDowell [58] used cubes to represent grains in the case of smooth specimens. Such model was used to calibrate model parameters from smooth specimen experiments. Hexagons are also used in 2D [59] or 3D extruded models [60, 61]. Octahedrons can also be found to generate a 3D geometry with a single grain shape. These types of modeling are relatively unrepresentative from a real microstructure and are mainly applied in statistical studies to evaluate the effect of a specific attribute while the others remain unchanged. For instance Guilhem *et al.* [59] investigated the effect of grain clusters in 2D models where grains were represented as regular hexagons. By changing the crystal orientations of the grains around a specific grain whose orientation was fixed, it has been shown that the orientation of a given grain is not the only critical parameters for its behavior. Indeed, its location (surface, core) and the orientation of its neighbor grains plays a significant role in the plastic activity.

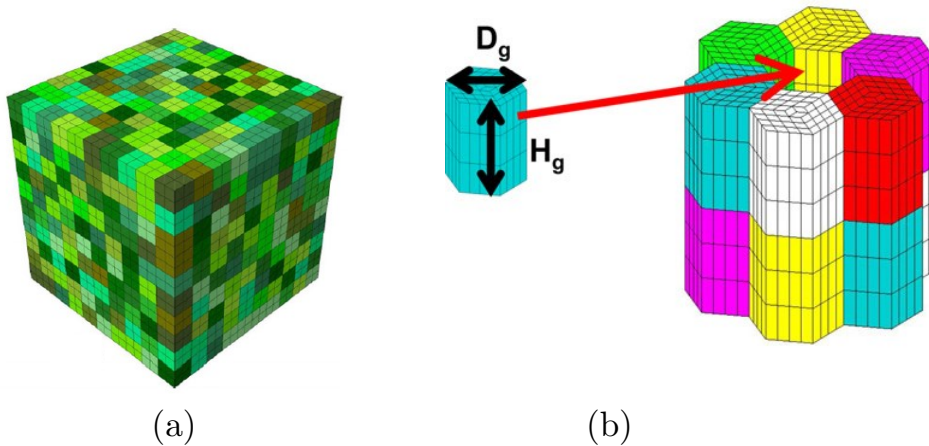


Figure I.22 – (a) Regular geometry used by Musinski and McDowell [58]. (b) Extruded hexagons used by Osterstock *et al.* [61].

More complex geometries are based on the decomposition of a 2D or 3D domain using a tessellation method [62]. Given a set of seeds $X = \{\mathbf{x}_1, \dots, \mathbf{x}_n\}$ and functions $D = \{d_1, \dots, d_n\}$, a tessellation is a partition of space based on dominance regions V_i :

$$V_i = \{\mathbf{x} \in \mathbb{R}^p | d_i(\mathbf{x}, \mathbf{x}_i) \leq d_j(\mathbf{x}, \mathbf{x}_j), \forall j \in \{1, \dots, n\} \setminus \{i\}\} \quad (\text{I.38})$$

The most commonly used tessellation is the Voronoi tessellation where the division function is simply the Euclidian distance between a point \mathbf{x} and a seed \mathbf{x}_i : $d = \|\mathbf{x} - \mathbf{x}_i\|$. The generated cells have non-regular convex geometries with the boundaries defined as segments of the bisector between two seeds. Consequently, edges are flat and two adjacent grains are only connected by one edge. This tessellation is the most applied method for the generation of polycrystalline aggregates [63–73]. Its main advantage lies in the simple definition of the grain boundaries by flat edges or surfaces. The seeds positioning can be based on a Poisson point process where seeds are randomly positioned in the given domain [74, 75]. However, it shows a tendency to generate small and sharp triangle cells in the case of a 2D model [75]. Besides, the grain size distribution cannot be controlled. Controlled Poisson Voronoi tessellation where seeds are positioned with an objective of minimum distance inter-seeds has shown to be successful to reproduce an objective of grain size distribution [76]. Nonetheless, it failed to capture higher moment of statistical distribution of grain morphology. Bertolino *et al.* emphasized the limited accuracy of the

mechanical fields evaluated from the Voronoi tessellation [63]. It was mainly concluded that a modeling scheme to account for the grain shape (aspect ratio) should be used. Groeber *et al.* [77] proposed to use a sequential Voronoi tessellation where one grain would be the union of several adjacent cells in order to represent the grain shape more accurately. More recently, more complex tessellations have been proposed to generate polycrystalline aggregates: the Johnson-Mehl tessellation and the multiplicatively weighted Voronoi (MW-Voronoi) tessellation [78–80]. While the use of weighted division function ensures an accurate grain size distribution, it was pointed out that the isotropy of the weights generates cells with high roundness so that they fail to reproduce the accurate morphology of the microstructure, especially when grains are elongated (Fig. I.23).

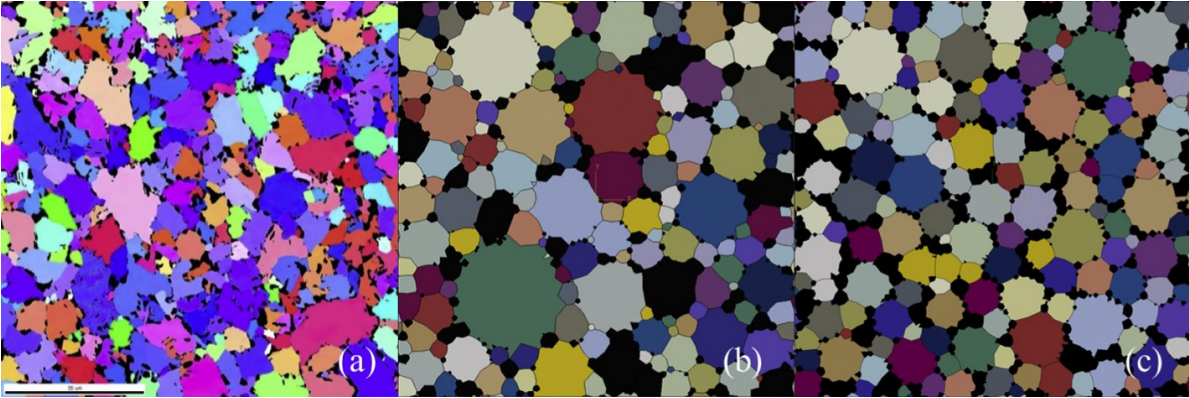


Figure I.23 – Synthetic dual-phase microstructure models based on MW-Voronoi tessellation compared with the microstructure analyzed by EBSD [79].

3.2.3 Meshing of polycrystalline aggregates

The numerical modeling of a polycrystalline aggregate in a FEM software can be based on the use of regular meshes, free meshes or the geometrical description of the grains. Regular meshes use square or cubic elements while free meshes require to use tetrahedon element to correctly follow the grain boundaries. Regular meshes present the main advantage to permit the definition of periodic boundary conditions (PBC) often necessary in homogenization methods. However, they represent a poor approximation of the grain boundaries which exhibit staircase shape. Also, mesh refinement can only be performed globally and not at some local zones of interest. A free mesh however respects the geometry of the grain boundary as nodes are directly positioned on it. As a consequence, excessively small and distorted elements may arise from small grains and sharp areas.

It is worth mentioning that the direct importation of a mesh, regular or free, limits the shape possibilities of the polycrystalline model to simple geometries. The modification of such model requires a careful control of the nodes and elements. Alternatively, explicitly reconstructing grains by computer-aided design (CAD) software facilitates the construction of models with complex shapes [81]. However, such tools are still relatively undeveloped.

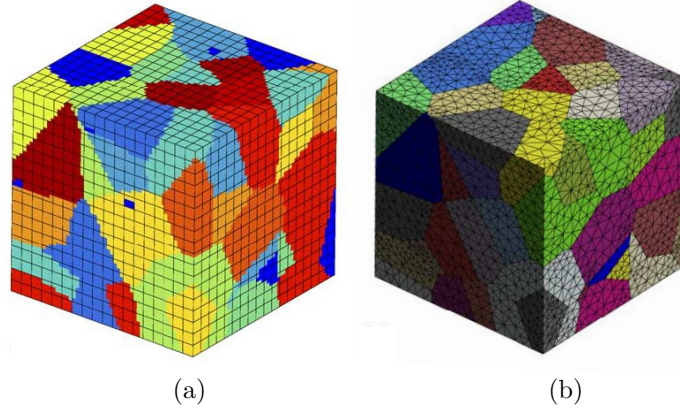


Figure I.24 – Voronoi tessellation: (a) regular mesh and (b) free mesh [82].

3.3 Micro-mechanical modeling of the elasto-plastic behavior

The modeling and evaluation of the mechanical fields in the polycrystals are often based on full-field simulations such as FEM. These simulations are referred as crystal plasticity finite element (CPFEM) models. Recently a spectral solver using Fast Fourier Transform (FFT) and suitable for the simulation of microstructures with PBC was also developed [83, 84]. The general framework of CPFEM is presented in this section.

3.3.1 Finite strain theory

Most of the crystal plasticity models follow the finite strain theory assuming the multiplicative decomposition of the total deformation gradient \mathbf{F} [85]:

$$\mathbf{F} = \mathbf{F}_e \mathbf{F}_p \quad (\text{I.39})$$

where \mathbf{F}_e is the elastic part of the deformation gradient tensor responsible for the rigid-body rotation and stretching of the crystal lattice and \mathbf{F}_p is the plastic part of the deformation gradient. This decomposition is represented in Fig. I.25. Such decomposition introduces an intermediate configuration often referred as relaxed configuration in which the material is only deformed plastically.

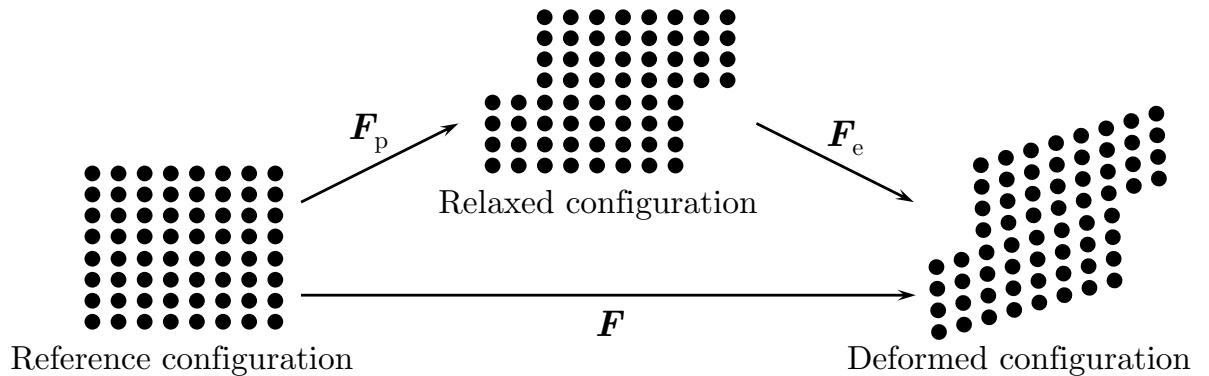


Figure I.25 – Schematic representation of the multiplicative decomposition of the deformation gradient \mathbf{F} .

The velocity gradient in the deformed configuration \mathbf{L} is defined as :

$$\mathbf{L} = \dot{\mathbf{F}} \mathbf{F}^{-1}. \quad (\text{I.40})$$

Applying the product rule of differentiation on Eq. 1.39 and 1.40 gives:

$$\dot{\mathbf{F}} = \dot{\mathbf{F}}_e \mathbf{F}_p + \mathbf{F}_e \dot{\mathbf{F}}_p \quad (\text{I.41})$$

Finally, the velocity gradient can be expressed by:

$$\mathbf{L} = \dot{\mathbf{F}}_e \mathbf{F}_e^{-1} + \dot{\mathbf{F}}_p (\mathbf{F}_p \mathbf{F}_p^{-1}) \mathbf{F}_e^{-1} = \mathbf{L}_e + \mathbf{F}_e (\mathbf{L}_p) \mathbf{F}_e^{-1} \quad (\text{I.42})$$

3.3.2 Elastic behavior

The elastic behavior of a grain is anisotropic. Considering a cubic crystal, the different symmetries of the lattice imply a cubic elasticity of the grain where the fourth order elasticity tensor \mathbb{C} is reduced to three independent coefficients C_{1111} , C_{1122} and C_{1212} and can be written as follows:

$$\mathbb{C} = \begin{pmatrix} C_{1111} & C_{1122} & C_{1122} & 0 & 0 & 0 \\ C_{1122} & C_{1111} & C_{1122} & 0 & 0 & 0 \\ C_{1122} & C_{1122} & C_{1111} & 0 & 0 & 0 \\ 0 & 0 & 0 & C_{1212} & 0 & 0 \\ 0 & 0 & 0 & 0 & C_{1212} & 0 \\ 0 & 0 & 0 & 0 & 0 & C_{1212} \end{pmatrix} \quad (\text{I.43})$$

The elastic Green-Lagrangian strain tensor is denoted by:

$$\mathbf{E}_e = \frac{1}{2} (\mathbf{F}_e^T \mathbf{F}_e - \mathbf{I}) \quad (\text{I.44})$$

where \mathbf{I} is the second order identity tensor. The second Piola-Kirchhoff stress tensor \mathbf{S} can therefore be expressed using the Hooke's law:

$$\mathbf{S} = \mathbb{C} : \mathbf{E}_e \quad (\text{I.45})$$

3.3.3 Plastic behavior

Assuming that plastic deformation is only caused by dislocation slip (twinning, transformation induced mechanisms, etc are not considered in this study), the plastic velocity gradient \mathbf{L}_p can be expressed as the sum of the shear rate on all slip systems [86]:

$$\mathbf{L}_p = \sum_{\alpha=1}^{N_{slip}} \dot{\gamma}^\alpha \mathbf{m}^\alpha \otimes \mathbf{n}^\alpha, \quad (\text{I.46})$$

where $\dot{\gamma}^\alpha$, \mathbf{m}^α and \mathbf{n}^α are the shear rate, slip direction and slip normal of the slip system α , respectively.

It remains to define the constitutive models relating the shear rate $\dot{\gamma}^\alpha$ to the stress tensor \mathbf{S} . Two types of constitutive models can be found in literature: phenomenological models and physics-based model [87]. The main difference lies in the type of internal state variable (ISV) used in their formulation.

Physics-based models use dislocation densities as internal states variables (ISVs) and Orowan type equation for the expression of the shear rate:

$$\dot{\gamma}^\alpha = \rho_m^\alpha b v^\alpha \quad (\text{I.47})$$

where ρ_m is the density of mobile dislocation, b the Burgers vector and v the dislocation velocity. Several models have been developed based on specific dislocation reactions: dipole formation, athermal annihilation, . . . to reproduce certain phenomena observed experimentally. For instance Déprés *et al.* [88] developed a model to account for intragranular kinematic hardening based on the appearance of dislocation dipoles that work as obstacles to plastic slip. This type of model will not be presented as they are not used in this study.

Phenomenological models mainly describe the material state in term of critical resolved shear stress τ_c^α for each slip system α . The shear rate on each slip system is then formulated as a function of the resolved shear stress $\tau^\alpha = \mathbf{S} : \mathbf{m}^\alpha \otimes \mathbf{n}^\alpha$ and critical resolved shear stress. The model proposed by Rice, Hutchinson and Peirce *et al.* is one of the most frequently used model and will be used in our study [86, 89–91]. The model considers a visco-plastic Norton type law:

$$\dot{\gamma}^\alpha = \dot{\gamma}_0 \left| \frac{\tau^\alpha}{\tau_c^\alpha} \right|^n \text{sgn}(\tau^\alpha) \quad (\text{I.48})$$

where $\dot{\gamma}_0$ is the reference shear rate and n is the rate sensitivity exponent. The slip resistance τ_c^α is set to evolve as:

$$\dot{\tau}_c^\alpha = \sum_{\beta} h^{\alpha\beta} |\dot{\gamma}^\beta| \quad (\text{I.49})$$

where $h^{\alpha\beta}$ is the hardening matrix that accounts for the influence of the shearing on the slip system β on the hardening of the slip α . The specific form of the hardening matrix is based on Bronkhorst *et al.* [92]:

$$h^{\alpha\beta} = q^{\alpha\beta} h^\beta \quad (\text{I.50})$$

with,

$$h^\beta = h_0 \left(1 - \frac{\tau_c^\beta}{\tau_{c_s}} \right)^a \quad (\text{I.51})$$

where h_0 , a and τ_{c_s} are the initial hardening coefficient, the hardening exponent and the saturated CRSS. It remains to define the interaction matrix $q^{\alpha\beta}$. The shape of the matrix depends on the crystal structure and so on the type of slip system. The materials studied in this thesis have a BCC structure, therefore the interaction matrix in this crystal will be presented, considering only the $\{110\}\langle\bar{1}11\rangle$ slip system. In such case, the interaction matrix includes 6 independent coefficient, characterizing different types of dislocation interaction [93]:

- q_0 : self-hardening
- q_1 : coplanar interaction
- q_2 : Hirth lock
- q_3 : collinear annihilation
- q_4 : glissile junction
- q_5 : Lomer-Cottrell sessile

The interaction matrix is represented in Table I.1. The interaction coefficients can be evaluated experimentally, for instance by single crystal experiments, or numerically using for example dislocation dynamics. However, for simplification, these parameters are usually set to 1.0 when α and β are coplanar and 1.4 otherwise, rendering the hardening anisotropic.

In this current form, this model is not entirely suitable for the reproduction of cyclic behavior as it does not account for any kinematic hardening effect (Bauschinger effect) characterized by the reduction of the yield stress when the flow stress is reversed. It is worth mentioning, that using this model with a polycrystal will exhibit a small kinematic hardening, also referred as latent kinematic hardening due to the difference in yielding for each grain of the aggregate [94]. Accordingly, Eq. 1.48 was modified to introduce a kinematic back-stress χ^α on each slip system α .

$$\dot{\gamma}^\alpha = \dot{\gamma}_0 \left| \frac{\tau^\alpha - \chi^\alpha}{\tau_c^\alpha} \right|^n \text{sgn}(\tau^\alpha - \chi^\alpha) \quad (\text{I.52})$$

Kinematic hardening is modeled using a simple Frederick-Armstrong rule [95]:

$$\dot{\chi}^\alpha = A\dot{\gamma}^\alpha - B|\dot{\gamma}^\alpha|\chi^\alpha \quad (\text{I.53})$$

Common FEM software such as Abaqus [96] do not possess such crystal plasticity model by default. It should therefore be implemented as a User-material (UMAT) subroutine based on FORTRAN language. The UMAT subroutine DAMASK (Düsseldorf Advanced Material Simulation Kit) [83] is used in this thesis as the finite strain framework and the phenomenological crystal plasticity model are already implemented. The phenomenological model was simply modified to account for the kinematic hardening effect as explained above.

Table I.1 – Interaction matrix in BCC crystal [93].

System	1	2	3	4	5	6	7	8	9	10	11	12
1	q_0	q_1	q_2	q_2	q_3	q_4	q_4	q_5	q_3	q_4	q_5	q_4
2	q_1	q_0	q_2	q_2	q_4	q_3	q_5	q_4	q_4	q_3	q_4	q_5
3	q_2	q_2	q_0	q_1	q_4	q_5	q_3	q_4	q_5	q_4	q_3	q_4
4	q_2	q_2	q_1	q_0	q_5	q_4	q_4	q_3	q_4	q_5	q_4	q_3
5	q_3	q_4	q_4	q_5	q_0	q_2	q_1	q_2	q_3	q_5	q_4	q_4
6	q_4	q_3	q_5	q_4	q_2	q_0	q_2	q_1	q_5	q_3	q_4	q_4
7	q_4	q_5	q_3	q_4	q_1	q_2	q_0	q_2	q_4	q_4	q_3	q_5
8	q_5	q_4	q_4	q_3	q_2	q_1	q_2	q_0	q_4	q_4	q_5	q_3
9	q_3	q_4	q_5	q_4	q_3	q_5	q_4	q_4	q_0	q_2	q_2	q_1
10	q_4	q_3	q_4	q_5	q_5	q_3	q_4	q_4	q_2	q_0	q_1	q_2
11	q_5	q_4	q_3	q_4	q_4	q_4	q_3	q_5	q_2	q_1	q_0	q_2
12	q_4	q_5	q_4	q_3	q_4	q_4	q_5	q_3	q_1	q_2	q_2	q_0

System	1	2	3	4	5	6	7	8	9	10	11	12
Slip normal	$\bar{1}\bar{1}0$	$\bar{1}\bar{1}0$	110	110	$10\bar{1}$	101	$10\bar{1}$	101	$01\bar{1}$	110	110	$01\bar{1}$
Slip direction	111	$11\bar{1}$	$\bar{1}\bar{1}1$	$\bar{1}\bar{1}\bar{1}$	111	$11\bar{1}$	$\bar{1}\bar{1}1$	$\bar{1}\bar{1}\bar{1}$	111	$11\bar{1}$	$\bar{1}\bar{1}1$	$\bar{1}\bar{1}\bar{1}$

3.4 Fatigue criteria and their applications

On the basis of experimental observations described in the Section 2, a wide variety of fatigue criteria has been developed to translate from a micro-mechanical point of view the mechanisms observed experimentally. Their role is to quantify the influence of certain parameters (microstructural, mechanical, environmental) on the fatigue behavior. Several class of criteria exist based on their approaches: empirical, local, global. The review is limited to fatigue criteria based on the critical plane approach.

A critical plane criterion assumes that failure of the material or structure is controlled by the most solicited plane. Traditionally, this concept was applied to macroscopic structures where the critical planes did not have any physical origin except from maximizing a certain criterion. However, based on the observation that nucleation and MSC growth under HCF conditions are strongly influenced by the crystallographic nature of grains, this approach was transposed into microstructural mechanics in which the critical planes are not randomly searched but correspond to discrete crystallographic planes. The notion of Fatigue Indicator Parameter (FIP) was introduced by McDowell and Dunne [97] to express this idea.

3.4.1 Fatigue Indicator Parameters

Following the works of Orowan [98], Dang Van [99] proposed a fatigue criterion based on the assumption that cracks do not nucleate when the response of the grains in the aggregate is elastically adapted. The criterion is a stress-based criterion using: the norm of the resolved shear stress τ on a slip system of normal \mathbf{n} and the hydrostatic stress σ_h . The criterion is defined as a linear combination of these two stress components:

$$\sigma_{DV} = \max_{\mathbf{n}, t} (\tau(\mathbf{n}, t) + \alpha_{DV} \sigma_h(t)) \leq \beta_{DV} \quad (\text{I.54})$$

where $\sigma_h(t) = \frac{1}{3} \text{Tr}(\boldsymbol{\sigma}(t))$ and α_{DV} and β_{DV} are parameters that can be experimentally identified based on the fatigue limit under tension-compression and torsion.

A FIP based on the Tanaka-Mura model described in the first section was also extensively used. The FIP is a strain-based criterion that takes into account the explicit length of the developed slip band and the plastic shear strain amplitude acting on it:

$$FIP_{TM}^\alpha = d \left(\frac{\Delta \gamma^\alpha}{2} \right)^2 \quad (\text{I.55})$$

Fatemi and Socie [100] proposed a mixed criterion that takes into account the plastic shear strain amplitude and the stress normal to the plane of the slip system α , σ_n^α as it promotes the decohesion and opening of a crack.

$$FIP_{FS}^\alpha = \frac{\Delta \gamma^\alpha}{2} \left(1 + k \frac{\sigma_n^\alpha}{\sigma_y} \right) \quad (\text{I.56})$$

where σ_y is the yield stress of the material and k a material parameter. The yield stress σ_y was used to normalize σ_n^α .

It is worth mentioning that these criteria are evaluated on each slip system independently meaning that they are better suited for loading conditions where single slip occurs, such as in HCF regime. Although these criteria were originally based on macroscopic fields and applied to structural mechanics problem, they have received extensive applications in the field of microstructural mechanics using CPFEM as we will see in the next section.

3.4.2 Numerical applications including polycrystalline aggregates

Fatigue crack initiation models

Several studies were proposed for the direct application of the Tanaka-Mura model. Hoshide and Kusuura [64, 65] developed a life prediction method based on the modeling of microstructures using 2D Voronoi tessellations. Each grain was randomly assigned a crystal direction and a single slip band passing through the center of the grain. The resolved shear stress acting on the slip band was evaluated using the Schmid law defined in Eq. 1.19 and the Tanaka-Mura relation in Eq. 1.23 was applied to evaluate the number of cycle for crack initiation. The procedure was repeated until a macro-crack has formed where a Paris' law model was used. Despite its simplicity, the method predicted crack path and fatigue life in relatively good agreement with experimental results for different materials and loading conditions. The method was transposed into FE by Brückner-Foit and Huang [101] and applied to martensitic steel. The procedure was the same than for Hoshide and Kusuura at the difference that the shear stress acting on the slip band was evaluated by FEM. The method was further extended by Kramberger *et al.* [102, 103] to account for multiple slip bands in one grain. The damage accumulated on each band was also recorded as several iterations were necessary to observe the formation of a macro-crack. Finally Briffod *et al.* [104] transposed the approach to pure α -iron material where they considered two orthogonal slip systems instead of one. Despite the fact that the materials were modeled using cubic elasticity and isotropic plasticity, these models emphasized the fact that the first crack to nucleate might not lead to the formation of a macro-crack if neighbor grains are poorly oriented.

One of the first numerical application of CPFEM for fatigue problems was proposed by Bennett and McDowell [105] in 2003. They analyzed three FIPs: the maximum shear strain amplitude, the Dang Van FIP and the Fatemi-Socie FIP. They employed a CP model similar to the one described in Eq. 1.48 assuming a pure kinematic hardening behavior (no isotropic hardening) and only two orthogonal slip systems. A simple 2D model where a grain was represented by one regular element of the mesh was considered. They analyzed the distribution of the fatigue parameters for two types of loading conditions: tension-compression and shear. Using a simplified crack growth model based on a constant FIP, they compared the predicted crack length Vs. FIP with the crack lengths measured experimentally on the surface of ferritic-martensitic steel subjected to the same loading conditions. They showed that the plastic strain amplitude and the Fatemi-Socie FIP could be well correlated to experimental results. However, the conclusions should be carefully accepted considering the high number of simplified assumptions made.

Guilhem *et al.* [59] analyzed the same parameters than Bennett and McDowell using a more realistic 2D model where grains are modeled with regular hexagons. They enriched the previous model by differentiating grains at the free surface and core grains and by accounting for the anisotropy of the elastic behavior. However, a single slip system was considered in this study. The distribution of the different parameters averaged per grain was studied based on the position of the grains (surface, core), their orientations and the orientation of the neighbor grains using the results of 800 simulations. They concluded that the crystal orientation of a grain is not the only critical parameter to be considered. In fact the location of the grain and the crystal orientations of the neighbor grains have a major contribution on the amplitude of the fatigue parameter. This work emphasized the importance of the cluster effect where a group of grains are critically oriented such that explicitly modeling grains and grain boundaries is a crucial aspect of these simulations.

Microstructurally short crack growth models

MSC growth has been the object of less numerical studies than crack initiation for several reasons. Such study requires the explicit modeling of a crack in a FEM model. Several methods exist to simulate a crack. The most common one is the introduction of duplicate nodes at the crack interfaces that are allowed to move independently from each other. This type of crack is often referred as *seam crack*. While this approach is relatively simple to implement, it requires the remeshing of the crack tip for every increment of the crack growth. Also, an interaction should be introduced between two duplicate nodes to avoid the two fracture surfaces to cross each other under compression. Alternatively, the extended finite element method (XFEM) can be used to model crack propagation without the need to remesh the model at each increment [106]. At the difference of a seam crack, cracks in XFEM do not necessarily follow the element nodes as elements are enriched with additional degree of freedom (DOF). A state of the art for this method can be found in [107]. So far this method has received few attention in crystal plasticity studies most likely due to a lack of compatibility between CP and XFEM elements libraries. A last approach is based on the introduction of a degraded stiffness matrix in the elements of the crack interface, such that the elements exhibit a very compliance and can deform excessively. It is worth mentioning that in both case the introduction of a crack may bring some numerical instabilities reducing the convergence rate of the model.

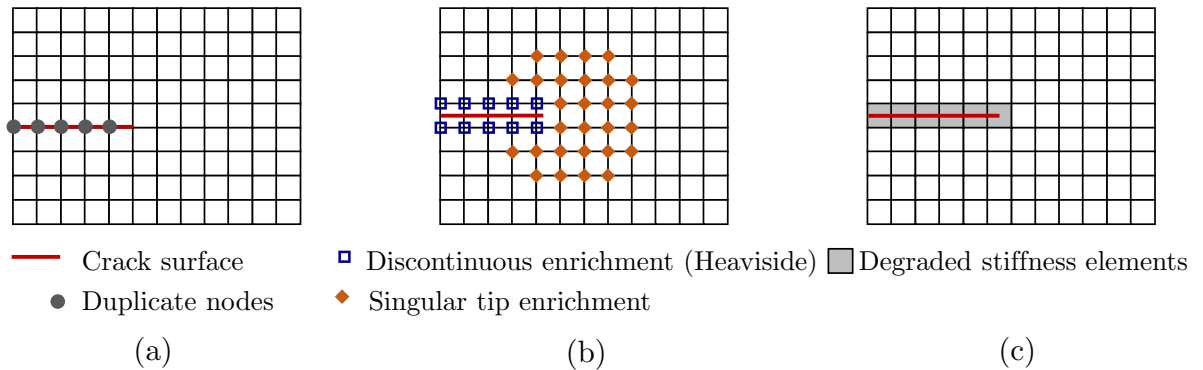


Figure I.26 – Schematic representation of the methods to represent a crack in FEM: (a) seam crack, (b) XFEM and (c) degraded stiffness.

Li *et al.* [108, 109] proposed a 3D crystal plasticity simulation of crack growth in BCC single crystals. The method is based on an iterative simulation and remeshing of the crack tip. Using a fatigue criterion based on the plastic activity around the crack tip, they predicted a crack path exhibiting a zig-zag shape. This method was then applied for the simulation of crack propagation in polycrystals reconstructed from X-ray tomography data [110]. While the results are promising, the computational cost associated with the iterative procedure renders this method prohibitively expensive.

To circumvent the need to explicitly model a crack, Castelluccio and McDowell [111] studied the relation between a Fatemi-Socie FIP and the crack tip displacement (CTD) in a notched copper single crystal. They emphasized the good correlation between the Δ CTD and the FIP suggesting that under certain conditions, it could be used as an indicator for the fatigue crack driving force. Based on this conclusion, they proposed a mesoscale approach for the simulation of MSC growth in polycrystals using a degraded stiffness method [112]. The Fatemi-Socie FIP was averaged over elements belonging to

the same slip plane and used as an indicator for the crack propagation path and for the quantification of the crack growth rate. One major conclusion of their work was that crack nucleation has a lower influence on the variability of fatigue life than MSC growth. They later enriched their conclusions based on a parametric study to observed the sensitivity of their approach for different strain ratios, deformation conditions and geometric discontinuities (presence of a defect or not). Overall, their results showed the same trends than most experimental observations [113].

A promising approach to consider the effect of grain boundary on MSC growth was developed by Musinski and McDowell [114] following the work of Zhai *et al.* [47, 115]. The effect of the grain boundary on MSC growth was accounted through the definition of a crystallographic grain boundary resistance based on twist and tilt angles defined in Eq. 1.23 and Eq. 1.24:

$$R_{GB}(\Psi, \theta) = R_f[1 - \exp(-(\Psi/\Psi_0)^n)] + (C_1 + C_2\Psi)[1 - \exp(-(\theta/\theta_0)^m)] \quad (\text{I.57})$$

where $R_f = 0.65$, $\Psi_0 = 20^\circ$, $n = 8$, $C_1 = 0.25$, $C_2 = 0.0075$, $m = 2$, and $\theta_0 = 15^\circ$ were calibrated based on experimental results [116]. A representation of this relation is given in Fig. 1.27.

They proposed a transgranular crack growth rate model based on this grain boundary resistance. However, it remains unclear whether this resistance should be included in a growth rate or in a retardation model at the grain boundary as it is not obvious how a slip system on an adjacent grain affects the growth of a crack inside a certain grain.

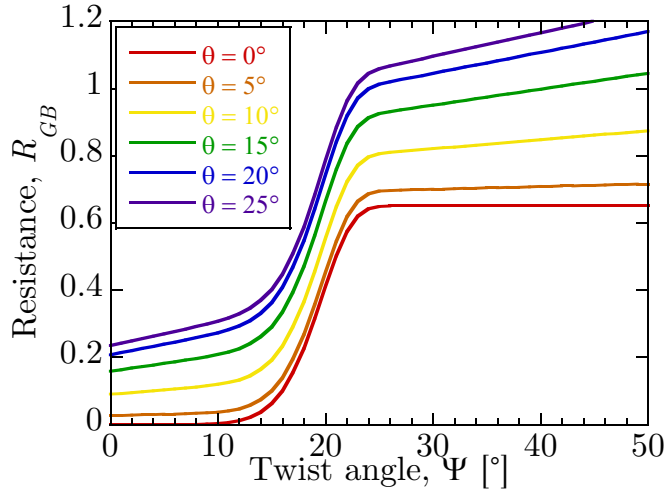


Figure 1.27 – Representation of the grain boundary resistance against the twist angle Ψ for 6 different values of tilt angle θ , based on [116].

3.4.3 Current limitations

McDowell and Dunne extensively reviewed the current potentials and limitations of the microstructure-sensitive approach for the fatigue problem [97]. These limitations can be gathered into several aspects: the microstructure description, the crystal plasticity approach and the models and methods of evaluation of a given FIP.

As described previously, the evaluation of the influence of a certain microstructural parameter is based on the simulation of a set of realizations that are said to be statistically

representative of a given material. However, we have seen that most of the proposed methods use simplified geometrical models, which rises the question of the reliability of the predictions.

The main concern raised by McDowell and Dunne was the current issue regarding the crystal plasticity models that lack realism such as the absence of slip transfer at the grain boundary. Besides, in the case of fatigue, strain localization schemes in dislocation structures (veins, PSB) do not exist. Such model would require a mesh size smaller than the size of the dislocation structures which would greatly reduce the size of the SVE. Also, most CPFEM models simulate fatigue conditions for a few number of cycles and specific methods for accelerating the simulations under cyclic conditions are currently lacking. We can however mention the work of Manchiraju *et al.* [117] who proposed a dual-time-scale finite element model suitable for cyclic simulations using an asymptotic expansion method. Besides, it was shown that the location of highest strain does not change after few cycles so that the prediction of location might be relatively accurate. Finally the question of the use of CPFEM itself for the prediction of crack initiation can also be raised. Indeed, the initiation process is based on some local slip irreversibility that continuum mechanic is unable to evaluate. Discrete dislocation dynamics seems more suitable to address this problem. However, it also faces the problem of the size of the model which so far is limited to simple geometries and boundary conditions.

Finally, a last limitation is regarding the models and methods for the evaluation of the FIP. Indeed, most methods rely on the average of mechanical fields inside each grain which render the method insensitive to local heterogeneities of plastic deformation and insensitive to microstructural attributes such as the grain shape. Besides, few models have been proposed to explicitly account for the effect of the grain boundary with the exception of the one cited above [114].

4 Summary and objectives of the research

We have presented in this chapter a general review of the problem of fatigue in metals. The scattering of fatigue is attributable to both intrinsic and extrinsic factors. The different mechanisms related to the formation and growth of micro-cracks under fatigue conditions were described and relevant models for the prediction of these mechanisms were reviewed. Finally, the current strategy in modeling and predicting fatigue using CPFEM and explicitly modeled polycrystalline aggregates was presented. The possibilities and limitations of this approach were critically discussed.

It has been emphasized that the microstructure, especially the morphology and crystallographic texture can have a significant influence on the fatigue performances. In literature, most of the polycrystalline models are based on simple geometries which due to their simplicity do not account for some microstructural parameters that may play an important role in fatigue problem such as the grain shape or sub-grain structures in the case of carbon steel for instance. Since the variability in fatigue performances is strongly influenced by the microstructure, the prediction of such scattering requires the simulation of a large set of statistical volume elements (SVE) that represent a given material with high fidelity. Accordingly in chapter 2, several original methods based on an anisotropic tessellation are proposed to generate synthetic polycrystalline aggregates. The material studied in this work are also presented from a microstructural point of view.

The evaluation of fatigue criteria in a microstructure-sensitive approach requires the usage of FEM combined with the calibrated crystal plasticity constitutive models. Since a material behaves much differently under cyclic conditions than under monotonic conditions, cyclic experiments should be conducted and a procedure for the identification of the parameters should be developed. This is the subject of the chapter 3. Fatigue experiments with notched specimen are also conducted to evaluate the nucleation life and microstructurally short crack growth rate for the different materials.

Finally we have shown that most criteria are based on the averaging of mechanical fields over a grain domain which makes them insensitive to intragranular heterogeneities as well as microstructural features (grain shape, grain boundaries). Accordingly, the fourth and last chapter is dedicated towards the simulation of polycrystalline aggregates under cyclic condition and the evaluation of various fatigue criteria sensitive to microstructural attributes. The predictive capabilities and limitations of the approaches will be critically discussed.

Chapter II

Microstructural characterization and modeling of synthetic polycrystalline aggregates

Contents

1	Introduction	42
2	Microstructural characterization of the materials	42
2.1	Chemical compositions and thermal treatments	42
2.2	Morphological and crystallographic analyses	47
3	Spatial tessellations for the generation of synthetic microstructures	58
3.1	Seed definition and sampling	58
3.2	Spatial tessellations	59
3.3	Reconstruction of grain boundaries	64
4	Analysis and reproduction of crystallographic texture	66
4.1	Descriptions of crystalline orientation	66
4.2	Orientation distribution function	67
4.3	Discretization of unweighted orientations	69
4.4	Discretization of weighted orientations	69
4.5	Discretization of orientations for martensite packets and blocks	70
5	Validation of the approaches	72
5.1	Comparison of synthetic and reconstructed grain boundaries	72
5.2	Comparisons between synthetic and real microstructures	73
5.3	Generation of martensitic microstructures	75
6	Summary	77

1 Introduction

This chapter is dedicated towards the microstructural characterization and modeling of the materials studied in this work. The primary objective of this chapter is to develop numerical tools to generate synthetic polycrystalline aggregates based on statistical data obtained from experimental observations. Since the final objective of this research is to simulate microstructures under cyclic conditions, a particular attention is addressed towards the exportability of the model into the finite element software Abaqus. More precisely, it is desired to propose a scalar representation of the polycrystalline aggregates such that complex geometries, free meshing and the introduction of explicit cracks are possible.

The chapter is decomposed into four sections. At first, the materials studied in this work are presented, the morphological and crystallographic features relevant for the generation of synthetic microstructures are described. The different developed methodologies for the generation of synthetic polycrystalline aggregates are then explained. The methods to reproduce a given crystallographic texture obtained from EBSD measurements are described and finally, some comparisons are made between real and synthetic microstructures to validate the different proposed approaches.

2 Microstructural characterization of the materials

2.1 Chemical compositions and thermal treatments

2.1.1 Chemical compositions

The materials investigated in this work are mainly low-alloy steels. They were delivered as a 15 mm hot-rolled sheets. The chemical compositions of the different materials are given in Table II.1. They are classified as low-carbon steels (hypo-eutectoid) as the carbon content is always comprised between 0.05 and 0.25 wt%. They show very similar chemical compositions. For each material, one specific alloying element was introduced/modified (highlighted in Table II.1). Molybdenum (Mo) and niobium (Nb) are known to favor alpha phase while carbon (C), chromium (Cr) and manganese (Mn) are alloying elements that stabilize the γ austenite. Also niobium is known to ease grain refinement. The presence of boron (B) in the case of the material E is known to contract the γ field on a Fe-C phase diagram.

Table II.1 – Chemical composition of the different low-carbon steels (in mass%, in ppm for B,N,O)

Steel	C	Si	Mn	P	S	Mo	Nb	Cr	Al	B	N	O
FP	0.07	<0.01	1.52	0.006	0.003	-	-	-	0.028	-	-	-
B	0.151	0.013	1.53	0.007	0.0020	0.193	-	-	0.028	-	21	21
C	0.156	0.012	1.52	0.006	0.0016	-	0.030	-	0.029	-	21	14
E	0.151	0.011	1.55	0.005	0.0015	-	-	-	0.029	10	27	13
SM570Q	0.093	0.228	1.56	0.01	0.002	0.03	0.027	0.14	0.036	1	37	10

A commercially-produced α -iron of high purity (99.5%) is also studied in this work. It is chosen as a starting material for our study due to its relative simplicity compared to other steels. Besides, some literature is available for both experimental and numerical studies.

2.1.2 Thermal treatments

Most of the materials with the exception of α -iron and ferrite-pearlite (FP) steel received a thermal treatment. From the different hot-rolled sheets, blocks of $12 \times 13 \times 85$ mm were cut along the rolling direction as shown in Fig. II.1. A specific and localized thermal treatment was then applied in the center of each block on a length of about 8 mm. Fig. II.2 shows a schematic representation of the two patterns. In both case the material is first heated with a heating rate of 50°C/s until reaching a temperature $T_1 = 1400^\circ\text{C}$ and $T_2 = 1000^\circ\text{C}$ in the pattern 1 and 2 respectively. The temperature is held for 5 s. In the first pattern, the material is then cooled at a cooling rate of 50°C/s until reaching the temperature T_2 where the cooling rates are identical. Several different cooling rates are applied at this stage: 50, 30, 10 and 1°C/s until reaching the temperature of 250°C . The material is kept at this temperature until the temperature becomes uniform throughout the cross-section (martempering), thus resulting in lower residual stresses that usually accompany martensitic formation.

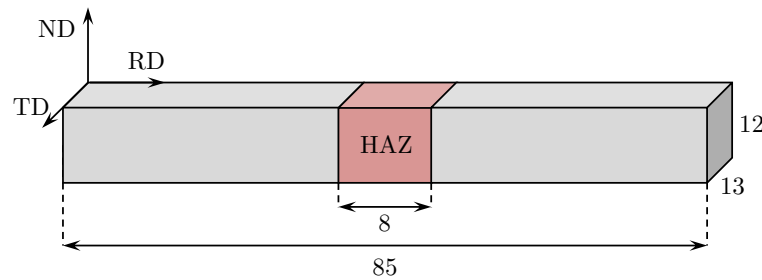


Figure II.1 – Dimensions of the blocks cut in the 15mm hot-rolled sheet for the localized heat-treatment.

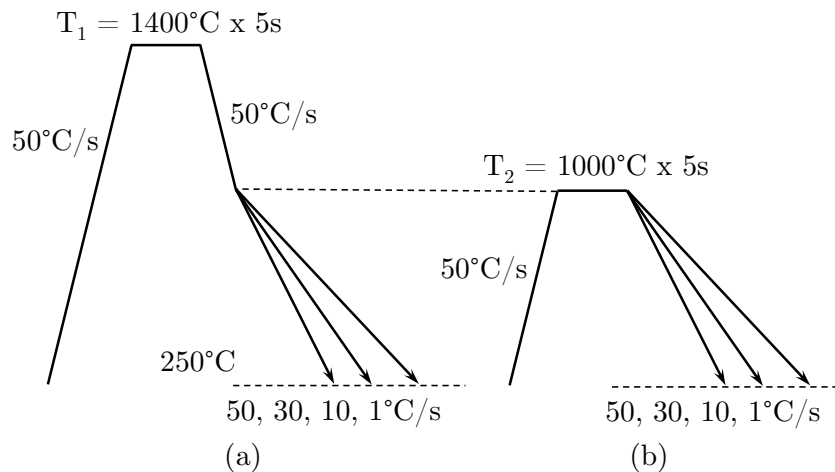


Figure II.2 – Scheme of the two treatment patterns with a peak temperature of (a) 1400°C and (b) 1000°C .

These thermal treatments can be described in two parts:

Austenitization: the steel is heated until reaching the austenite domain in which its crystal structure changes from BCC to FCC. The austenite domain on a Fe-C diagram is approximately located between 723 and 1400 °C for the low-carbon steels of our study. The size of the austenite grain is determined by this step. Grain size generally increases with the peak temperature. In this regard, the main difference between the two thermal treatment patterns is the peak temperature reached. Coarse microstructure is therefore expected for materials subjected to the pattern 1.

Quenching : in this step, the material is cooled extremely quickly. Consequently, displacive transformations have time to take place but not diffusive transformations leading to the formation of meta-stable phases: bainite and martensite and to the absence of thermodynamically stable pearlite.

2.1.3 Martensitic transformation

The martensitic transformation is athermal and occurs below a certain temperature referred as martensite-start temperature M_s . The extent of martensitic transformation is often described based on the Koistinen-Marburger relation:

$$V_{\alpha'} = 1 - \exp(\beta(M_s - T_q)) \quad (\text{II.1})$$

where $V_{\alpha'}$ is the fraction of martensite, T_q is the temperature to which the temperature is cooled and $\beta = -0.011$ is a constant. In the case of low-carbon steels, the Andrews relation is generally applied to estimate the temperature M_s based on the weight fraction of alloying elements. This relation is given by:

$$M_s = 539 - 423\%C - 30.4\%Mn - 17.7\%Ni - 12.1\%Cr - 7.5\%Mo \quad (\text{II.2})$$

It is admitted in this relation that each alloying element has an independent influence on the temperature M_s . In practice, alloying elements decrease M_s . The main contribution comes from the carbon where a variation of 0.1% leads to a reduction of M_s by more than 40°C. The presence of manganese in all the studied material also contributes toward the reduction of this temperature. Also, the addition of molybdenum in the case of the B materials decreases the start temperature.

From a microstructural point of view, the martensitic transformation is described as a shear mechanism accompanied with a volume expansion. Carbon atoms are trapped in the voids of the FCC austenite and cannot form the stable ferrite and cementite phases. They have to stay in the same position during the transition of the austenite phase to the martensite phase. The FCC crystal structure may accept a lot of carbon atoms in its tetrahedral and octahedral sites. This is not the case for the BCC crystal which will, therefore, become saturated in carbon. Carbon atoms will occupy the octahedral sites of the BCC structure inducing a tetragonal deformation in the [001] axis. The crystal structure of the martensite is body-centered tetragonal (BCT). However, for low-carbon steel (<0.2%), the crystal structure is very close to a BCC. In the context of our study, we will then assume that the martensite has a BCC crystal structure.

The transition from the "parent" austenite to the "child" martensite occurs following specific orientation relations (OR). The interface between the martensite and the prior austenite is called *habit plane*. In low-carbon steel, the Kurdjumov-Sachs (KS) OR is mainly observed:

$$\{111\}_{\gamma} // \{011\}_{\alpha'}; \langle \bar{1}01 \rangle_{\gamma} // \langle \bar{1}\bar{1}1 \rangle_{\alpha'} \quad (\text{II.3})$$

where the (011) plane of the α' crystal lies parallel to one of the γ $\langle 111 \rangle$ plane. Similarly, one of the α' $\langle \bar{1}\bar{1}1 \rangle$ direction is parallel to one of the γ $\langle \bar{1}01 \rangle$ direction. The choice of 4 governing planes and 6 governing directions leads to 24 possible variants. We can cite also the Pitsch, Nishiyama-Wasserman, Greninger-Troiano ORs that can be found in other types of steels. An illustration of the lattice correspondence between the martensite and the austenite lattice is given in Fig. II.3. The KS OR will be further described in Section 4.

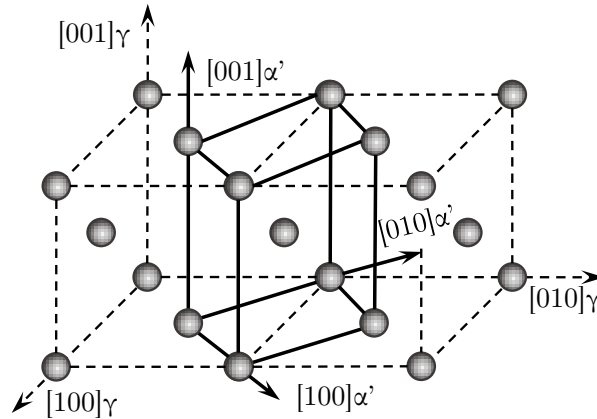


Figure II.3 – Lattice correspondence between austenite and martensite crystals.

2.1.4 Phase distribution

The formation of martensite is strongly dependent on the cooling rate which is affected by the chemical composition of the steel and by the prior austenite grain size. Continuous cooling transformation (CCT) diagram is often used to predict which phase transformation will take place in the material based on a given cooling rate. These diagrams are generally built based on dilatometry analysis. Alternatively, they may be predicted using specific software such as JMatPro. Fig. II.4 shows the predicted CCT diagram by JMatPro for the B material subjected to the first thermal treatment pattern. With a cooling rate of 10°C/s , the microstructure is predicted to be entirely made of martensite. This is consistent with the application of the Eq. II.1 and II.2 with the chemical composition given in Table II.1. Table II.2 summarizes the different heat treatments applied to the different materials as well as the phase fraction predicted by the software JMatPro. A name is given to each material based on the initial material and the heat treatment pattern in order to ease their descriptions in the rest of the thesis.

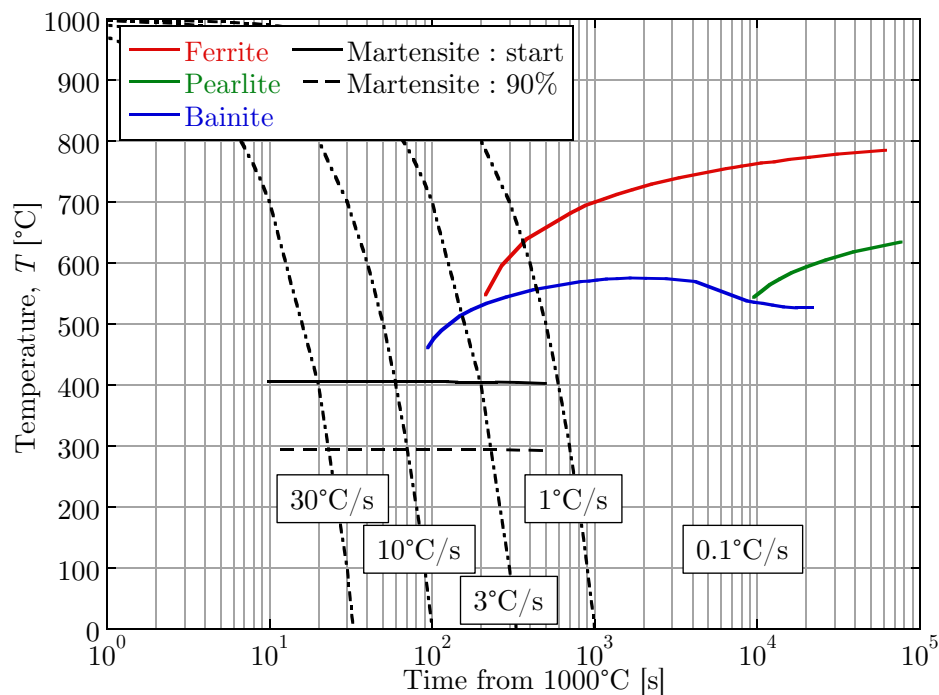


Figure II.4 – CCT diagram of the B material subjected to the first thermal treatment pattern

Table II.2 – Materials studied in this research.

Steel	Heat treatment		Phase fraction [%]				Name
	\nearrow [°C]	\searrow [°C/s]	Ferrite	Pearlite	Bainite	Martensite	
α -Fe	-	-	100	0	0	0	α -iron
FP	-	-	91.8	8.2	0	0	FP
B	1000	1	44.3	0.6	55.1	0	B10-01
		30	5.4	0	70.6	24	B10-30
	1400	10	0.2	0	1.6	98.2	B14-10
C	1000	30	17.5	0	82.5	0	C10-30
E	1400	10	1.9	0	9.4	88.7	E14-10
SM570Q	1400	10	0.6	0	0.3	99.1	57-14-10
	1000	50	10.8	0	8.1	81.1	57-10-50

2.2 Morphological and crystallographic analyses

Specimens for the microstructural characterization were cut (in the heat affected zone (HAZ) for the heat-treated materials), mechanically polished and ion beam cross polished (CP). Microstructural observations were done using an optical microscope in the case of the heat-treated specimens in order to observe the prior austenite grains. In every case, observations were performed on the normal direction (ND) face of the specimen as shown in Fig. II.1. The simulations conducted in this work mainly focused on three materials: α -iron, FP steel and B14-10 steel. The choice of B14-10 steel was motivated by the fact that we can assume it is entirely composed of martensite and that the prior austenite grains are very large which allowed us to analyze the martensitic microstructure more precisely. Therefore, the analysis presented in this section focuses only on these three materials.

The observations are described material by material. Scanning electron microscopic (SEM) observations, as well as Electron Back Scattering Diffraction (EBSD) analyses, were performed for all the materials. EBSD observations and texture measurements were conducted using the software *TSL OIM Analysis 7*.

2.2.1 α -iron

EBSD analysis was conducted on a $450 \times 600 \mu\text{m}$ window, with a step size of $3 \mu\text{m}$. The material is constituted of a single ferrite phase. The EBSD data was cleaned to remove unindexed pixels and to attribute to each grain a single orientation based on the average orientation of all the pixels constituting the grain. The EBSD map is composed of 221 grains.

Microstructure analysis

Fig. II.5(a) shows the image quality (IQ) map of α -iron. Instead of characterizing the material in term of grain size distribution as it is traditionally the case, the grains morphology is here described using an ellipse fitting process following the work of Groeber *et al.* [56, 77]. In their work, several EBSD data were obtained by serial sectioning such that grains were described by ellipsoids. Ellipsoids were characterized in term of aspect ratios, spatial orientations, surface-to-volume ratio, and volume. Accordingly, in our study each grain is fitted into an ellipse that can be characterized by three parameters: the grain major axis a , the aspect ratio b/a (b being the minor axis) and the ellipse orientation angle θ relative to the global coordinates. The ellipse fitting process is performed using the software *TSL OIM Analysis 7*. At first, the major axis and orientation of each ellipse are determined by connecting the two furthest pixels of a grain. The minor axis is then adjusted so that the area of the ellipse πab corresponds to the grain area. It can be mentioned that another method based on the least-square fitting of the ellipse to the perimeter points of the grain also exists but is not used in our study for the reason that we explicitly seek the area of the ellipse to match the area of the grain. The fitted ellipses are reported on the IQ map in Fig. II.5(a).

Several observations can be made from the ellipse fitting process. First, it is noted that ellipses can overlap each other and partially lie outside the domain. Also, some regions may not belong to any ellipse. The area occupied by non-overlapping ellipses represents about 82.5% of the domain; the overlapping regions represent 8.4% and the

empty space 9.1%. These observations will be useful in the microstructure generation methods presented in Section 3.

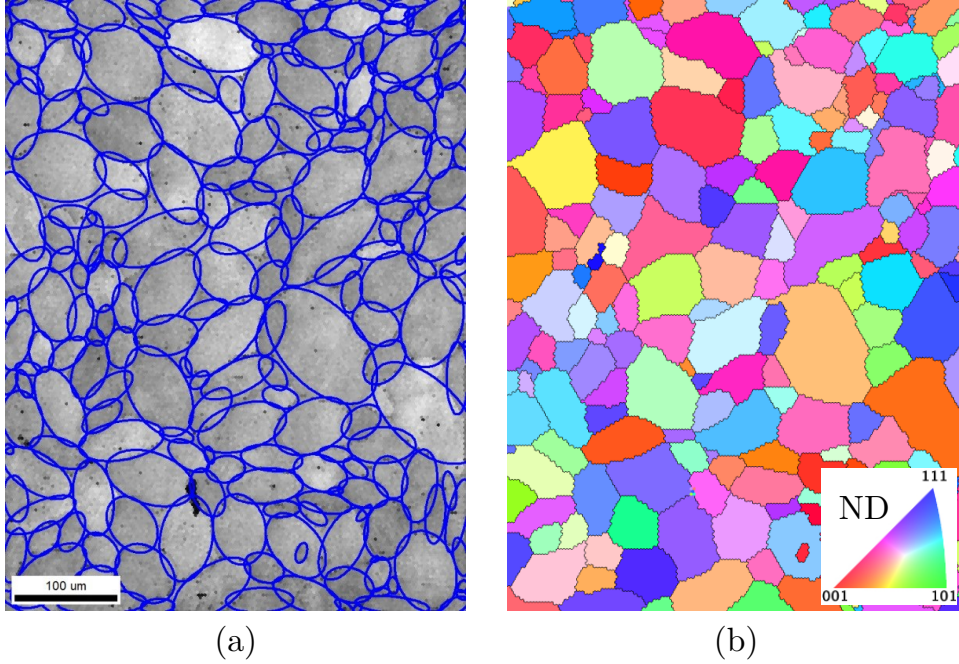


Figure II.5 – (a) IQ map of the α -iron with and ellipse fitted to each grain. (b) EBSD map with IPF color coding.

The ellipse data are then fitted with probability distribution functions (PDF) using the maximum likelihood method and the software Matlab. The histograms, PDF and cumulative distribution functions (CDF) are shown in Fig. II.6. For the grain major axis a , considering the positive skewness of the histogram, the log-normal distribution is used as a fitting distribution. The gamma distribution is also sometimes used to describe the grain size distribution. The log-normal probability density function is given by

$$f(x|\mu, \sigma) = \frac{1}{x\sigma\sqrt{2\pi}} \exp\left(-\frac{(\ln x - \mu)^2}{2\sigma^2}\right) ; x > 0 \quad (\text{II.4})$$

where μ and σ are the location and scale parameters respectively. The estimated parameters are $\mu = 3.05$ and $\sigma = 0.573$. The mean major axis length is about $24.8 \mu\text{m}$, and the standard deviation is about $15.1 \mu\text{m}$.

Next, in view of the relative symmetry of the histogram of the aspect ratio b/a , the normal distribution is used as a fitting function. The normal probability density function is given by

$$f(x|\mu, \sigma) = \frac{1}{x\sigma\sqrt{2\pi}} \exp\left(-\frac{(x-\mu)^2}{2\sigma^2}\right) \quad (\text{II.5})$$

where μ and σ are the mean and standard deviation respectively. The estimated parameters for the distribution are $\mu = 0.513$ and $\sigma = 0.117$. It is worth noting that the normal distribution is centered around 0.5 suggesting that the use of the average grain size and therefore the approximation of the grains with circles is not appropriate in our study. Finally, the histogram of the grain orientation does not reveal any particular distribution. Accordingly, the grain orientations are fitted with a non-parametric distribution based on normal kernel smoothing function of 5° bandwidth. A shorter bandwidth results in a

strongly oscillating distribution while a larger bandwidth tends to smooth the distribution. Overall the distribution is evenly spread in the orientation range. It is therefore possible to consider an uniform distribution for the grain orientation without a loss of information.

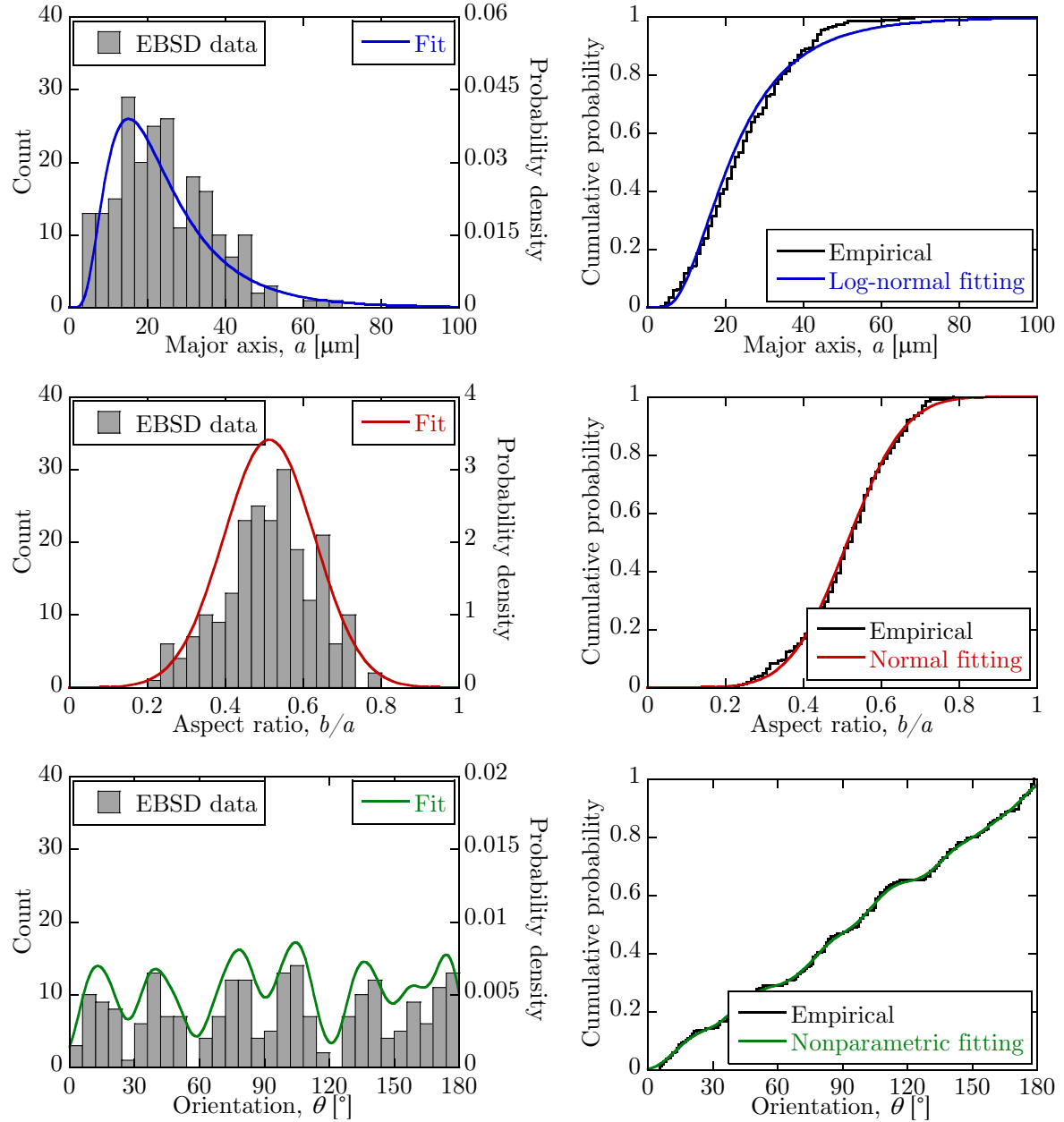


Figure II.6 – Histograms and empirical and fitted cumulative distribution functions of the grain major axis a , aspect ratio b/a and orientation θ for the α -iron.

Texture analysis

Fig. II.5(b) shows the EBSD map with inverse pole figure (IPF) color coding of the α -iron. In order to describe the texture of the material, the pole figures are evaluated based on the calculation of the orientation distribution function (ODF). The definition of the ODF will be given in Section 4. The estimation of the ODF from the EBSD data is performed using the toolbox MTEX [118] for Matlab. The continuous ODF is calculated

through a series expansion of spherical Gaussian distribution with a half-width of 10° . Fig. II.7 shows the $\{100\}$, $\{110\}$ and $\{111\}$ pole figures calculated from the ODF.

The material does not exhibit any strong texture as the pole figure densities are mainly centered around 1 which correspond to a uniform ODF. However, few peaks are still present with an intensity close to 2. These peaks may be related to some local micro-texture or most likely to the lack of representativity of the EBSD map which only contains 221 grains. The calculation of the ODF with a half-width of 5° , shows peaks with an intensity of about 3.5.

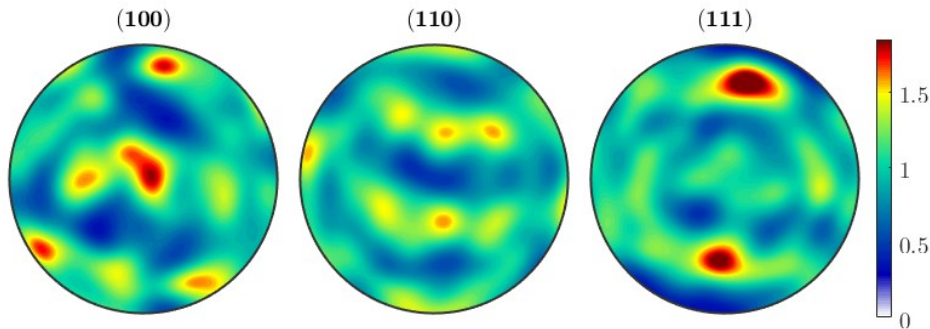


Figure II.7 – $\{100\}$, $\{110\}$ and $\{111\}$ pole figures reconstructed from the ODF of the α -iron.

2.2.2 Ferrite-Pearlite steel

For FP steel, EBSD analysis was performed on a $200 \times 400 \mu\text{m}$ window, with a step size of $1 \mu\text{m}$.

Microstructure analysis

The material is used and observed as-received. Therefore, considering the carbon content of 0.07%, a pearlite fraction of about 8.2% is expected. To differentiate the two phases, two parameters are used: the image quality (IQ) and the Kernel Average Misorientation (KAM). The IQ describes the relative quality of a diffraction pattern which is affected by the local distortion of the crystal lattice. Any variation of the lattice curvature will reduce the quality and the pixels will appear darker. Accordingly, the IQ is enabled to highlight several features such as grain boundaries, strain trace, and lath structure. The KAM corresponds to the average misorientation of the center of a kernel with all the points at its perimeter. It can be estimated based on the first or n th nearest neighbor. When extended to all the elements inside a grain, it is referred as Grain Average Misorientation (GAM). Considering the lamellar structure of pearlite, it is expected that the IQ and the KAM will be able to separate the two phases. It is worth mentioning that the step size of $1 \mu\text{m}$ is too high to be able to observe any lamellar patterns.

Fig. II.8 shows the IQ map, KAM map and IPF map of the material. The threshold of the IQ to separate ferrite from pearlite is adjusted so that regions highlighted in the KAM map appear in black on the IPF map. With this threshold, the pearlite fraction is about 4.5% which is lower than the one predicted from the Fe-C diagram. This can be related to the fact that pearlite is not randomly positioned but localized in banded regions meaning that the pearlite content varies in the ND direction. EBSD analyses are also performed in the TD and RD sections and reveal pearlite contents of 5.6% and 8.2%

respectively. Here again, the relatively small window size might not be representative enough of the material and EBSD analysis on a larger window might have been necessary.

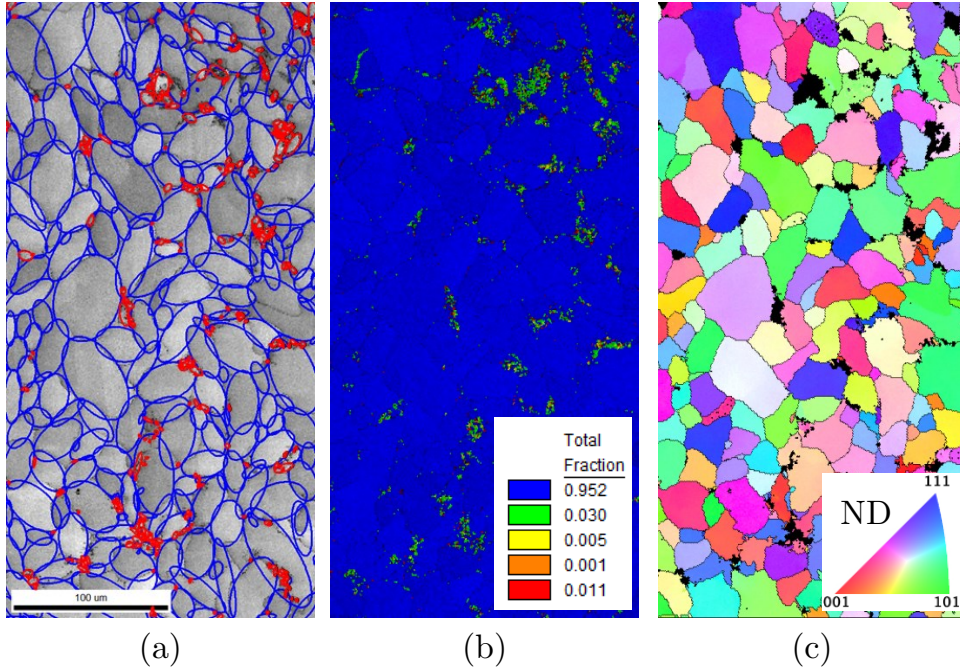


Figure II.8 – (a) IQ map of FP steel with and ellipse fitted to each grain. Blue ellipses correspond to ferrite grains, red ellipses to pearlite grains. (b) KAM map discretized with 5 levels. Ferrite grains appear in blue. (c) EBSD map with IPF color coding, pearlite grains appear in black.

Ellipses are also extracted and fitted to the same probability distributions than in the case of the α -iron. The data are reported in Fig. II.9 and II.10 for the ferrite and pearlite phases, respectively. The parameters of the log-normal and normal distributions for the major axis and aspect ratio for both phases are reported in Table II.3. The mean major axis length is about $14 \mu\text{m}$ and the standard deviation is about $10 \mu\text{m}$ for the ferrite grains. It can again be observed that the ellipse aspect ratio is also centered around 0.5. Besides in this material, ellipses show a preferential direction as the distribution of the orientation θ exhibits a peak on the PDF around 90° (inflection on the CDF) which corresponds to the rolling direction.

Table II.3 – Parameters of the fitted distribution for the FP-steel.

Phase	Ferrite	Pearlite
Phase fraction	95.2%	4.80%
Major axis, a	μ	2.43
	σ	0.649
Aspect ratio, b/a	μ	0.479
	σ	0.120

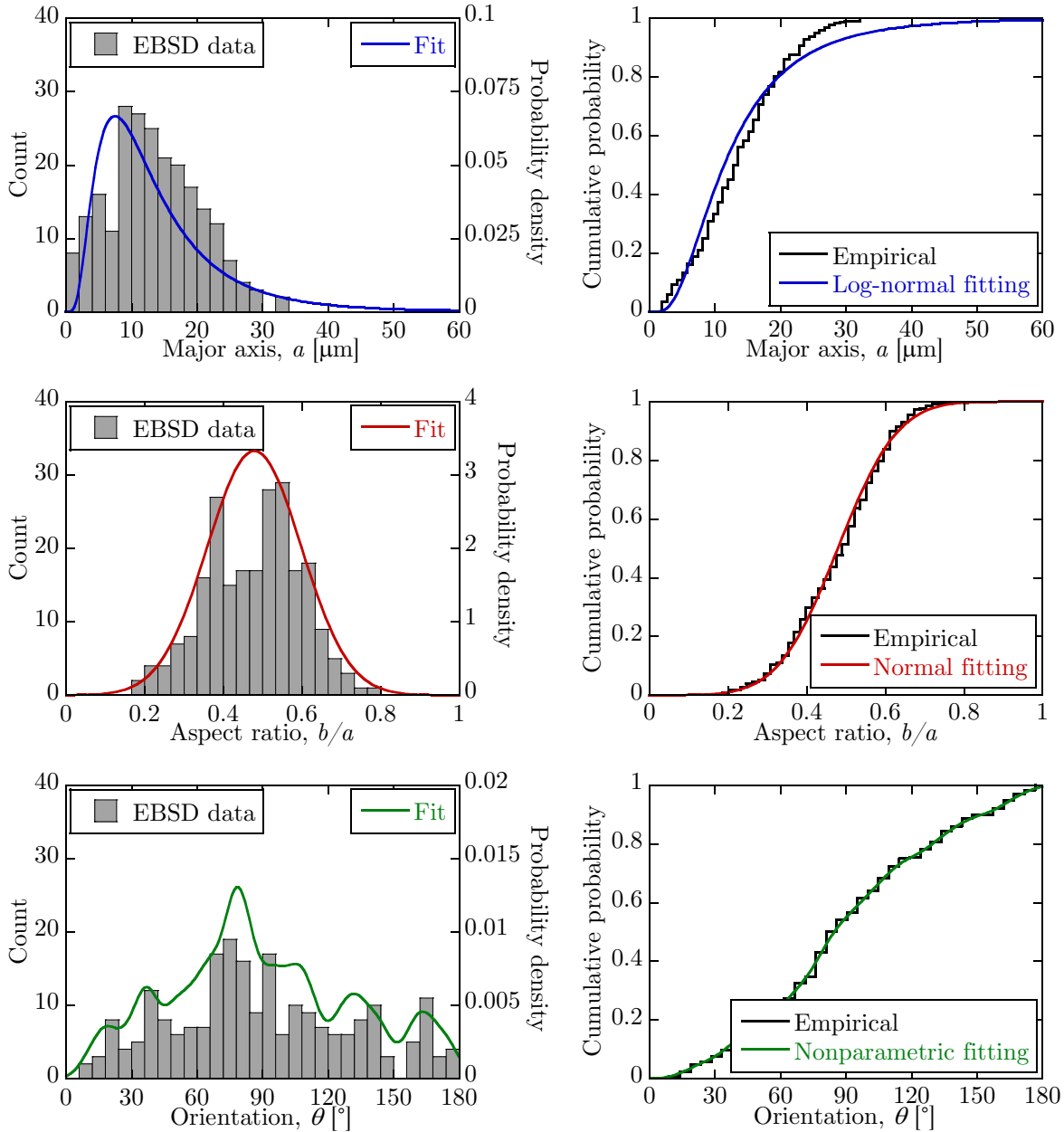


Figure II.9 – Histograms and empirical and fitted cumulative distribution functions of the grain major axis a , aspect ratio b/a and orientation θ for the ferrite of the FP steel.

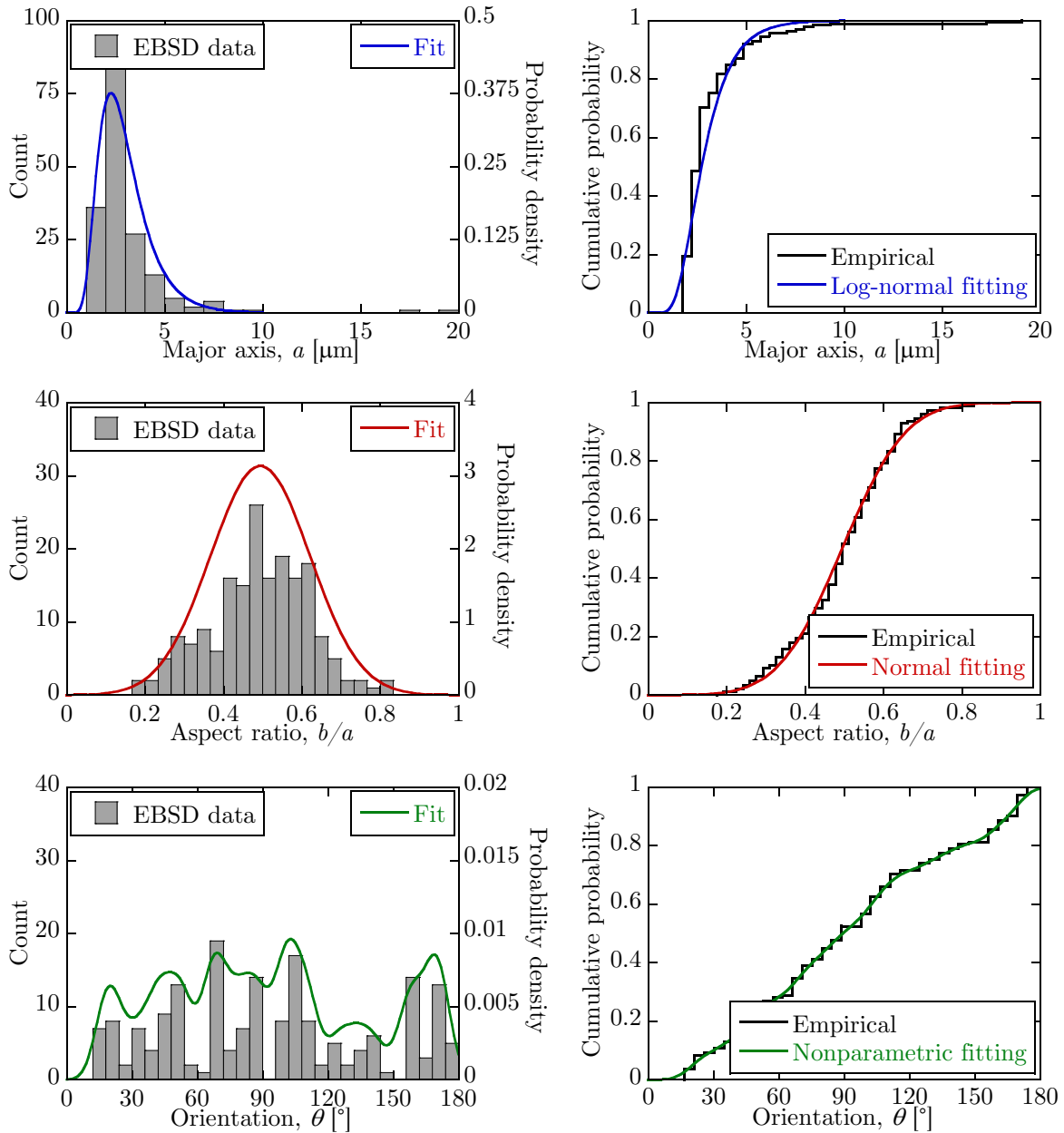


Figure II.10 – Histograms and empirical and fitted cumulative distribution functions of the grain major axis a , aspect ratio b/a and orientation θ for the pearlite of the FP steel.

Texture analysis

Fig. II.11 shows the $\{100\}$, $\{110\}$ and $\{111\}$ pole figures calculated from the ODF of the FP steel. Compared to α -iron, FP steel shows a lower texture as the density is close to 1. The few peaks may here again be attributed to the relatively low number of grains (228 in Fig. II.6).

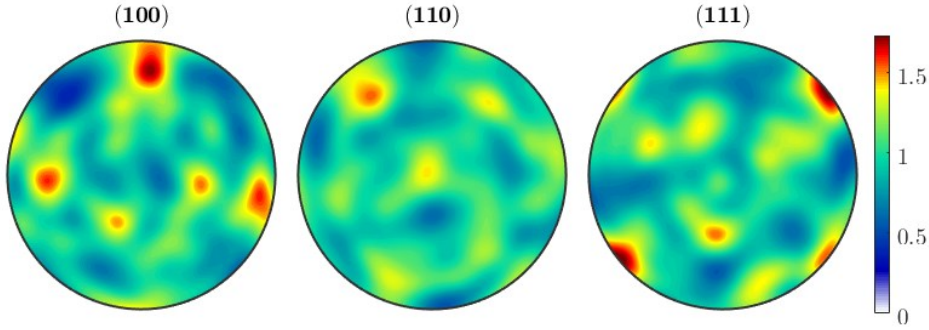


Figure II.11 – $\{100\}$, $\{110\}$ and $\{111\}$ pole figures reconstructed from the ODF of the FP steel.

2.2.3 B14-10 steel

As opposed to the previous materials, the microstructural study of B14-10 steel (and most of the other steels) requires several processes due to the different structures that can be observed in a martensitic steel.

To characterize the martensitic microstructure, we follow the description proposed by Morito *et al.* [119] and Kitahara *et al.* [120]. A schematic diagram of the decomposition is shown in Fig. II.12(a). Packets are defined as groups of laths sharing the same habit plane (4 possibilities) and blocks correspond to groups of laths sharing the same direction (6 possibilities per habit). A representation of the 24 variants of a $[100]$ prior austenite crystal orientation is shown on a $\{110\}$ pole figure in Fig. II.12(b). The blue points correspond to the parent crystal orientation, the red points are the 24 variants. This type of pattern is typical of a martensitic grain and will be used to identify the grains and separate the different packets within a martensite grain.

Prior austenite grains are first observed by optical microscope on the specimen as shown in Fig. II.13 (a). The grain boundaries are revealed using a hot corrosion method. The grain boundaries are manually drawn and the average grain size is estimated using the Jeffries planimetric method. At first, the number of grains inside n_{inside} and intercepting $n_{intercept}$ the micrograph are counted. The number of grains is recommended to be higher than 50. From Fig. II.13 (a), $n_{inside} = 49$ and $n_{intercept} = 36$. The average grain area is finally given by:

$$A_{avg} = \frac{A}{M^2(n_{inside} + 0.5n_{intercept})} \quad (\text{II.6})$$

where A is the area and M is the magnification. The average grain size corresponds to the square root of the average grain area. Applying this formula to the micrograph in Fig. II.13 (a), an average grain size of $535 \mu\text{m}$ is obtained.

Four EBSD analyses were conducted on $500 \times 500 \mu\text{m}$ windows, with a step size of $1 \mu\text{m}$. Fig. II.13 (b) depicts the four EBSD maps with IPF color coding. The treatment of

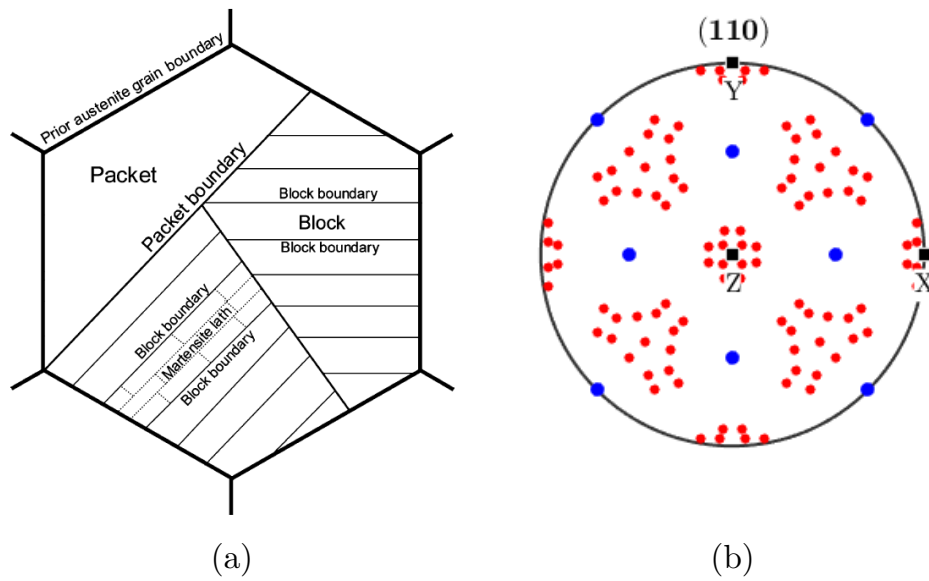


Figure II.12 – (a) Schematic diagram of the hierarchical decomposition of martensite [120]. (b) $\{110\}$ pole figure of the 24 variants (in red) of a $[100]$ prior austenite crystal orientation (in blue).

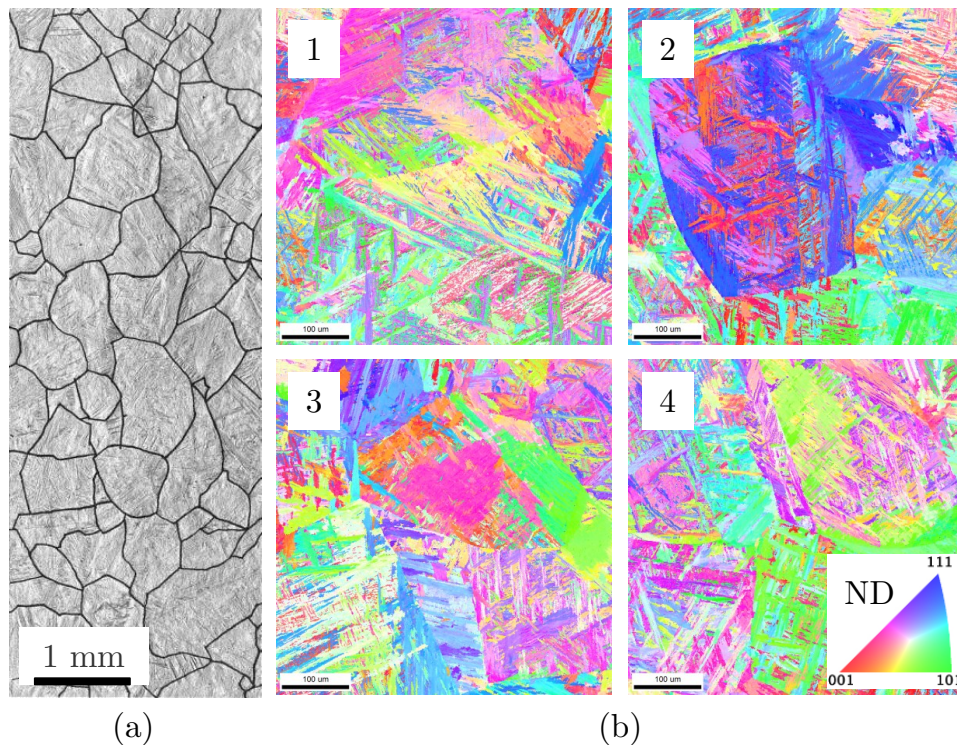


Figure II.13 – (a) Optical micrograph of the B14-10 material. (b) $500 \times 500 \mu\text{m}$ EBSD maps with IPF color coding.

the EBSD maps for the analysis can be decomposed in several successive steps summarized in Fig. II.14 and described as follows:

1. **Identification of the prior austenite grains within the EBSD map:** this step is an iterative cropping procedure. At first, the $\{110\}$ pole figure of the EBSD map is represented and the map is cut until a single pattern, similar to that of Fig. II.12 is obtained. Isolated points on the pole figure and on the EBSD map are

- then assigned to the closest group during a cleanup process. Fig. II.14(b) shows an isolated prior austenite grain as well as its $\{110\}$ pole figure.
2. **Identification of the packets:** from the $\{110\}$ pole figure of a single grain, variants belonging to the same habit plane are highlighted and used to extract the indexed points belonging to it in the EBSD map. Fig. II.14(c) shows the identified packets and Fig. II.14(d) represents one isolated packet.
 3. **Ellipse fitting of the blocks:** this step is similar to the ellipse fitting process described for the two previous materials. However, as laths are not considered in our study, a tolerance angle of 11° is set to remove the possible presence of lath boundaries within a given block as lath boundaries usually exhibit a misorientation angle of 10.5° .

Due to the size of the prior austenite grains compared to the window size, few complete grains (3-5) occupy each of the EBSD maps. A grain should contain all the 24 variants of the KS OR in order to be analyzed. Indeed, according to Morito *et al.* [119], all six possible variants are formed with an equal volume fraction in a given packet.

Fig. II.15 shows an example of an isolated grain as well as the density distributions of the major axis length, aspect ratio and orientation of the blocks in each packet. The conclusions drawn from the observation of this result is general as similar data were found for other grains. Blocks present the same distributions of major axis and aspect ratio, independently of the packets. The density of the major axis seems to indicate a relatively small average length ($<10 \mu\text{m}$). However, this density does not account for the actual area occupied by each block. In general, a bi-modal block distribution is observed where each packet contains few large blocks of the size of the packets and a large number of small blocks. The aspect ratio distributions also show that blocks are elongated with a mean aspect ratio of about 0.23 and a maximum at around 0.8. The last aspect concerns the orientation of the blocks. As can be seen, it is not random as each packet seems to have a preferred orientation.

When representing the trace of the $\{111\}_\gamma$ plane, it is noticed that the elongated direction was parallel to one of these planes. In fact, when calculating the orientation of the $[\bar{1}\bar{1}1]$ or $[\bar{1}1\bar{1}]$ directions, it was found that one of them is always close to being parallel with the direction of elongation. This is consistent with the extensive observations of Morito *et al.* [119, 121] who showed that the boundaries of blocks and sub-blocks are almost parallel to the $\langle 101 \rangle$ directions in low and ultra-low carbon steels.

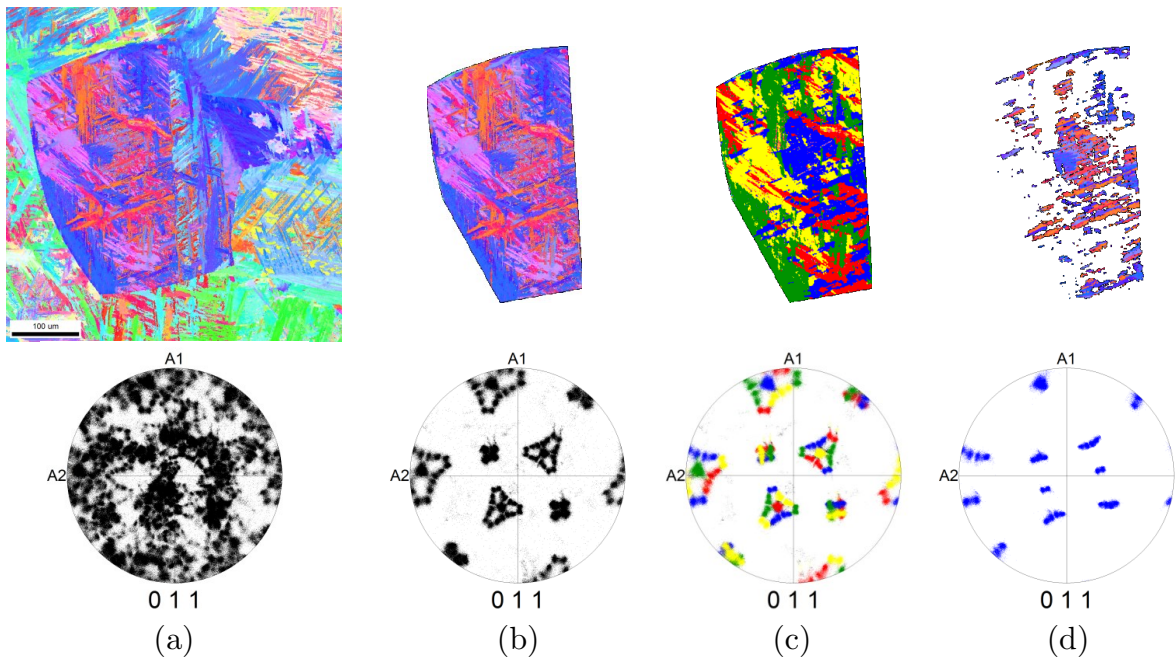


Figure II.14 – (a) Initial EBSD map. (b) Isolated grain. (c) Identification of the four packets based on the orientations in the pole figure. (d) Analysis of one packet using an ellipse fitting process.

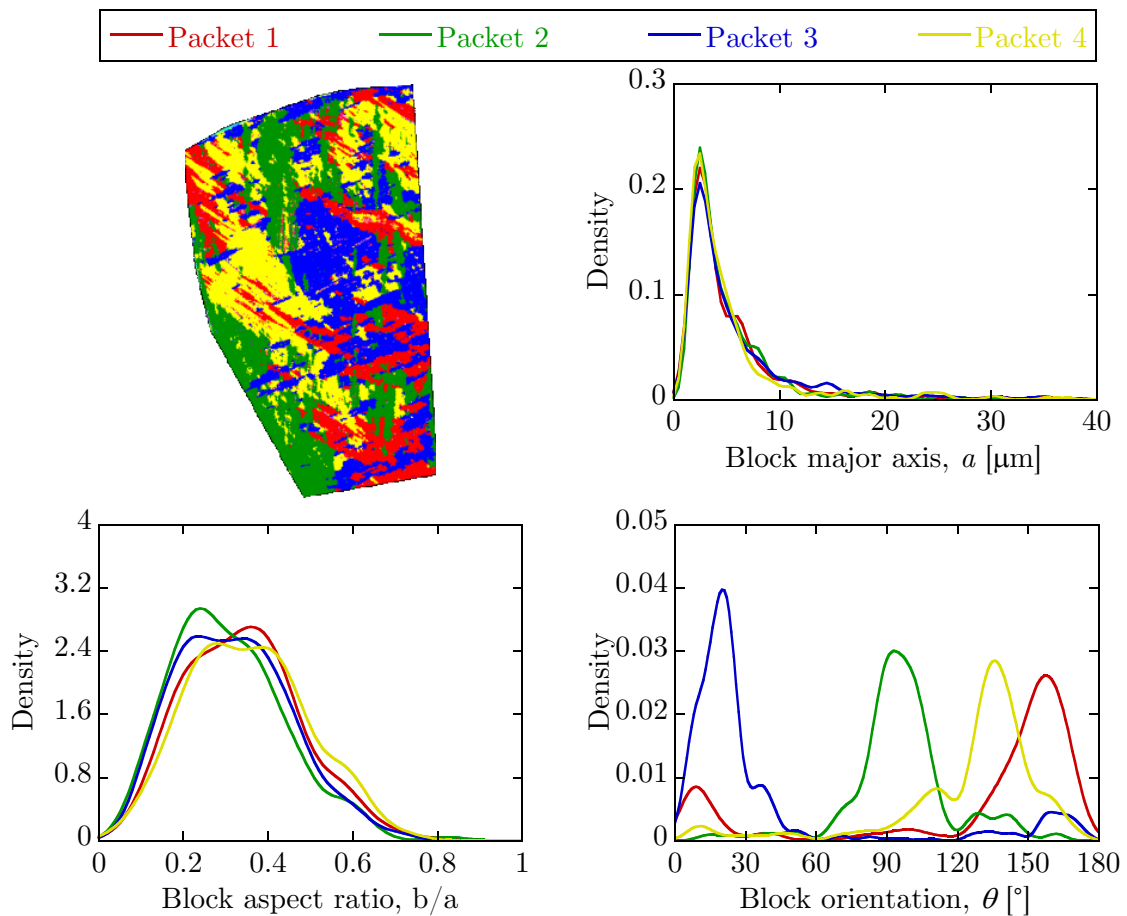


Figure II.15 – Probability densities of the major axis, aspect ratio and orientation of the block in the four packets of the isolated grain in Fig. II.14.

3 Spatial tessellations for the generation of synthetic microstructures

The microstructural observation of the materials by EBSD analyses revealed several scales of heterogeneity. For α -iron and FP steel the main scale arises from the different crystal orientation of each grain. In the case of martensitic steels, at least three scales may be considered: prior austenite grains, packets, and blocks. The ellipse fitting process also highlighted the fact that grains are generally not equiaxed since their aspect ratio are not close to 1. It seems therefore necessary to develop procedures that can reproduce such anisotropy and multi-scale heterogeneity.

The generation of synthetic microstructures is based on the tessellation method as presented in Chapter I. A tessellation is a partition of space through the definition of dominance regions V_i [62]:

$$V_i = \{\mathbf{x} \in \mathbb{R}^p \mid d_i(\mathbf{x}, \mathbf{x}_i) \leq d_j(\mathbf{x}, \mathbf{x}_j), \forall j \in \{1, \dots, n\} \setminus \{i\}\} \quad (\text{II.7})$$

A tessellation requires three information: a domain Ω , a set of seeds or kernel $X = \{\mathbf{x}_1, \dots, \mathbf{x}_n\}$ and a set of metric functions $D = \{d_1, \dots, d_n\}$.

3.1 Seed definition and sampling

Let Ω be a domain of \mathbb{R}^2 corresponding to the size of the microstructure to be generated. The objective of this section is to inform Ω with a set of seeds. Seeds are described as ellipses based on the observations made in Section 2. They are sampled from CDF such as the one determined in the previous section and a random number generator following a uniform distribution. The number of seeds n is increased until the total surface occupied by the ellipses exceeds a given threshold proportional to the domain area:

$$\pi \sum_{i=1}^n a_i b_i \geq (1 + \lambda)A \quad (\text{II.8})$$

where a_i and b_i respectively correspond to the major and minor axis of the ellipse i , λ is an efficiency factor and A is the area of the domain Ω . Considering the overlapping and empty area evaluated in the ellipse fitting of the EBSD measurements, λ is initially set to 20%. It can be mentioned that the major axis and aspect ratio are sampled independently.

Once the ellipses are sampled, they are positioned into the domain. Random closed packing (RCP) of non-overlapping disks or spheres is often used to position the seeds into the domain [122–125]. It is worth saying that the circle packing problem is a NP-complet problem meaning that there is no existing algorithm solving the problem in polynomial time. One can distinguish two types of algorithms: sequential and rearrangement methods. Here, a relaxed random sequential addition (RSA) algorithm is used [122]. The original RSA is based on three rules:

1. Objects are sequentially and randomly positioned.
2. Objects may not overlap.
3. Already inserted objects may not move.

The second rule comes in contradiction with the ellipse fitting process which allows them to overlap. Besides, as ellipses cannot overlap, the resulting grains are necessarily

larger than their corresponding ellipses. However, the areas of the ellipses are set to correspond to the area of the final grains. It will then be necessary to perform a controlling loop to ensure the correct size distribution which will require the modification of the initial statistical distributions. Accordingly, in this study, the close packing algorithm is relaxed by allowing the ellipses to overlap with the simple condition:

$$\frac{(x - x_i)^2}{a^2} + \frac{(y - y_i)^2}{b^2} > (1 + \beta)^2 \quad (\text{II.9})$$

where β is an overlap percentage as proposed by St-Pierre *et al.* and is set to 20% [126]. We will see in the last section that such relaxation grants an accurate representation of the grain size distribution. The irreversibility implied by the third rule means that the RSA may fail to position the ellipses so that several trials may be necessary to find a good configuration. The ellipses are positioned starting from the largest to the smallest.

Fig. II.16 shows an example of a final configuration at the end of the seeding process. The ellipses are sampled from the data of α -iron and the domain is $400 \times 400 \mu\text{m}$. The area occupied by a single ellipse represents 76.9% of the domain, the empty area 9.76% and the overlap area, 13.34%. These values are in good agreement with experimental data.

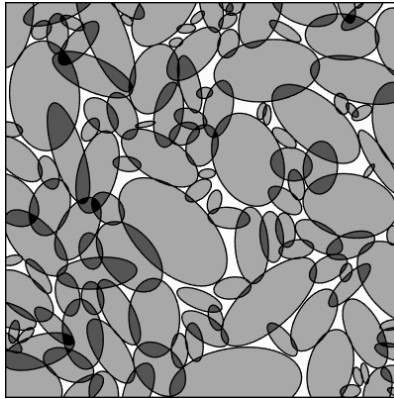


Figure II.16 – Example of a final configuration of the seed sampling process.

3.2 Spatial tessellations

3.2.1 Anisotropic tessellation

Since the set of seeds is known, the set of metric functions $D = \{d_1, \dots, d_n\}$ remains to be defined. When the function d_i is the Euclidian norm between two points:

$$d_i(\mathbf{x}, \mathbf{x}_i) = \|\mathbf{x} - \mathbf{x}_i\| \quad (\text{II.10})$$

the resulting tessellation is the Voronoi tessellation. A generalization of the Euclidian distance, named the Minkowski distance of order p is defined as:

$$d_p(\mathbf{x}, \mathbf{x}_i) = \left(\sum_{i=1}^q |x_i - y_i|^p \right)^{\frac{1}{p}} \quad (\text{II.11})$$

where q is the dimension of the domain space ($q = 2$ in our case). When $p = 1$ or $p = 2$ the Minkowski distance is the absolute value or the Euclidian distance respectively. Note that the Minkowski distance is a metric function only when $p \geq 1$ as Eq. II.11 violates

the triangle inequality otherwise. The dominance region defined in Eq. III.23 can then be interpreted as the growth of a cell with the shape controlled by the function d_p . Fig. II.17 illustrates the shape of the cell growth using the Minkowski distance for different value of p in \mathbb{R}^2 .

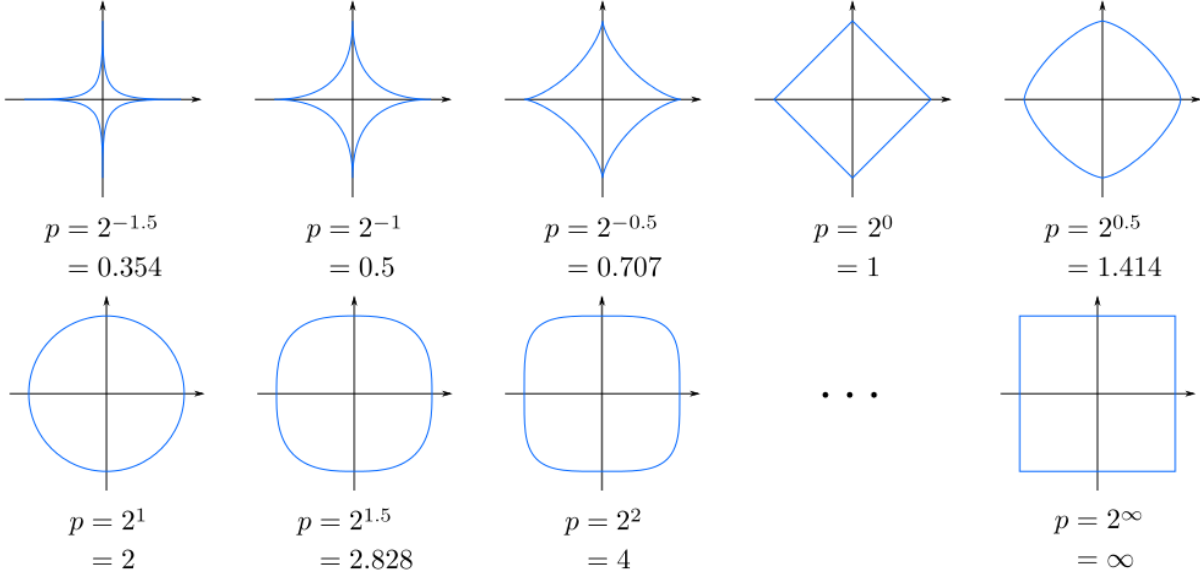


Figure II.17 – Representation of the unit circle for different values of p

Several remarks can be made from the observation of Fig. II.17. First, in every case, the growth shows at least orthotropic symmetry, with the exception of the Euclidian norm which is isotropic.

The following discussion is restrained to such a particular case where $p = 2$ as it corresponds to the Voronoi tessellation. The Voronoi diagram is composed of convex cells with linear boundaries separating two adjacent dominance regions. One of the main difficulties when using the Voronoi tessellation for microstructure modeling is that each cell grows identically so that the final microstructure is only dependent on the initial seeds position. Therefore, to ensure a certain grain size distribution, the seeds positioning should be carefully controlled. Indeed, in the case of randomly positioned seeds, the grain size distribution often follows a normal distribution which deviates from most observations [77]. Several methods exist to control the seed positioning to ensure a certain grain size distribution and shape regularity [76].

Alternatively, weighted tessellations such as the Laguerre tessellation or the multiplicatively weighted Voronoi (MW-Voronoi) tessellation directly consider the grain size objective by attributing a different weight to each kernel [127, 128]. The division function of the Laguerre tessellation is defined by:

$$d(\mathbf{x}, \mathbf{x}_i) = \|(\mathbf{x} - \mathbf{x}_i)\| - w_i \tag{II.12}$$

The division function of the MW-Voronoi tessellation is given by:

$$d(\mathbf{x}, \mathbf{x}_i) = \|w_i(\mathbf{x} - \mathbf{x}_i)\| \tag{II.13}$$

In such case, the resulting cells are curved based on segments of Apollonius circles, with convex and concave edges. The growth is here again isotropic which leads to cells with high roundness.

3. SPATIAL TESSELLATIONS FOR THE GENERATION OF SYNTHETIC MICROSTRUCTURES

As a consequence, in order to model the grain morphology with a higher morphology that accounts for the grain shapes, an anisotropic tessellation is proposed that uses the information stored in the end of the ellipse sampling process. The function is defined by

$$d(\mathbf{x}, \mathbf{x}_i) = \|\mathbf{W}_i(\mathbf{x} - \mathbf{x}_i)\| \quad (\text{II.14})$$

where the anisotropic weight matrix \mathbf{W}_i is given by

$$\mathbf{W}_i = \begin{pmatrix} \frac{\cos \theta_i}{a_i} & \frac{\sin \theta_i}{b_i} \\ -\frac{\sin \theta_i}{b_i} & \frac{\cos \theta_i}{a_i} \end{pmatrix} \quad (\text{II.15})$$

Developing Eq. II.14 with Eq. II.15, one can recognize the formula of a rotated ellipse and interpret the subsequent tessellation as an anisotropic MW-Voronoi diagram (later simply referred as anisotropic tessellation) in which the weight is dependent on the direction defined by the center of the ellipse \mathbf{x}_i and the point \mathbf{x} compared to the ellipse angle θ_i . The weight is at its maximum when the direction is aligned with the major axis and decreases until reaching a minimum when aligned with the ellipse minor axis. For the particular case where the ellipse is a circle, the function is equivalent to the Eq. II.12 such that the anisotropic tessellation can be seen as a generalization of the MW-Voronoi diagram.

Fig. II.18 represents the Voronoi, MW-Voronoi and anisotropic tessellations of the seeds in Fig. II.24. In the case of the MW-Voronoi tessellation, the weight w_i is set to $1/\sqrt{a_i b_i}$ as it corresponds to a circular seed with the same area than the ellipse seed. The area of the generated cells against the area of the ellipses are reported in Fig. II.19 for the three tessellations. Overall, the cell area of the MW-Voronoi tessellation and the anisotropic tessellation agree correctly with the ellipse area. In the case of the Voronoi tessellation, the cells area are more uniform. Indeed, one can notice that cells corresponding to small ellipses are larger than the ellipses areas. This observation is reversed for the large ellipses. This was to be expected as the Voronoi tessellation does not hold any information except the initial seed position while the two other tessellations contain weight relative to an area objective. Of course, one can argue that the ellipse positioning is not suitable for the Voronoi tessellation. Controlled Poisson Voronoi tessellation has indeed shown to be successful to reproduce a certain grain size distribution [76]. However, the shape can only be reproduced for a material with a high regularity. It can be noted especially for small seeds, that the tessellated grains present a high roundness in the case of the MW-Voronoi tessellation while they are almost fully elliptical in the anisotropic tessellation.

While several algorithms exist to construct the Voronoi and the MW-Voronoi diagrams [62, 129], the higher complexity due to the anisotropic weight render an analytical formulation of the cell boundaries difficult in our case. In order to simplify the construction of the tessellation, we first adopt a raster formulation where the domain is meshed with regular elements. For a given element centered on \mathbf{x} , it becomes straightforward to evaluate to which dominance region it belongs according to Eq. III.23. The precision of the tessellation is directly controlled by the density of the mesh. Despite not explicitly calculating the boundaries, this method presents the advantage to make a model that can be easily exported into finite element software. The regular mesh is also particularly suitable for simulations in which periodic boundary conditions (PBC) are requested. In this regard, periodic tessellations may be necessary. They are presented in the next section.

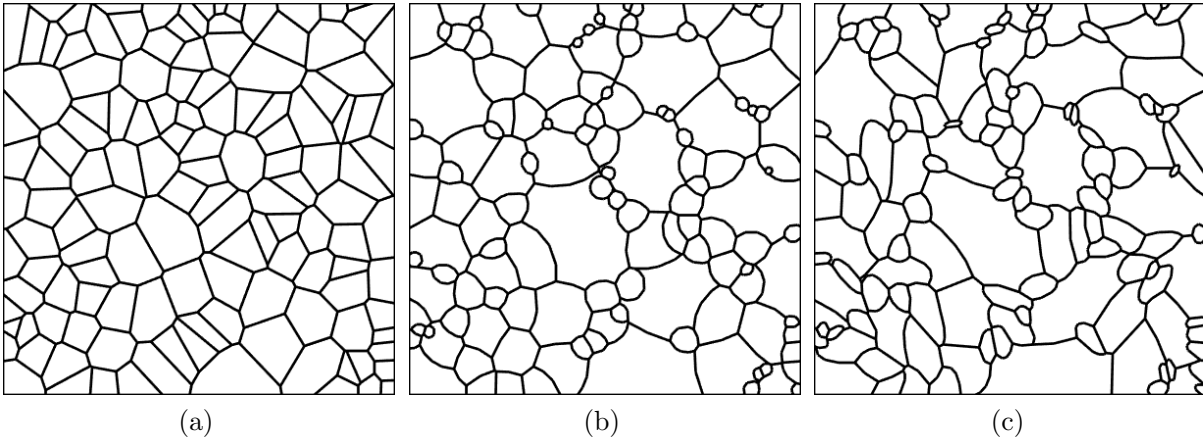


Figure II.18 – Voronoi, multiplicatively weighted Voronoi and anisotropic tessellations of the final configuration of the seed sampling in Fig. II.16.

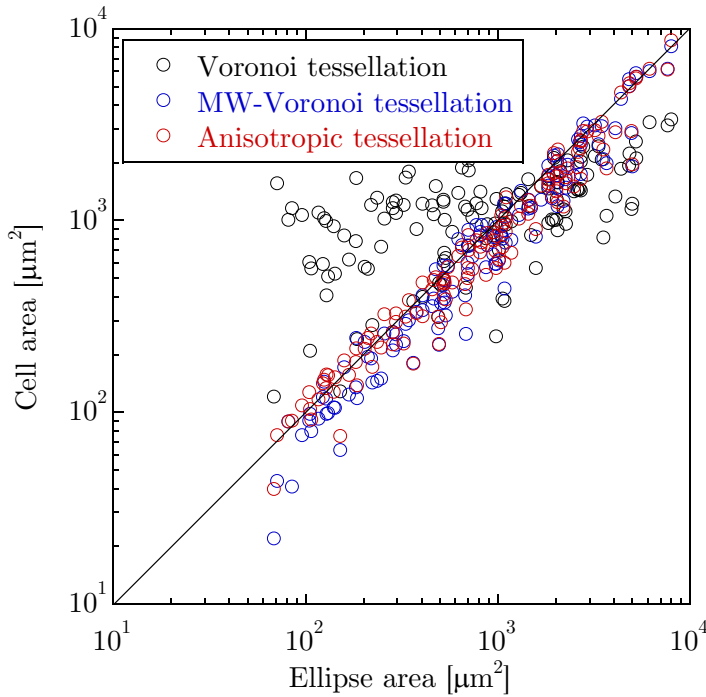


Figure II.19 – Comparison of the area of the cells of the three tessellations in Fig. II.18 with the area of the ellipses in Fig II.16.

3.2.2 Periodic tessellation

In some particular studies, such as for homogenization problems or in order to reduce edge effects induced by uniform load or displacement conditions on the edge of the domain, it is desired to simulate periodic or semi-periodic aggregates. A simple method to construct a periodic tessellation is presented here.

At first, seeds are sampled and positioned in a given sub-domain in the same way as presented previously (blue ellipses in Fig. II.20 (a)). These ellipses are then periodically replicated by translation in all the directions, with a period length of the initial sub-domain size. The tessellation is then performed on the complete domain composed of the 9 sub-domains. Fig. II.20 (b) shows the resulting tessellation. As can be seen, only the sub-domain in the middle of the domain is fully periodic. The subdomains on the left/right or top/bottom are semi-periodic.

3. SPATIAL TESSELLATIONS FOR THE GENERATION OF SYNTHETIC MICROSTRUCTURES

In order to apply periodic boundary conditions, the nodes of the mesh on one edge of the sub-domain should match the nodes on the opposite edge. Raster tessellations are therefore very appropriate in this case. It is also possible to enforce a given node distribution on the edge and mesh the model with free elements as demonstrated by Sharaf *et al.* and Guilhem [80, 130].

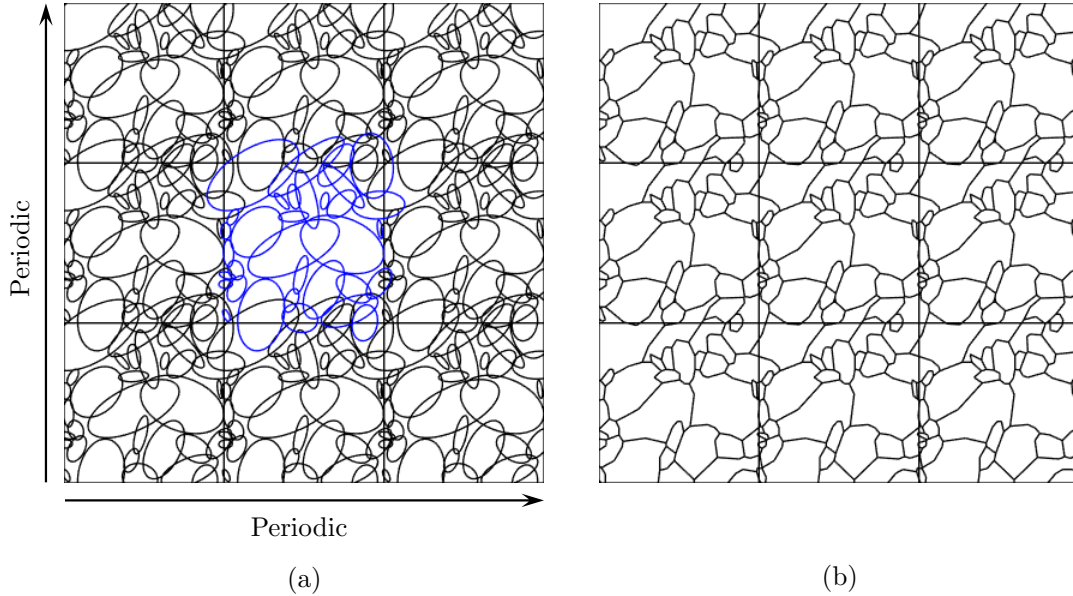


Figure II.20 – (a) Example of a replicated seeds by translation in the two orthogonal directions. (b) Anisotropic tessellation of the domain composed of 9 similar sub-domains. The sub-domain in the center is fully periodic.

3.2.3 Multi-scale tessellation

So far the proposed method is appropriate for materials where the main scale of heterogeneity is the grain scale such that the domain inside each grain is assumed to be uniform. However, some materials in our study exhibit a variety of sub-grain morphologies (packet, block, lath, ...) that play a significant role in deformation and strain localization mechanisms. These materials can be referred as multi-scale materials. This section presents a multi-scale tessellation with a particular emphasis on martensitic microstructure. For ease of explanation, the same decomposition as the martensite structure is used to describe the sub-group categories: grain, packet, block.

Assuming it is possible to statistically describe the morphological distribution of each of these groups, the method described previously can be sequentially applied as follows:

1. **Seed sampling and tessellation of the prior austenite grains:** the output of this step is a raster tessellation where each element of the grid is attributed a grain number.
2. For grain i in the domain:
 - (a) **Seed sampling of the packets in the grain i :** in this step, the RSA algorithm is again applied for the seed positioning with a restriction on the possible locations of the ellipse centers inside the grain i .
 - (b) **Tessellation of the packets in the grain i :** based on a multi-scale tessellation function that takes into argument the raster tessellation of the upper scale,

the grain i , and the seeds of the current scale and returns a raster tessellation at the current scale, bounded to the domain of the grain i .

- (c) For packet j in the grain i :
 - i. **Seed sampling and tessellation of the blocks in the packet j .**
 - ii. ...

The principle of the multi-scale tessellation function is described as follows. At first, a raster tessellation is performed on all the domain with the seeds of a given grain/packet. Then elements outside the grain/packet are set to belong to no group. In this way, the final tessellation at a given scale is simply the sum of several tessellations in different sub-domains. The main drawback of this method is its time complexity as one can notice that there will be as many tessellations as the sum of the domains number on each scale: $1 + n_{grain} + n_{packet}$. However, this approach is flexible enough to enable a given type of tessellation at a certain scale and a different one at another scale. For instance, blocks in martensite are often observed parallel to each other in low-carbon steels. It is therefore possible to use a Voronoi tessellation with aligned seeds or the anisotropic tessellation with parallel ellipses to ensure the desired shape. Fig. II.21 shows an example of two consecutive multi-scale tessellations. Bold, normal and dot lines represent the first, second and third scale tessellation respectively.

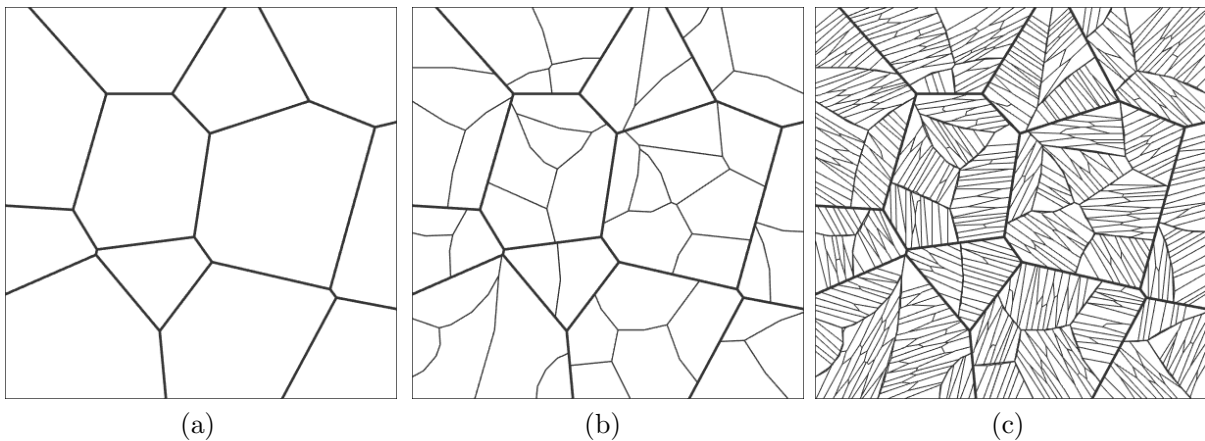


Figure II.21 – Example of a multi-scale tessellation. (a) Prior austenite grain boundaries. (b) Tessellation inside each grain for the packet boundaries. (c) Tessellation inside each packet for the block boundaries.

3.3 Reconstruction of grain boundaries

While raster tessellations using regular meshes are particularly appropriate for problems involving PBC, they require a large number of elements to correctly reproduce the microstructure. When multi-scale tessellations are performed, the precision is bounded by the number of elements describing the lowest scale. Besides, grain boundaries will be staircase structures with corners that will likely generate local stress concentrations. Accordingly, it is necessary to reconstruct in a certain way the grain boundaries in order to circumvent these issues. The approach proposed in this study is based on a similar method existing in the *TSL OIM* software. The principle of the approach is depicted in Fig. II.22. At first, the triple points and the nodes of the grain boundaries are identified

3. SPATIAL TESSELLATIONS FOR THE GENERATION OF SYNTHETIC MICROSTRUCTURES

(black dots and segments on Fig. II.22). The definition of a triple point is given by:

$$TP = \{\mathbf{x} \in \mathbb{R}^p | d_i(\mathbf{x}, \mathbf{x}_i) = d_j(\mathbf{x}, \mathbf{x}_j) = d_k(\mathbf{x}, \mathbf{x}_k), \forall i, j, k \in \{1, \dots, n\}, i \neq j \neq k\} \quad (\text{II.16})$$

where i, j, k correspond to the index of internal nodes. Triple points on the edge of the domain may have only two neighbor grains.

An initial boundary is then drawn by connecting the two triple points. The distance of each node of the grain boundary from the line is calculated and if the furthest point distance d_{max} is higher than a given tolerance (generally a multiple of the element size), the line is split into two parts at this location. The process is then repeated for the two newly created lines until the tolerance condition is met in all the portions of the grain boundary.

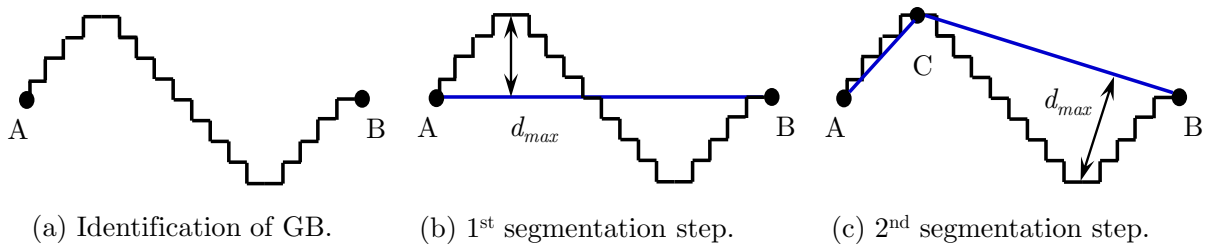


Figure II.22 – Schematic representation of the steps for the grain boundary reconstruction.

Fig. II.23 shows an example of the grain boundary reconstruction process with three tolerance distances: 0, 1 and 2 element size. With no tolerance, the grain boundary follows node by node the elements so that no smoothing is applied. With a tolerance of 1 element, most of the staircase have disappeared and the grain boundaries are composed of several segments. With a tolerance of 2 elements, the grain boundaries are almost entirely smooth. An advantage of this approach is that the quality of the reconstruction is directly dependent on the mesh resolution. Therefore it is possible to generate accurate reconstructions without the need to find the exact mathematical expression and geometries for the grain boundaries that may require advanced algorithms.

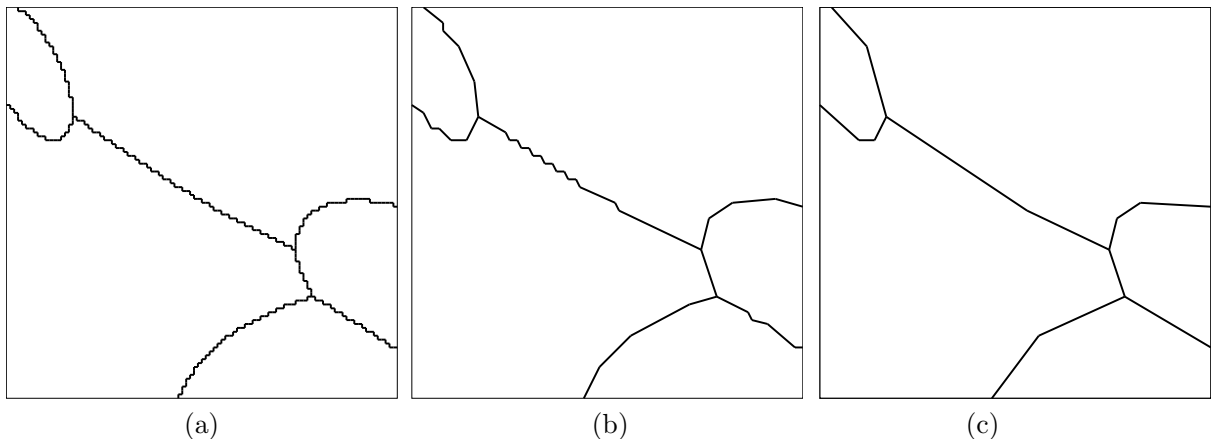


Figure II.23 – Example of grain boundary reconstruction with (a) 0 element tolerance, (b) 1 element tolerance and (c) 2 elements tolerance.

In the end of the procedure, a file is generated that contains the size of the domain, the number of seeds and their center and all the line segments defining the grain boundaries. A python script was then made to reconstruct the tessellation in the FE software Abaqus.

4 Analysis and reproduction of crystallographic texture

The previous section focused on the generation of the geometry of the microstructure. In this section, the methods to attribute to each grain a specific crystal orientation are presented.

4.1 Descriptions of crystalline orientation

The orientation g of a crystal lattice is defined by a rotation matrix $\underline{\underline{g}}$ which can be described in several ways: Euler angles, quaternion, Miller index ... In this work, the Euler angles and the quaternion are mainly used. A brief description is given here.

4.1.1 Euler angles

Using the Bunge convention [131], the orientation using the Euler angle is given by $g = (\varphi_1, \phi, \varphi_2)$ that corresponds to three successive rotations as shown in Fig. II.24:

- rotation of angle φ_1 around Z_0 ;
- rotation of angle ϕ around X_1 ;
- rotation of angle φ_2 around Z_2 .

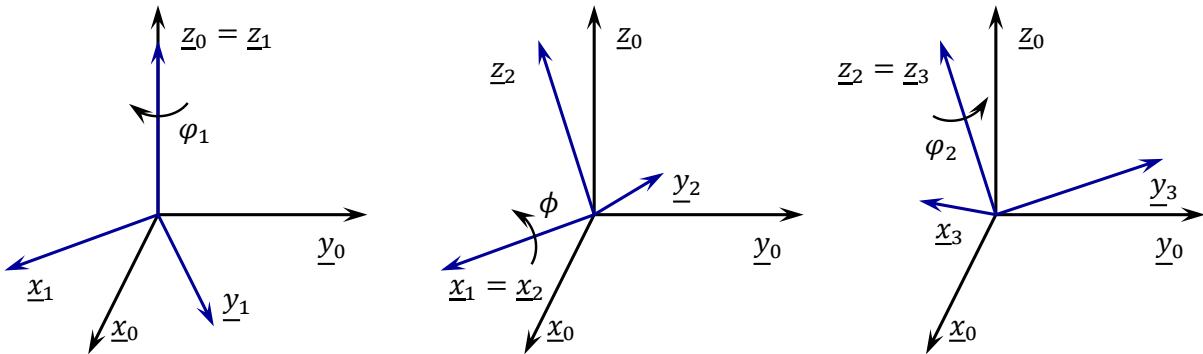


Figure II.24 – Representation of the Euler angles.

The three successive rotations (also referred as intrinsic rotations) occur according to the axes of a moving reference system. Mathematically such rotation can also be written using a fixed coordinate system and applying the rotation in inverse order (extrinsic rotations): $\varphi_2 \rightarrow \phi \rightarrow \varphi_1$. Based on this definition, the rotation matrix $\underline{\underline{g}}$ is given by:

$$\underline{\underline{g}} = \begin{pmatrix} \cos \varphi_1 & -\sin \varphi_1 & 0 \\ \sin \varphi_1 & \cos \varphi_1 & 0 \\ 0 & 0 & 1 \end{pmatrix} \begin{pmatrix} 1 & 0 & 0 \\ 0 & \cos \phi & -\sin \phi \\ 0 & \sin \phi & \cos \phi \end{pmatrix} \begin{pmatrix} \cos \varphi_2 & -\sin \varphi_2 & 0 \\ \sin \varphi_2 & \cos \varphi_2 & 0 \\ 0 & 0 & 1 \end{pmatrix} \quad (\text{II.17})$$

The rotation matrix $\underline{\underline{g}}$ is used to premultiply a direction vector.

4.1.2 Quaternions

While less popular, quaternions are well suited for the description of rotation operations. A quaternion is an hypercomplex number composed of a rotation angle θ and a unitary axis of rotation $\mathbf{n} = (n_1, n_2, n_3)$:

$$\mathbf{q}(\theta, \mathbf{n}) = \mathbf{q}(\theta, n_1\mathbf{i} + n_2\mathbf{j} + n_3\mathbf{k}) \quad (\text{II.18})$$

$$\mathbf{q}(\theta, \mathbf{n}) = \cos\left(\frac{\theta}{2}\right) + \sin\left(\frac{\theta}{2}\right)[n_1\mathbf{i} + n_2\mathbf{j} + n_3\mathbf{k}] \quad (\text{II.19})$$

with $i^2 = j^2 = k^2 = ijk = -1$. With these notations, if we define an initial orientation \mathbf{q}_{ini} and a rotation \mathbf{q}_{rot} then the orientation of the rotation of \mathbf{q}_{ini} by \mathbf{q}_{rot} is simply given by:

$$\mathbf{q}_{fin} = \mathbf{q}_{ini} \cdot \mathbf{q}_{rot} \quad (\text{II.20})$$

It is important to notice that the multiplication of quaternions is not a commutative operation such that $\mathbf{q}_{ini} \cdot \mathbf{q}_{rot} \neq \mathbf{q}_{rot} \cdot \mathbf{q}_{ini}$. The relations to switch from Euler angles to quaternions are given below:

$$\begin{cases} q_0 = \cos\left(\frac{\phi}{2}\right)\cos\left(\frac{\varphi_1 + \varphi_2}{2}\right) \\ q_1 = \sin\left(\frac{\phi}{2}\right)\cos\left(\frac{\varphi_1 - \varphi_2}{2}\right) \\ q_2 = \sin\left(\frac{\phi}{2}\right)\sin\left(\frac{\varphi_1 - \varphi_2}{2}\right) \\ q_3 = \cos\left(\frac{\phi}{2}\right)\sin\left(\frac{\varphi_1 + \varphi_2}{2}\right) \end{cases} \quad (\text{II.21})$$

with

$$\begin{cases} q_0 = \cos\left(\frac{\theta}{2}\right) \\ q_1 = n_1\sin\left(\frac{\theta}{2}\right) \\ q_2 = n_2\sin\left(\frac{\theta}{2}\right) \\ q_3 = n_3\sin\left(\frac{\theta}{2}\right) \end{cases} \quad (\text{II.22})$$

4.2 Orientation distribution function

The texture of the material can be quantified by the orientation distribution function (ODF) which is the probability $f(g)$ to find an elementary volume dV with an orientation between g and $g + dg$

$$f(g) = \frac{1}{dg} \frac{dV(g)}{V} \quad (\text{II.23})$$

where the elementary volume dg is given by:

$$dg = \frac{1}{8\pi^2} d\varphi_1 \sin(\varphi_1) d\phi d\varphi_2 \quad (\text{II.24})$$

using the Bunge notation. The factor $1/8\pi^2$ is introduced to ensure that the integral of the ODF is normalized to 1 over the Euler domain. With no specimen nor crystal symmetry, the Euler space is defined on the domain D :

$$D = \{(\varphi_1, \phi, \varphi_2) \in \mathbb{R}^3 \mid 0 \leq \varphi_1 \leq 2\pi; 0 \leq \phi \leq \pi; 0 \leq \varphi_2 \leq 2\pi\} \quad (\text{II.25})$$

Due to the cubic symmetry of the crystal lattice, the Euler space can be reduced to 24 equivalent sub-domains. However, as some frontiers are curved, it is convenient to consider only 8 equivalent sub-domains Z defined by:

$$Z = \{(\varphi_1, \phi, \varphi_2) \in \mathbb{R}^3 | 0 \leq \varphi_1 \leq 2\pi; 0 \leq \phi \leq \frac{\pi}{2}; 0 \leq \varphi_2 \leq \frac{\pi}{2}\} \quad (\text{II.26})$$

The estimation of the ODF from the EBSD data is performed using the toolbox MTEX [118] for Matlab. The continuous ODF is calculated through a series expansion of spherical Gaussian distribution with a half-width of 10° . Fig. II.25 and II.26 show the ODF in $\varphi_1 - \phi$ planes with slices in the φ_2 direction distant of 15° for the α -iron and the FP steel. As observed in Section 2, α -iron shows a stronger texture than FP steel, as the ODF density is close to 2 in a large portion of the ODF. Peaks are present in both cases with an intensity of about 3.5.

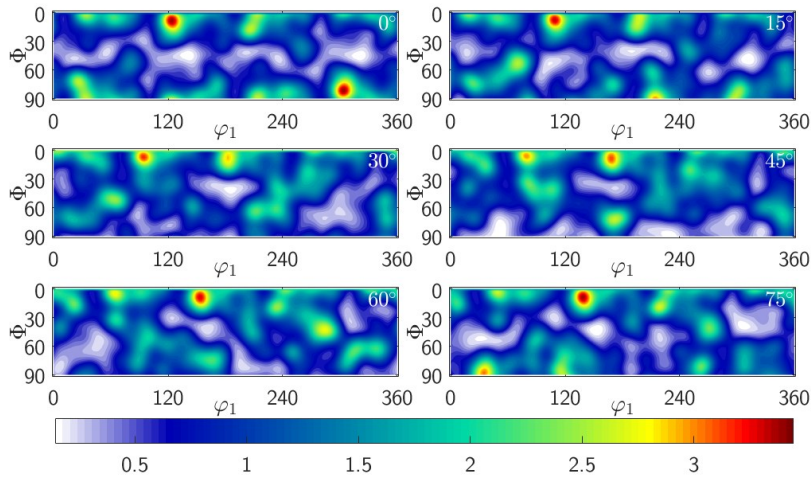


Figure II.25 – ODF calculated from the EBSD of the α -iron.

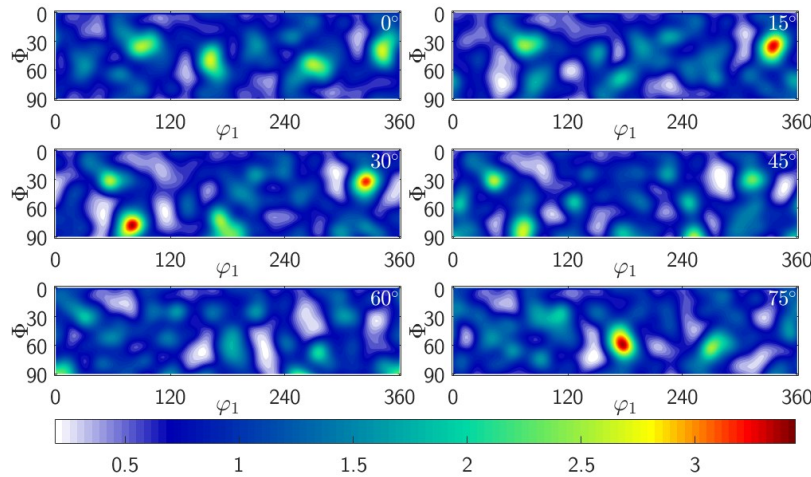


Figure II.26 – ODF calculated from the EBSD of the FP steel.

4.3 Discretization of unweighted orientations

Let us consider a microstructure containing N_g grains of equal area/volume. The objective of this section is to assign to each grain a lattice orientation based on the ODF. The sampling method of equally weighted orientation is based on the algorithm of Toth and Van Houtte [132]. First, the Euler space is divided into N equal boxes so that the ODF can be integrated inside each volume:

$$f_i = \oint_{box_i} f(g) dg \quad (\text{II.27})$$

It is possible to define a path in the Euler space where each box is crossed once. The cumulative ODF is then defined as the sum of the ODF inside each box on the path. Finally, one can randomly draw a number x between 0 and 1 using a random number generator and a uniform distribution. The orientation g_i will correspond to the box where

$$F(g_i) \leq x < F(g_{i+1}) \quad (\text{II.28})$$

as shown in Fig. II.27. The process is repeated for the N_g grains in the model. This method presents two main drawbacks. When the number of orientations is small, the sampling generates sharp textures. To answer this issue, Eisenlohr and Roters [133] developed a hybrid semi-probabilistic semi-deterministic algorithm to keep the quality of the sampling. However, the method is only suitable for equally weighted orientations which is not the case for a general microstructure.

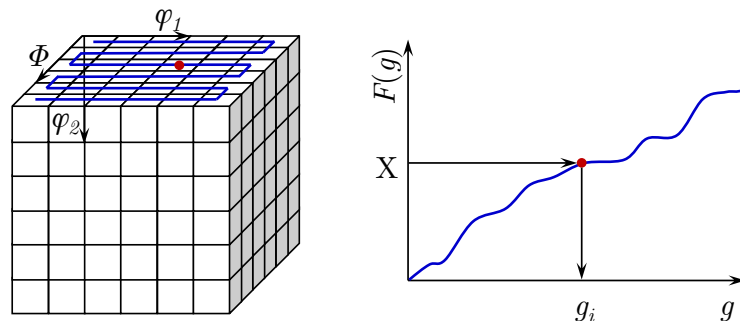


Figure II.27 – Scheme of the Euler space with a path drawn and corresponding cumulative ODF.

4.4 Discretization of weighted orientations

Melchior and Delannay [134] proposed a method suitable for unequally weighted orientations. This algorithm will be used in our study as the grains are unlikely to have equal areas. The general procedure will be briefly presented in this section.

First, each grain is assigned an integer N_i proportional to their area so that

$$\sum_{i=1}^{N_g} N_i = N_{ori} \quad (\text{II.29})$$

represents the total number of orientations to be drawn from the ODF. The drawing is based on the algorithm from previous section. Then orientations are organized to form N_g groups where the group k contains N_k orientations with disorientation lower than a

given threshold (5° in this work). The disorientation angle α between two crystal lattices a and b corresponds to the smallest rotation angle bringing one lattice onto the other. Using quaternions, it is simply defined as:

$$\alpha^{ab} = 2 * \arccos(|q_0^a q_0^b + q_1^a q_1^b + q_2^a q_2^b + q_3^a q_3^b|) \quad (\text{II.30})$$

In practice, a $N_{ori} \times N_{ori}$ matrix M is built where $M(i, j) = 1$ if the disorientation $\alpha^{ij} < 5^\circ$ and zero otherwise. Orientations are then picked to form N_g groups, starting from the largest to the smallest grain, as large grains contain more orientations. The final orientation given to grain k is then the average orientation of these N_k orientations. The quality of the selected orientations is evaluated by calculating the misfit e between the ODF of the synthetic microstructure and the real one:

$$e = \frac{\int (f_{exp}(g) - f_{gen}(g))^2 dg}{\int (f_{exp}(g))^2 dg} \quad (\text{II.31})$$

4.5 Discretization of orientations for martensite packets and blocks

The diffusionless transformation from austenite γ to martensite or bainite α' is not random but occurs following specific crystallographic ORs where the *children* phase inherit its *parent* phase *via* these ORs. The most commonly observed OR in low-carbon steels is the Kurdjumov-Sachs (KS) OR (Fig. II.28):

$$\{111\}_\gamma // \{011\}_{\alpha'}; \langle \bar{1}01 \rangle_\gamma // \langle \bar{1}\bar{1}1 \rangle_{\alpha'} \quad (\text{II.32})$$

where the (011) plane of the α' crystal lies parallel to one of the γ $\langle 111 \rangle$ plane. Similarly, one of the α' $\langle \bar{1}\bar{1}1 \rangle$ direction is parallel to one of the γ $\langle \bar{1}01 \rangle$ direction. The choice of 4 governing planes and 6 governing directions leads to 24 possible variants, summarized in Table II.4.

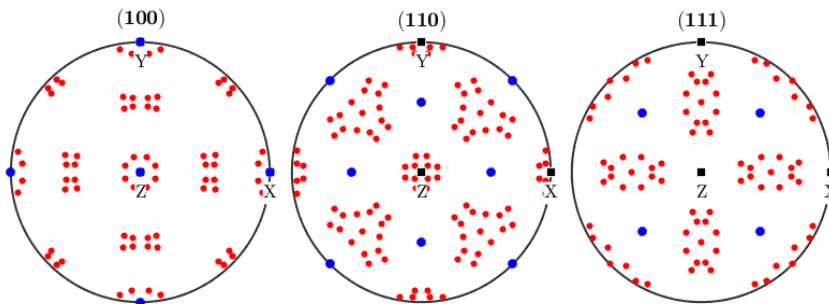


Figure II.28 – Pole figures of the Kurdjumov-Sachs orientation relations for a [100] prior austenite crystal.

At this point, we seek to attribute to each packet or block an orientation. Given the crystal orientation of the prior austenite grain, a packet or block is attributed one of the 24 possible variants. In this regard, the orientation of the child is defined by:

$$\mathbf{q}_{\alpha'} = \mathbf{q}_\gamma \cdot \mathbf{q}_{KS} \quad (\text{II.33})$$

4. ANALYSIS AND REPRODUCTION OF CRYSTALLOGRAPHIC TEXTURE

with \mathbf{q}_{KS} , the rotation bringing one of the γ planes and directions to one of the α' planes and directions defined in Table II.4. The 24 possible rotations \mathbf{q}_{KS} are calculated as follows:

$$\mathbf{q}_{KS} = \mathbf{q}_{\gamma}^{-1} \cdot \mathbf{q}_{\alpha'} \quad (\text{II.34})$$

While this method is straightforward, it requires the knowledge of the prior austenite grain crystal orientation which is not directly obtainable from EBSD data but requires some backward texture calculation to estimate the parent orientation from the child orientation [135].

Table II.4 – Twenty-four variants of the Kurdjumov-Sachs relationship.

Variant No.	Plane parallel $(\gamma)//(\alpha')$	Direction parallel $[\gamma]//[\alpha']$	Variant No.	Plane parallel $(\gamma)//(\alpha')$	Direction parallel $[\gamma]//[\alpha']$
V1		$[\bar{1}01]//[\bar{1}\bar{1}\bar{1}]$	V13		$[0\bar{1}\bar{1}]//[\bar{1}\bar{1}\bar{1}]$
V2		$[\bar{1}01]//[\bar{1}\bar{1}\bar{1}]$	V14		$[0\bar{1}\bar{1}]//[\bar{1}\bar{1}\bar{1}]$
V3	$(111)\gamma$	$[01\bar{1}]//[\bar{1}\bar{1}\bar{1}]$	V15	$(\bar{1}\bar{1}\bar{1})\gamma$	$[\bar{1}0\bar{1}]//[\bar{1}\bar{1}\bar{1}]$
V4	$//(011)\alpha'$	$[01\bar{1}]//[\bar{1}\bar{1}\bar{1}]$	V16	$//(011)\alpha'$	$[\bar{1}0\bar{1}]//[\bar{1}\bar{1}\bar{1}]$
V5		$[1\bar{1}0]//[\bar{1}\bar{1}\bar{1}]$	V17		$[110]//[\bar{1}\bar{1}\bar{1}]$
V6		$[1\bar{1}0]//[\bar{1}\bar{1}\bar{1}]$	V18		$[110]//[\bar{1}\bar{1}\bar{1}]$
V7		$[10\bar{1}]//[\bar{1}\bar{1}\bar{1}]$	V19		$[\bar{1}\bar{1}0]//[\bar{1}\bar{1}\bar{1}]$
V8		$[10\bar{1}]//[\bar{1}\bar{1}\bar{1}]$	V20		$[\bar{1}\bar{1}0]//[\bar{1}\bar{1}\bar{1}]$
V9	$(1\bar{1}\bar{1})\gamma$	$[\bar{1}\bar{1}0]//[\bar{1}\bar{1}\bar{1}]$	V21	$(11\bar{1})\gamma$	$[0\bar{1}\bar{1}]//[\bar{1}\bar{1}\bar{1}]$
V10	$//(011)\alpha'$	$[\bar{1}\bar{1}0]//[\bar{1}\bar{1}\bar{1}]$	V22	$//(011)\alpha'$	$[0\bar{1}\bar{1}]//[\bar{1}\bar{1}\bar{1}]$
V11		$[101]//[\bar{1}\bar{1}\bar{1}]$	V23		$[011]//[\bar{1}\bar{1}\bar{1}]$
V12		$[101]//[\bar{1}\bar{1}\bar{1}]$	V24		$[011]//[\bar{1}\bar{1}\bar{1}]$

5 Validation of the approaches

In this section, comparisons are made between experimental and numerical features in order to validate or emphasize the limitations of the different developed methods.

5.1 Comparison of synthetic and reconstructed grain boundaries

In order to highlight the capability of the anisotropic tessellation to reproduce grain morphology with high accuracy using only the data obtained from ellipses, a comparison is made between real and synthetic grain boundaries. While the ellipse fitting process mainly served to characterize the microstructures, the ellipses in Fig. II.5 and II.8 can also be directly used as input parameter for the anisotropic tessellation. The grain boundaries evaluated from the EBSD data (in blue) and those calculated by anisotropic tessellation (in red) are superimposed over the IQ map of α -iron and FP steel in Fig. II.29. Overall, a very good agreement is found for the two microstructures. We can however note a small discrepancy in the case of FP steel for very small pearlite grains. It is most likely due to the low number of pixels to represent these grains on both the EBSD map and the raster tessellation.

From these results, it seems that ellipses and their positions in the domain provide enough information to accurately reproduce a given microstructure using anisotropic tessellation. In this regard, the critical part in the generation of synthetic microstructure procedure is the seed sampling, where both the generation and positioning of ellipses should be carefully done and verified. This is the subject of the next section.

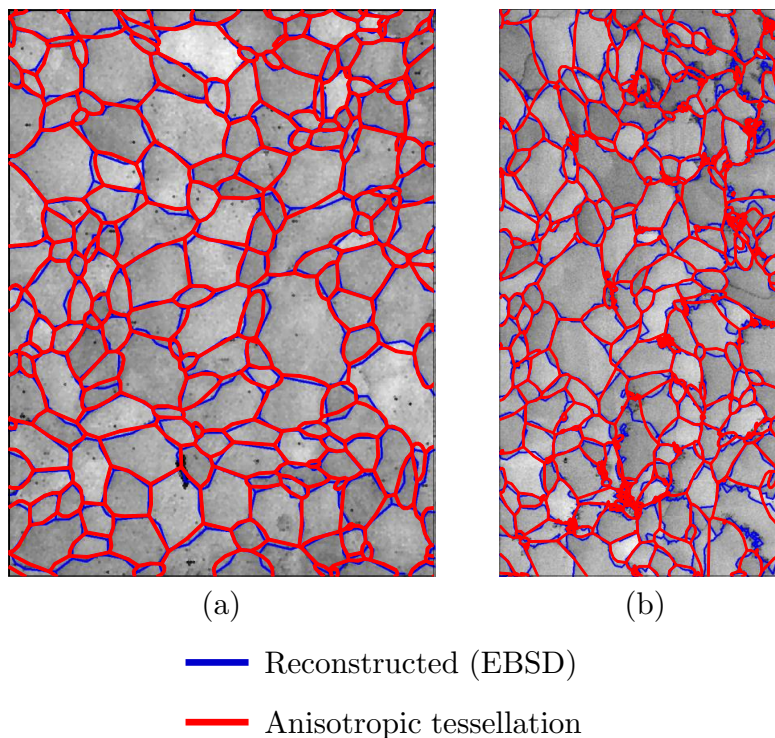


Figure II.29 – IQ map of (a) α -iron ($450 \times 600 \mu\text{m}$) and (b) FP steel ($200 \times 400 \mu\text{m}$) with reconstructed grain boundaries (in blue) and generated grain boundaries by anisotropic tessellation of the ellipses in Fig. II.5 and II.8.

5.2 Comparisons between synthetic and real microstructures

The methodology presented in Section 3 is applied to generate synthetic microstructures for both α -iron and FP steel. The statistical data obtained in Section 2 are used as input parameters. For the sake of comparison between experimental and synthetic microstructures, the size of the domains are set to be the same as the EBSD data: $450 \times 600 \mu\text{m}$ for α -iron and $200 \times 400 \mu\text{m}$ for FP steel. In the case of FP steel, a pearlite fraction of 8.2% is fixed. Due to the significant size difference between ferrite and pearlite grains in FP steel, ferrite seeds are positioned first and then pearlite seeds are sampled. Fig. II.30 shows an example of synthetic microstructure for the two materials, using IPF color coding. The pearlite grains are in black in the case of FP steel.

To quantitatively compare the microstructures, the average grain size distribution is calculated and compared with the experimental one. The definition of the grain size is based on the grain area A_{gr} :

$$d_{gr} = 2\sqrt{\frac{A_{gr}}{\pi}} \quad (\text{II.35})$$

The grain size distributions are fitted to the log-normal distribution. The parameters are summarized in Table II.5. Overall a good agreement is found between the grain size distributions of the real and synthetic microstructures. The pearlite content is slightly higher than the objective of 8.2%.

Fig. II.31 shows the pole figures of the two synthetic microstructures. They can be compared to the experimental pole figures displayed in Fig. II.6 and II.11. As can be seen, the few major peaks present in the real microstructures are correctly reproduced. However, the magnitude of the peaks and valleys are closer to 1 meaning that the overall textures are smoother than the real one. The error between the synthetic and real ODF are 22.95% and 24.3% for α -iron and FP steel respectively. These values are in good agreement with the original paper [134]. It can be mentioned that random orientations lead to an error of about 60% and applying the method of Toth and Van Houtte [132] gives an error of about 35%.

Table II.5 – Phase fraction and log-normal parameters of the fitted grain size distribution for the experimental and synthetic α -iron and FP steel.

	α -iron		FP steel			
	Experiment	Synthetic	Experiment		Synthetic	
	Ferrite	Ferrite	Ferrite	Pearlite	Ferrite	Pearlite
Fraction [%]	100	100	91.8	8.2	91.3	8.7
μ [-]	3.39	3.35	2.73	1.32	2.70	1.99
σ [-]	0.599	0.543	0.663	0.389	0.581	0.347

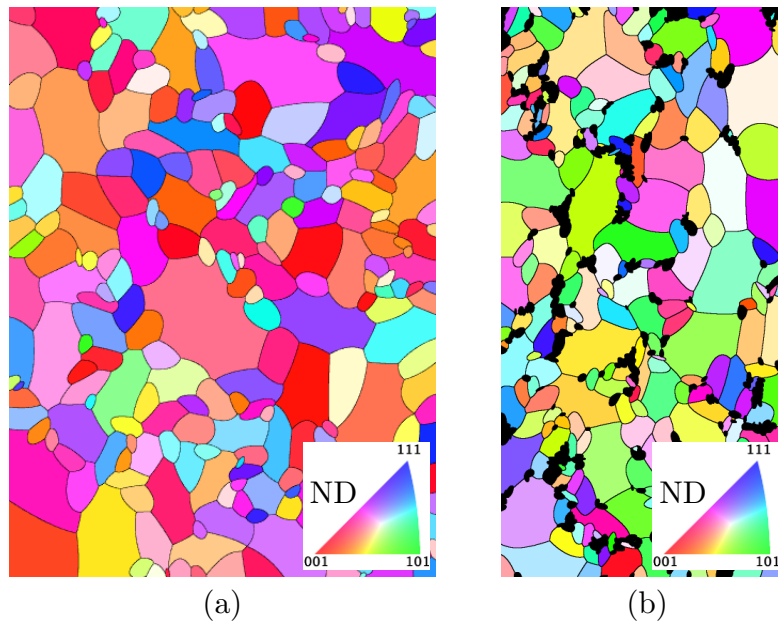


Figure II.30 – IPF map of synthetic (a) α -iron ($450 \times 600 \mu\text{m}$) and (b) FP steel ($200 \times 400 \mu\text{m}$) generated from the data evaluated in Section 2.

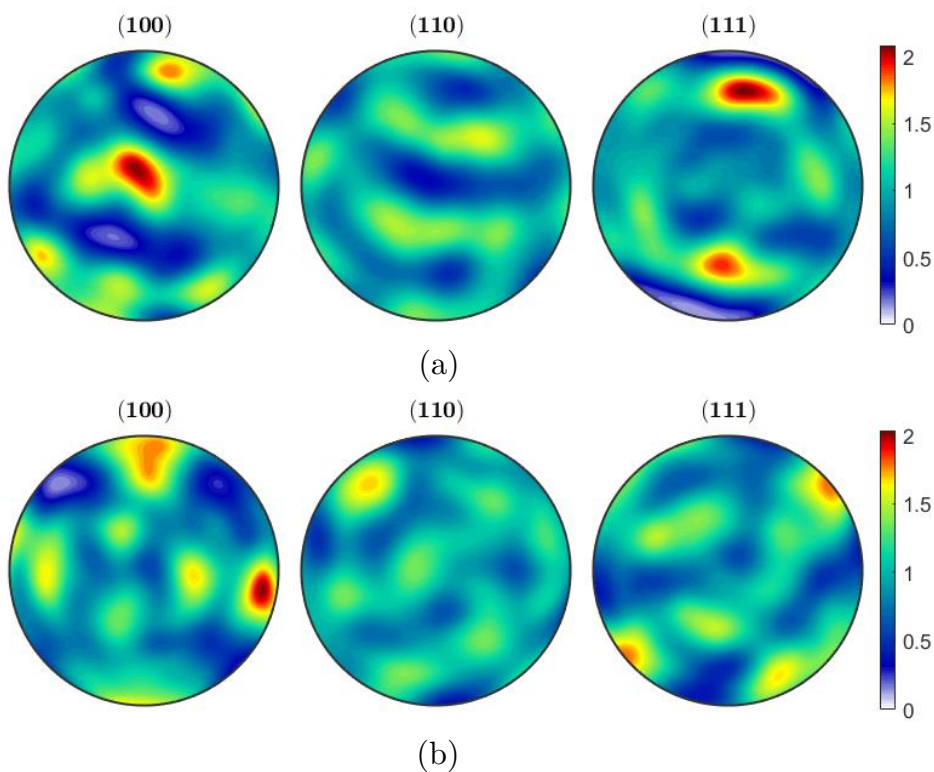


Figure II.31 – $\{100\}$, $\{110\}$ and $\{111\}$ pole figures synthetic (a) α -iron ($450 \times 600 \mu\text{m}$) and (b) FP steel ($200 \times 400 \mu\text{m}$) generated from the microstructures in Fig. II.30.

5.3 Generation of martensitic microstructures

Due to the lack of statistical data obtained from the measurement by optical microscope, the prior austenite grain size distribution is based on a log-normal distribution where the parameters μ and σ are adjusted so that the mean grain size corresponds to the measured one $d_{gr} = 535\mu\text{m}$: $\mu = 5.5$ and $\sigma = 0.4$. To ensure a certain regularity in the grain morphology, the Laguerre tessellation defined in Eq. II.12 is used with a weight parameter $w_i = r_i^2$ where r_i is the radius of the grain i . Once the tessellation of the prior austenite grains is performed, each grain is assigned a crystal orientation using a uniform ODF and the algorithm proposed by Melchior and Delannay [134]. Indeed due to the small window size of the EBSD map, the construction of an ODF is not representative nor does it represent the orientation of the prior austenite grain. Therefore it was decided to assume a random orientation for the prior austenite.

From the observation of the packets partitioning within prior austenite grains, the four packets defined by their habit planes should be present within a prior austenite grain as long as it is large enough. Hence, packet radius is set to follow an uniform distribution bounded in the following interval [100; 150] (in μm). In average, prior austenite grains are divided into 4 packets with larger grains containing about 7 to 10 packets. The approach presented in the previous section is used to attribute to each packet an orientation based on the prior austenite grain orientation to which they belong. The procedure is biased to enforce that packets orientation have different habit planes such that in the case of a grain composed of 4 packets, the 4 habit planes are present.

Knowing the $(011)_{\alpha'}$ habit plane of a given packet and the fact that the elongated direction of martensite blocks are parallel to the $[10\bar{1}]_{\gamma}$ or $[01\bar{1}]_{\gamma}$ direction, the orientation of the martensite block is calculated as the projection of the variant direction on the ND plane. Therefore, within a given packet, all the blocks share the same orientation. Blocks are defined as ellipses with a major axis of 100 μm and a minor axis varying between 10 to 15 μm . Blocks geometry is obtained through the anisotropic tessellation from Section 3. Finally, the orientation of each block is sampled from the 6 available variants within the habit plane of the packet.

Fig. II.32(a) depicts an example of a martensitic microstructure on a $2000 \times 2000 \mu\text{m}$ window. The grain, packet and block boundaries are drawn with bold, normal and dot lines respectively. Fig. II.32(b) shows the same microstructure with each packet colored according to its orientation following the IPF color coding. As can be seen, for large grains, several packets sharing the same habit plane are present with parallel blocks and similar orientations.

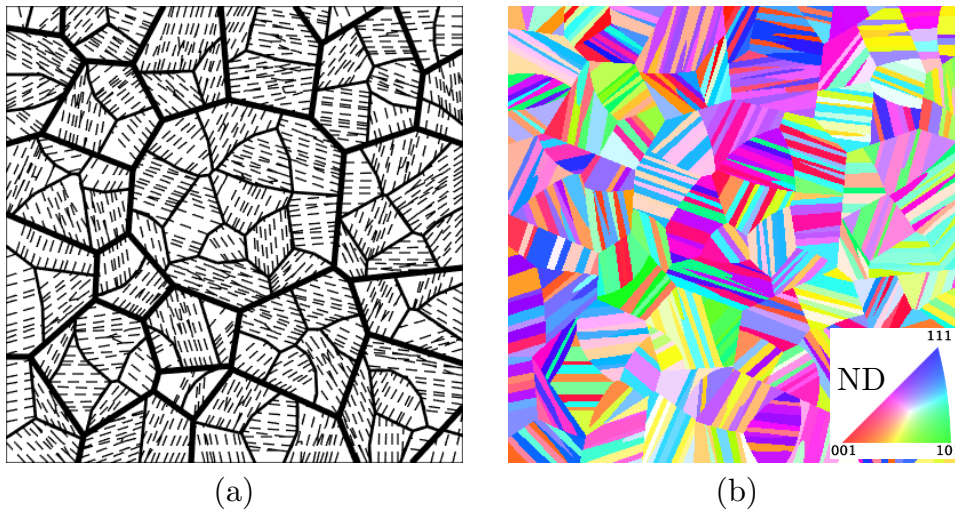


Figure II.32 – (a) Multi-scale tessellation representing a martensitic microstructure on a $2000 \times 2000 \mu\text{m}$ window. (b) Corresponding IPF color map.

6 Summary

In this chapter, the different materials studied in this work have been presented and analyzed from a microstructural point of view using mainly EBSD analysis.

In the case of α -iron and FP steel, the grain morphology could be well described by an ellipse fitting procedure since there exists a single scale of heterogeneity arising from the different crystal orientations that are assumed to be uniform within a given grain. In the case of martensite, several scales of heterogeneity are present which render this approach inappropriate as it does not make any difference between the different boundary types: prior austenite grain, packet and block boundary. Hence, a procedure was applied to identify, separate and quantify the different scales of heterogeneity.

Several procedures have been developed to generate and export 2D synthetic microstructures with realistic geometries based on statistical data obtained from the previous analysis. They include an anisotropic tessellation, a multi-scale tessellation and a grain boundary reconstruction algorithm. The anisotropic tessellation has been compared with the Voronoi and MW-Voronoi tessellations and has shown to provide a better control on both the shape and size of the generated cells.

The texture of the material was reproduced based on the algorithm proposed by Melchior and Delannay [134]. In the case of martensitic structure, "*parent to child*" and "*child to child*" approaches were described to attribute to each packet/block a crystal orientation using, for instance, the Kurdjumov-Sachs orientation relation in the case of low-carbon martensitic steels.

The methods were validated through the comparisons between experimental and synthetic data. The anisotropic tessellation showed a very good capability to reproduce the real grain boundaries. The sampling process correctly managed to generate microstructures with a grain size distribution objective for α -iron and FP steel. Finally, a procedure was developed for the generation of the martensitic microstructure.

The proposed approaches were described only in the case of 2D models, however, most of the methods were transposed to 3D with the exception of the grain boundary reconstruction. This last point might require specific algorithms such as the one proposed by Quey *et al.* [66].

Chapter III

Characterization and modeling of the mechanical behavior of the materials under cyclic loadings

Contents

1	Introduction	80
2	Constitutive models and identification strategies	80
2.1	J_2 -plasticity model	80
2.2	Phenomenological crystal plasticity model	81
2.3	Microstructure-based modeling of the pearlite behavior	82
2.4	Identification strategies	83
3	Experimental methods	86
3.1	Strain-controlled fatigue experiments	86
3.2	Load-controlled fatigue experiments	87
4	Results and Discussion	91
4.1	Strain-controlled fatigue experiments	91
4.2	Parameters identification	98
4.3	Load-controlled fatigue experiments	104
5	Summary	118

1 Introduction

In this chapter, the mechanical behavior of the materials are characterized under cyclic conditions. The first objective of this chapter is to provide experimental data suitable for the identification of the parameters of the elasto-plastic constitutive models used in this work. This calibration is based on an inverse analysis of stabilized stress-strain hysteresis curves obtained from cyclic strain-controlled experiments. The second objective of this chapter is to evaluate the behavior of the materials under high-cycle fatigue conditions using load-controlled experiments. More precisely, it is wished to quantitatively characterize the early stage of fatigue damage: crack initiation and MSC growth. For this reason, specific specimen and experimental conditions were used to record the surface specimen during the experiment.

The chapter is decomposed into three sections. At first, the constitutive models are presented and the strategies and hypothesis for the evaluation of the parameters are described. Then the experimental methods and specimen are explained for both strain-controlled and load-controlled fatigue experiments. An experiment using a micro-scale specimen coupled with EBSD analysis is also presented. Finally the experimental results as well as the calibrated parameters are presented and discussed.

2 Constitutive models and identification strategies

A suitable model for cyclic simulations is expected to reproduce some basic phenomena observed experimentally [94, 95]: cyclic hardening/softening, kinematic hardening due to the change in plastic slope (Bauschinger effect), relaxation of mean stress under strain control or ratcheting under load control, and memory of past deformation. The simulations conducted in Chapter IV require two types of constitutive model: a macroscopic isotropic model based on the second invariant of the deviatoric stress tensor (referred as the J_2 -plasticity model) and a crystal plasticity model. Both models should include isotropic and kinematic hardening in order to account for the phenomena cited previously. Isotropic hardening accounts for the increase of the elastic domain size while kinematic hardening is characterized by a translation of the domain.

2.1 J_2 -plasticity model

The macroscopic constitutive model is based on the second invariant J_2 , of the deviatoric part \mathbf{s} of the Cauchy stress tensor $\boldsymbol{\sigma}$:

$$J_2 = \frac{1}{2} \mathbf{s} : \mathbf{s} = \frac{1}{2} \text{tr}(\mathbf{s}^2) \quad (\text{III.1})$$

The yield surface f is based on the von Mises stress $\sqrt{3J_2}$ and defined as follows:

$$f = \sqrt{3J_2(\mathbf{s} - \boldsymbol{\alpha}^{dev})} - \sigma_y = \sqrt{\frac{3}{2}(\boldsymbol{\sigma} - \boldsymbol{\alpha})^{dev} : (\boldsymbol{\sigma} - \boldsymbol{\alpha})^{dev}} - \sigma_y \quad (\text{III.2})$$

where $\boldsymbol{\alpha}$ is a kinematic back-stress tensor and σ_y is the yield stress of the material. Isotropic hardening is modeled by changing the yield stress following the model proposed by Voce [136]:

$$\sigma_y = \sigma_0 + Q_\infty(1 - e^{-b\bar{\epsilon}^{pl}}) \quad (\text{III.3})$$

where σ_0 is the yield stress at zero plastic strain, Q_∞ is the maximum change in the yield surface, b is the rate of the hardening and $\bar{\varepsilon}^{pl}$ is the equivalent plastic strain. Several back-stresses α_k are used to capture the kinematic hardening response at different strain ranges:

$$\boldsymbol{\alpha} = \sum_{k=1}^N \boldsymbol{\alpha}_k \quad (\text{III.4})$$

where the evolution of each back-stress is defined by a non-linear Frederick-Armstrong rule:

$$\dot{\boldsymbol{\alpha}}_k = \frac{C_k}{\sigma_y} (\boldsymbol{\sigma} - \boldsymbol{\alpha}) \dot{\bar{\varepsilon}}^{pl} - \gamma_k \boldsymbol{\alpha}_k \dot{\bar{\varepsilon}}^{pl} \quad (\text{III.5})$$

where C_k and γ_k are material parameters to be calibrated. The J_2 -plasticity model is available in the Abaqus library and is coupled with an algorithm to evaluate its parameters based on stabilized stress-strain curves.

2.2 Phenomenological crystal plasticity model

The crystal plasticity model is the phenomenological model described in Chapter I. The main equations are restated here. The material state is described in term of critical resolved shear stress (CRSS) τ_c^α and kinematic back-stress χ^α on each slip system α . The shear rate on each slip system α is given by a Norton type law:

$$\dot{\gamma}^\alpha = \dot{\gamma}_0 \left| \frac{\tau^\alpha - \chi^\alpha}{\tau_c^\alpha} \right|^n \text{sgn}(\tau^\alpha - \chi^\alpha). \quad (\text{III.6})$$

Work hardening is considered by modifying the CRSSs:

$$\dot{\tau}_c^\alpha = \sum_{\beta} h^{\alpha\beta} |\dot{\gamma}^\beta| \quad (\text{III.7})$$

with

$$h^{\alpha\beta} = q^{\alpha\beta} h^\beta = q^{\alpha\beta} h_0 \left(1 - \frac{\tau_c^\beta}{\tau_{c_s}}\right)^a \quad (\text{III.8})$$

where h_0 , a and τ_{c_s} are the initial hardening coefficient, the hardening exponent and the saturated CRSS. To reduce the number of unknown parameters a common simplification is made for the hardening coefficients $q^{\alpha\beta}$. $q^{\alpha\beta} = 1.0$ when slip systems are coplanar while it is 1.4 otherwise.

$$\dot{\chi}^\alpha = A \dot{\gamma}^\alpha - B |\dot{\gamma}^\alpha| \chi^\alpha \quad (\text{III.9})$$

Kinematic hardening is here again modeled using a Frederick-Armstrong rule:

$$\dot{\chi}^\alpha = A \dot{\gamma}^\alpha - B |\dot{\gamma}^\alpha| \chi^\alpha \quad (\text{III.10})$$

where A and B are materials parameters. The model is implemented in the UMAT toolkit of Abaqus: DAMASK [83]. It was simply modified to incorporate the kinematic back-stress which is absent in the default model. This model is chosen instead of a more realistic dislocation-based representation due to the relatively low number of parameters and internal state variables. Besides, considering a BCC lattice, up to 48 slip systems can be considered as shown in Chapter I. The simulations conducted in this work are limited to only 12 slip systems: $\{110\}\langle\bar{1}11\rangle$.

2.3 Microstructure-based modeling of the pearlite behavior

In the case of FP steel, the ferrite phase is modeled using the CP model previously described while the pearlite phase is modeled based on a micromechanical model. Indeed, considering the low amount of pearlite (8.2%) and the difficulty to calibrate two materials with one experiment, it was decided to fix the parameters of pearlite before the identification phase as done for instance by Sharaf *et al.* [80]. Besides, due to the low stress level considered in the case of fatigue simulations, pearlite grains are not expected to exhibit significant plasticity.

Laschet *et al.* [137], assuming an orthotropic elastic behavior, evaluated these coefficients by modeling a bi-lamella RVE composed of ferrite and cementite that represents the pearlite structure and using an asymptotic homogenization scheme. The homogenized elasticity matrix in the reference axis system $\mathbf{e}_x, \mathbf{e}_y, \mathbf{e}_z$ (the z -direction corresponds to the periodic direction of ferrite/pearlite) was given as follows (in GPa):

$$\mathbb{C}^{eff} = \begin{pmatrix} 288.4 & 87.1 & 100.2 & 5.69 & -8.93 & -13.35 \\ 87.1 & 279.0 & 114.5 & 13.69 & 15.72 & 0.69 \\ 100.2 & 114.5 & 269.9 & -18.97 & -7.44 & 11.72 \\ 5.69 & 13.69 & -18.97 & 44.31 & -10.25 & 10.79 \\ -8.93 & 15.72 & -7.44 & -10.25 & 65.86 & -24.48 \\ -13.35 & 0.69 & 11.72 & 10.79 & -24.48 & 73.54 \end{pmatrix} \quad (\text{III.11})$$

The elasticity matrix highlights a coupling between extension and shear components as the non diagonal coefficients C_{ij} for $i > 3$ are non-zero. However, the values are relatively low. Accordingly, in this work, pearlite is modeled as an isotropic material. The elastic coefficients C_{11} and C_{12} are set as the mean values of the C_{ii} and C_{ij} evaluated by Laschet *et al.*: $C_{11} = 279.1$ GPa and $C_{12} = 100.6$ GPa.

The plastic flow is based on the microstructure-based model proposed by Allain and Bouaziz [138]. In this model, plastic deformation is assumed to occur only in ferrite phases between cementite lamellae and is directly controlled by the interlamellar spacings s . The flow stress σ_p is given by:

$$\sigma_p(\varepsilon_p) = \sigma_0^{Fer} + \frac{\mu Mb}{s} + \frac{K}{g} [1 - \exp(-\frac{g\varepsilon_p}{2})] \quad (\text{III.12})$$

where σ_0^{Fer} is the critical stress due to lattice friction, μ the shear modulus ($\mu = 80$ GPa), M the Taylor factor ($M = 3$), b Burger's vector ($b = 2.5 \times 10^{-10}$ m), K and g are empirical constants that are used to model a Voce type work hardening ($K = 38$ GPa and $g = 70$). Due to the small pearlite grain size and the low resolution of the EBSD data, it was not possible to determine the interlamellar spacing s . Accordingly, it was set to $0.2 \mu\text{m}$ following the work of Sharaf *et al.* who studied a FP steel with close properties [80]. Finally, the initial yield stress is based on an empirical relation dependent on the chemical composition of the material.

$$\begin{aligned} \sigma_0^{Fer} = & 77 + 80(\% \text{Mn}) + 750(\% \text{P}) + 60(\% \text{Si}) + 80(\% \text{Cu}) + 45(\% \text{Ni}) + 60(\% \text{Cr}) \\ & + 11(\% \text{Mo}) + 5000(\% \text{N}_{ss}) \end{aligned} \quad (\text{III.13})$$

Considering the chemical composition given in Chapter II, the flow stress can be calculated and is represented in Fig. III.1.

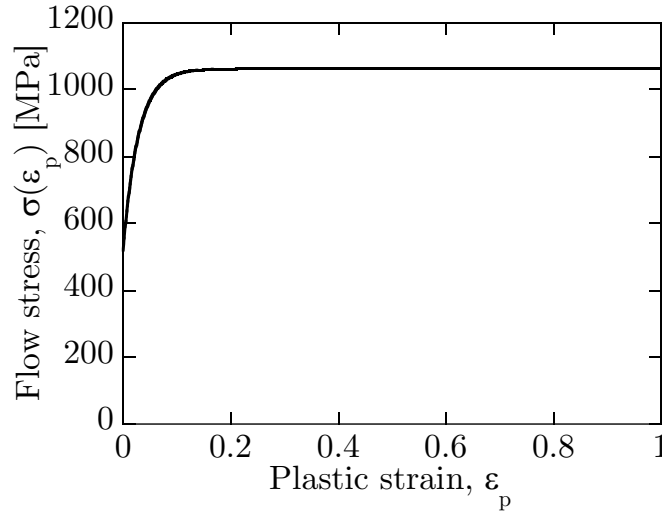


Figure III.1 – Flow stress of pearlite.

2.4 Identification strategies

The J_2 -plasticity model is calibrated using the optimization algorithm available in Abaqus. Therefore, no description will be given. Considering the crystal plasticity model, two calibration strategies are proposed: a fast but slightly inaccurate mean field Lin-Taylor model and a slow but more accurate model based on a 3D RVE and homogenization theory. They are presented in this section.

2.4.1 Taylor-Lin model

The Taylor-Lin or isostrain model is based on the assumption that the deformation in each grain of a polycrystalline aggregate is equal to the total deformation applied to the aggregate itself. From a mechanical point of view, it is equivalent to having several springs in parallel subjected to the same imposed displacement. The macroscopic deformation is equal to the deformation of each spring while the total load is the sum of the reaction force of each spring. Considering the finite strain framework described in Chapter I, this assumption can be formally written as an equality of deformation gradient tensors:

$$\mathbf{F}^g = \bar{\mathbf{F}}, \quad \forall g \in [1, n] \quad (\text{III.14})$$

where \mathbf{F}^g is the deformation gradient tensor of the grain g and $\bar{\mathbf{F}}$ is the mean deformation gradient tensor.

The average stress in each grain \mathbf{S}^g is first computed and only depends on the crystal orientation of the grain as no interaction between grains is considered. The macroscopic stress \mathbf{S} is then calculated as the average of the stresses of all grains:

$$\mathbf{S} = \sum_{g=1}^N \nu^g \mathbf{S}^g \quad (\text{III.15})$$

with ν^g the volume fraction of grain g . The isostrain model is known to represent the upper bound of the constitutive response of an aggregate. Alternatively the isostress model is known to represent the lower bound.

In practice, a single hexahedron element (C3D8) is modeled in Abaqus with periodic boundary conditions applied to each node and a macroscopic strain tensor similar to the

one applied in experiments. 100 grains of equal volume fraction are considered. Fig. III.2(a) shows the single element used in Abaqus. This model is applied to roughly evaluate the crystal plasticity parameters. They are then more precisely calibrated using a 3D RVE presented in the next section. Indeed, as only a single element is used, the simulation is extremely fast which permits to compute a large number of simulations in an acceptable time.

2.4.2 Homogenization of a 3D RVE

The second approach is based on the application of the homogenization theory on a three-dimensional polycrystalline aggregate. A brief description of the principle is given here.

Let us first consider an orthonormal coordinate system $(O, \mathbf{e}_1, \mathbf{e}_2, \mathbf{e}_3)$ and a Y -periodic medium Ω whose base cell is described by:

$$Y =]-\frac{l_1}{2}, \frac{l_1}{2}[\times]-\frac{l_2}{2}, \frac{l_2}{2}[\times]-\frac{l_3}{2}, \frac{l_3}{2}[\quad (\text{III.16})$$

A field X is Y -periodic if

$$\mathbf{y}' - \mathbf{y} = \sum_{i=1}^3 k_i l_i \mathbf{e}_i \quad \text{with} \quad \mathbf{k} = (k_1, k_2, k_3) \in \mathbb{Z}^3 \implies X(\mathbf{y}') = X(\mathbf{y}) \quad (\text{III.17})$$

In the following, upper case letters $\boldsymbol{\Sigma}$ and \mathbf{E} represent the uniform macroscopic stress and strain tensor respectively while lower case $\boldsymbol{\sigma}$ and $\boldsymbol{\varepsilon}$ represent the local Y -periodic stress and deformation fields. We admit that the field $\boldsymbol{\varepsilon}(\mathbf{y})$ is kinematically admissible if and only if, it is derived from a displacement of the form:

$$\mathbf{u}(\mathbf{y}) = \mathbf{E} \cdot \mathbf{y} + \mathbf{v}(\mathbf{y}), \quad \forall \mathbf{y} \in \Omega \quad (\text{III.18})$$

where \mathbf{v} is a Y -periodic displacement field. Let us verify that the average strain tensor $\langle \boldsymbol{\varepsilon} \rangle$ is equal to the imposed macroscopic strain \mathbf{E} , where we defined the average operator $\langle \cdot \rangle$:

$$\langle X \rangle = \frac{1}{|Y|} \int_{\mathbf{y} \in Y} X(\mathbf{y}) dy_1 dy_2 dy_3 \quad (\text{III.19})$$

Based on Eq. III.18,, the local strain tensor is given by:

$$\boldsymbol{\varepsilon} = \frac{1}{2}(\nabla \mathbf{u} + \nabla \mathbf{u}^T) = \frac{1}{2}(\mathbf{E} + \nabla \mathbf{v} + \mathbf{E}^T + \nabla \mathbf{v}^T) = \mathbf{E} + \frac{1}{2}(\nabla \mathbf{v} + \nabla \mathbf{v}^T) \quad (\text{III.20})$$

The average strain tensor $\langle \boldsymbol{\varepsilon} \rangle$ is given by:

$$\langle \boldsymbol{\varepsilon} \rangle = \frac{1}{|Y|} \int_{\mathbf{y} \in Y} (\mathbf{E} + \frac{1}{2}(\nabla \mathbf{v} + \nabla \mathbf{v}^T)) dV = \mathbf{E} + \frac{1}{2|Y|} \int_{\mathbf{y} \in Y} (\nabla \mathbf{v} + \nabla \mathbf{v}^T) dV \quad (\text{III.21})$$

Therefore,

$$\langle \boldsymbol{\varepsilon} \rangle \equiv \mathbf{E} \Leftrightarrow \frac{1}{2|Y|} \int_{\mathbf{y} \in Y} (\nabla \mathbf{v} + \nabla \mathbf{v}^T) dV = 0 \quad (\text{III.22})$$

In order to prove the right part of Eq. III.22, we apply the following integration by part:

$$\int_{\mathbf{y} \in V} \boldsymbol{\sigma} : \boldsymbol{\varepsilon} dV = \int_{\mathbf{y} \in V} -(\text{div} \boldsymbol{\sigma}) \cdot \mathbf{u} dV + \int_{\mathbf{y} \in \partial V} (\boldsymbol{\sigma} \cdot \mathbf{n}) \cdot \mathbf{u} dS \quad (\text{III.23})$$

Considering $V = Y$, $\boldsymbol{\sigma} = \boldsymbol{\sigma}^0$ uniform and $\boldsymbol{\varepsilon} = \boldsymbol{\varepsilon}^{per}$, the strain tensor of the periodic displacement \mathbf{v} , we obtain:

$$\boldsymbol{\sigma}^0 : \int_{\mathbf{y} \in Y} \boldsymbol{\varepsilon}^{per} dV = 0 + \int_{\mathbf{y} \in \partial Y} (\boldsymbol{\sigma}^0 \cdot \mathbf{n}) \cdot \mathbf{v} dS \quad (\text{III.24})$$

For pairs of points $(\mathbf{y}, \mathbf{y}')$ verifying Eq. III.19 and located on ∂Y , we have $\boldsymbol{\sigma}^0 \cdot \mathbf{n}(\mathbf{y}') = -\boldsymbol{\sigma}^0 \cdot \mathbf{n}(\mathbf{y})$ and $\mathbf{v}(\mathbf{y}') = \mathbf{v}(\mathbf{y})$ for all $\boldsymbol{\sigma}^0$ leading to the correct results.

In practice, a 3D polycrystalline aggregate composed of 400 grains is generated based on a Voronoi tessellation using the open-source software Neper [66]. Diard *et al.* [82] recommended a minimum of 27 integration points per grain in order to correctly estimate the average response of the grain. The RVE is meshed with 17^3 regular hexahedron elements (C3D8) as shown in Fig. III.2. This leads to approximately 100 integration points per grain. Periodic boundary conditions (PBC) are applied on each pair of nodes of the model. Despite the fact that the RVE used is not fully periodic, the use of PBCs yields a response between the upper and lower bounds imposed by a uniform strain and stress conditions respectively. In fact, increasing the size of the RVE should give the same mean response with the three types of conditions. PBCs simply grant a faster convergence to the mean response for a lower RVE size. In practice, multiple points constraint method is repetitively used to impose the periodic displacements of the surface nodes. Due to the large number of nodes (18^3), a procedure was written in python script to define these constraints. It is worth mentioning that PBCs significantly increase the computational cost. Once the mechanical response is computed, the average stress tensor $\langle \boldsymbol{\sigma} \rangle$ is evaluated:

$$\langle \boldsymbol{\sigma} \rangle = \frac{1}{|Y|} \int_{\mathbf{y} \in Y} \boldsymbol{\sigma} dV \quad (\text{III.25})$$

In the same fashion it is possible to show that $\langle \boldsymbol{\sigma} \rangle = \boldsymbol{\Sigma}$.

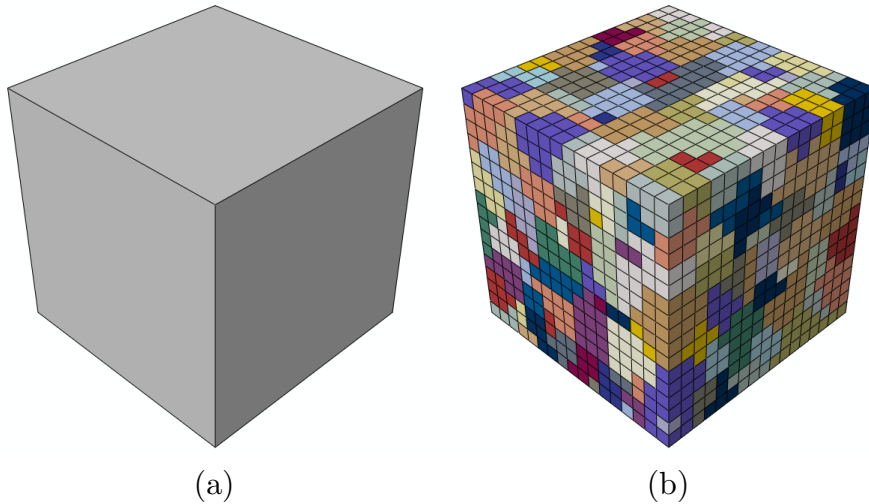


Figure III.2 – (a) Single hexahedron elements used for the Taylor model. (b) 3D RVE composed of 400 grains.

3 Experimental methods

The present section aims to describe the experiments conducted for all the materials. Two types of experiments under cyclic loading were undertaken. Strain-controlled fatigue experiments were first performed in order to bring experimental data to calibrate the constitutive models described in the previous section. Indeed, in order to fit the plasticity parameters, especially the kinematic hardening parameters, a minimum of plasticity is needed to be observed and measured. Results of these experiments were also used to determine the loading conditions for load-controlled fatigue experiments. These tests were used to evaluate the fatigue strength and crack growth rate of the materials.

3.1 Strain-controlled fatigue experiments

Low-cycle fatigue (LCF) experiments under strain-controlled conditions were conducted on all the materials in this work. Considering the local heat treatment applied to some of the materials, smooth cylindrical specimens with a 8 mm gauge length were machined from blocks. Fig. III.3 shows the geometry of the specimens. The dimensions were chosen following ASTM standard E606-92.

Fully reversed strain-controlled experiments were conducted at constant strain rate $\dot{\epsilon} = 2 \times 10^{-3} \text{ s}^{-1}$ on a 50 kN tension-compression machine (Servopulser 50kN, Shimadzu). The strain was recorded and controlled using a 8 mm clip-on extensometer having a measurement range of ± 4 mm. To prevent the sharp knives of the extensometer from sliding or even cutting the specimen during the experiments, a plastic tape was rolled around the specimen at the positions of the blades as shown in Fig. III.4. Most of the specimens broke in the center of the gauge area.

Four different strain amplitudes, $\Delta\epsilon/2$ were considered and the frequencies of the experiments were adjusted to keep the same strain rate. The experimental conditions are summarized in Table III.1. Despite a careful control of the PID setting of the extensometer, a discrepancy between the ordered and the actual strain was observed for the first few cycles. Nonetheless, the applied strain never exceeded the maximum one.

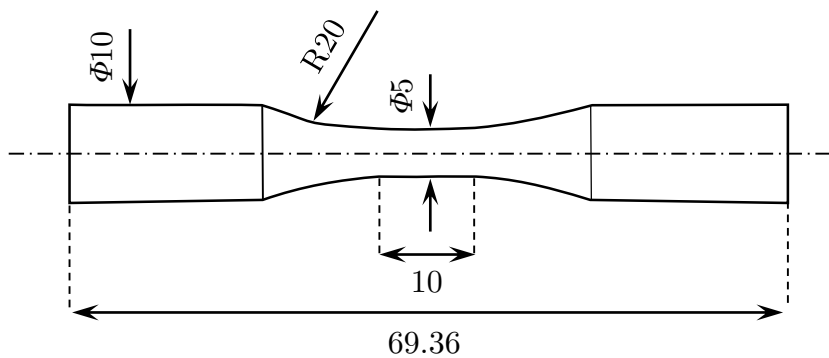


Figure III.3 – Geometry of smooth specimens used for low-cycle fatigue tests (dimensions in mm).



Figure III.4 – Smooth specimen with the extensometer attached.

Table III.1 – Experimental conditions for the LCF experiments

$\Delta\varepsilon/2$ [%]	0.2	0.3	0.4	0.5
$\dot{\varepsilon}$ [s^{-1}]	2×10^{-3}	2×10^{-3}	2×10^{-3}	2×10^{-3}
f [Hz]	0.25	0.166	0.125	0.1

3.2 Load-controlled fatigue experiments

3.2.1 Specimens and conditions

The load-controlled fatigue tests objectives are to evaluate the fatigue strength of the materials, to estimate the number of cycles for crack initiation and to measure the crack growth rate. Due to the local thermal treatment received by the materials, a specific specimen geometry was proposed. It is shown in Fig. III.5. The gauge area consists in a flat rectangular part of dimensions $2 \times 10 \times 10$ mm. An elliptic notch of aspect ratio $a/b = 1/3$ and depth b was made in the center of the specimen by laser cutting. 3D linear elastic analyses reveal a stress concentration factor of 1.4 and a relatively uniform stress in the gauge area as depicted in Fig. III.6.

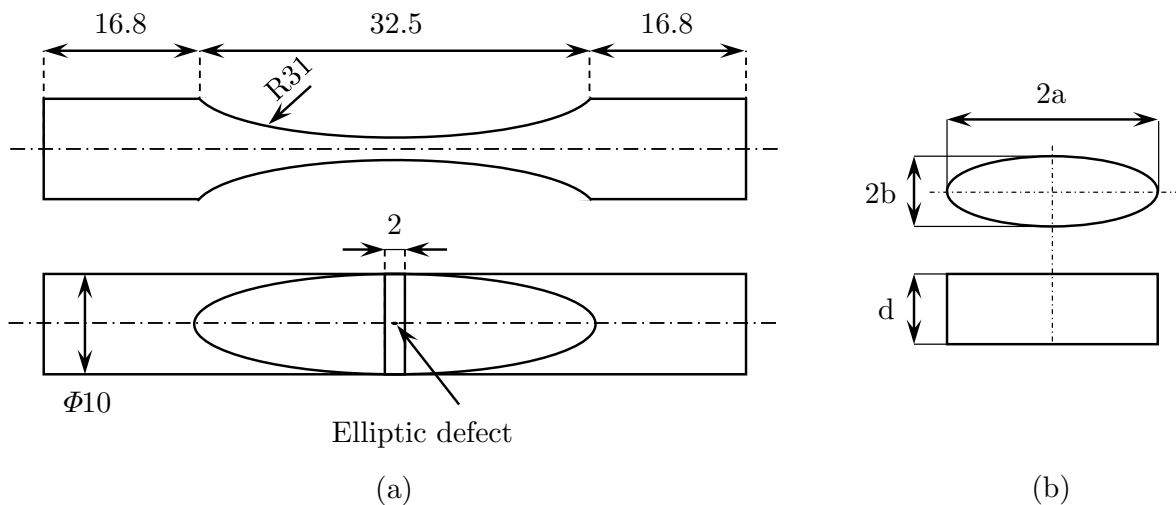


Figure III.5 – (a) Geometry of the specimen used for load-controlled fatigue tests. (b) Geometry of the elliptical notch in the center of the specimen (dimensions in mm).

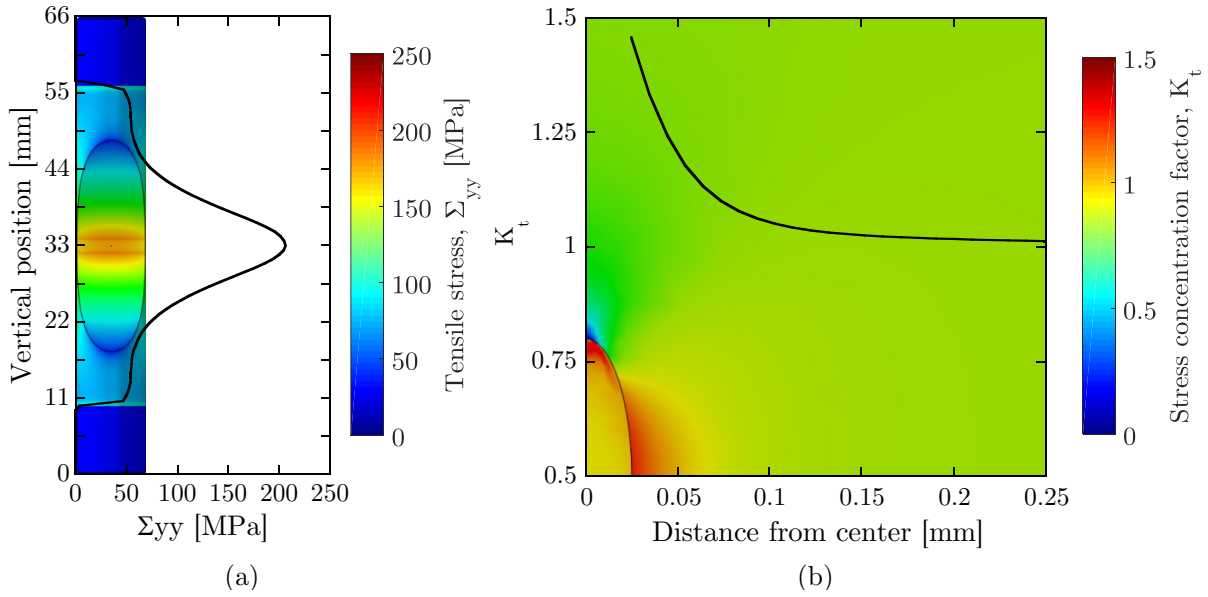


Figure III.6 – (a) Distribution of the tensile stress calculated for an elastic behavior. (b) Stress concentration factor near the notch.

The purpose of the notch is to be able to observe the formation and the early growth of a crack without significantly affecting the fatigue limit of the material [7, 9]. It is necessary to consider a notch size larger than the average grain size to prevent the notch from being totally located inside a grain or from having a too low number of grains in its vicinity that might significantly increase the scattering. Indeed, while the presence of the notch favors the crack initiation and propagation, the low number of grains and therefore the lack of representativity in its vicinity might yield the nucleation of a crack in a grain which in the absence of the defect would have not been favorably oriented. Accordingly, considering the two different heat treatments, two notch sizes were used: $150 \times 50 \times 50 \mu\text{m}$ and $600 \times 200 \times 100 \mu\text{m}$. Large notches were used for the materials subjected to the first thermal treatment pattern (peak temperature at 1400°C) as the prior austenite grain size was found to be of several hundreds of microns. Small notches were used for the other materials.

The specimens were machined and the clamped area were finished by cylindrical grinding. The gauge area on the notch side was polished by gradual finely emery paper starting from # 240 grade and finally buffed to obtain a mirror-like surface. The surface on the opposite side was polished by emery paper of grade # 600. Finally, the notch was made by laser cut. Several laser cutting procedures were tested to reduce the local irregularities produced by the process. Fig. III.7 shows the two different notches observed by SEM. As can be seen, the process seems to introduce significant irregularities on the side and in the depth of the notch. While such defects might not be detrimental to the fatigue limit of the material, they are very likely to reduce the fatigue strength and especially the initiation life. It can be noted that the large notch shows a smoother side than the small notch. Also, the shape of the notch is better respected in this case than for the small notch where the depth presents a high sharpness. The laser cutting pattern is also clearly visible in the case of the large notch.

Fatigue experiments were conducted on two identical hydraulic machines with a maximum load capacity of $\pm 50 \text{ kN}$ at frequency $f = 20 \text{ Hz}$ and sinus wave signal. Tests were performed at two different stress ratios $R = -1$ and 0.1 with the exception of α -iron and

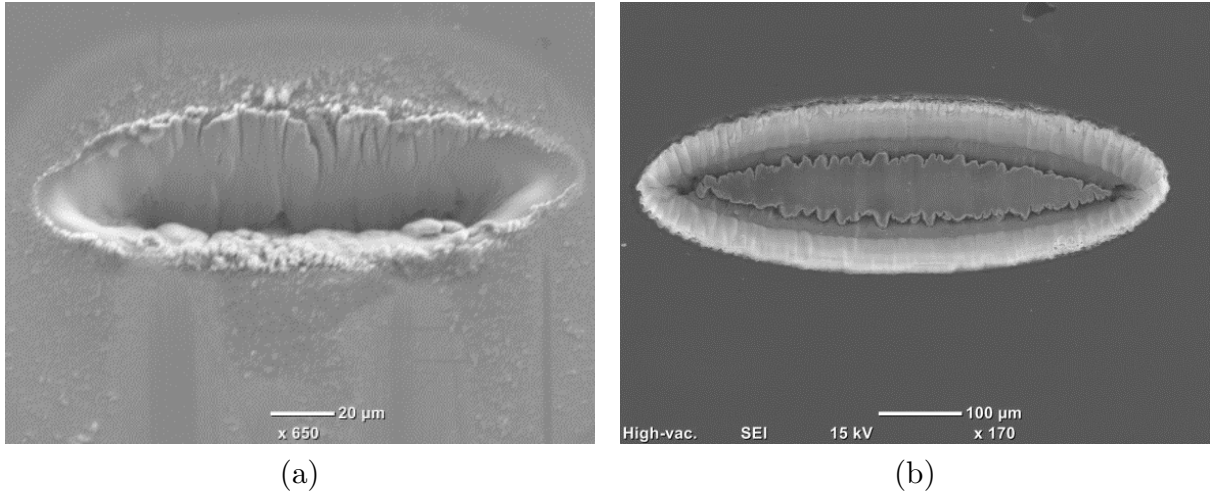


Figure III.7 – (a) Small notch. (b) Large notch.

FP steel where only fully reversed experiments were conducted. The experiments were conducted up to 10^7 cycles. In order to record the crack length, an optical microscope was used to record the specimen surface at specific intervals. The experiments were paused at regular intervals and a set of 40 pictures was taken during one slow triangular cycle. These 40 pictures were used by another researcher to evaluate the crack opening stress and determine the crack closure effect using digital image correlation (DIC) approach. In our case, only the pictures taken at the maximum stress were used as the cracks were the most visible at such position. The complete procedure is shown in Fig. III.8 as well as the experimental setup. The intervals were decomposed as follows:

- Below 10^4 cycles: a set of pictures is taken every 100 cycles for a total of 10^2 picture sets.
- Between 10^4 and 10^5 cycles: a set of pictures is taken every 10^3 cycles for a total of 90 picture sets.
- Between 10^5 and 10^6 cycles: a set of pictures is taken every 10^4 cycles for a total of 90 picture sets.
- Above 10^6 cycles: a set of pictures is taken every 10^5 cycles for a total of 90 picture sets.

Such decomposition was found to be a good compromise between the time to conduct an experiment and the number of piece of data.

3.2.2 Crack growth measurement

Crack length was measured on each side of the elliptic notch and unless explicitly mentioned, the crack growth rate was calculated independently for the two cracks. Indeed, the main objective of the crack growth measurement is to evaluate the growth rate in the MSC regime. Accordingly, we can assume that due to the presence of the notch, the two cracks grow independently as they might not be connected before they reach a certain length. The crack length is then defined as the horizontal extension of the crack plus half the notch width.

The common way to calculate the crack growth rate involves the simple secant method based on the calculation of the slope between two adjacent data points (Eq. III.26).

$$\left. \frac{da}{dN} \right|_{\bar{a}_i} = \frac{a_{i+1} - a_i}{N_{i+1} - N_i} \quad (\text{III.26})$$

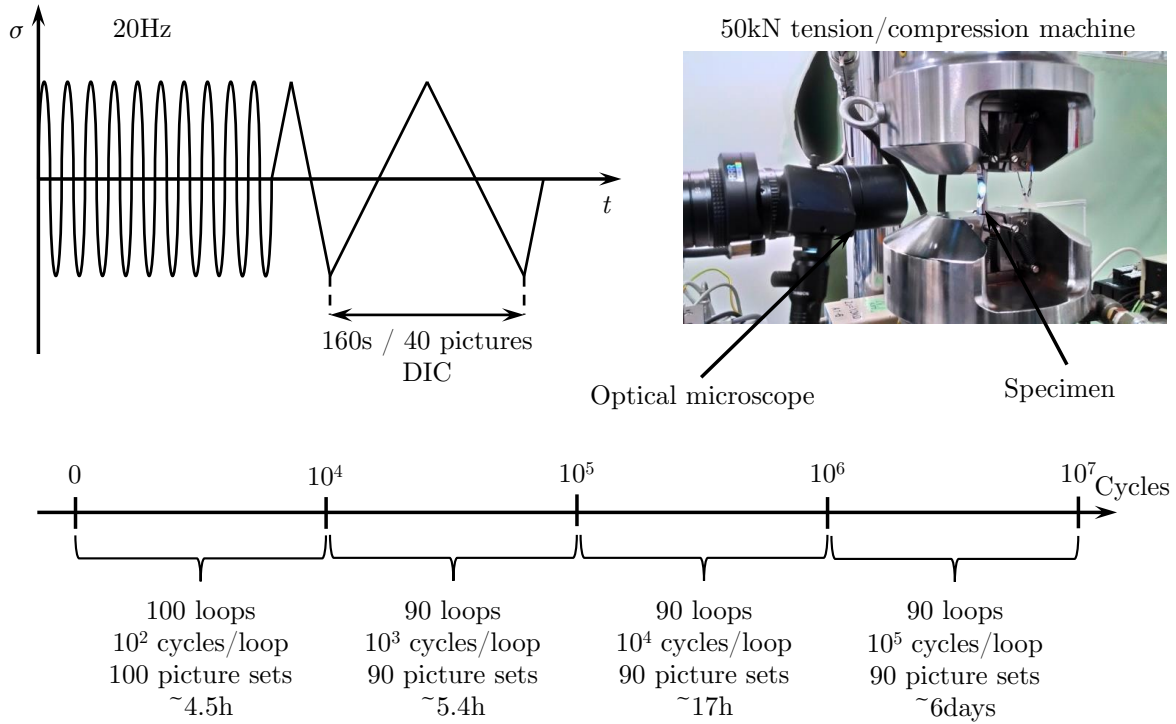


Figure III.8 – Procedure of the fatigue test.

However, for small-crack measurement, the strong variability of growth rate might be attributable to measurement errors. Indeed, if we define \bar{a} as the measured crack length, it can be decomposed as:

$$\bar{a} = a + \epsilon \Rightarrow \frac{\Delta \bar{a}}{\Delta N} = \frac{\Delta a}{\Delta N} + \frac{\Delta \epsilon}{\Delta N} \quad (\text{III.27})$$

where a is the real crack length and ϵ the measurement error. Accordingly, when the crack becomes smaller and smaller, the contribution of the error increases. Consequently, we follow the recommendation of ASTM standard E647-00 to use an incremental polynomial method. The crack length is fitted to a second-order polynomial using an odd number of data points (7 in our case) and Eq. III.28:

$$\bar{a}_i = b_0 + b_1 \left(\frac{N_i - C_1}{C_2} \right) + b_2 \left(\frac{N_i - C_1}{C_2} \right)^2 \quad (\text{III.28})$$

The growth rate is then calculated by derivation of Eq. III.28:

$$\left. \frac{da}{dN} \right|_{\bar{a}_i} = \frac{b_1}{C_2} + 2b_2 \frac{N_i - C_1}{C_2^2} \quad (\text{III.29})$$

When a crack is stopped, successive pictures of similar crack length are not considered.

4 Results and Discussion

4.1 Strain-controlled fatigue experiments

4.1.1 Cyclic stress response

Cyclic stress response for the different materials are shown in Fig. III.9(a), III.10(a), III.11(a), III.12(a), III.13(a), III.14(a), III.15(a), III.16(a) and III.17(a), where the stress amplitude $\Delta\sigma/2$ is represented against the number of cycles. All materials, with the exception of α -iron and FP steel, exhibit a first phase of cyclic hardening irrespective of the applied strain amplitude. As a general trend, hardening rate is slower at lower strain amplitude and continues for a larger number of cycles. For instance, at 0.2% strain hardening continues up to 50 to 100 cycles in most materials while hardening finishes around 10 to 20 cycles for 0.4 and 0.5% applied strain. These observations are consistent with literature data on low-carbon steels [139–142]. Following this stage, softening is observed on all the materials as the stress amplitude decreases. Here again, softening rate is higher at higher strain. This softening stage continues until reaching a stable stress condition. However, in some cases, mainly at higher strain amplitude, failure occurs before a stable stress condition is reached.

The effect of the thermal treatment on the cyclic stress response can be observed by comparing Fig. III.12, III.13 and III.14. The higher cooling rate of the B10-30 material compared with the B10-01 material increases the strength of the material since the martensite volume fraction increases. Therefore, higher stress amplitudes are reached for every loading conditions. On the other hand, hardening and softening are more significant at higher cooling rate. In contrast, no significant difference in term of stress amplitude is observed between B10-30 and B14-10 steels. However, while B10-30 reaches a stable stress condition at each strain amplitude, it is not the case for B14-10 material where failure occurs during the softening stage. B14-10 steel therefore exhibits a lower ductility than B30-10 as it cannot adapt for every strain condition.

4.1.2 Cyclic stress-strain curve

To confirm these observations, cyclic stress-strain (CSS) curves were drawn by considering stress-strain hysteresis curves at half-life or near half-life. Although in some cases stable stress conditions were not achieved, the half-life can be assumed to represent a nearly stabilized behavior. The stress-strain hysteresis curves and the CSS curves are represented in Fig. III.9(b), III.10(b), III.11(b), III.12(b), III.13(b), III.14(b), III.15(b), III.16(b) and III.17(b) for each material. The tips of the stable hysteresis curves are used to estimate the CSS curves based on a Ramberg-Osgood relation:

$$\varepsilon = \varepsilon_{el} + \varepsilon_{pl} = \frac{\sigma}{E} + \left(\frac{\sigma}{K}\right)^{\frac{1}{n}} \quad (\text{III.30})$$

where E is the Young modulus, K is the cyclic strain hardening coefficient and n is the cyclic hardening strain exponent. Parameters K and n are estimated by linear regression of the peak stress against the plastic strain on a log-log graph and are reported in Table III.2 for all the materials with the coefficient of determination R^2 and the cyclic yield stress at 0.2% strain, $\sigma_{0.002}$. In every case a Young modulus $E = 210$ GPa was considered.

The hardening nature of the CSS curves is reflected through the value of the cyclic strain hardening exponent n , where a high value implies a high strain hardening. It is

Table III.2 – Cyclic properties of the different steels.

Material	Cyclic stress response				Strain-life behavior	
	K [MPa]	n [-]	$\sigma_{0.002}$ [MPa]	R^2	ϵ'_f	c
α -iron	732	0.16	273	0.98	0.070	-0.44
FP steel	1153	0.24	263	0.98	0.065	-0.44
B10-01	657	0.097	357	0.92	0.31	-0.61
B10-30	1017	0.12	473	0.98	2.4	-0.79
B14-10	802	0.079	489	0.99	3.5	-0.94
C10-30	902	0.14	382	0.97	0.57	-0.64
E14-10	716	0.059	493	0.94	70.4	-1.3
57-14-10	658	0.057	462	0.85	5.7	-0.99
57-10-50	986	0.14	422	0.96	3.1	-0.81

notable here that the mechanical properties of the steels subjected to the same thermal treatment pattern are very similar despite the difference in microstructure. In the case of the *14-10* materials, the hardening exponents are close to 0 meaning an almost perfectly plastic behavior in high strain region. Comparing the 0.2% cyclic yield stress in the case of the B material, the cooling rate seems to be the main factor contributing to the increase in the yield stress.

Comparing α -iron and FP steel, one can notice that despite having different cyclic stress responses in terms of stress amplitude, the stabilized hysteresis curves are very close in term of peak stress. This is also confirmed by the cyclic yield stresses that differ by only 10MPa. However, the shape of the hystereses are slightly different. It is therefore expected that the parameters of the constitutive models will be relatively close for the isotropic hardening components and different for the kinematic hardening components.

4.1.3 Strain-life behavior

The plastic strain amplitude $\frac{\Delta\epsilon^p}{2}$ versus the number of reversals to failure $2N_f$ for all the materials is shown in Fig. III.14. The strain-life data have been analyzed according to the Coffin-Manson relation:

$$\frac{\Delta\epsilon^p}{2} = \epsilon'_f (2N_f)^c \quad (\text{III.31})$$

where ϵ'_f and c are the fatigue ductility exponent and the fatigue ductility coefficient respectively. The estimated parameters for each material are reported in Table III.2.

Considering α -iron and FP steel, no significant difference is observed in the strain-life behavior as the Coffin-Manson parameters are very close. This was expected since the cyclic stress responses were very similar. For the other materials, the difference in cyclic life between the steels gradually decreases with the increase in the strain amplitude. At low plastic strain, the number of cycles to failure is mainly related to the microstructure and the strength of the material while at higher strain amplitude, the cyclic deformation is relatively homogeneous in the material leading to a lower dependency on the microstructure. Indeed, two trends are clearly visible on Fig. III.14 when the plastic strain amplitude de-

creases. Materials subjected to the first thermal treatment pattern (B14-10, E14-10 and 57-14-10) exhibit a higher slope and therefore a lower ductility exponent than the materials subjected to the second treatment pattern. This difference outlines the poor ductility of the B14-10, E14-10 and 57-14-10 materials.

The observation of the fracture surface confirmed this conclusion as shown in Fig. III.19. Indeed, in the case of the B10-01 and B10-30 materials subjected to the same strain amplitude of 0.2%, the fracture surface is relatively smooth with a clear transition between crack propagation and final failure stages. On the other hand, the fracture surface of the B14-10 material is very sharp, exhibiting intergranular fracture. Similar observations were made for the other materials with same heat treatment. In fact, the sharp fracture surface of the B14-10 steel suggests that the crack propagation is still in stage I (mode II shearing mechanism).

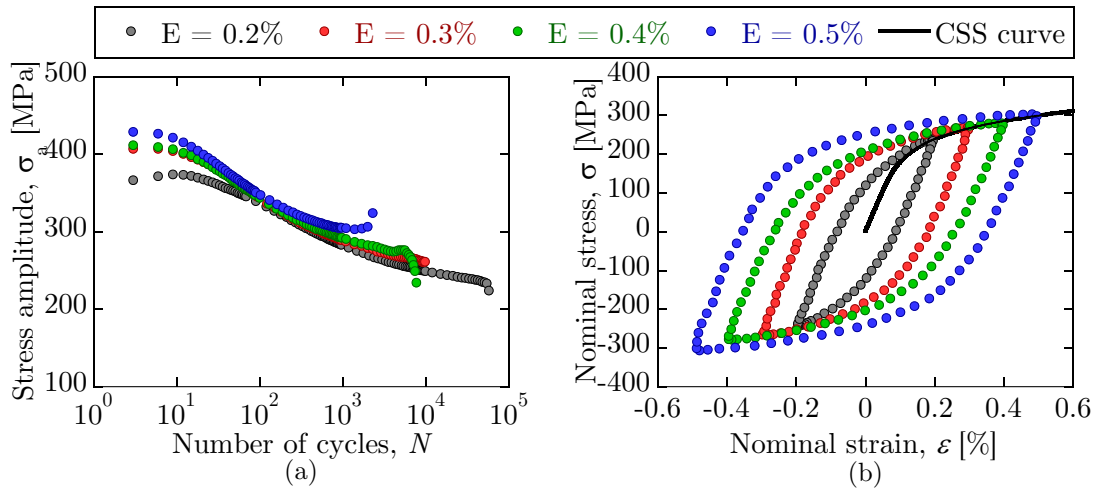


Figure III.9 – (a) Stress amplitude against the number of cycles and (b) hysteresis and CSS curves of α -iron.

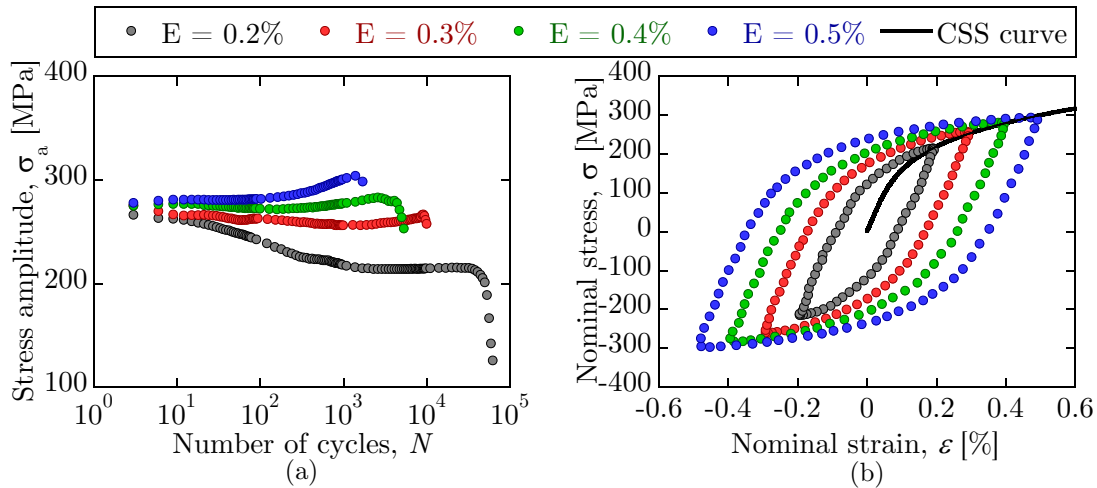


Figure III.10 – (a) Stress amplitude against the number of cycles and (b) hysteresis and CSS curves of FP steel.

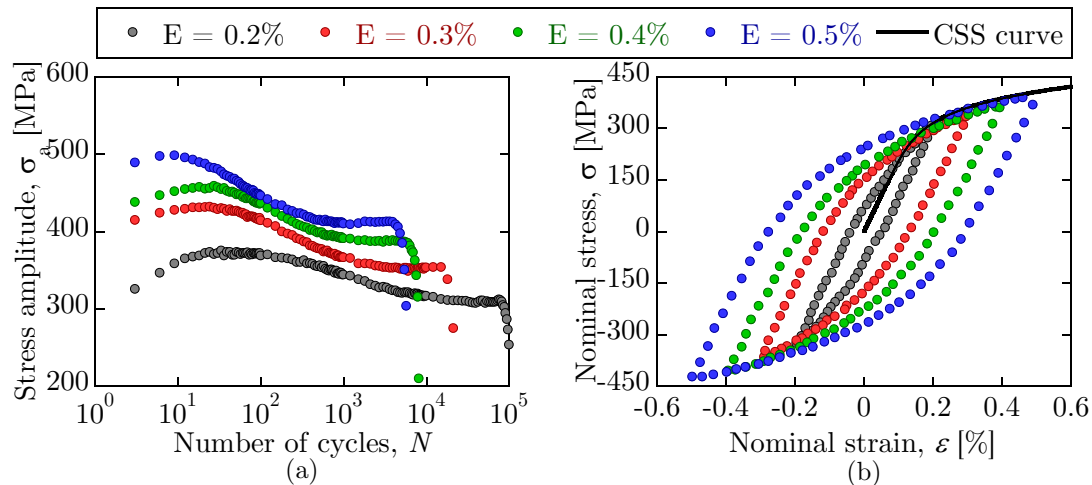


Figure III.11 – (a) Stress amplitude against the number of cycles and (b) hysteresis and CSS curves of C10-30 steel.

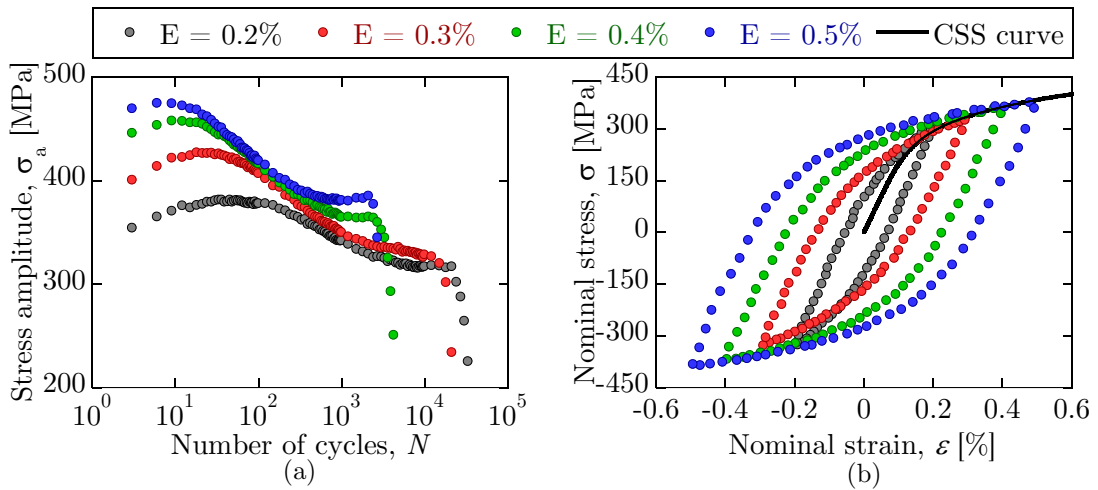


Figure III.12 – (a) Stress amplitude against the number of cycles and (b) hysteresis and CSS curves of B10-01 steel.

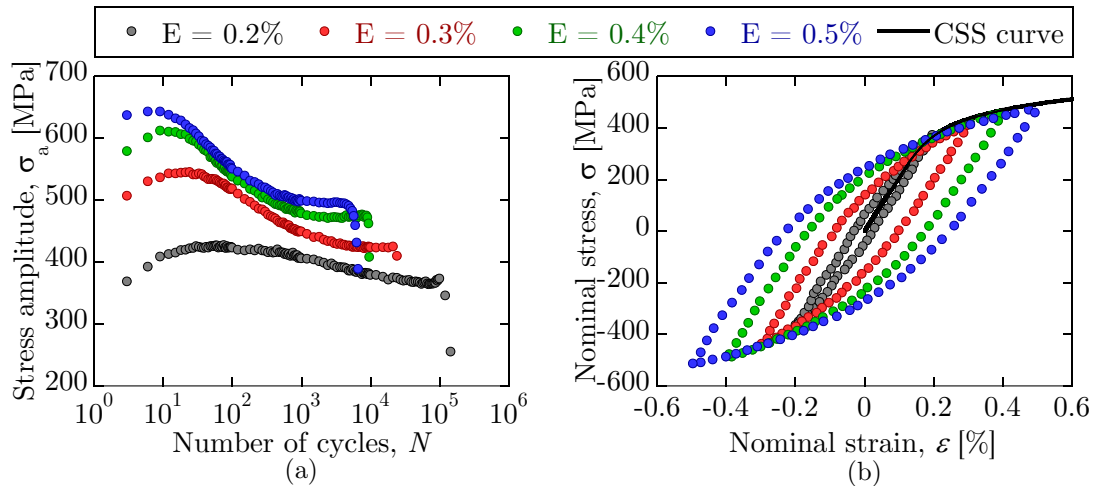


Figure III.13 – (a) Stress amplitude against the number of cycles and (b) hysteresis and CSS curves of B10-30 steel.

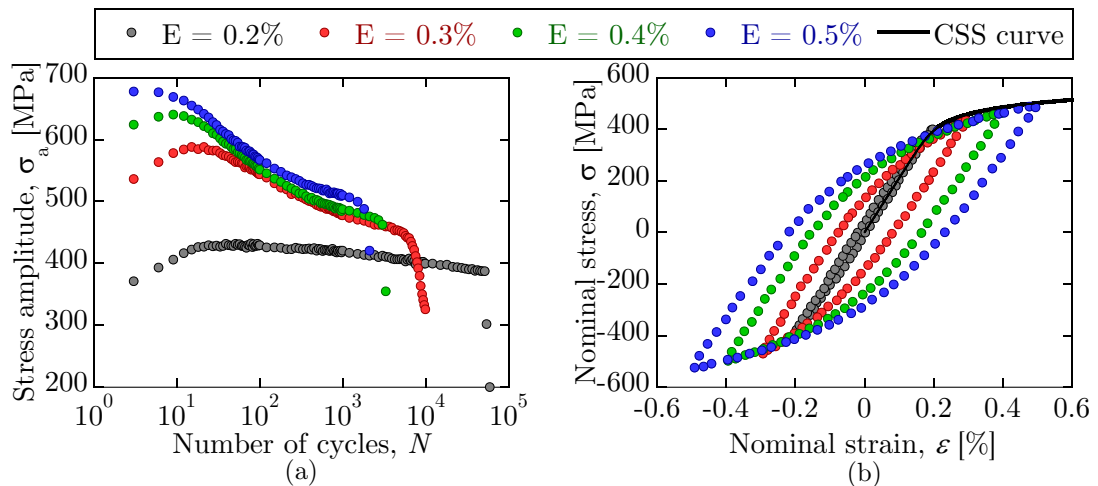


Figure III.14 – (a) Stress amplitude against the number of cycles and (b) hysteresis and CSS curves of B14-10 steel.

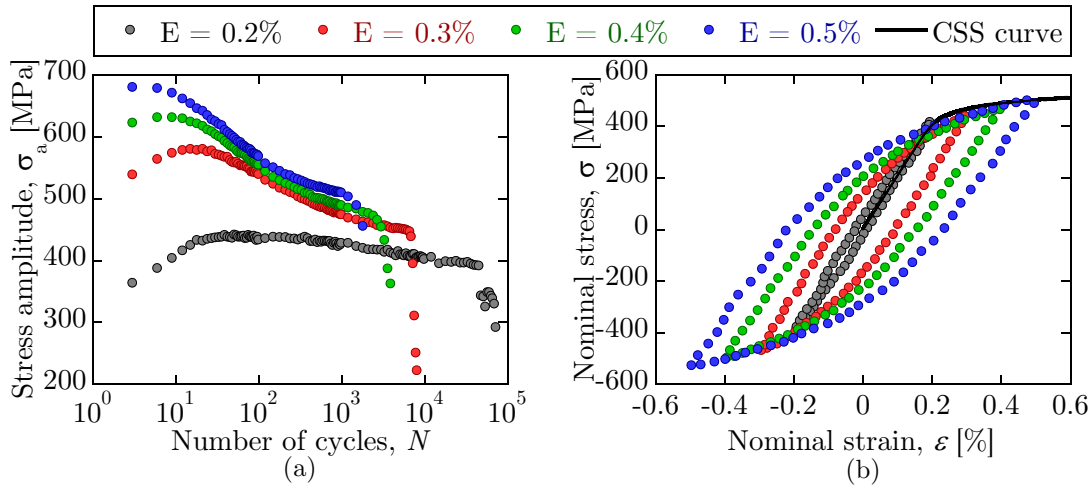


Figure III.15 – (a) Stress amplitude against the number of cycles and (b) hysteresis and CSS curves of E14-10 steel.

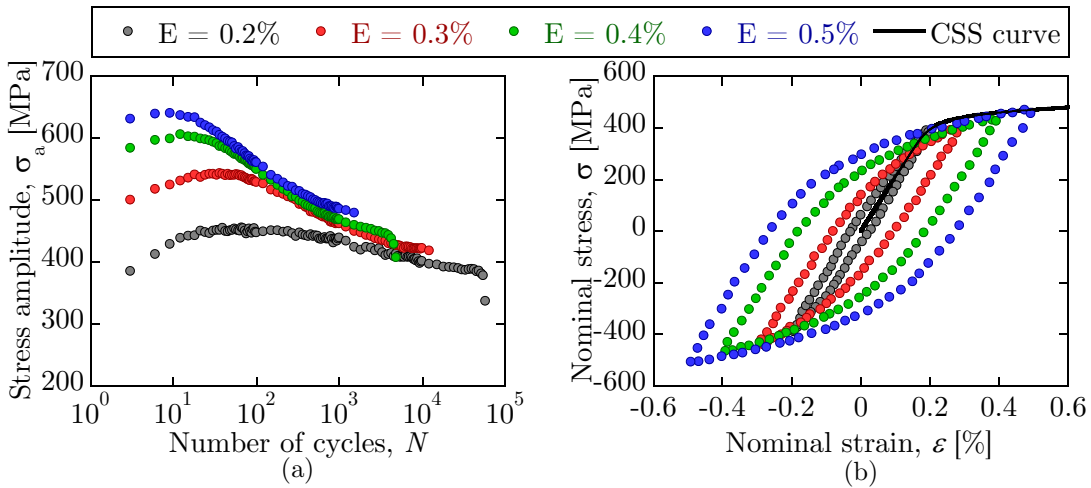


Figure III.16 – (a) Stress amplitude against the number of cycles and (b) hysteresis and CSS curves of 57-14-10 steel.

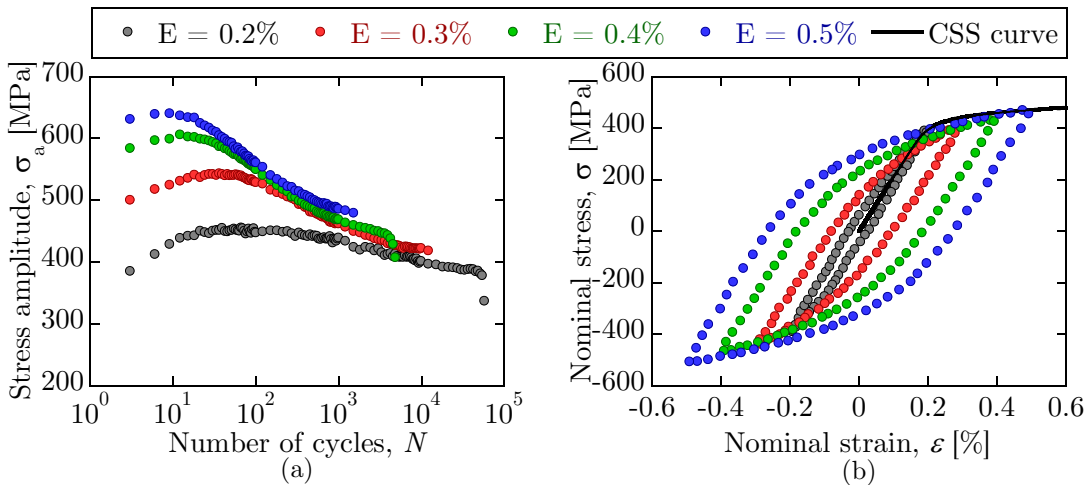


Figure III.17 – (a) Stress amplitude against the number of cycles and (b) hysteresis and CSS curves of 57-10-50 steel.

4. RESULTS AND DISCUSSION

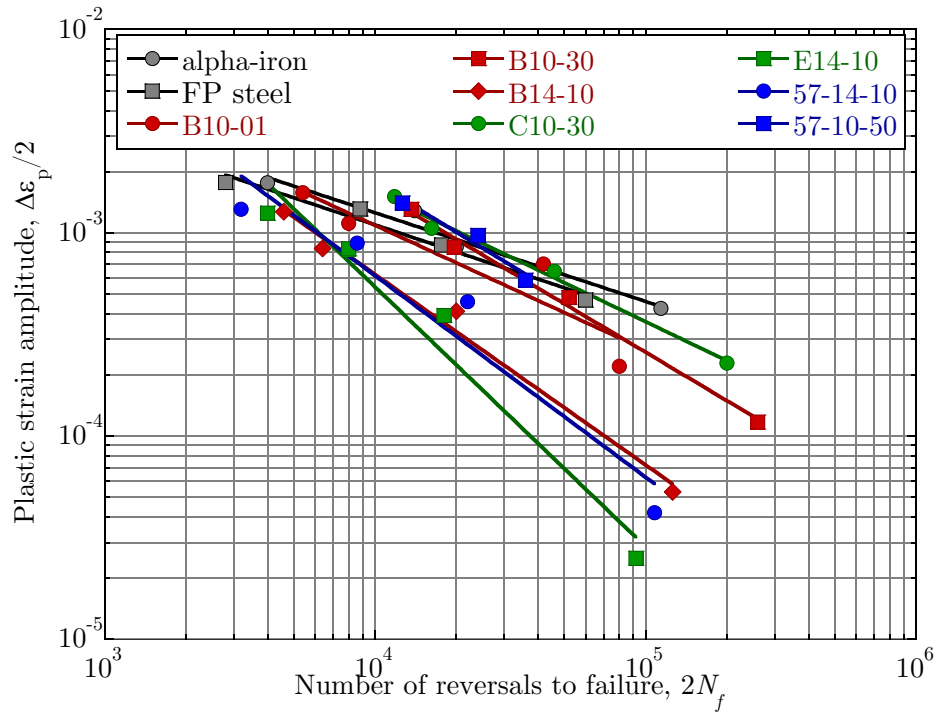


Figure III.18 – Coffin-Manson curves for the different steels.

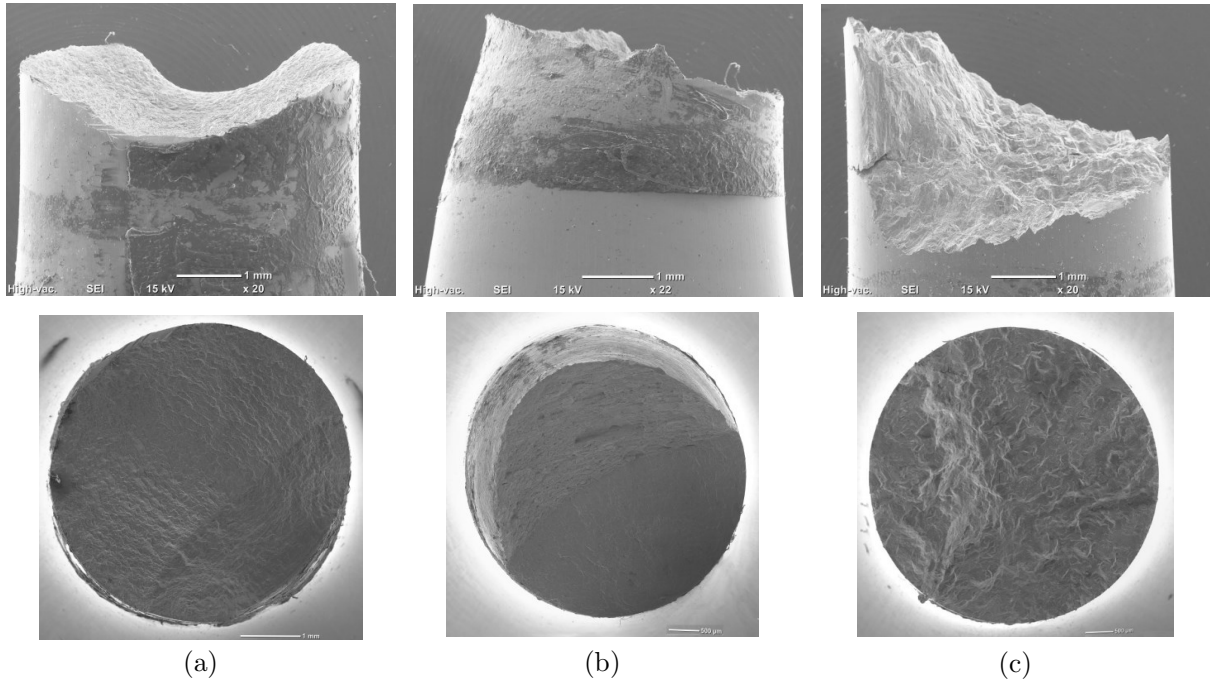


Figure III.19 – SEM observation of fracture surface of (a) B10-01, (b) B10-30 and (c) B14-10 steels subjected to 0.2% strain amplitude.

4.2 Parameters identification

The previous section has highlighted the presence of three main phases in most of the materials under cyclic condition: a hardening phase of ten to a hundred cycles followed by a softening phase until approximately half-life which ends up in a relatively stable behavior for the second half-life. Ideally, the characterization of the material parameters would be based on the complete cyclic stress-strain history. However, the two models (J_2 and CP) considered in this study cannot reproduce both hardening and softening as only one hardening variable is implemented in each model: σ_y and τ_c . Moreover, the CP model does not account for the microstructural changes occurring during the cyclic loading with the appearance of dislocation structures where the strain will mainly localize and where dislocation formation and annihilation will be in equilibrium. Finally, the simulation of a complete loading history is computationally demanding and therefore inappropriate for a calibration procedure. For these reasons it was decided to calibrate the parameters assuming only a hardening phase until reaching a saturated stage corresponding to the experimental stable hysteresis curves. The parameters calibration was carried out for the three materials numerically studied in the next chapter: α -iron, FP and B14-10 steels. In each case, the elastic constants were taken from literature.

4.2.1 J_2 -plasticity model

The identification of the parameters of the J_2 model is carried out in two steps. At first the kinematic hardening parameters are identified using the optimization module of Abaqus and the stable hysteresis curve for the higher applied strain amplitude (0.5%). The isotropic hardening parameters, σ_0 , Q_∞ and b are then selected so that the stabilized hysteresis curve in the end of the simulation (20 cycles) matches the experimental one. For every material, five kinematic back-stresses are considered. Finally the hysteresis curves at lower strain are computed and compared to the experimental one for validation.

Fig. III.20 and III.21 represent the stable experimental and numerical stress-strain hysteresis curves for α -iron and FP steel respectively. Overall a good agreement is achieved between the experiments and the J_2 model. However, some discrepancies are observable especially at 0.2% strain. It is worth noticing that while the model predicts a symmetric hysteresis, this is not always the case in experiments, especially in the first cycles where residual stresses might be present. The parameters of the J_2 model are reported in Table III.3. As expected the parameters are slightly different between α -iron and FP steel due to the difference in shape of the hysteresis curves while peak stresses are close. Consequently the kinematic hardening parameters are different which in return implies different isotropic hardening parameters. It is worth noticing that some γ_k parameters are very close meaning that the corresponding kinematic back-stresses act in the same strain range. Therefore, it would have been possible to fit the experimental hysteresis curves with a lower number of back-stress. However, a higher number of back-stresses does not increase the computational cost.

4.2.2 Crystal plasticity model

The transition from an isotropic model to a crystal plasticity model is not straightforward as there is no explicit relation between the behavior of a grain in an aggregate and the global response of the aggregate. Indeed, using a CP model with only an isotropic hardening law will still produce a kinematic hardening effect, also known as latent harde-

Table III.3 – Parameters of the J_2 model for the different materials.

Material	Elasticity		Isotropic hardening			Kinematic hardening	
	E [MPa]	ν [-]	σ_0 [MPa]	Q_∞ [MPa]	b	C_k [MPa]	γ_k
α -iron	210	0.3	135	60	7	6775	361
						10197	359
						10686	360
						28110	1466
						133471	3948
FP steel	210	0.3	90	50	4	28641	357
						27657	1528
						30591	1525
						51577	9055
						109542	8403

ning, at the polycrystal scale due to the fact that each grain will harden differently and at different strain. Therefore, the parameters identified in the previous section cannot be used to identify the CP parameters. Also, due to impossibility to evaluate the mechanical fields at the grain scale during the experiments, the identification of the CP parameters is also based on the macroscopic stabilized response of the materials. Five parameters are mainly considered: τ_{c_0} , τ_{c_s} , h_0 , A and B . The elastic constant are taken from literature [143, 144].

The identification strategy is very similar to that for the J_2 model. At first, simulations are conducted using the Taylor-Lin model presented in Section 2 at the highest applied strain amplitude, 0.5%. The kinematic hardening parameters are first calibrated to correctly fit the shape of the hysteresis curves. Then simulations are conducted at lower strain to fix the isotropic hardening parameter such that the stabilized response of the model could match the experimental data. A condition was set to the initial value of the CRSS τ_{c_0} such that the yield stress of the material cannot be higher than the one evaluated from the CSS curve. In other word, the first 1/4 cycle should always lie below the CSS curve. Once the parameters are set, simulations using the 3D RVE are conducted to adjust them more precisely. As we know that the Taylor-Lin model constitutes the upper bound of the material behavior, the parameters were set to lead to a slightly higher hysteresis curve such that the results from the RVE could better match.

This strategy is slightly different for B14-10 steel due to the very significant softening observable at strain amplitudes over 0.2% and the very limited hardening and softening at 0.2% strain amplitude. As fatigue simulations will be conducted at stress close to or below the stable stress at 0.2% strain amplitude, it was decided to calibrate the kinematic hardening parameters based on the 0.5% stress-strain hysteresis curve and fix the isotropic hardening parameters to match the 0.2% hysteresis curve. Due to the very low plasticity measured at this strain range, the hysteresis curve is very irregular. This might be due to measurement errors during the test. Indeed, assuming a constant measurement error with the strain amplitude, the contribution of the error will be higher at lower strain than at higher strain. In both case the model were subjected to 20 cycles. The CP parameters

are summarized in Table III.4.

The hysteresis curves simulated by the Taylor-Lin model and the 3D RVE are shown in Fig. III.22, III.23 and III.24 for α -iron, FP steel and B14-10 steel. As expected, the hysteresis curves obtained with the 3D RVE are constantly smaller than their counterpart using the Taylor-Lin model. Overall a good agreement is found between the experimental and simulated curves. However, it is worth pointing out, especially for the B14-10 steel that a slight asymmetry can be observed between the compression and tension portions of the curves for high strain amplitude. Such observation can be made for most of the results presented in the previous section. This discrepancy between tension and compression may be attributed to the presence of cracks in the material which under tension may open and therefore reduce the macroscopic stress. However, this asymmetry cannot be reproduced numerically which explains why the hysteresis curves better match the compression portion than the tension one.

While reproducing quite accurately the hysteresis data, such identification procedure is relatively approximate. The calibration of the local behavior at the grain is based on the average macroscopic behavior. A better approach could be to perform an *in situ* experiment with EBSD analysis and reproduce the exact same microstructure numerically. The measurement of the strain at the surface of the specimen could be performed for instance by DIC analysis [145]. However, this approach is also incomplete as the microstructure sub-surface remains unknown. Besides, the current crystal plasticity model does not account for microstructural changes such as the appearance of dislocation structures where the strain localizes. Finally, it is also unclear whether or not a single set of parameters can be used to simulate a material for different strain amplitudes. Indeed, we assumed that it was possible to find such a set but since the stabilized hysteresis curves depend on the total loading history, it is highly probable that it is not the case.

Table III.4 – Parameters of the CP model for the different materials.

Parameters	α -iron	FP steel	B14-10
C_{11} [GPa]	233.3	233.3	268.0
C_{12} [GPa]	135.5	135.5	111.0
C_{44} [GPa]	118.0	118.0	79.0
$\dot{\gamma}_0$ [s^{-1}]	10^{-3}	10^{-3}	10^{-3}
n	4	4	20
τ_{c0} [MPa]	60	50	140
τ_{cs} [MPa]	110	110	200
h_0 [MPa]	150	150	150
A [MPa]	33000	26000	70000
B	900	1000	900

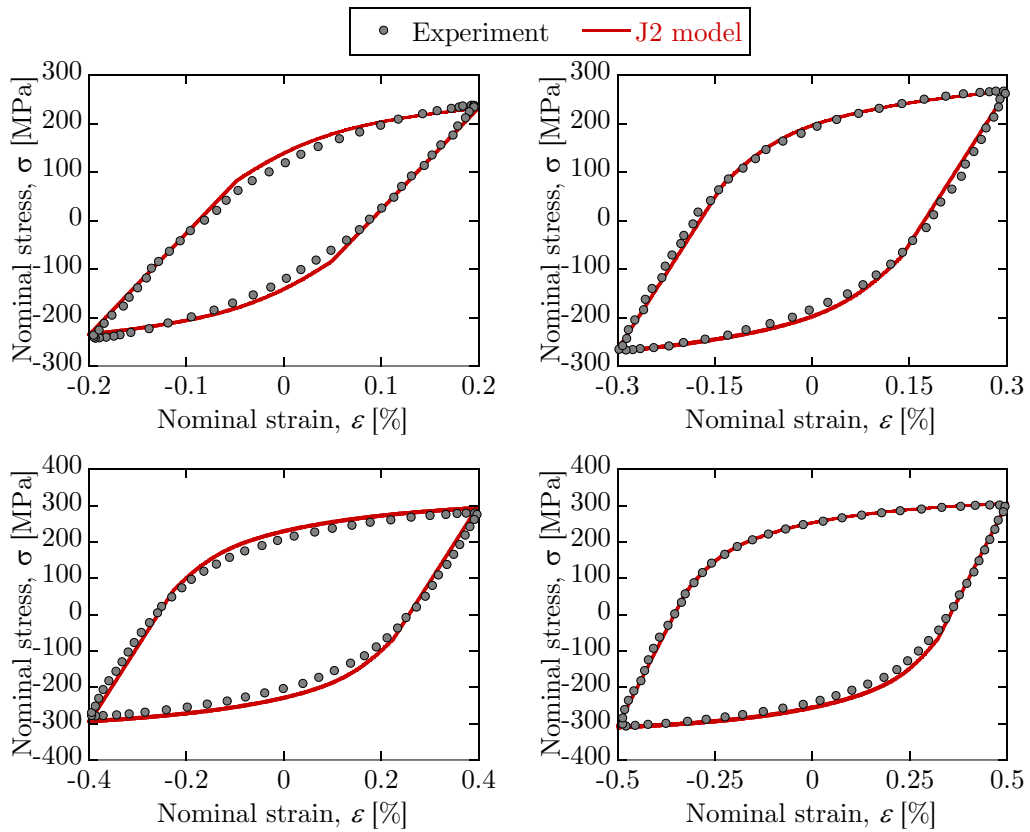


Figure III.20 – Comparison between the experimental and the simulated hysteresis curves based on the J_2 model for α -iron.

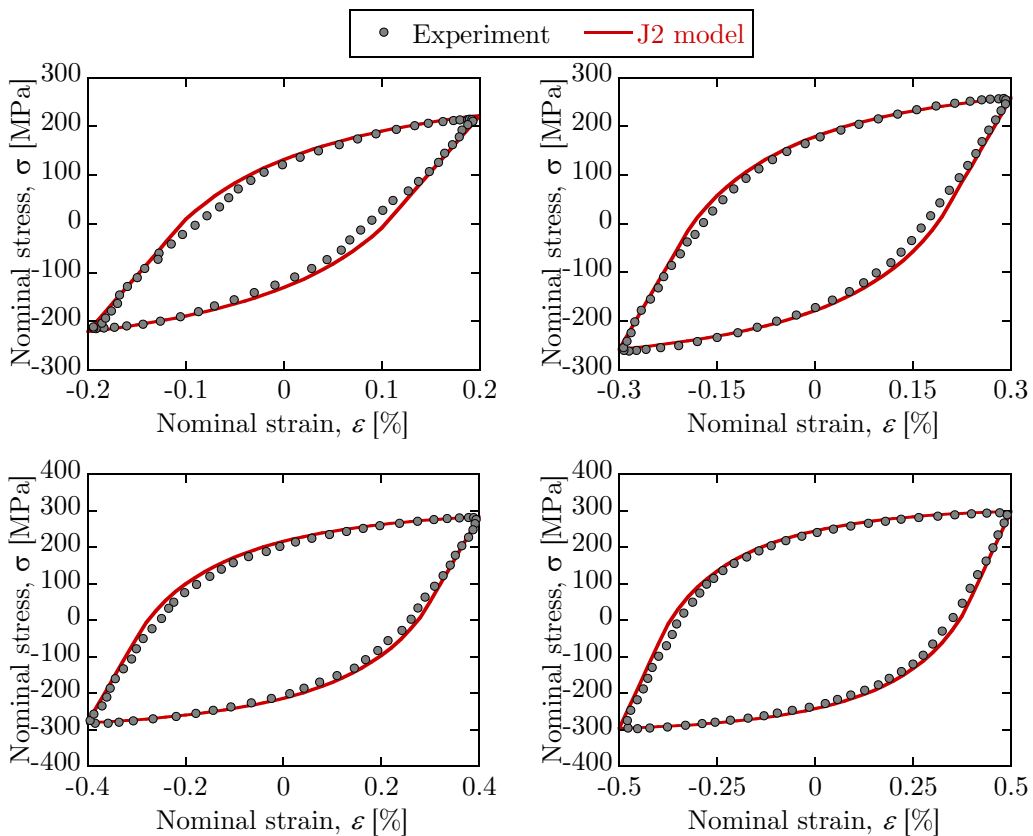


Figure III.21 – Comparison between the experimental and the simulated hysteresis curves based on the J_2 model for FP steel.

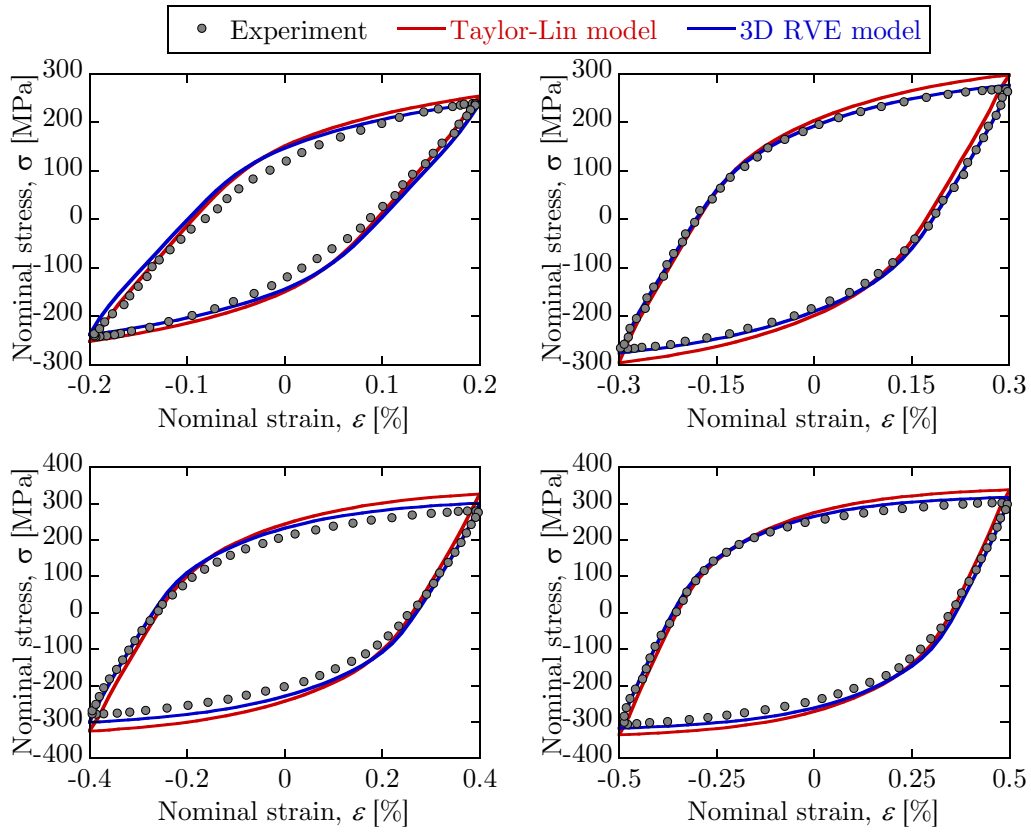


Figure III.22 – Comparison between the experimental and the simulated hysteresis curves based on the CP model for α -iron.

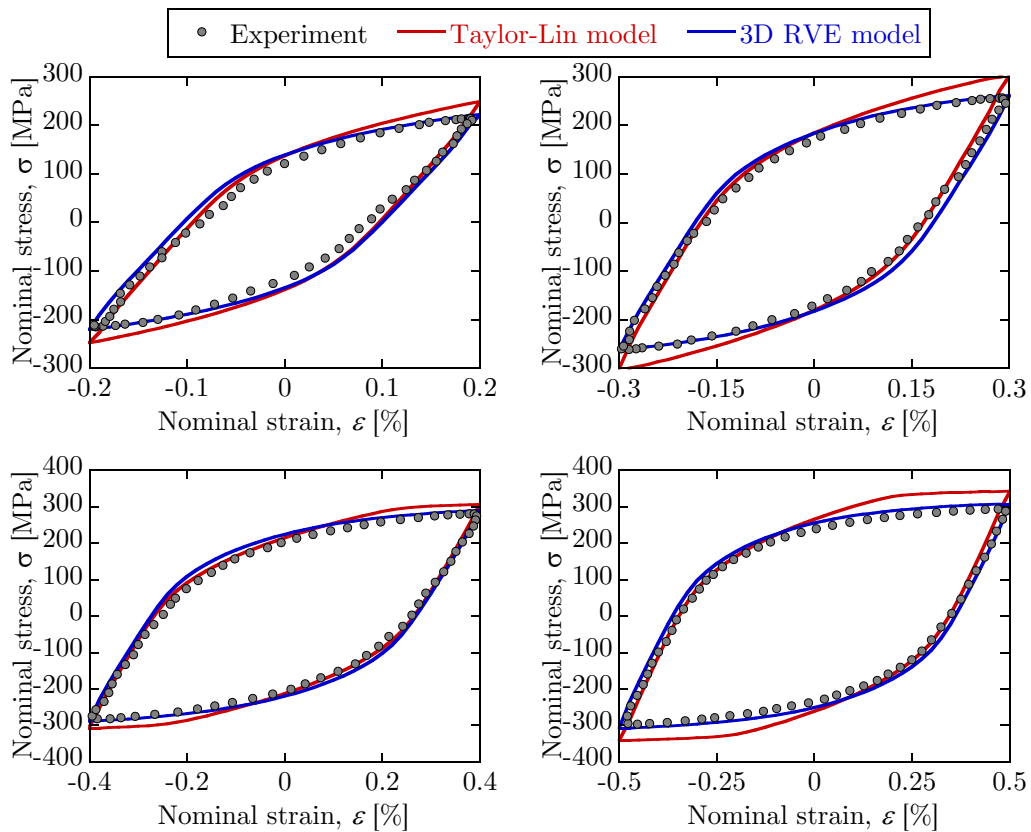


Figure III.23 – Comparison between the experimental and the simulated hysteresis curves based on the CP model for FP steel.

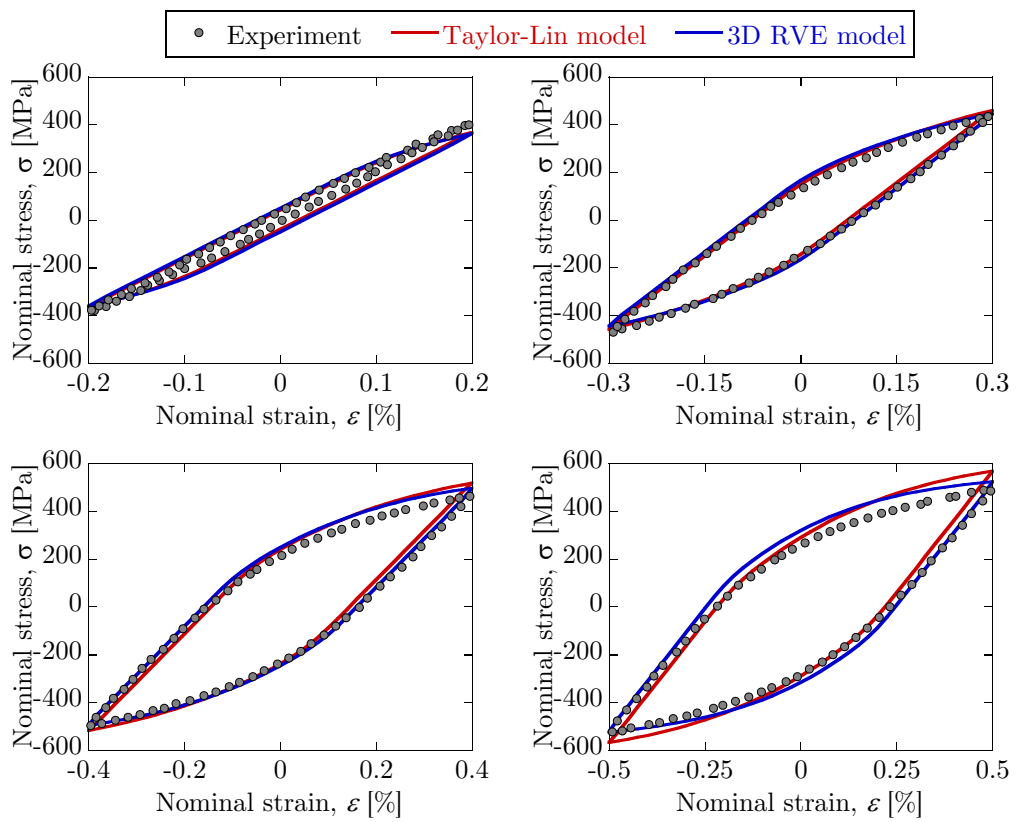


Figure III.24 – Comparison between the experimental and the simulated hysteresis curves based on the CP model for B14-10 steel.

4.3 Load-controlled fatigue experiments

4.3.1 Study of fatigue lives

Whöler curves

The results of the load-controlled fatigue experiments with the notched specimens are summarized in the Whöler curves displayed in Fig. III.25 and III.26 for small and large notch respectively. With the exception of α -iron and FP steel, all the figures include the experiments conducted at $R=-1$ and $R=0.1$ stress ratio. Due to the small number of specimens for each material and stress conditions, a fatigue limit at 10^7 cycles was not always obtained. Specimens that did not fail at 10^7 cycles were not used for another test at higher stress amplitude since slip traces were clearly visible on the surface of the specimens, especially in the case of small grain size materials. In most specimen under $R=0.1$ stress ratio, macroscopic plasticity was observed in the first few hundreds cycles, but no ratcheting did occur.

In the case of small notch specimens (Fig. III.25), the B10-30 and 57-10-50 steels show the highest fatigue limits and fatigue strengths while FP steel has the lowest performances, as expected from the results of the strain-controlled tests. The slope of the S-N curve does not vary much from one materials to another. The endurance limit as well as the fatigue strength tend to drop with the increase in the R ratio. However, the slope does not change significantly.

Considering large notch specimens, the three materials exhibit very similar behavior. The slopes of the S-N curves are much higher than the other materials which indicates a worse fatigue strength. The fatigue limit is also lower. A higher sensitivity to the stress ratio is also noticed as both the fatigue strength and the fatigue limit decreased more than for small notch specimens.

The comparison of the Whöler curves suggests that steels subjected to similar heat treatment patterns exhibit close fatigue performances. As a general trend, the first treatment pattern (peak temperature of 1400°C) deteriorates both the fatigue limit and strength. The cooling rate seems to affect the fatigue performances as higher cooling rate tends to increase the strength and endurance limit. These observations are consistent with that made for LCF tests and may be attributed to the increase in the grain size for the thermal treatment effect, and bainite/martensite fraction for the cooling rate effect.

Crack initiation

In every specimen crack initiation leading to the final failure occurred on the surface on the polished side. No pores, inclusions or internal defects were found on the fracture surface near the initiation sites. However, in most of the B14-10 and E14-10 specimens under $R=-1$ stress ratio, the major crack did not initiate and propagate from the elliptic defect but near the transition between the flat and the curved part of the specimen (± 1 mm from the notch center). Surprisingly, in such case, crack always initiated on the polished side and not on the rear side despite a worse finishing surface. This may be attributed to the fact that the notch generates an asymmetrical stress distribution on the surface of the specimen between the front and rear faces. Besides, a simple 3D linear elastic simulation of the complete specimen revealed a locally higher principal stress at the transition between the curved and flat portions than in the center of the specimen, far from the notch. It can explain the constant observation of the final fracture at this

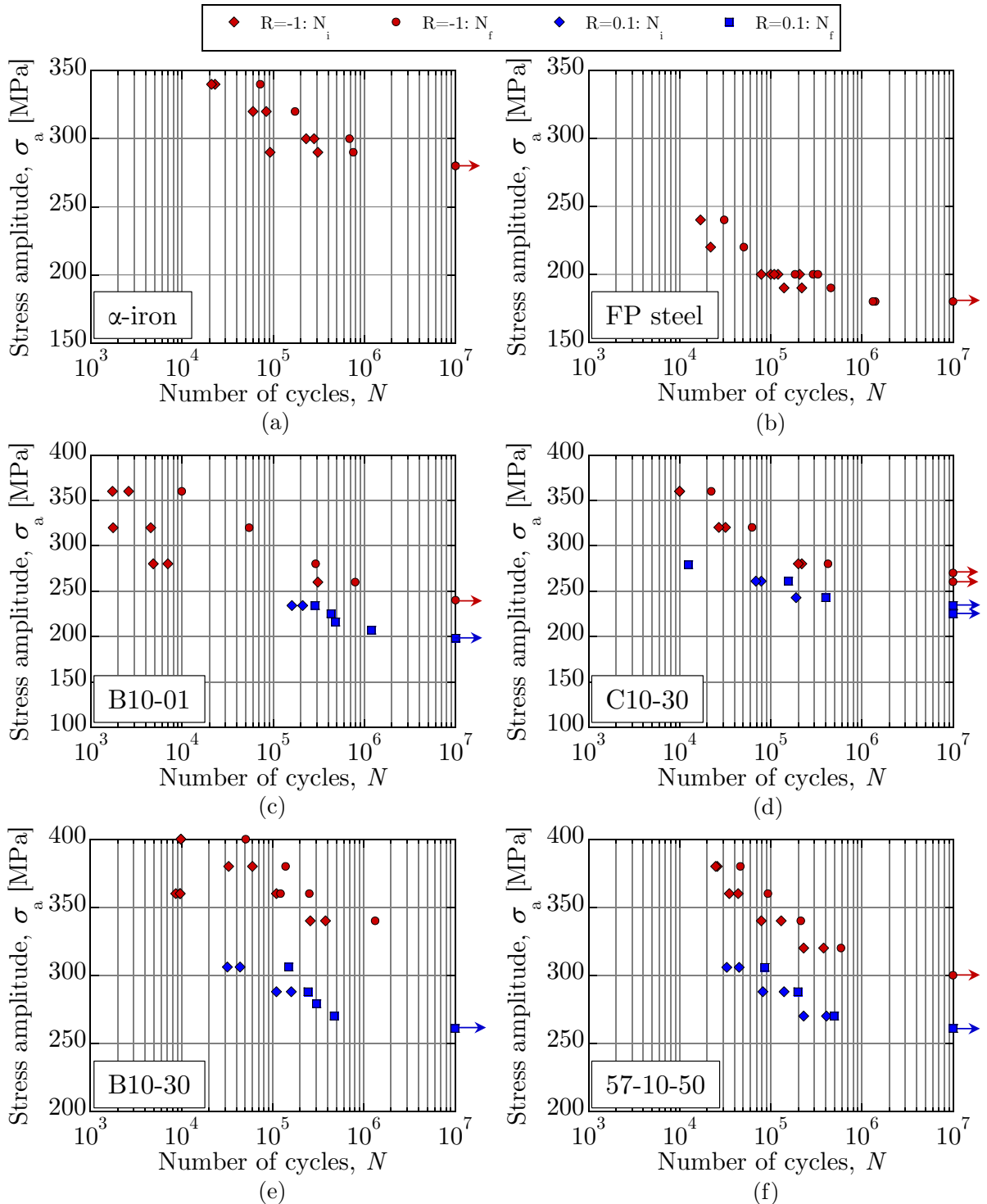


Figure III.25 – Results of the fatigue experiments for (a) α -iron, (b) FP steel, (c) B10-01, (d) C10-30, (e) B10-30 and (f) 57-10-50 steels. Arrow indicates a test conducted without failure.

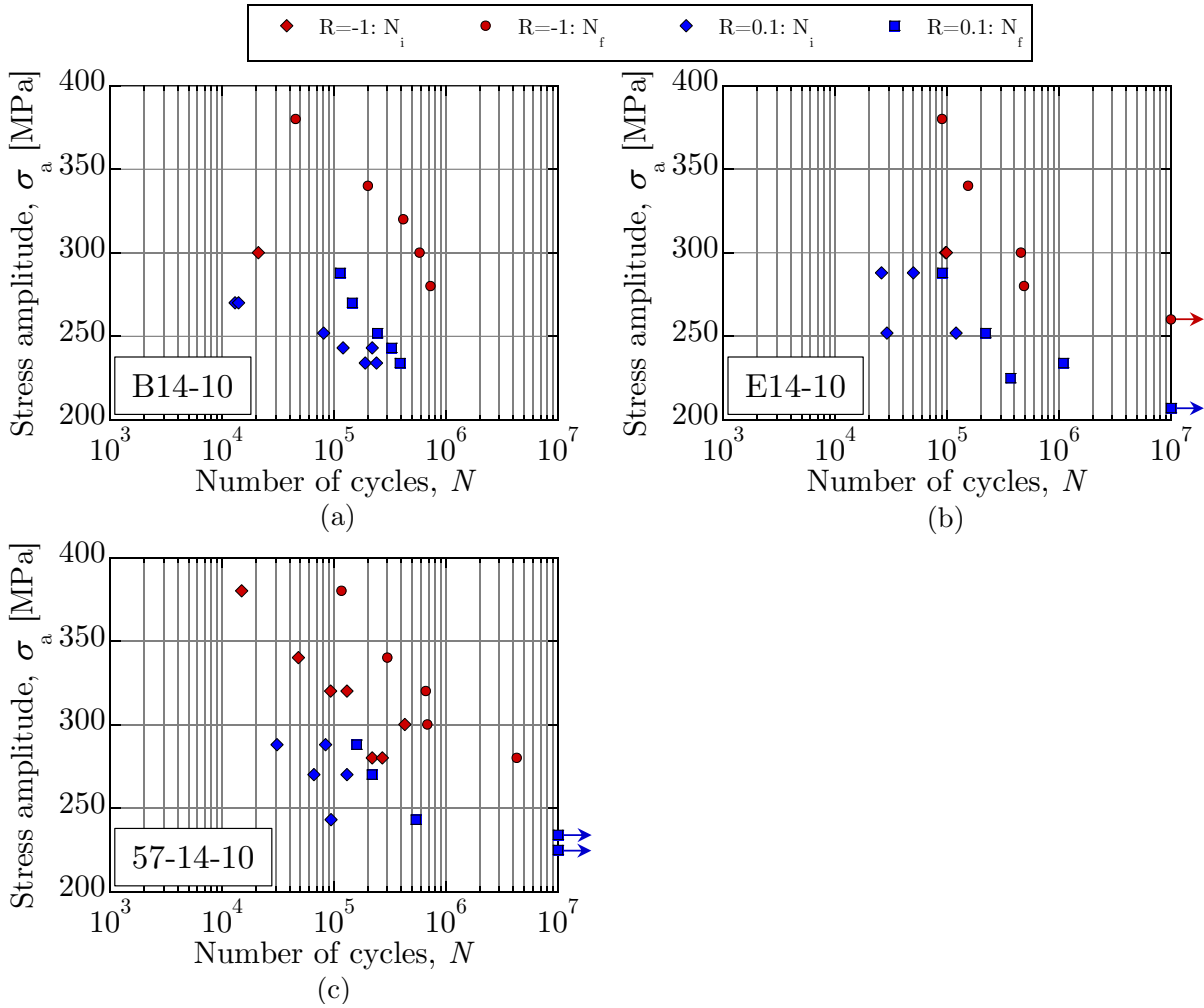


Figure III.26 – Results of the fatigue experiments for (a) B14-10, (b) E14-10, (c) 57-14-10 steels. Arrow indicates a test conducted without failure.

location when the crack did not initiate from the notch.

The initiation of the crack outside of the notch might be related to the relationship between the notch size and the grain size. Indeed, in these two materials, the average grain size (535 μm and 767 μm for the B14-10 and E14-10 steels respectively) is of the same order or even larger than the notch size. Consequently, few grains are surrounding the notch (especially in the depth as the notch depth is 100 μm in these cases). If these grains are not particularly well oriented (in term of crystal lattice) for a crack to nucleate then a crack might appear elsewhere. Although in some cases, cracks were observed in the vicinity of the notch, they were quickly stopped most likely at a grain boundary and final failure occurred due to the propagation of another crack. This observation is confirmed by the fact that the 57-14-10 steels always failed from the notch and exhibited an average grain size of 380 μm smaller than the notch size. These conclusions are consistent with a recent study of Lorenzino and Navarro [146] who studied the effects of the grain size on the notch sensitivity under fatigue conditions. They developed a method to produce "supersized" grains of pure aluminum and undertook experimentations by varying the grain and notch size. They showed that an increase in the notch size while keeping the grain size constant resulted in a decrease in the fatigue limit, as extensively reviewed by Murakami and Endo [7–9]. They enriched this conclusion by highlighting that above a certain ratio of grain size to notch size, the presence of the notch might be totally

4. RESULTS AND DISCUSSION

irrelevant as the crack might not even initiate from the notch.

Finally, when initiating on the notch, the cracks did not always appear at the position of highest stress concentration factor but were well scattered on the notch side as shown in Fig. III.27. It can be attributed to the effect of the microstructure but also to the presence of small defects generated in the depth of the notch by the laser cutting process as shown in Fig. III.7. In fact, in few cases, the analysis of the fracture surface revealed an initiation in the depth of the notch which could not be observed during the experiment due to the difficulty to light inside the notch. In several cases, the appearance of the crack was not a sudden event but rather a continuous process starting by the appearance of slip traces on the surface. When the formation of the crack was clearly observable between two successive picture sets, the number of cycles was recorded and reported in Fig. III.25 and III.26. For each experiment, crack nucleation on each side of the notch was measured. As can be seen, the initiation of the crack represents between 10 to 60% of the total life of the specimen. No clear trend is observed when decreasing the stress amplitude as the fraction of initiation to total life does not monotonically increase nor decrease. Within the same specimen, the initiation life of a crack on each side of the notch can be very scattered. It is very likely that in such case the first crack, while propagating, may reach the other side of the notch before a crack initiates independently. It is worth noting that in small notch specimens slip traces were often observed on all the surface, even in the HCF regime (Fig. III.27(a-c)). Such slip traces were almost absent for large notch specimens (Fig. III.27(d-f)). Finally, specimens that did not fail after 10^7 cycles often exhibited small cracks in the vicinity of the notch. This observation confirms that the fatigue limit is not the stress amplitude below which no crack nucleates but the stress below which no crack propagates due to impassable barriers.

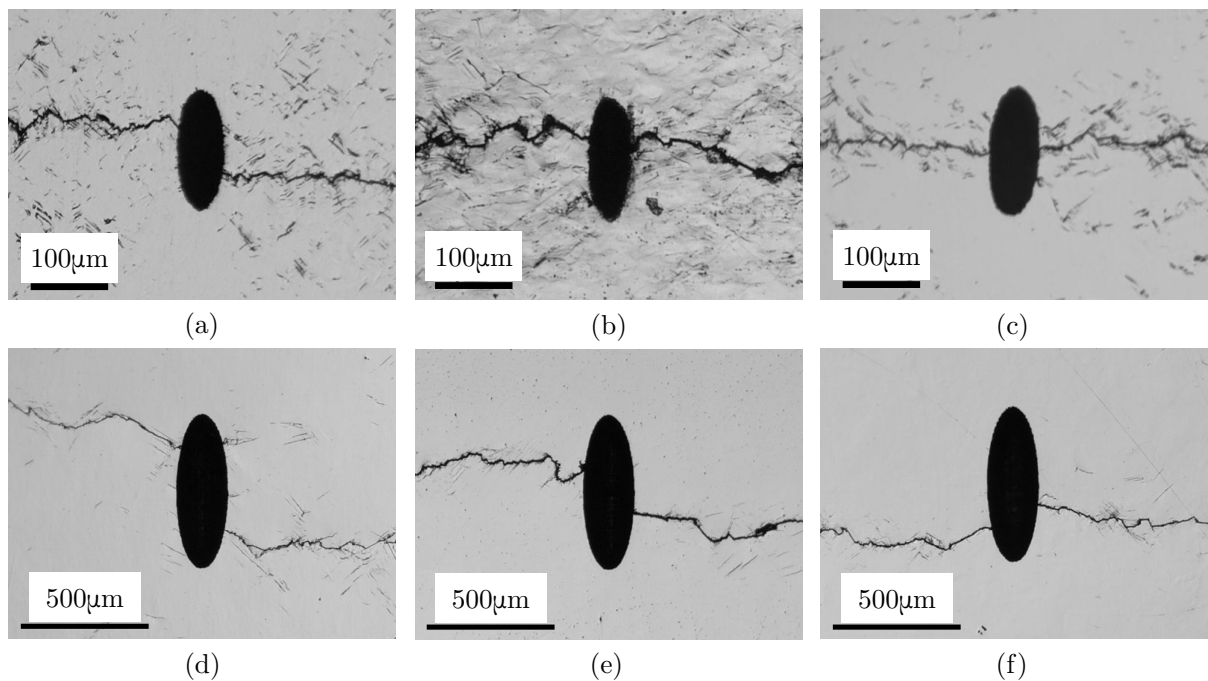


Figure III.27 – Example of crack patterns around the elliptic notch for (a) an α -iron (290 MPa), (b) FP steel (200 MPa), (c) B10-01 (260 MPa), (d) B14-10 (300 MPa), (e) E14-10 (288 MPa) and (f) 57-14-10 (300MPa).

Fracture surface

Under negative stress ratio, features on the fracture surfaces were often obliterated due to the crack closure and the constant rubbing of the two faces. Typical fracture surfaces of the materials subjected to the two thermal treatments are shown in Fig. III.28 and Fig. III.29 for stress ratio $R=-1$. Steels subjected to the second heat treatment exhibit a reduced roughness surface with a semi-circular crack front. Striations related to mode I crack propagation could be found about 100 μm from the notch as depicted in Fig. III.28(c). These striations were obviously more pronounced under $R=0.1$ stress ratio. The observation is different in the case of steels subjected to the first heat treatment. The sharp fracture surfaces mostly exhibit intergranular facets and no clear crack front is observable. A semi-circular pattern is still visible in Fig III.29 when the crack reaches the rear face and split into two cracks. Besides, striations were not found in the vicinity but a few millimeters from the notch as shown in Fig. III.29(c) which suggests that the crack propagation for most of the life of the specimen is controlled by mode II shear-mechanism and the transition to long crack growth regime occurs late or is even absent. The measurement of crack growth rate and the comparison with typical crack propagation laws for long cracks should confirm or not this observation.

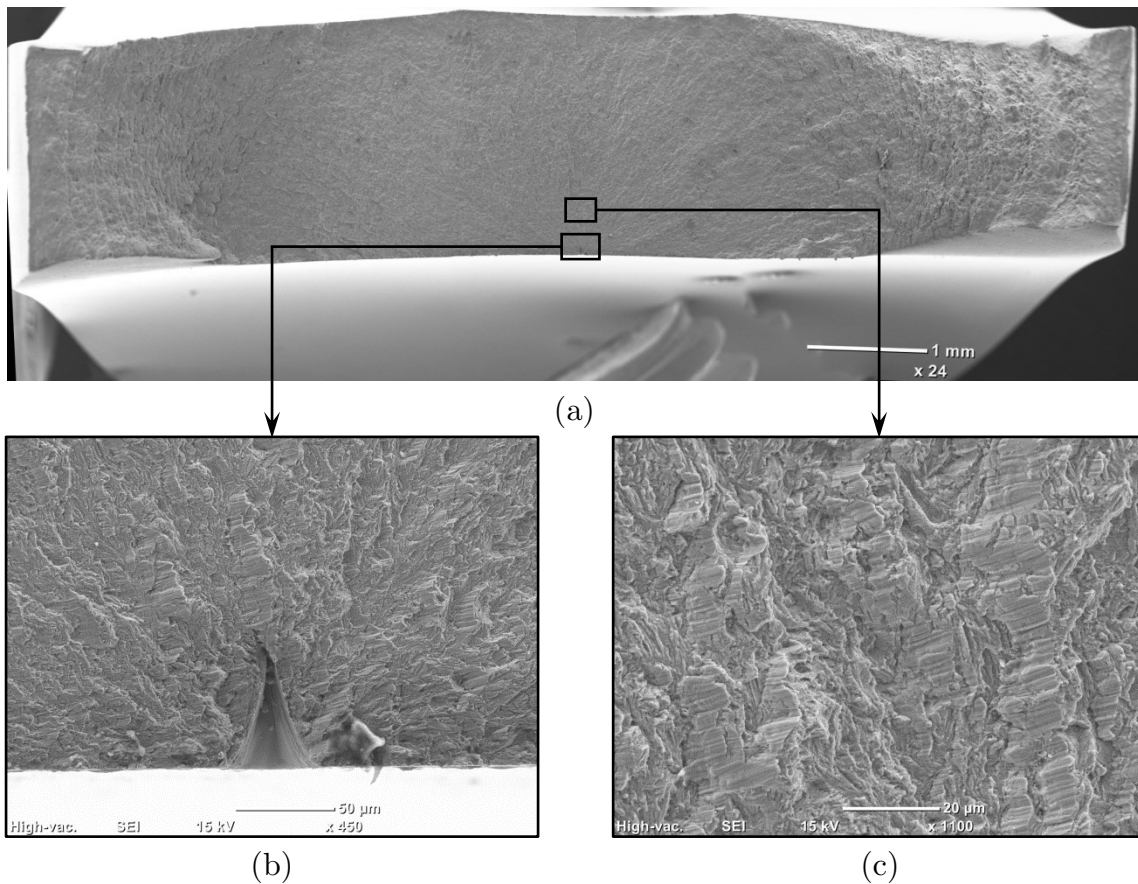


Figure III.28 – (a) Fracture surface of the 57-10-50 steels subjected to $\sigma_a=320$ MPa with $R=-1$. (b) Close-up observation near the notch. (c) Striations about 100 μm from the notch.

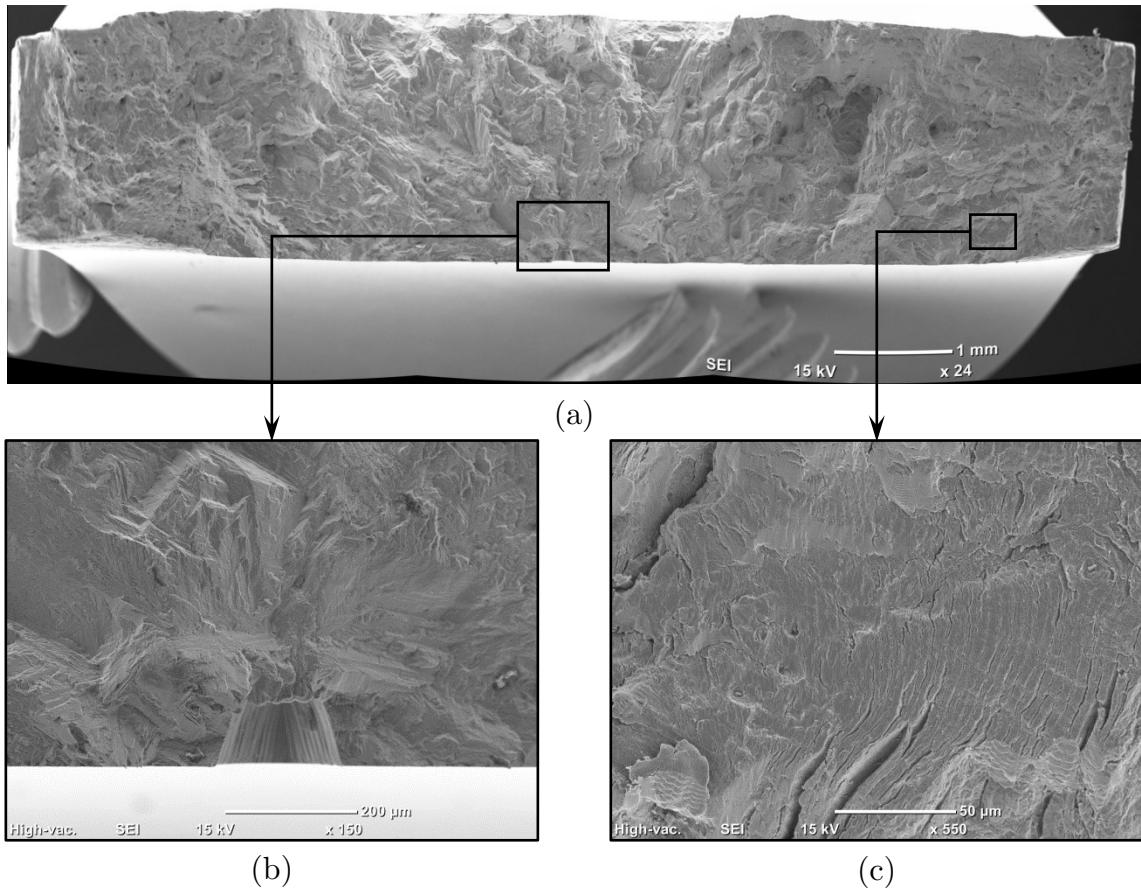


Figure III.29 – (a) Fracture surface of the E14-10 steels subjected to $\sigma_a=300$ MPa with $R=-1$. (b) Close-up observation near the notch. (c) Striations about 4 mm from the notch.

4.3.2 Study of crack growth

Stress intensity factor

In order to compare the crack growth rates with the classic growth rate behavior of long cracks, it is necessary to estimate the stress intensity factor range. From the literature review and based on the observation of the fracture surface, we can assume a semi-circular crack shape. In this case, the stress intensity factor range is expressed as:

$$\Delta K = F_C \Delta \sigma \sqrt{\pi a} \quad (\text{III.32})$$

where $a = b$ is the depth of the semi-circular crack as depicted in Fig. III.30 and F_C is a function dependent on the crack length and the geometry of the specimen. We adopt the empirical formula obtained by Isida *et al.* [147] using the body force method:

$$\begin{aligned} F_C = & 1.1362 - 0.3927\mu - 0.345\mu^2 + 0.2623\mu^3 \\ & + \lambda(-0.2179 + 0.2354\mu + 0.3773\mu^2 - 0.4189\mu^3) \\ & + \lambda^2(5.0486 - 16.7939\mu + 19.986\mu^2 - 8.0212\mu^3) \\ & + \lambda^3(-2.6383 + 8.6007\mu - 9.6007\mu^2 + 3.5118\mu^3) \end{aligned} \quad (\text{III.33})$$

with $\mu = b/a$ and $\lambda = b/t$. This relation is valid for $0.125 \leq \mu \leq 1.0$, $\lambda \leq 0.6$ and Poisson ratio $\nu = 0.3$. Given the dimension of the specimen, it means a crack length less than 1.2 μm .

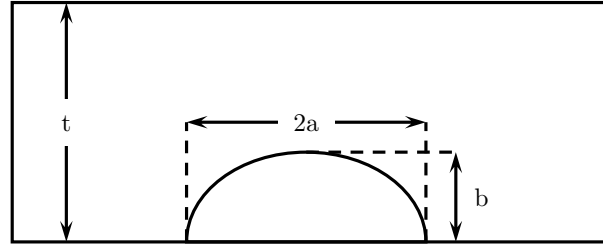


Figure III.30 – Schematic representation of a semi-elliptical surface crack in finite-thickness plate.

It is worth mentioning that the crack is considered to be horizontal, perpendicular to the loading direction, which is not always observed in the early stage of crack growth.

Crack growth rate

Crack propagation is traditionally represented as a function of the stress intensity factor range as it allows comparing different loading conditions on a single graph. However, this way of representing data is not convenient when the crack is smaller than the notch as a small crack length increase will barely affect the stress intensity factor. Besides, the purpose is not to evaluate crack growth parameters (CT specimens are more suitable in this case) but rather to study how microstructurally short crack growth deviates from long crack growth models. It was therefore decided to represent the results in term of da/dn Vs. a .

Since experiments were conducted for two different stress ratios, it is necessary to apply a model accounting for this effect. Walker proposed a modified Paris law including the stress ratio through the introduction of an effective stress intensity parameter. However, it does not consider any stress intensity factor range threshold where the crack growth rate is almost zero. Kohout [148] developed a new function to model the three stages of crack growth curves for different cycle asymmetries as described in Chapter I. Near threshold and Paris' region, the general equation is given by:

$$\frac{da}{dN} = C \left[\frac{\Delta K}{(1-R)^\gamma} \right]^p \left\{ \left[\frac{\Delta K}{(1-R)^\gamma} \right]^{m-p} \Delta K_{th}^p \right\} \quad (\text{III.34})$$

where ΔK_{th} is the stress intensity factor range threshold, m , p and $0 < \gamma < 1$ are exponents to be calibrated to experimental data. A simplification of this model consists in assuming $p = m$ as it was found that they have similar values:

$$\frac{da}{dN} = C \left\{ \left[\frac{\Delta K}{(1-R)^\gamma} \right]^m - \Delta K_{th}^m \right\} \quad (\text{III.35})$$

Due to the absence of literature data on the materials considered in this work, we use some of the regression parameters obtained by Kohout [148] on carbon steels: $m = 3.14$ and $\gamma = 0.7$, C and ΔK_{th} are adjusted to fit our experimental results. As explained earlier, the precise estimation of the parameters is not the objective of this section.

Fig. III.31 and III.32 present some of the experimentally measured crack lengths against the number of cycles and crack growth rate against the crack length for different steels under various stress conditions. These experiments are representative of the HCF behavior as the fatigue lives exceed 10^5 cycles. Besides, for higher stress amplitudes, several cracks were found and crack propagation was altered by crack coalescences. They

correspond to the 6 crack patterns shown in Fig. III.27. Fig. III.31 regroups the results for small notch specimens where the window size was about 1 mm. Therefore, crack length was often measured up to 500 μm , except in some cases where we could change the magnification before the crack reached the edge of the window (for example Fig. III.31(a)). Fig. III.32 regroups the results for the large notch specimens where the maximum measured crack length was about 1 mm on each side of the notch. In both case, the crack length was measured independently on each side of the notch, and half the notch width was added to the total length.

As a general observation, it is clear that the microstructure plays an important role in the early propagation of the cracks. Acceleration, deceleration and blocking periods are noticeable in most of these graphs. This effect diminishes and almost disappears when the crack length reaches about 100 μm for the small notch specimens. Beyond this length, left and right cracks propagate at the same rate and it is very likely that they are connected and form a single crack. The slope of the growth rate is indeed very close to the theoretical one for long crack. This is confirmed by the observation of striations on the fracture surface about 100 μm from the notch in Fig. III.28. On the opposite, no clear transition to long crack growth was found for the specimens with a large notch until several mm which is confirmed by the absence of striations on the fracture surface.

Considering the crack growth rates, several oscillations were often observed such as in Fig. III.31(b) and (d). In some cases such as in Fig. III.31(f), oscillations could not be found. In fact, these oscillations exhibit periods close to the average grain size of the materials. For instance, it was shown that the α -iron average grain diameter is about 33 μm which matches well the oscillations in Fig. III.31(b). Looking at the crack growth rate of the large notch specimen, several oscillations are also constantly found on each side of the notch. Among the three materials depicted in Fig. III.32, the 57-14-10 has the lowest average grain size of 390 μm and the transition to long crack is found after three clear periods. On the other hand the E14-10 steel has the largest average grain size of about 770 μm . It is worth reminding that the crack length corresponds to the horizontal portion of the crack. Accordingly to more precisely compare the oscillation period with the grain size, the crack length should be divided by the cosine of the crack angle with the horizontal direction. Scattering in the crack growth rate between the left and right crack is also observed. It appears that when the second crack nucleates, its growth is generally faster than the first crack as the later one might enhance its propagation. This is particularly noticeable on Fig. III.32(f).

Finally, we can estimate the proportion of the fatigue life taken by the initiation and MSC propagation stages. From the graphs in Fig. III.31, 70 to 80% of the total life is spent in the stage I. Similar conclusions should not be drawn from Fig. III.32 since the long crack growth regime was almost never reached.

As a general conclusion, microstructurally short cracks were found to propagate faster than the growth rate predicted for long cracks. Oscillations in crack growth were prominent up to a crack length close to 2-3 grain diameters. Transition from microstructure-sensitive to microstructure-insensitive was mainly observed in small notch specimen where the grain size never exceeds 100 μm . The lack of clear transition in the case of large notch specimen is related to the scale effect as the specimen is too small for the crack to reach the long crack growth regime. Most of these results are consistent with those found by other researchers [25, 39, 149].

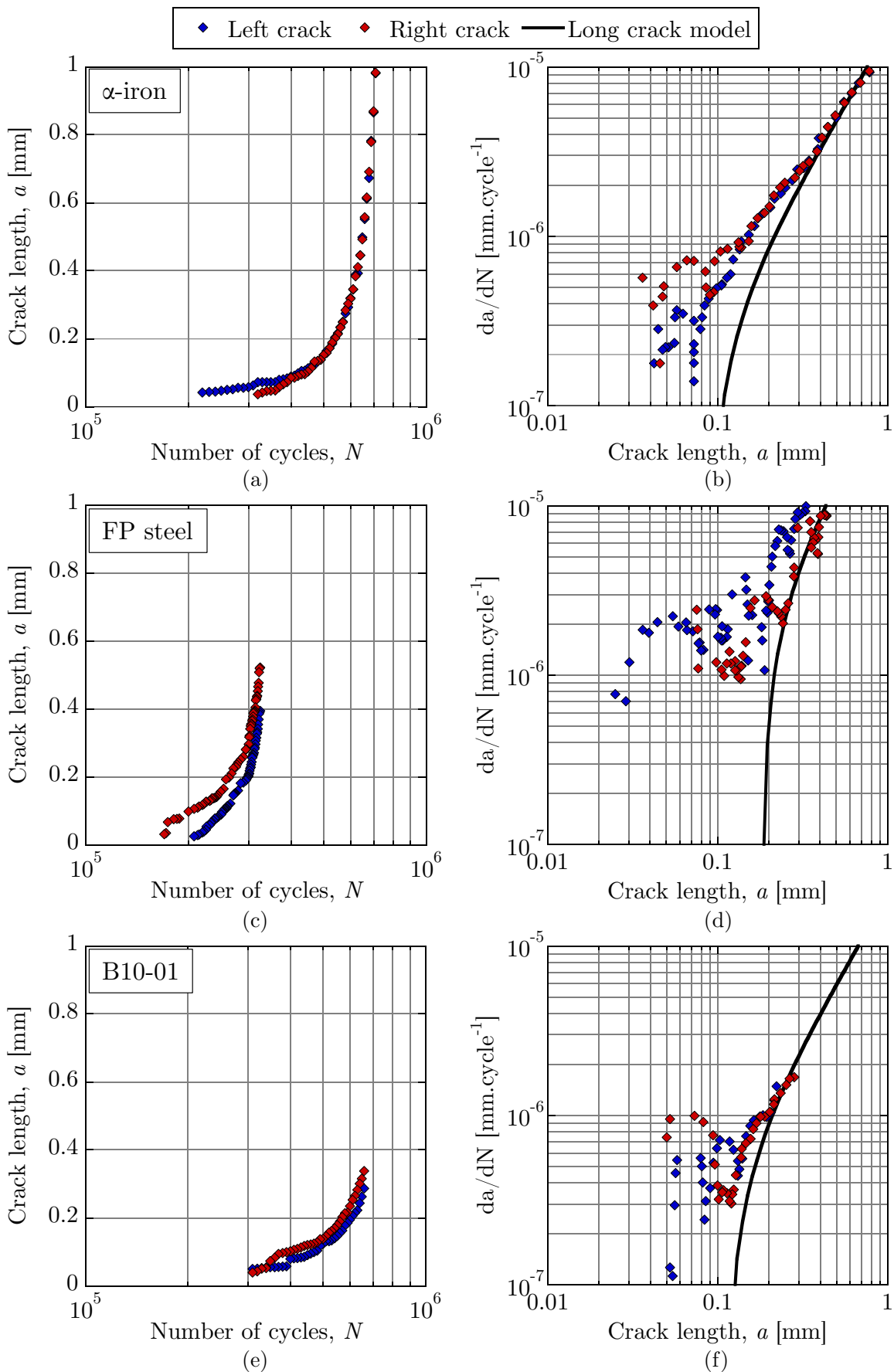


Figure III.31 – Crack length versus the number of cycles and crack growth rate versus the crack length for three different small notch specimens.

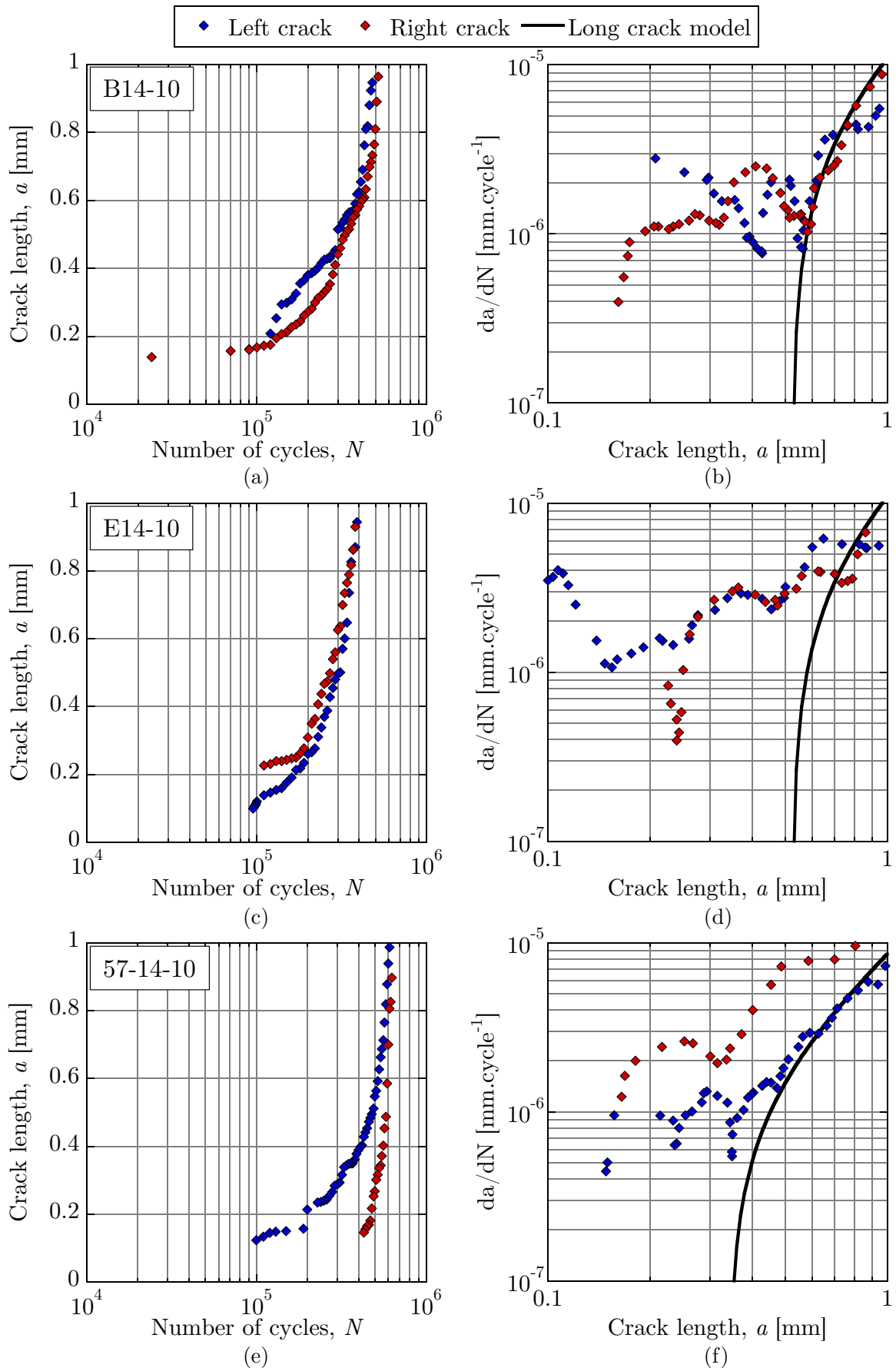


Figure III.32 – Crack length versus the number of cycles and crack growth rate versus the crack length for three different large notch specimens.

4.3.3 EBSD analysis of the crack path

In the previous section, it was showed that before reaching a sufficient length, crack often exhibits an oscillatory behavior of its growth rate and direction. In this section, we follow the work of Zhai *et al.* [47, 150–152] and Proudhon [153] who conducted EBSD analyses on cracked specimen and correlated the deflection at the grain boundary with the twist and tilt angles between the slips systems in two neighboring grains. The material studied in their work was a FCC aluminum so that only four slip planes were evaluated : $\{111\}$, $\{\bar{1}11\}$, $\{1\bar{1}1\}$, $\{11\bar{1}\}$. Due to the BCC lattice of the α -iron, more slip systems exist: $\{110\}\langle\bar{1}11\rangle$, $\{112\}\langle11\bar{1}\rangle$ and $\{123\}\langle11\bar{1}\rangle$. We limit the study by considering only the $\{110\}\langle\bar{1}11\rangle$ slip system. The specimen analyzed is the FP steel subjected to a stress amplitude of 200MPa and depicted in Fig. III.27(b). The experiment was interrupted before the complete failure of the specimen, the gauge area was cut and polished and EBSD analysis was performed for the crack on each side of the notch. The procedure for the evaluation of the different parameters is first described.

Procedure for the evaluation of the twist/tilt angles and Schmid factor

At first, the crystal orientations of two neighbor grains are extracted and used to build the rotation matrices:

$$R(\varphi_1, \phi, \varphi_2) = \begin{pmatrix} c_1c_2 - s_1cs_2 & -c_1s_2 - s_1cc_2 & s_1s \\ c_2s_1 + c_1cs_2 & c_1cc_2 - s_1s_2 & -c_1s \\ ss_2 & sc_2 & c \end{pmatrix} \quad (\text{III.36})$$

with

$$\begin{cases} c_1 = \cos\varphi_1 & s_1 = \sin\varphi_1 \\ c = \cos\phi & s = \sin\phi \\ c_2 = \cos\varphi_2 & s_2 = \sin\varphi_2 \end{cases} \quad (\text{III.37})$$

where $(\varphi_1, \phi, \varphi_2)$ are the Euler angles of the crystal in the grain. Since local fluctuations of the Euler angles exist within a grain, the average crystal orientation is considered for the evaluation of these angles. Assuming \mathbf{n} and \mathbf{m} are the vector normal to a slip plane and the vector parallel to a slip direction in the crystal reference frame, the corresponding vectors \mathbf{n}_i and \mathbf{m}_i in the specimen frame (XYZ) are given by:

$$\mathbf{n}_i = R_i \cdot \mathbf{n} \quad \text{and} \quad \mathbf{m}_i = R_i \cdot \mathbf{m} \quad (\text{III.38})$$

The Schmid factors of the different slip planes are evaluated by calculating:

$$SF_i = \max_{j=1,2} |\mathbf{n}_i \cdot \mathbf{e}_y \times \mathbf{m}_j \cdot \mathbf{e}_y| \quad (\text{III.39})$$

Finally the angle α_p of crack propagation is evaluated by calculating the trace of a given slip plane at the surface of the specimen and is compared to the measured angle α_o .

Analysis of crack paths

Fig. III.33 and III.34 show the optical microscope pictures and EBSD maps of the right and left crack, respectively. The analyzed grains are referred with an upper case letter. Several observations can be made before evaluating the crystallographic nature of

the cracks. Due to the polishing of the surfaces, the pictures correspond to subsurface crack path so that the crack path is slightly different than the one in Fig. III.27(b). The laser cutting also led to a fluctuating surface on the notch edge so that cracks appeared to initiate in valley of these oscillations where the stress concentration is the highest. The EBSD pictures revealed mainly a transgranular crack propagation. Locally cracks may become intergranular especially when getting closer to small grains as they don't manage to cross. Finally, significant lattice rotation related to the deformation of the grains can be observed in most of the grains near the crack path. These distortions introduce an uncertainty when calculating the parameters described previously so that it is not advisable to consider the average crystal orientation per grain. Accordingly, it was decided to estimate an average orientation from a region relatively homogeneous and far from the crack.

The presence of a crack naturally affects diffraction pattern of EBSD image which consequently reduces the image quality (IQ). However, with this parameter the crack pattern does not appear clearly as can be seen on the EBSD map in Fig. III.33(b) and III.34(b) as pixels near the crack also exhibit a low IQ. Therefore, crack angles were measured from optical microscope observations. Compared with the observation of Zhai *et al.* [47, 150–152] and Proudhon [153], the crack path is not clearly straight within a grain. Indeed, the material they investigated were high-strength aluminum alloys which due to their low stacking-fault energy mainly deform by planar slip so that straight cracks and slip traces may be observed. On the other hand, low-carbon steels mainly exhibit wavy slip due to the easy cross slip of screw dislocations so that the crack pattern and slip traces may not be well defined. Hence, crack path angles were mainly measured for regions where the pattern was relatively straight. They are reported in Fig. III.33(a) and III.34(a). Table III.5 and III.6 summarize the crystal orientation, Schmid factor, slip trace and crack path orientation for the crack patterns in Fig. III.33 and III.34, respectively. The Euler angles ($\varphi_1, \Phi, \varphi_2$) are reported below the grain name.

It is generally possible to find a slip system whose trace matches the crack orientation with a precision of about 10° which suggest that short crack propagation occurs according to crystallographic planes. However, in some cases, for instance in grain C in Fig. III.33, no slip system was found to match the near vertical crack. It is therefore possible that this trace correspond to another slip system or even to a cleavage plane since the crack path is extremely sharp. In the case of grains A, which are the grains where cracks initiated, it seems that the path orientation matches the slip system with the highest Schmid factor. Interestingly, the initiated grain on the right side is relatively poorly oriented as the maximum Schmid factor is about 0.35. For the left side, crack clearly appears to oscillate and these oscillations fit the two slip systems with the highest Schmid factor. For other grains, the crack path does not always match the highest slip system, suggesting that the stress redistribution due to the presence of the crack might activate secondary slip systems. Another reason could be that the grains beneath the surface have an influence on the activate slip system. Unfortunately, such hypothesis is difficult to verify without 3D observations such as by X-ray microtomography.

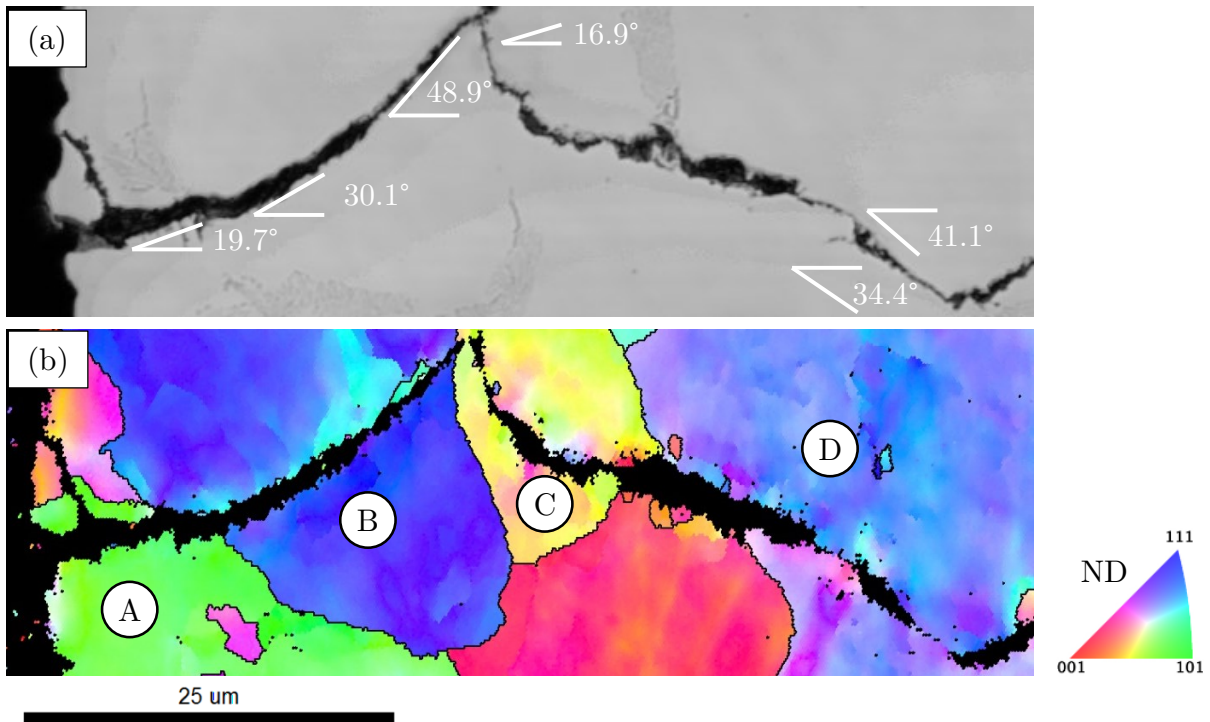


Figure III.33 – (a) Optical microscope picture and (b) EBSD map of the right crack of the FP steel subjected to a stress amplitude of 200 MPa.

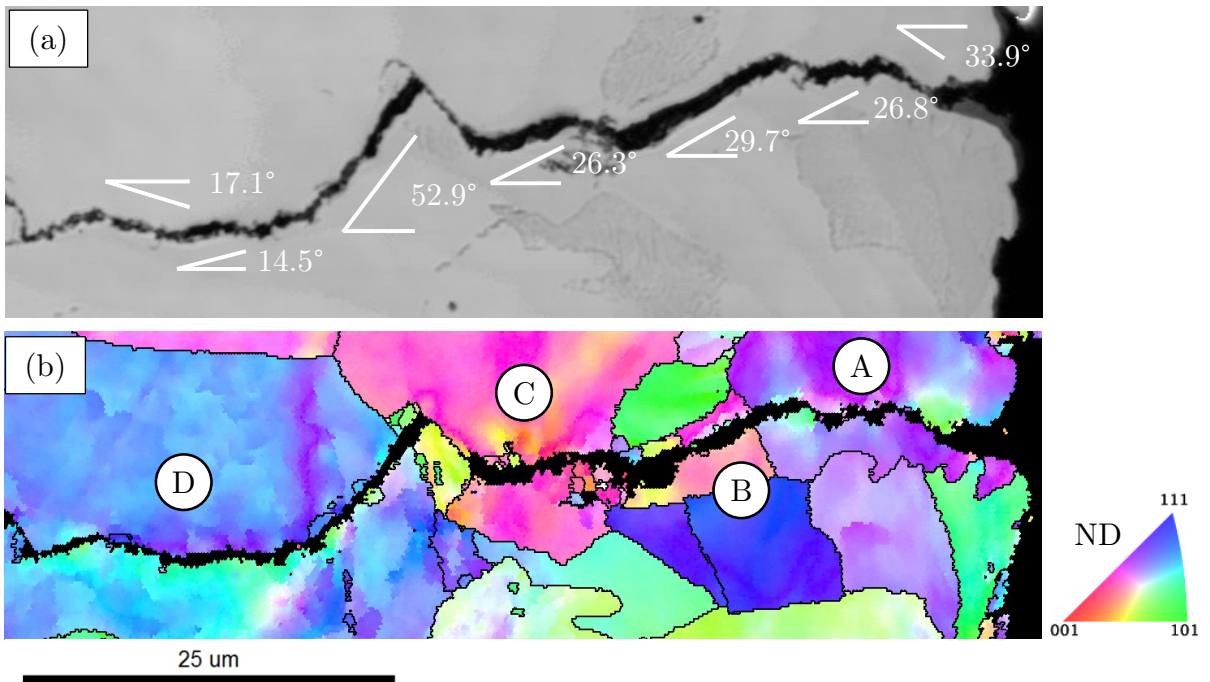


Figure III.34 – (a) Optical microscope picture and (b) EBSD map of the left crack of the FP steel subjected to a stress amplitude of 200 MPa.

4. RESULTS AND DISCUSSION

Table III.5 – Evaluation of the Schmid factor and slip trace angles of the grains in right crack from Fig. III.33

Grain	Slip plane	SF	α_p [°]	α_o [°]	Grain	Slip plane	SF	α_p [°]	α_o [°]
A 236 37.7 96.1	011	0.008	-89.4	19.7	C 39.8 26.3 358	011	0.175	-54.4	16.9
	$0\bar{1}1$	0.294	27.6			$0\bar{1}1$	0.357	-51.6	
	101	0.142	-3.16			101	0.459	14.5	
	$\bar{1}01$	0.345	-30.0			$\bar{1}01$	0.332	62.3	
	110	0.354	23.0			110	0.158	79.8	
	$\bar{1}\bar{1}0$	0.151	-79.9		$\bar{1}\bar{1}0$	0.285	-3.97		
B 124 55.7 218	011	0.404	59.6	48.9	D 129 44.9 235	011	0.222	75.4	-34.4
	$0\bar{1}1$	0.387	-24.2			$0\bar{1}1$	0.355	-30.9	
	101	0.041	-0.153			101	0.257	14.9	
	$\bar{1}01$	0.024	-87.4			$\bar{1}01$	0.168	-63.3	
	110	0.427	21.1			110	0.390	53.0	
	$\bar{1}\bar{1}0$	0.411	-60.2		$\bar{1}\bar{1}0$	0.479	-43.9	-41.1	

Table III.6 – Evaluation of the Schmid factor and slip trace angles of the grains in left crack from Fig. III.34

Grain	Slip plane	SF	α_p [°]	α_o [°]	Grain	Slip plane	SF	α_p [°]	α_o [°]
A 197 36.9 137	011	0.188	77.1	26.8	C 327 24.8 63	011	0.339	-32.9	26.3
	$0\bar{1}1$	0.311	15.8			$0\bar{1}1$	0.184	-76.4	
	101	0.423	21.4			101	0.381	7.22	
	$\bar{1}01$	0.492	-40.4			$\bar{1}01$	0.478	36.3	
	110	0.304	18.8			110	0.197	76.3	
	$\bar{1}\bar{1}0$	0.235	-70.4		$\bar{1}\bar{1}0$	0.295	-17.0		
B 208 22.5 116	011	0.261	69.9	29.7	D 48.4 53.4 334	011	0.302	17.2	14.5
	$0\bar{1}1$	0.378	30.2			$0\bar{1}1$	0.371	-59.8	
	101	0.384	-16.6			101	0.170	-1.51	
	$\bar{1}01$	0.472	-41.4			$\bar{1}01$	0.118	-79.4	
	110	0.210	11.1			110	0.420	59.9	
	$\bar{1}\bar{1}0$	0.122	-81.6		$\bar{1}\bar{1}0$	0.472	-11.9	-17.1	

5 Summary

This chapter was dedicated towards the mechanical characterization of the different steels under uniaxial cyclic conditions.

At first, series of strain-controlled low-cycle fatigue experiments under fully reversed tension-compression were conducted at four different strain amplitudes: 0.2%, 0.3%, 0.4% and 0.5%. In most of the materials, the cyclic stress response revealed three phases which durations relative to the failure life varied with the strain amplitude:

- a first hardening phase of ten to hundred cycles characterized by an increase in the stress amplitude;
- a second softening phase until nearly half-life where a decrease in the stress amplitude is observed;
- a final phase up to the failure of the specimen where the cyclic behavior of the material is relatively stable.

These trends are relatively common and were also observed in literature for various low-carbon steels [140–142]. The strain-life behavior revealed two trends depending on the prior thermal treatment applied to the materials. Overall, steels subjected to the first treatment pattern show a lower ductility.

Two constitutive models used in this work were presented: an isotropic J_2 model and a phenomenological crystal plasticity model. In both cases the materials parameters were calibrated from the stabilized stress-strain hysteresis curves assuming only an hardening phase until the saturated stage is reached. In the case of the J_2 model, the procedure available in the FE software was applied to estimate the parameters for α -iron and FP steel. Considering the CP model, the cubic elastic coefficient for the ferrite and martensite were taken from literature [143, 144]. The identification of the CP parameters was based on two simulation strategies: a fast Taylor-Lin model and an homogenization method based on a 3D RVE with PBC. The models were loaded with the same conditions as in experiments in term of strain amplitude and strain rates. The parameters were identified so as to minimize the difference between the experimental and simulated stress-strain hysteresis curves. For similar CP parameters, the hysteresis obtained with Taylor-Lin model are always over the one from the homogenization of the RVE. This was expected since the Taylor-Lin model is known to be an upper-bound of the true behavior of the material. Overall, parameters could be find that provide a good agreement with the experimental data for the three materials numerically studied in the next chapter.

Load-controlled fatigue experiments were then conducted at two R ratio (-1 and 0.1) to evaluate the high-cycle fatigue behavior of the steels. The experiments were performed on specimen including an elliptic notch of aspect ratio 1/3 in order to measure the growth of microstructurally short cracks without significantly affecting the fatigue limit and strength. In most cases, cracks were found to initiate in contact of the elliptic defect, except for the 14 – 10 materials were due to the larger grain size compared with the notch size, cracks often initiated far from it. The initiated cracks were not always found near the highest stress concentration region but were well scattered around the notch. Also, no trend was found between the initiation lives and the stress amplitude. Measurement of the crack length revealed an oscillatory behavior of the crack growth rate, especially in large notch specimen where cracks were found to accelerate, decelerate or even stop. The observation of the fracture surface revealed that cracks in large notch specimen mainly propagate under mode II shear mechanism suggesting that the stage II crack propagation

was not yet reached when the final failure occurred. Overall, about 2-3 grain sizes were necessary for the crack to transition from stage I to stage II.

The quantitative study of crack path with EBSD analysis revealed that cracks mainly propagated transgranularly with few intergranular propagation due to the presence of small grains. Comparisons of slip traces with crack orientation suggested that short crack propagation is mainly crystallographic. However, the propagation was not always found to be on the slip system with the highest Schmid factor, suggesting that the local stress near the crack tip may play a significant role in the activated slip system. Also estimations of the twist and tilt angles at the grain boundaries were not attempted due to the lack of information on the 3D nature of the grain boundaries.

Chapter IV

Numerical simulations of polycrystalline aggregates under cyclic conditions

Contents

1	Introduction	122
2	Description of the models for the evaluation of initiation and early growth of fatigue cracks	122
2.1	Fatigue crack initiation	122
2.2	Microstructurally short crack (MSC) growth	125
2.3	Grain boundary retardation	126
3	Investigation of the influence of grain morphology and texture on fatigue crack initiation	129
3.1	Introduction	129
3.2	Description of the numerical models	129
3.3	Results and discussion	133
3.4	Conclusions	140
4	Simulations of stage I fatigue cracks in notched polycrystalline aggregates	141
4.1	Introduction	141
4.2	Description of the numerical models	141
4.3	Results and discussion	145
4.4	Conclusions	167
5	Investigation of the strain localization in martensitic microstructure under fatigue conditions	168
5.1	Introduction	168
5.2	Description of the numerical models	168
5.3	Results and discussion	170
5.4	Conclusions	173

1 Introduction

This final chapter focuses on the numerical simulations of polycrystalline aggregates under fatigue conditions. Since in the absence of internal defect, fatigue failure mainly initiates from the surface of the material, the simulations conducted in this part are two-dimensional. The main objective of this chapter is to propose models and methods suitable for the study of fatigue crack initiation and MSC growth from a mesoscopic point of view. A particular emphasis is made on the capabilities and limitations of the proposed approaches to catch and reproduce phenomena experimentally observed in the previous chapter or from literature.

The chapter is decomposed in several sections. At first, the models considered for the different fatigue mechanisms are presented and the methods for their evaluations are described. Some comparisons are made with existing methods. The predictive capabilities of the model are assessed through three relatively independent numerical studies. The first one is a parametric study to evaluate the sensitivity of the models and methods to morphological and crystallographic variations. Thereafter, simulations are conducted on α -iron and FP steel notched microstructures generated by the methods presented in Chapter II. Finally, a set of simulations are conducted on martensitic microstructures in order to evaluate the influence of the different scales of heterogeneity on the strain localization and therefore on the prediction of crack initiation.

2 Description of the models for the evaluation of initiation and early growth of fatigue cracks

2.1 Fatigue crack initiation

2.1.1 Definition of the FIP

The choice of a FIP to evaluate a driving force promoting the formation and growth of a crack is not unique but depends on the type of mechanism leading to the appearance of a crack. In this work, crack nucleation is assumed to be crystallographic and transgranular. The evaluation of fatigue crack formation is based on a critical plane formulation of the Tanaka-Mura model described in Chapter I [33]. In the model, the number of cycles for crack initiation is given by:

$$N_i = \frac{A}{d} \left(\frac{\Delta\gamma_{pl}}{2} \right)^{-2} \quad (\text{IV.1})$$

where A is a constant of the material, $\Delta\gamma_{pl}$ the plastic shear strain range and d the slip band size. Due to strong assumptions in the model (irreversibility of the dislocation motion, uniform stress, absence of hardening), the determination of the constant A is not straightforward and often requires a fitting from experiment results. Accordingly the following critical plane FIP^α based on the Tanaka-Mura model formulated in Eq. IV.1 is used:

$$FIP^\alpha = d \left(\frac{\Delta\gamma^\alpha}{2} \right)^2 \quad (\text{IV.2})$$

where $\Delta\gamma^\alpha$ is the plastic shear strain range on the slip system α .

2.1.2 Evaluation of the FIP

In the literature, the most common method to evaluate a FIP is based on the averaging of the FIP on the surface/volume of the grain. Considering Eq. IV.2, the average shear strain range can be evaluated as:

$$\Delta\gamma_{avg}^{\alpha} = \langle \Delta\gamma^{\alpha} \rangle_{gr} = \frac{1}{V_{gr}} \int_{V_{gr}} \Delta\gamma^{\alpha}(e) dV = \frac{1}{V_{gr}} \sum_{e=1}^{N_{elem}} \Delta\gamma^{\alpha}(e) V(e) \quad (IV.3)$$

where e would stand for the integration point or the centroid of a given element. This method is convenient as it significantly reduces the sensitivity of the mesh and because its implementation is relatively simple. However, the averaging removes the sensitivity to intragranular heterogeneity which might arise especially in large grains. Also, when evaluating the FIP in Eq. IV.2, one should inform the size of the slip band d . It is often chosen as the average grain size. Accordingly, there is no sensitivity to grain morphology as elongated or equiaxed grains of same area will have same average grain size.

Considering the three-dimensional nature of the crystal orientation, a slip system is unlikely to have its normal belonging to the plane of the 2D model (i.e. the slip plane being perpendicular to the plane of the model). Therefore, the FIP defined in Eq. IV.2 is evaluated on potential crack paths (PCP) defined by the intersection of a given slip plane with the plane of the model as depicted in Fig. IV.1.

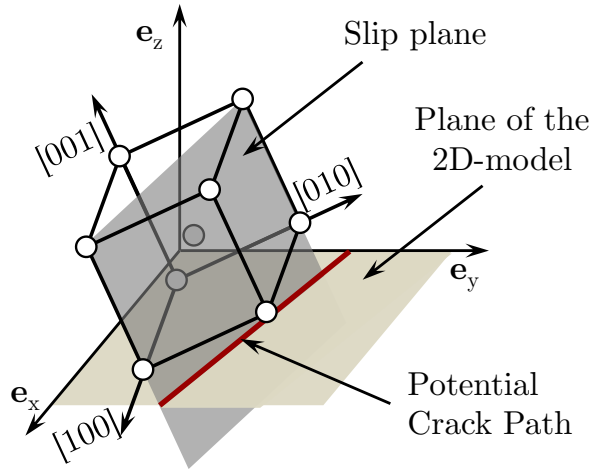


Figure IV.1 – Scheme of the definition of a potential crack path.

At first the rotation matrix based on the Euler angles $(\varphi_1, \phi, \varphi_2)$ is constructed for each grain:

$$R(\varphi_1, \phi, \varphi_2) = \begin{pmatrix} c_1c_2 - s_1cs_2 & -c_1s_2 - s_1cc_2 & s_1s \\ c_2s_1 + c_1cs_2 & c_1cc_2 - s_1s_2 & -c_1s \\ ss_2 & sc_2 & c \end{pmatrix} \quad (IV.4)$$

with

$$\begin{cases} c_1 = \cos\varphi_1 & s_1 = \sin\varphi_1 \\ c = \cos\phi & s = \sin\phi \\ c_2 = \cos\varphi_2 & s_2 = \sin\varphi_2 \end{cases} \quad (IV.5)$$

In this matrix, the Euler angles correspond to the initial Euler angles such that local rotations of the crystal inside each grain are not considered. Let's consider the (110) slip

plane, its normal vector \mathbf{n} is given by:

$$\mathbf{n} = R. \begin{pmatrix} 1 \\ 1 \\ 0 \end{pmatrix} \quad (\text{IV.6})$$

The direction of the PCP defined by the intersection of the (110) plane with the $(x - y)$ plane is given by:

$$\mathbf{u} = \mathbf{n} \times \begin{pmatrix} 0 \\ 0 \\ 1 \end{pmatrix} \quad (\text{IV.7})$$

The indexes of the slip systems in the DAMASK library are summarized in Table IV.1.

Table IV.1 – Index of the slip systems in the DAMASK library.

Slip normal	Slip direction	DAMASK index
(011)	$[\bar{1}\bar{1}1]$	1
	$[\bar{1}\bar{1}\bar{1}]$	2
$(0\bar{1}1)$	$[111]$	3
	$[\bar{1}11]$	4
(101)	$[\bar{1}11]$	5
	$[\bar{1}\bar{1}\bar{1}]$	6
$(\bar{1}01)$	$[111]$	7
	$[1\bar{1}\bar{1}]$	8
(110)	$[\bar{1}11]$	9
	$[\bar{1}1\bar{1}]$	10
$(\bar{1}10)$	$[111]$	11
	$[11\bar{1}]$	12

For each slip system of each grain, multiple spaced PCPs are drawn to evaluate the FIP. The PCP having the highest FIP is considered as the most likely location for a crack to nucleate. It is worth mentioning that slip systems having the same slip plane share the same PCPs. The complete procedure is written with python scripts. Due to the non convex shape of the grains, a particular care has been taken to prevent a path to cross another grain. Fig. IV.2 shows an example of the PCPs evaluated in a grain. The spacing between two PCPs is set according to the average mesh size as it bounds the precision of the analysis. The path highlighted in red corresponds to the one having the highest FIP. It can be noticed that a surface average would have predicted the same slip system.

From a practical point of view, paths are defined between two nodes of the hull for a given grain. Therefore, they are not exactly parallel to the slip direction, nor exactly equidistant. The plastic shear strain amplitude $\Delta\gamma^\alpha/2$ is finally averaged over the length of the PCP d :

$$\frac{\Delta\gamma^\alpha}{2} = \frac{1}{d} \sum_{i=1}^n \left(\frac{\Delta\gamma_i^\alpha}{2} \right) d_i \quad (\text{IV.8})$$

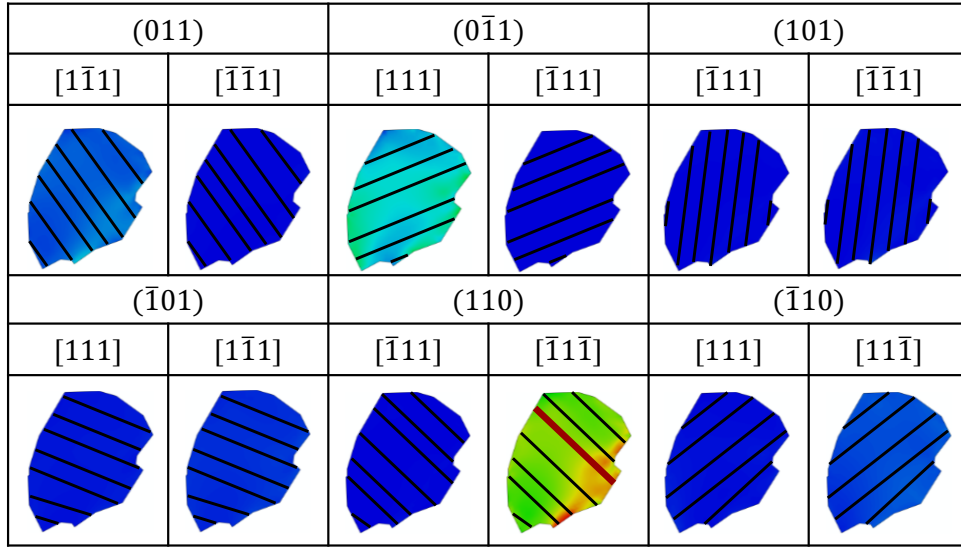


Figure IV.2 – Example of the PCPs evaluated in a grain.

where $\Delta\gamma_i^\alpha$ is the average plastic shear strain range on the segment i of length d_i .

As opposed to the surface/volume average, the proposed approach is sensitive to local strain heterogeneity and to the morphology of the grain. In addition to this regularization, such method brings information about the direction of the crack and allows defining an explicit crack as will be explained in the next section.

2.2 Microstructurally short crack (MSC) growth

As described in Chapter I, different kind of models exist to translate the propagation of a microstructurally short crack. It is generally assumed that a crack will propagate by the irreversible accumulation of dislocations at the crack tip through a shear mechanism similar to that of crack initiation. Also, MSCs often exhibit an oscillatory growth behavior when representing da/dN against a or ΔK . Indeed, the crack tends to accelerate after having crossed a grain boundary and inversely tends to slow down when it approaches a grain boundary. This observation is generally explained by the fact that the slip band ahead of the crack tip changes in size during the propagation such that less and less dislocations are emitted during a cycle. Ideally, it would be necessary to explicitly measure the evolution of the shear strain range with the crack length by introducing a crack of different lengths inside the grain. However, such method is time consuming and is inconvenient as the introduction and modification of a crack would require a remeshing procedure and iterative simulations. Accordingly, it was decided to evaluate MSC growth rate using a phenomenological model based on the Hobson model [42]:

$$\frac{da}{dN} = C(d - a)^{1-\beta} a^\beta \quad (\text{IV.9})$$

where a is the length of the crack inside the grain and $d - a$ is the length of the remaining slip band where dislocations are produced. The parameter β directly controls the shape and the transition of the growth rate as shown in Fig. IV.3.

However, a limitation of this model is that it is purely geometric and does not account for the actual plastic deformation in the slip band. Miller proposed to consider the plastic

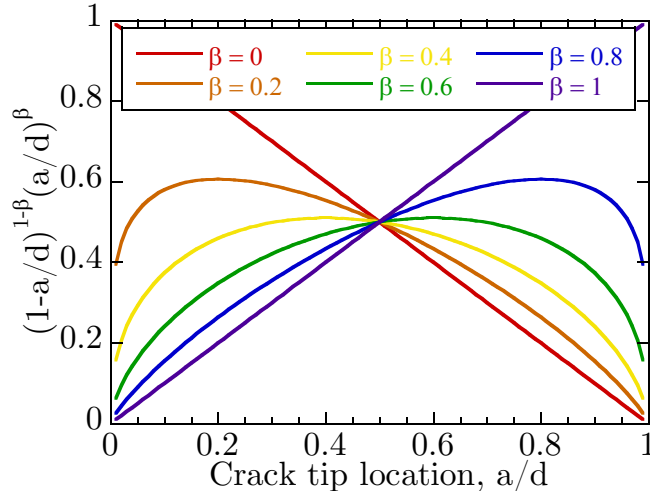


Figure IV.3 – Representation of the Hobson model of MSC growth for different values of the parameter β .

shear strain range $\Delta\gamma$ acting on the slip band [25]:

$$\frac{da}{dN} = A(\Delta\gamma)^n(d-a) \quad (\text{IV.10})$$

This model only assumed a decrease in the growth rate. Hence, a general model is proposed based on a combination of the two previous models:

$$\frac{da}{dN} = B(\Delta\gamma^\alpha)^n(d-a)^{1-\beta}a^\beta \quad (\text{IV.11})$$

In this model, the plastic strain range on the slip system α is averaged over the slip band in the same way as described in the previous section.

2.3 Grain boundary retardation

Two correlated phenomena may be observed when a crack reaches a grain boundary: a deflection from its original direction and a retardation at the grain boundary for a certain amount of time. An extensive work has been performed by Wen and coworkers on the influence of the twist angle on the crack growth rate [150–152]. They proposed a modified Paris' law to account for the effect of the grain boundary on the growth rate in rolled aluminum alloy:

$$\frac{da}{dN} = C(\Delta K_{eff} - R(\Psi))^m \quad (\text{IV.12})$$

where ΔK_{eff} is the effective stress intensity factor range assuming a semi-circular crack and R is a resistance based on the twist angle Ψ and defined by a Weibull distribution:

$$R(\Psi) = R_f[1 - \exp\{-(\Psi/\Psi_0)^n\}] \quad (\text{IV.13})$$

where R_f , Ψ_0 and n are parameters fitted to experimental crack growth.

In his thesis, Musinski [116] emphasized the lack of applicability of the concept of similitude for short cracks and therefore proposed to consider a crack growth model with a similar form than described previously:

$$\frac{da}{dN} = A.FIP^\alpha[1 - R(\Psi, \theta).(a/d)^2] - \Delta CTD_{th} \quad (\text{IV.14})$$

2. DESCRIPTION OF THE MODELS FOR THE EVALUATION OF INITIATION AND EARLY GROWTH OF FATIGUE CRACKS

where the resistance $R(\Psi, \theta)$ is a modification of Eq. IV.13 to account for the twist angle θ .

$$R(\Psi, \theta) = R_f[1 - \exp(-(\Psi/\Psi_0)^n)] + (C_1 + C_2\Psi)[1 - \exp(-(\theta/\theta_0)^m)] \quad (\text{IV.15})$$

where $R_f = 0.65$, $\Psi_0 = 20^\circ$, $n = 8$, $C_1 = 0.25$, $C_2 = 0.0075$, $m = 2$, and $\beta_0 = 15^\circ$. A representation of this relation is given in Fig. IV.4.

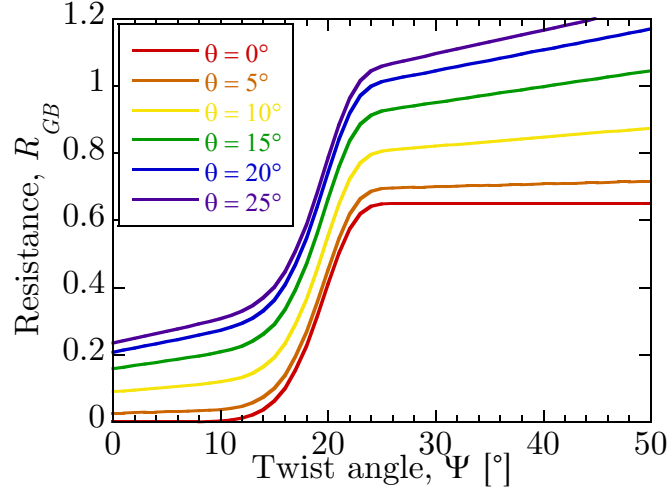


Figure IV.4 – Representation of the grain boundary resistance against the twist angle Ψ for 6 different values of tilt angle θ , based on [116].

It was assumed that a crack would propagate transgranularly on a slip system having the lowest resistance. While the growth rate model effectively reproduces an oscillatory behavior, it is quite unclear how the resistance which is calculated between two grains could affect the growth rate in the first grain. Also, the model does not consider the probable stress redistribution in the neighbor grain when the crack propagates and reaches the grain boundary. Indeed, it is extremely possible that the slip system showing the lowest grain boundary resistance also exhibits a very low plastic activity such that the crack would propagate easier on a slip system where the plastic strain is higher. Finally, the model does not account for the retardation at the grain boundary until a sufficient plastic zone ahead of the crack tip has matured enough.

Accordingly, a different approach is proposed in this work. The crack growth rate is assumed to follow the Eq. IV.11 independently of the next grain. Following the work of Morris *et al.* [48], a number of cycle for the incubation and coalescence of a new crack can be written in the same form as the Tanaka-Mura model:

$$N_{block} = \frac{C}{d} \left(\frac{\Delta\gamma_{pl}}{2} \right)^{-2} \quad (\text{IV.16})$$

The model is modified to account for the geometrical discontinuity that needs to be overcome at the grain boundary by combining Eq. IV.16 with the resistance defined in Eq. IV.15:

$$N_{block} = \frac{C}{d} \left(\frac{\Delta\gamma_{pl}}{2} \right)^{-2} R(\Psi, \theta) \quad (\text{IV.17})$$

It is worth pointing out that when the resistance is zero, meaning that the twist and tilt angle are zero, the crack is not blocked at the grain boundary. This is consistent with the fact that a zero resistance implies that the two grains share the same crystal orientation and can therefore be considered as a single one.

A critical plane FIP is here again proposed to quantify the retardation time on each slip system:

$$FIP^\alpha = d \left(\frac{\Delta\gamma^\alpha}{2} \right)^2 R(\Psi, \theta)^{-1} \quad (\text{IV.18})$$

Once a crack is introduced in a microstructure, 12 possible PCPs connected with the crack tip and whose direction are also calculated based on the projection method described in the crack initiation section. Fig. IV.5 shows an example of the PCPs evaluated in a grain in contact with a crack tip. The resistances are also reported. Since the resistance is based on the slip normal, coplanar slip systems have the same resistance. As can be seen in this example, the lowest resistance is found for the $(0\bar{1}1)$ slip plane, but the slip line do not coincide with the shear strain distribution. On the contrary, the $(\bar{1}10)[11\bar{1}]$ slip system has a higher grain boundary resistance but the shear strain is much higher and in the same direction as the slip line. A crack will therefore propagate easier on this slip system.



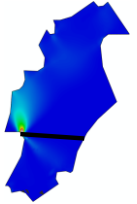
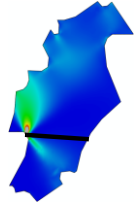

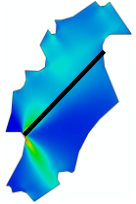

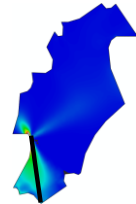

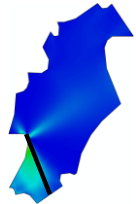

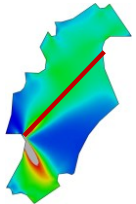
(011)		$(0\bar{1}1)$		(101)	
$[1\bar{1}1]$	$[\bar{1}\bar{1}1]$	$[111]$	$[\bar{1}11]$	$[\bar{1}11]$	$[\bar{1}\bar{1}1]$
1.47	1.47	0.23	0.23	1.23	1.23
					
$(\bar{1}01)$		(110)		$(\bar{1}10)$	
$[111]$	$[1\bar{1}1]$	$[\bar{1}11]$	$[\bar{1}\bar{1}\bar{1}]$	$[111]$	$[11\bar{1}]$
1.28	1.28	1.51	1.51	0.47	0.47
					

Figure IV.5 – Example of the PCPs evaluated in a grain adjacent to an existing crack. The grain boundary resistances are also reported.

3 Investigation of the influence of grain morphology and texture on fatigue crack initiation

3.1 Introduction

In most of microstructure-sensitive studies, the main source of variability is introduced by varying the crystal orientation within an aggregate keeping other microstructural attributes unchanged. Only recently, Castelluccio and McDowell [154] studied the effect of the presence of "as-large-as" (ALA) grains which size is much larger than the average grain size in Ni-base superalloy. They showed that the existence of such grain strongly affects the lower tails of fatigue lives. This case study revealed the importance of considering the extreme occurrences not only of mechanical fields but also of microstructural attributes to not underestimate the scattering related to the formation of fatigue cracks. Indeed, materials are often subjected to thermomechanical process for their application that can significantly affect the initial microstructure and texture. In steel industry, cold rolling technique is often applied to improve the properties and formability of steel sheets. Such process often involves a certain grain refinement and elongation as well as specific crystallographic textures characterized in term of fibers.

The objective of the present section is therefore to numerically evaluate the influence of various sources of anisotropy arising from a rolling process on fatigue crack initiation. More specifically, focus is aimed towards the role of the grain size distribution, grain morphology and rolling texture.

3.2 Description of the numerical models

3.2.1 Modeling of the polycrystalline aggregates

The modeling of the polycrystals is based on the two-dimensional anisotropic tessellation method presented in Chapter II.

Three different types of microstructures are considered in this study. They are denoted M_1 , M_2 and M_3 and are defined based on the statistical distributions used to sample the ellipses. In all cases, the probability distribution function (PDF) of the major axis follows a log-normal distribution:

$$f(x|\mu, \sigma) = \frac{1}{x\sigma\sqrt{2\pi}} \exp\left(-\frac{(\ln x - \mu)^2}{2\sigma^2}\right); \quad x > 0 \quad (\text{IV.19})$$

where μ and σ are the location and scale parameters respectively. The aspect ratios of the ellipses are defined using the normal PDF:

$$g(x|\mu, \sigma) = \frac{1}{x\sigma\sqrt{2\pi}} \exp\left(-\frac{(x-\mu)^2}{2\sigma^2}\right) \quad (\text{IV.20})$$

where μ and σ are the mean and standard deviation respectively. The PDF parameters of the microstructure M_1 are based on the ellipse fitting of the pure α -iron specimen. For the microstructure M_2 the PDF parameters of the major axis are adjusted so that the mean grain size is the same as in microstructure M_1 but the standard deviation is one third of the one of M_1 . The grain size is calculated based on the area of each grain:

$$d_{gr} = 2\sqrt{\frac{A_{gr}}{\pi}} \quad (\text{IV.21})$$

The parameters for the microstructure M_3 are adjusted so that the standard deviation and mean grain size are similar to M_2 but the grains are elongated in the y -direction. In the microstructures M_1 and M_2 , the orientation of the ellipse is random while to model a rolled microstructure it follows a normal distribution centered around 90° with a standard deviation of 5° in the microstructures M_3 . The different parameters of the PDF for the three types of microstructure are summarized in Table IV.2. The square domain has a size of 0.4 mm. In average, the microstructure M_1 is composed of 130 grains while it is about 180 for the microstructures M_2 and M_3 . The log-normal distribution of the grain size for each microstructure case is displayed in Fig. IV.6.

Table IV.2 – Parameters of the PDF for the three microstructures.

Microstructure		M_1	M_2	M_3
Major axis a [μm]	μ	3.05	3.20	3.6
	σ	0.57	0.16	0.16
Aspect ratio b/a	μ	0.51	0.51	0.25
	σ	0.12	0.12	0.05
Orientation θ [$^\circ$]	μ	Random	Random	90
	σ			5
Grain size d_{gr} [μm]	Mean	33.7	32.1	33.6
	STD	21.2	7.9	7.8

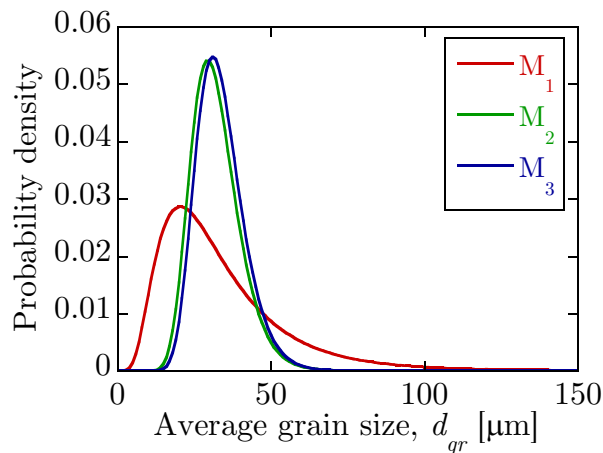


Figure IV.6 – Log-normal distribution functions of the grain size for the three microstructure cases.

3.2.2 Modeling of the cold rolling texture

In order to evaluate the effect of the cold rolling, two types of crystallographic textures are considered: a uniform texture and a rolled texture in the y -direction. When cold rolled, a BCC material generally exhibits a combination of two fiber textures: the α fiber characterized by the $\langle 110 \rangle$ direction parallel to the rolling direction (RD) and the γ fiber

characterized by the $\langle 111 \rangle$ direction parallel to the normal direction (ND) [155]:

$$\alpha\text{-fiber: } \langle 110 \rangle \parallel \text{RD} \quad \{001\}\langle 110 \rangle \text{ to } \{111\}\langle 110 \rangle \quad (\text{IV.22})$$

$$\gamma\text{-fiber: } \langle 111 \rangle \parallel \text{ND} \quad \{111\}\langle 110 \rangle \text{ to } \{111\}\langle 112 \rangle \quad (\text{IV.23})$$

At first, the orientation distribution function (ODF) of the uniform or rolled texture is generated using the toolbox MTEX [118] for Matlab. In the case of the rolled texture, the ODF is defined as the sum of two fiber ODFs using the von Mises-Fisher distribution with a half-width of 10° . Fig. IV.7 depicts the $\varphi_2 = 45^\circ$ section of the ODF representing the cold rolling texture. It is worth saying that this ODF represents an ideal case and experimental observations often show deviations from the two fibers.

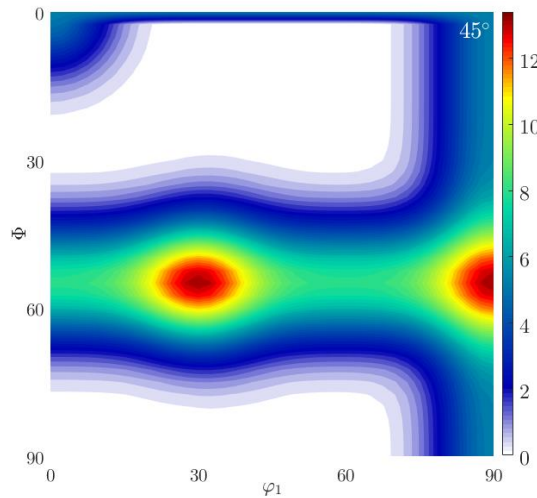


Figure IV.7 – $\varphi_2 = 45^\circ$ section of the ODF of a cold rolling texture in the Euler space.

Since the grain size is not uniform, the algorithm developed by Melchior and Delannay [134] is used to attribute a single orientation to each grain based on their size which ensures an accurate reproduction of the initial ODF. Fig. IV.8 shows an example of the $\{100\}$, $\{110\}$ and $\{111\}$ pole figures of a uniform and rolled texture. The α and γ fibers are clearly visible on the $\{110\}$ and $\{111\}$ pole figures. It can be noted that the cold rolled texture only generates an axial symmetry around the $(x - z)$ plane so that a slight difference between the textures in the rolling and transverse direction may be observed due to a less pronounced α -fiber in the transverse direction.

3.2.3 Cases studied

In order to evaluate the effect of each source of variability separately, different cases are considered by combining the type of microstructure and texture. They are depicted in Fig. IV.9. Since the microstructure M_3 and the rolled texture introduce a macroscopic anisotropy, whether geometric or crystallographic, cases considering either of these situations (*Cases 3, 4* and *5*) are loaded in the x and y -direction. For each case, 20 unique microstructures are generated in order to obtain sufficient statistical data. A total of 160 simulations are therefore conducted in this study.

The microstructures are exported into the FE software and discretized with four-node plane strain elements (CPE4) with an average size of $4 \mu\text{m}$. This leads to an average of 280 integration points per grain for the microstructures M_2 and M_3 . In the microstructures

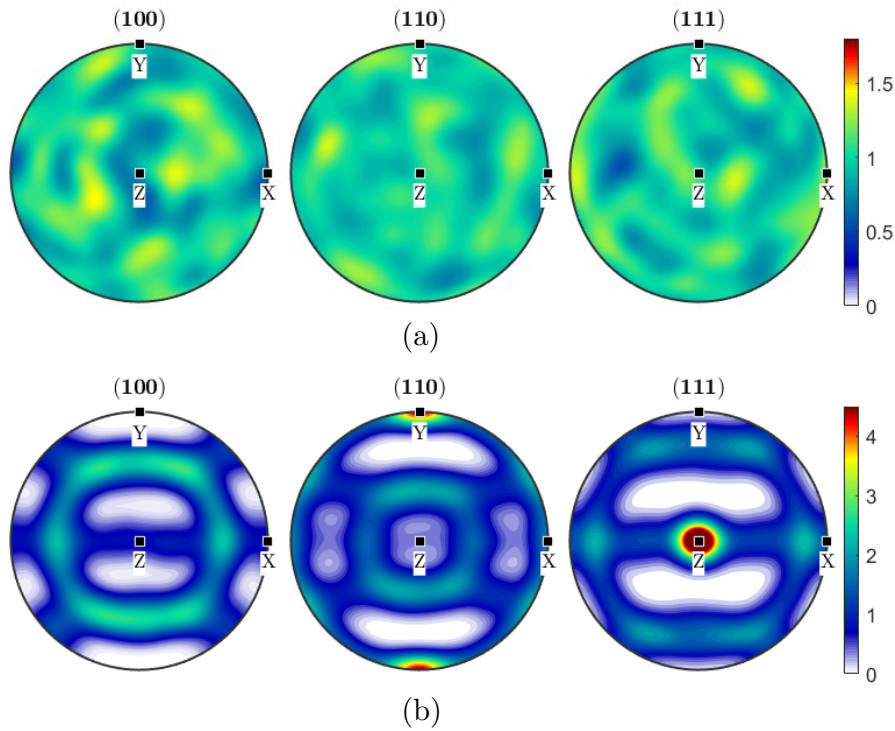


Figure IV.8 – Pole figures of (a) a uniform texture and (b) a rolled BCC texture in the y -direction.

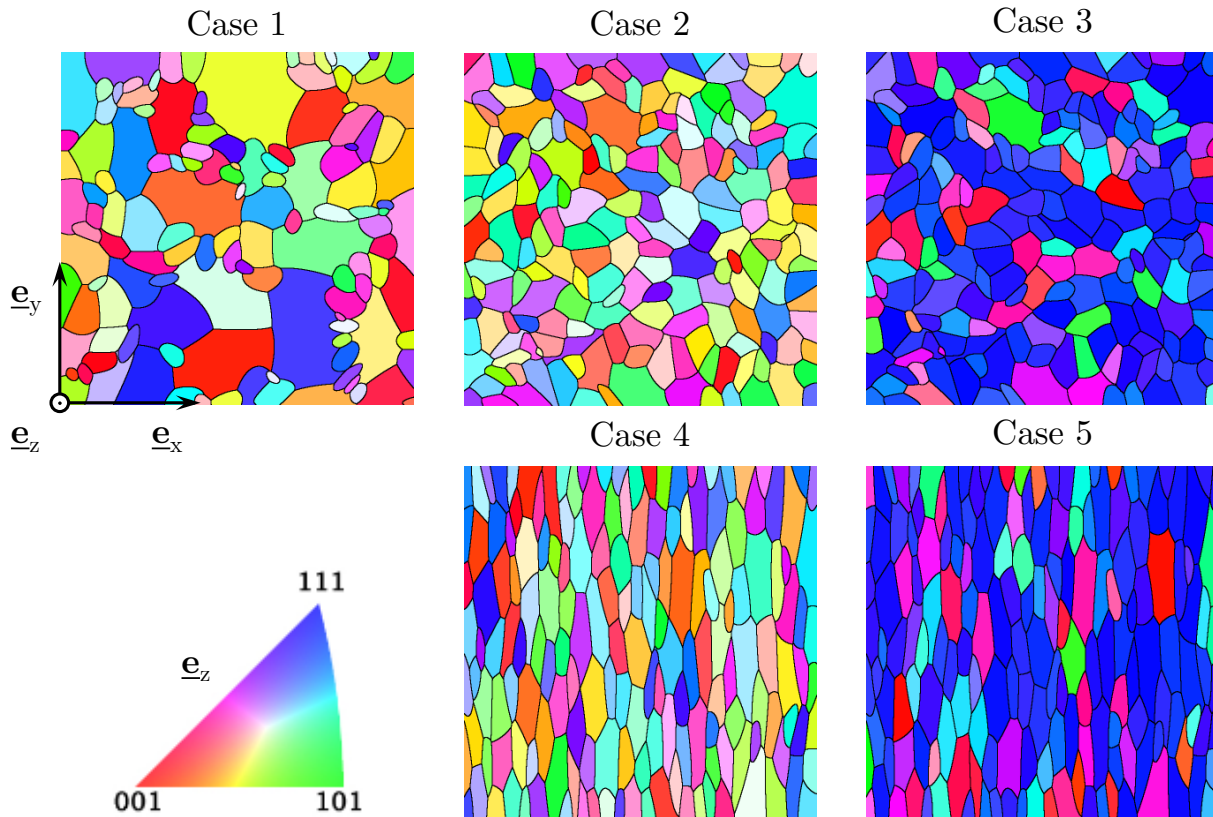


Figure IV.9 – Illustration of the different microstructures studied.

M_1 , largest grains contain about 800 elements and therefore 3200 integration points. The models are loaded in fully reversed tension-compression whether in the x or y -direction with a stress amplitude of 280MPa for 10 cycles. It is modeled by imposing a displacement

$U = 0$ to the lower or left edge of the aggregate and a cyclic macroscopic stress $\Sigma(t) = \Sigma_{amp} \sin(0.4\pi t)$ to the upper or right edge. To prevent rigid body motion, the displacement of the bottom left corner is also constrained. The results are analyzed using the last loading cycle of the simulations.

3.3 Results and discussion

3.3.1 Analysis of the mechanical response

Since the fatigue criterion considered in this study is based on a critical plane approach, slip systems within a grain are assumed to contribute independently towards the formation of a crack. Therefore, the mechanical field of interest is whether the local plastic strain or resolved shear stress acting on each individual slip system and not the total plastic strain accumulated over all the slip systems. Accordingly, the mechanical response of the aggregates is represented by computing the Effective Schmid Factor (ESF) m_{eff} at the Gauss points [60]:

$$m_{eff} = \max_{\alpha} \left(\frac{|\tau_{\alpha}^{\alpha}|}{\Sigma} \right) \quad (\text{IV.24})$$

where τ_{α}^{α} is the resolved shear stress amplitude on the slip system α and Σ is the applied macroscopic stress. Fig. IV.10 represents the ESF for one microstructure of each case. The same microstructure model is used for *Cases 3, 4* and *5* in order to observe the effect of the loading direction. It is worth saying that while the Schmid factor, which is a purely crystallographic parameter, is bounded between about 0.274 and 0.5 for uniaxial loading considering only the $\{110\}\langle\bar{1}11\rangle$ slip system, this is not necessarily the case for the ESF due to grains interaction, for instance by the presence of clusters [59] that might locally raise the stress. Accordingly, the ESF is bounded between 0.25 and 0.5 to ease the comparison between the different cases. Hence, parts appearing in gray represent regions with an ESF over 0.5 while parts in black represent region with an ESF below 0.25. This figure emphasizes the significant heterogeneity of the deformation within an aggregate and for different aggregates. Both intragranular and intergranular heterogeneities are noticeable, especially in large grains of *Case 1*. The ESF can vary from over 0.5 to about 0.35 within the same grain suggesting that evaluation methods of a criterion based on a volume average will underestimate the high plastic activity that can take place locally within a grain. Also, the highest ESF values are not always found near the edge of the domain suggesting that the boundary conditions directly applied to the edge of the aggregates do not significantly affect the results. Within a grain, the highest ESF is preferentially found close to grain boundaries or triple points.

Comparing microstructures with same texture, the intensity of the ESF is very similar regardless of the microstructure type. This observation is directly imputable to the absence of size effect in the phenomenological constitutive model. The highest ESFs are always found in uniformly textured microstructures with a value of about 0.6 while lowest ESFs are found in rolled texture with values near 0.2. Interestingly, when looking at the crystal orientation of the grains with the lowest ESF in Fig. IV.10 for the rolled texture, it always corresponds to the grains with the $[001]$ direction parallel to the z -direction meaning that it is mostly in grains with a weak γ -fiber. Overall, the mechanical response of aggregates with random texture is more scattered than that with rolled texture which stresses the significant role of the crystalline orientation on the strain localization and amplitude.

Focusing on the effect of the loading direction, the distributions of the ESF are almost identical independently of the microstructure or texture type. However, the values of the ESF are slightly different. This observation was also found by Guilhem *et al.* [59] who explained that the slope σ_{22}/σ_{11} is close to -1 when grains deform plastically.

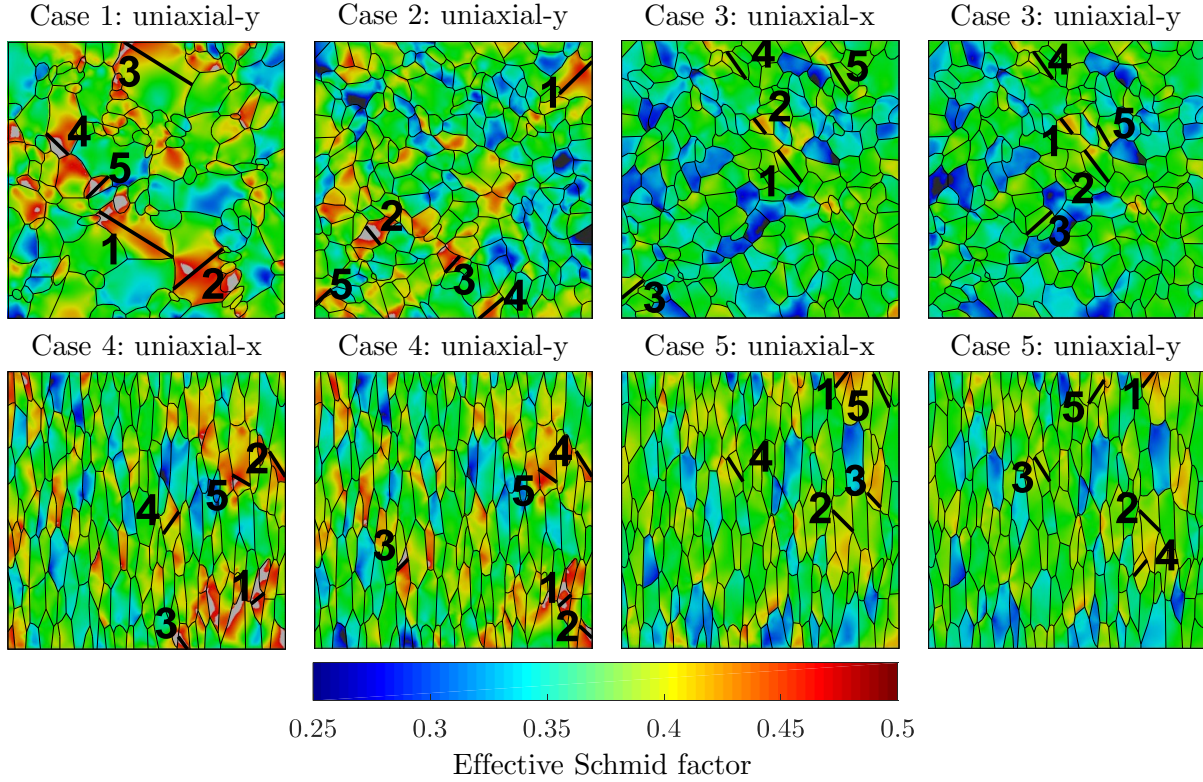


Figure IV.10 – Effective Schmid factor maps computed in the last simulated cycle for one microstructure per case.

3.3.2 Analysis of the FIP distributions

Fig. IV.11 reports the cumulative distributions of the fatigue criterion in an aggregate for the different cases studied. The highest FIP within a grain is considered. Gray lines represent the distribution per aggregates while red lines represent all the data for a same case. Relevant statistical data are reported in Table IV.3. It can be observed that the FIP scatters on about three orders of magnitude for *Case 1* while it is about 2 and 1.5 orders of magnitude for the other cases depending on the texture. Since the data varies on several orders of magnitude, the coefficient of variation (CV) defined as the ratio of the standard deviation to the mean is also reported. In order to evaluate the asymmetry of the distributions, the skewness of the samples is computed.

The effect of the microstructure type on the FIP distribution is first analyzed by comparing *Cases 1, 2* and *4*. It is noted that the mean and standard deviation decrease which is attributable to the lower standard deviation of the grain size of the microstructures M_2 and M_3 . Interestingly, the mean value does not decrease much between *Cases 1* and *2* compared with *Case 4* which suggests that the grain morphology in term of aspect ratio and orientation may have a significant effect. It is also observed that the skewness of the distributions decreases meaning that the average behavior of the aggregate is more symmetric around the mean value in the *Cases 2* and *4* compared with *Case 1*. Finally, it

3. INVESTIGATION OF THE INFLUENCE OF GRAIN MORPHOLOGY AND TEXTURE ON FATIGUE CRACK INITIATION

can be noted that the FIP distribution is slightly different in *Case 4* whether it is loaded in the x or y -direction.

The effect of the texture may be studied by comparing *Cases 2* and *4* with *Cases 3* and *5*. Here again, the mean value, standard deviation and skewness decrease between uniform and rolled textured microstructures. An uniform texture tends to induce significant variability of the FIP within microstructures of a same case while the response of textured aggregates varies less from aggregate to aggregate. The weaker texture in the x -direction also tends to increase the variability of the FIP distribution.

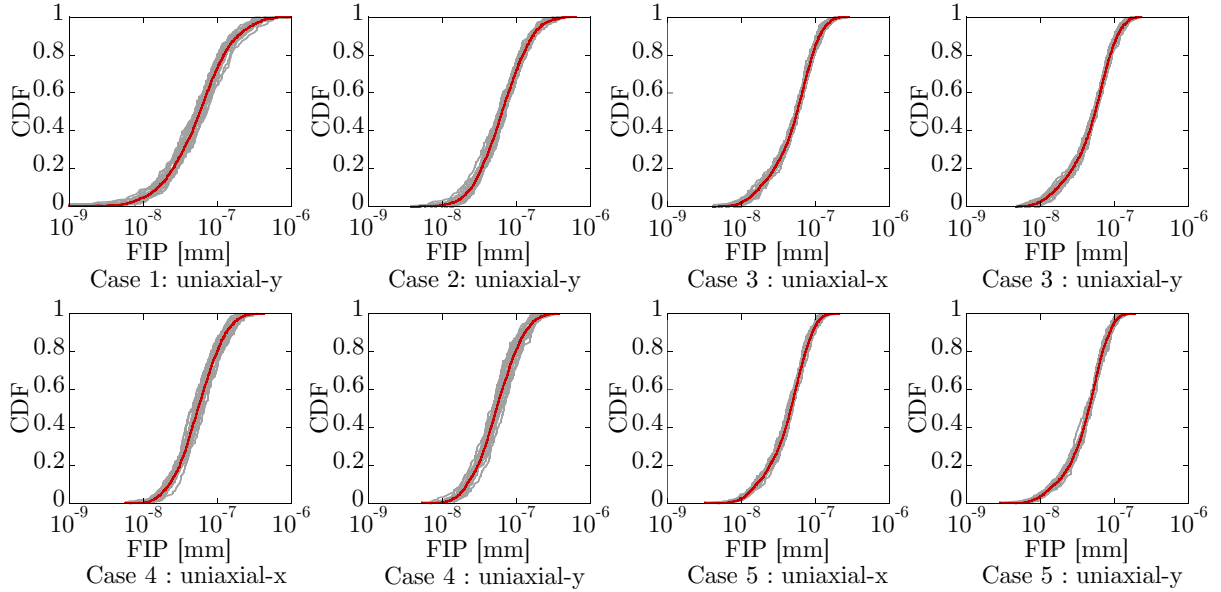


Figure IV.11 – Cumulative distribution functions of the Tanaka-Mura FIP for the different cases studied.

Table IV.3 – Statistical data of the fatigue criterion.

Case	Fatigue indicator parameter			
	Mean	Std dev.	CV	Skewness
Case 1	8.89e-8	1.03e-7	1.16	4.20
Case 2	8.45e-8	6.82e-8	0.807	2.21
Case 3: x -dir	6.26e-8	3.88e-8	0.620	1.06
Case 3: y -dir	5.99e-8	3.64e-8	0.608	0.959
Case 4: x -dir	6.91e-8	4.86e-8	0.703	1.71
Case 4: y -dir	6.76e-8	4.76e-8	0.704	4.69
Case 5: x -dir	5.09e-8	2.91e-8	0.572	0.866
Case 5: y -dir	4.85e-8	2.69e-8	0.553	0.762

Fig. IV.12 presents inverse pole figures of the Schmid factor of the $\{110\}\langle\bar{1}11\rangle$ slip system. For each case, the crystal orientation of about 2000 randomly selected grains among the 20 realizations are plotted as well as the orientation of the grain with the highest FIP for each realization. At first, it can be mentioned that the algorithm used to

draw and attribute orientations effectively produces orientations that are well distributed in the standard triangle. It is worth saying that directly sampling orientations from the Euler space tends to generate a higher number of orientations near the $[001]$ direction in the standard triangle, resulting in a not uniform texture. As can be seen, highest FIPs are preferentially found in high Schmid factor regions but do not necessarily correspond to the highest Schmid factor within an aggregate. Considering the cases with a rolling texture, it is observed that the α and γ -fibers generate orientations that avoid the highest Schmid factor region when loaded in the rolling or transverse direction. However, when loaded in the x -direction, the orientations scatter on a wider domain which might explain the slight increase in the standard deviation noticed previously. Here, highest FIPs are found close to the high Schmid factor region but not always as some FIPs are located near the $[110]$ direction.

At this point, it seems important to remind that BCC iron possesses 48 available slip systems: $\{110\}\langle\bar{1}11\rangle$, $\{112\}\langle 11\bar{1}\rangle$ and $\{123\}\langle 11\bar{1}\rangle$. Regions of low Schmid factor for the $\{110\}\langle\bar{1}11\rangle$ slip systems correspond to region of higher Schmid factor for the two other slip systems. However, introducing additional slip systems increases the computational cost and requires additional parameters to be calibrated.

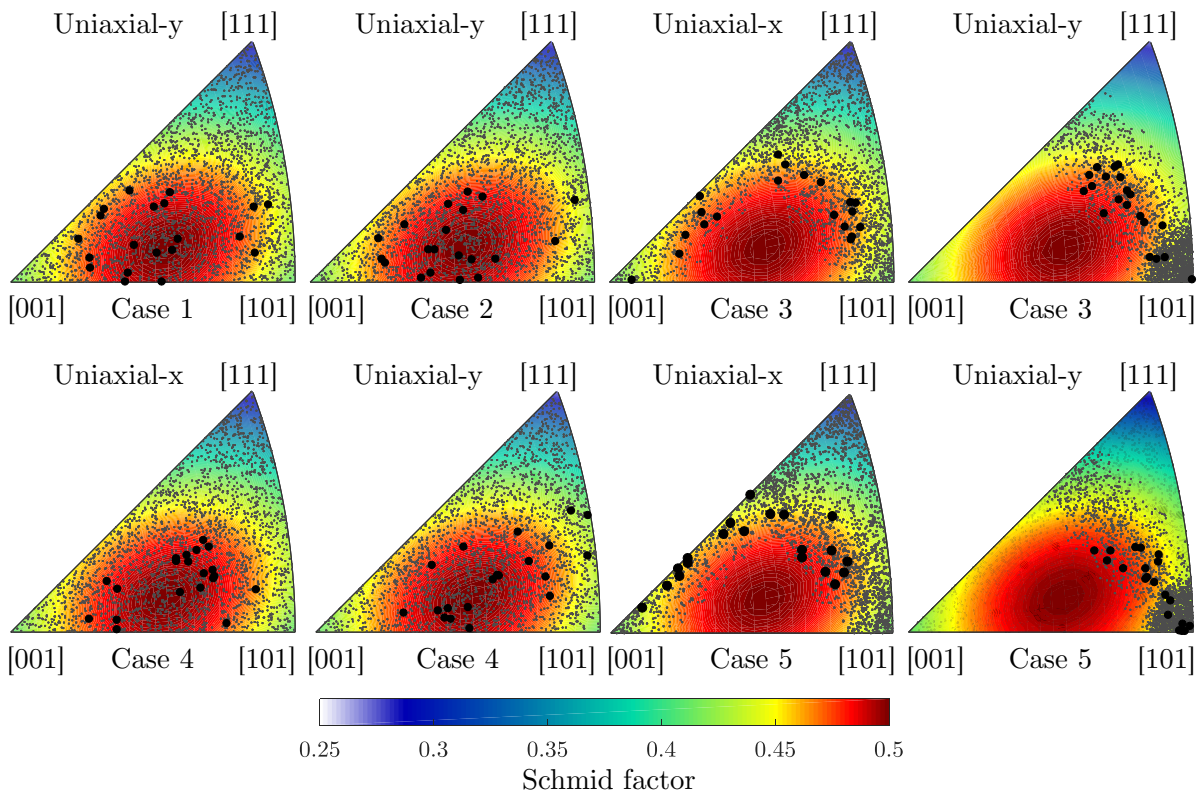


Figure IV.12 – Inverse pole figures from the loading axis (x or y) including iso-surfaces of highest Schmid factor. Dots represent all the grains and black filled circles refer to the grains with the highest FIP.

To further investigate the distribution of FIPs, Fig. IV.13 shows the plastic strain averaged on the PCP of the highest FIP per grain against the length of the PCP. The color of the circles represents the intensity of the FIP in log-scale since it varies on several orders of magnitude. The effect of the grain size distribution, grain shape and texture are clearly visible in this figure. Naturally, reducing the standard deviation of the grain size distribution decreased the maximum observable PCPs and therefore removed the extreme

3. INVESTIGATION OF THE INFLUENCE OF GRAIN MORPHOLOGY AND TEXTURE ON FATIGUE CRACK INITIATION

values from these regions. It can be seen that the grain morphology has an influence on the FIP distribution as lower number of grains have both a high plastic strain and a long PCP. The rolled texture mainly reduces the maximum plastic strain.

From Fig. IV.13 it can be noticed that similar FIPs can be reached by grains having different plastic strain amplitudes and sizes. Indeed, by considering a slip band size on which the plastic strain accumulates, the Tanaka-Mura model introduces a competition between different grains in an aggregate. Initiation may not arise from the grain with the highest plastic strain amplitude if its size is small as the total accumulated plastic strain over the slip band may not be very high. It also implicitly accounts for the fact that the crack will reach a lower size before being blocked by the grain boundaries and therefore will have a lower driving force for crack propagation.

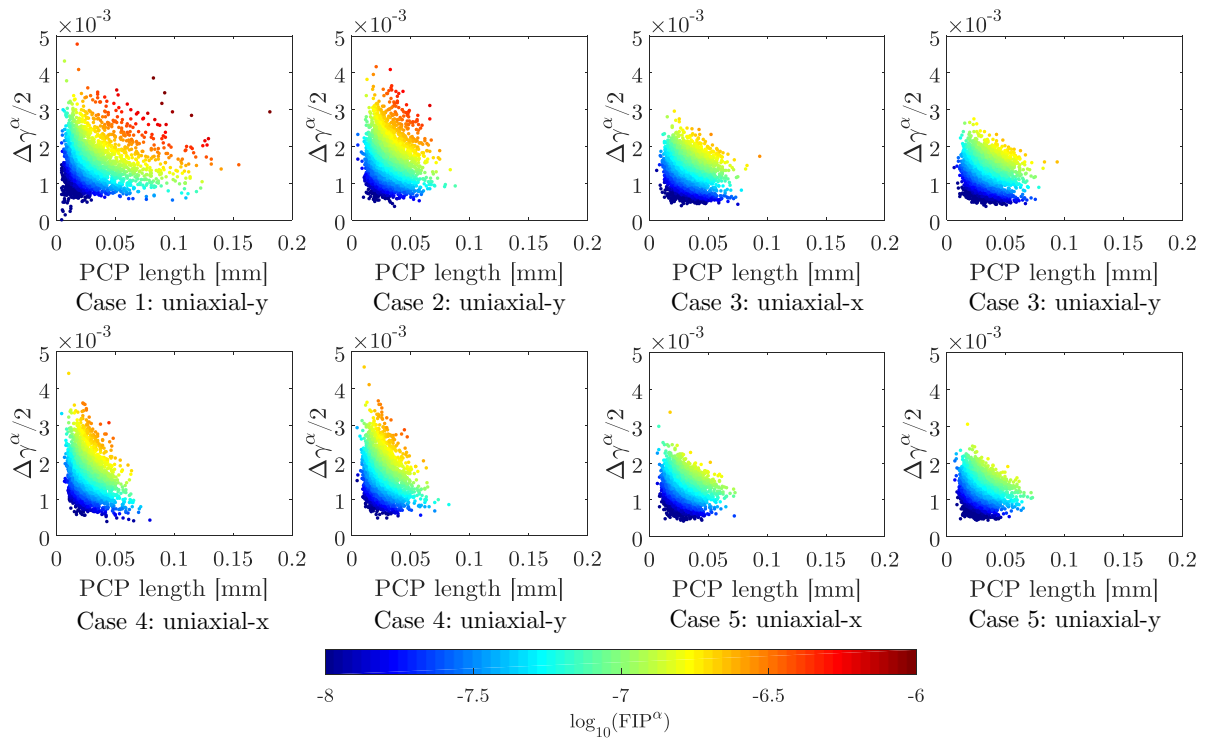


Figure IV.13 – Distributions of the average plastic strain amplitude against the length of the PCP. The color indicates the value of the FIP.

3.3.3 Analysis of the extreme value FIPs

Since fatigue crack initiation is not controlled by the average response of the aggregate but by the local extreme values this section focuses on the maximum FIP per microstructure as a direct indication of the driving force for the formation of a crack. Under HCF conditions, it can be indeed assumed that failure is controlled by the appearance and growth of a single crack. The location of the five highest FIPs per microstructure are reported in Fig. IV.10. The procedure seems to correctly isolate the path with the highest FIP within a grain.

We focus on the explicit value of the inverse extreme FIP as it provides a direct quantification of the number of cycles required for a crack to nucleate according to the Tanaka-Mura model [33]. Fig. IV.14 shows the extreme inverse FIPs for all the cases studied, the mean value is also represented in each case. The statistical data for each

case are reported in Table IV.4. As expected, *Case 1* exhibits the shortest lives and the highest dispersion with a scattering of about one order of magnitude. However, when compared with *Case 2*, it can be noticed that the improvement in the mean value does not come from a general increase of the inverse FIP but only an increase in the lower tail as the maximum inverse FIPs are similar in both cases. The reduction in the grain size variability does not actually improve the fatigue strength but only decreases the global scattering. In this regard, we point out that the statistical data used to generate *Case 1* microstructures directly come from EBSD measurement meaning that they represent a relatively realistic situation. On the other hand, the reduction in the standard deviation of the grain size distribution in the other cases tends to reproduce similar distributions obtained using Voronoi tessellation of randomly positioned seeds. This remark is important as to understand that, while convenient in its usage, Voronoi tessellations may actually underestimate the scattering in fatigue lives of a given material if used as a predictive tool as they only reproduce the mean behavior of a material but do not catch extreme events. We also remind that the CP model is not scale dependent and the use of such constitutive model should stress even more the importance of a correct microstructure representation.

The effect of the grain shape tends to increase the mean crack initiation lives but keep the scattering constant as the CV does not change significantly between *Cases 2* and *4* or *Cases 3* and *5*. Loading in the x -direction seems to make no difference in the case of an uniform texture, but tends to decrease the mean value and increase the scattering for a rolled texture. Overall a rolling texture improves both the mean initiation life and the dispersion. A decrease in the fatigue lives between the loadings in the x and y -directions is observed for both *Cases 3* and *5*.

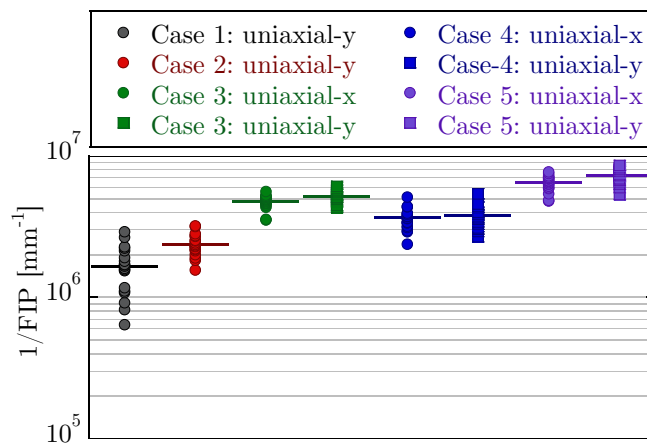


Figure IV.14 – Distribution of the extreme inverse FIPs for each case. Horizontal lines represent the mean value.

3.3.4 Analysis of the twist and tilt angles

The study finally focuses on the analysis of the twist and tilt angles between the slip system of the PCPs determined previously and its adjacent grains as parameters to quantify how easily cracks can cross grain boundaries. Fig. IV.15 depicts the cumulative probabilities of the twist and tilt angles for the different cases studied and for two specific slip systems in the neighbor grains. Indeed, since no explicit crack is introduced, it is not possible to predict accurately the stresses redistribution ahead of the crack tips.

3. INVESTIGATION OF THE INFLUENCE OF GRAIN MORPHOLOGY AND TEXTURE ON FATIGUE CRACK INITIATION

Table IV.4 – Statistical data of the extreme value inverse FIP.

	Inverse FIP				
	Min	Max	Mean	SD	CV
Case 1	6.39e5	2.91e6	1.65e6	5.96e6	0.362
Case 2	1.56e6	3.19e6	2.36e6	4.14e5	0.175
Case 3: x -dir	3.53e6	5.60e6	4.76e6	5.10e5	0.107
Case 3: y -dir	4.32e6	6.09e6	5.20e6	5.90e5	0.113
Case 4: x -dir	2.95e6	5.11z6	3.80e6	6.71e5	0.177
Case 4: y -dir	2.68e6	5.39e6	3.77e6	6.49e5	0.172
Case 5: x -dir	4.78e6	7.71e6	6.50e6	8.34e5	0.128
Case 5: y -dir	5.34e6	8.59e6	7.25e6	8.13e5	0.112

Accordingly, we consider two possible slip planes: the slip plane providing the lowest twist angle and the slip system with the highest plastic activity.

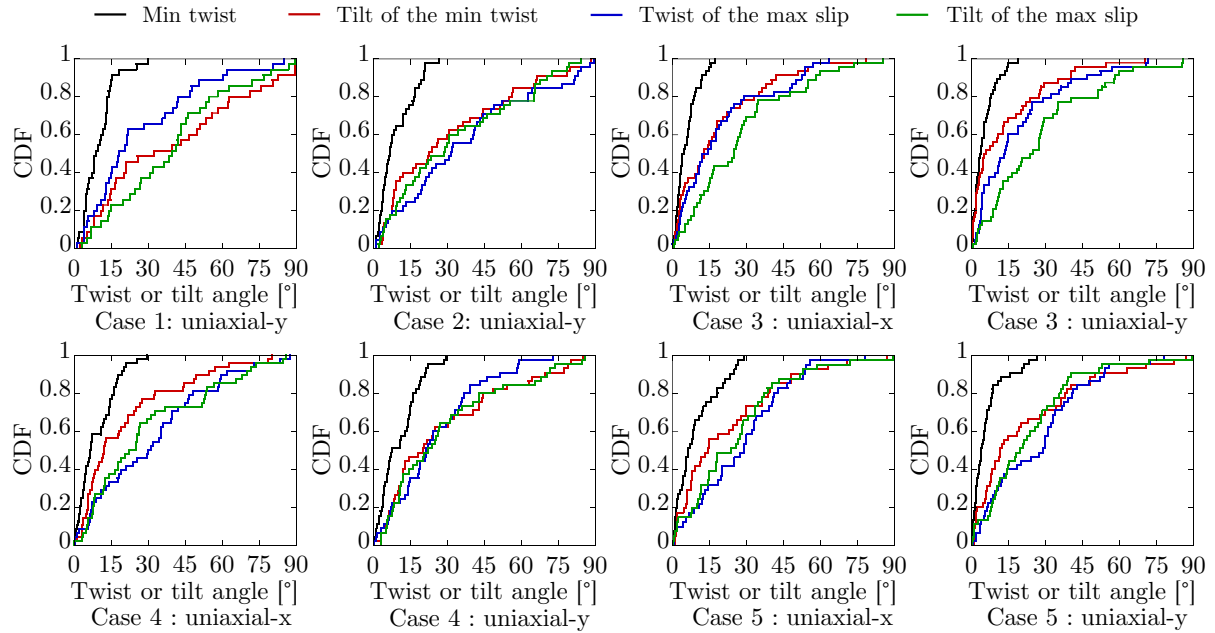


Figure IV.15 – Cumulative distribution functions of the twist and tilt angles for the different cases.

Considering the minimum twist angle, it can be observed that it never exceeds 30° , independently of the case studied. Comparing similar microstructures, it seems that rolled textures tend to produce more twist angles below 15° than uniform ones. The corresponding tilt angle also exhibits different distributions whether the texture is random or not. Indeed, in *Cases 1* and *2*, the tilt angle is almost uniformly distributed in the $[0, 90]$ interval while it seems that the distribution is not random but mainly concentrated in a low angle region for rolled textures. The average minimum twist angle is about 10° for an uniform texture with a standard deviation of about 7° while the mean value is near 6° for a rolled texture with a standard deviation of about 6° . Similar observations

may be drawn from the twist angles of the most activated slip systems. Indeed, while it seems to scatter between 0 to 90° for uniform textures, the minimum twist angle is mostly found below 60° for rolled textures (*Cases 3 and 5*). Finally looking at the effect of the grain morphology, the twist and tilt angles are often higher for the microstructures M_3 suggesting that grain boundaries parallel to the loading direction should have a higher resistance to crack propagation than randomly oriented grain boundaries.

All these observations suggest that while a rolled texture provides better orientation against crack initiation, the lower angles at the grain boundary should induce lower resistance against crack propagation. As the scattering in fatigue lives is not only controlled by the initiation but also by the propagation of microstructurally short cracks, this leads to think that scattering should not vary significantly in the case of rolled textures.

3.4 Conclusions

The main purpose of the study was to evaluate the influence of several morphological parameters as well as rolled texture on the fatigue crack initiation using finite element simulations. In order to study separately the effect of each parameter, various polycrystalline aggregates were modeled based on an anisotropic tessellation. Several concluding remarks can be made:

- The grain size distribution affects both the average aggregates reaction as well as the extreme events for crack initiation. Reducing the grain size variability decreases the scattering. In this regard, accurate reproduction of a grain size distribution is crucial to not underestimate the actual scattering in fatigue lives.
- Both the elongated morphology and rolling texture improve the crack initiation lives and decrease the variability. It seems therefore important to consider not only the average grain size based on grain area but the effective grain size within a particular direction.
- Analyses of twist and tilt angles suggested that the rolling texture might provide lower resistance to crack propagation compared with a random texture. However the differences were not so significant. Specific parametric study on bicrystals may provide additional information.

Finally, a main limitation of the study of undamaged microstructures for the prediction of fatigue performances is the absence of the stress redistribution due to the presence of a crack. The variability of the fatigue lives is not only related to the initiation of cracks but also to the propagation across the first few grains.

4 Simulations of stage I fatigue cracks in notched polycrystalline aggregates

4.1 Introduction

The simulations conducted in this section aim to reproduce the geometry and loading conditions of the experiments conducted in the previous chapter. Since absolute prediction and reproduction of the fatigue behavior is still a challenge [97], the study focuses on the crack initiation and propagation across the first grain boundary in a comparative manner by simulating microstructures representative of α -iron and FP steel. A particular attention is addressed towards the importance of the introduction of an explicit crack in order to study the influence of the microstructure on crack propagation. Considering the size gap between the average grain size of the two materials and the specimen size, a complete modeling of the gauge area using polycrystalline aggregates is too computationally demanding. To circumvent this limitation a two-scale modeling strategy is presented where an explicit microstructure is only considered around the notch. This approach is justified by the fact that most of the cracks leading to final failure in these two steels originated and propagated from the notch. Two types of simulations are conducted: uncracked microstructures and microstructures including an initial crack on each side of the notch.

This section is organized as follows. At first the numerical models, approximations and modeling methods are presented. The results of the simulations are then analyzed for the uncracked microstructures to begin with, and cracked microstructure thereafter.

4.2 Description of the numerical models

A recurring problem in simulating polycrystalline aggregates is the question of the boundary conditions. Several types of boundary conditions can be found in literature: stress or displacement control, periodic or semi-periodic boundary conditions, embedment in an isotropic matrix. In this study, in order to reproduce in a reasonable time the fatigue tests conducted, a submodeling technique is adopted to reduce the size of the model. A submodeling technique *"is used to study a local part of a model with a refined mesh based on interpolation of the solution from an initial (undeformed), relatively coarse, global model"* [156]. This method presents the advantage to provide relatively realistic BC without the need to simulate large microstructures. Besides a single global model is only needed for the simulation of several sub-models thus reducing the total computational time.

4.2.1 Global model

Since the models of microstructures are two-dimensional, the global model used to define the boundary conditions on the edges of the aggregates is also two-dimensional. The geometry and mesh of the global model are displayed in Fig. IV.16, with an elliptic notch having similar dimensions than in experiments, i.e. $50 \times 150 \mu\text{m}$. The model is meshed with four-nodes plane strain elements (CPE4), with strongly refined mesh in the notch area in order to obtain accurate displacement fields for the boundary conditions of the submodels. The J_2 -plasticity model calibrated in Chapter III is applied as a constitutive model. The boundary conditions are also represented in Fig. IV.16. A linear elastic

analysis revealed a stress concentration factor of 1.6 slightly higher than the 1.4 found in the 3D case.

The vertical displacement of the lower edge is constrained ($u_y = 0$). The horizontal displacement of the bottom-left edge corner is constrained as well ($u_x = 0$) to prevent any rigid body motion. Finally stress boundary conditions are applied on the upper edge of the model ($\Sigma(t) = \Sigma_{amp} \sin(0.4\pi t)$). The global and local models are subjected to 10 loading cycles with a stress ratio $R=-1$ and different stress amplitudes for each steel. The results discussed in the next part are all based on the last simulated cycle. Table summarizes the simulation conditions for the two steels.

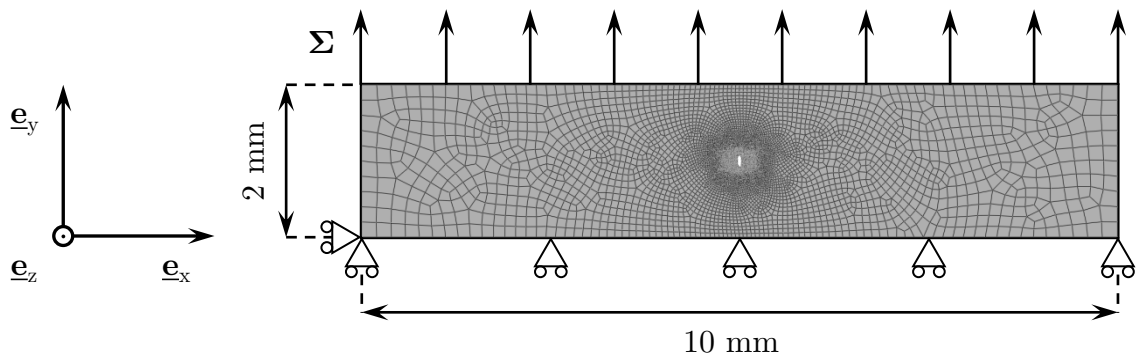


Figure IV.16 – Geometry of the global model used to simulate the boundary conditions for the sub-models.

Table IV.5 – Simulation conditions of the global model.

	α -iron	FP steel
Σ_{amp} [MPa]	280, 300, 320	200, 220, 240
Stress ratio	-1	-1
No. cycles	10	10

The macroscopic stress-strain curves of the global model for the two materials and the different stress conditions are shown in Fig. IV.17. Plastic deformation is observed in each loading case. At the end of the 10 cycles, a nearly stabilized plastic shakedown is reached since the hysteresis curves are almost closed with no net accumulation of plastic deformation. Ratcheting is not observed in any case. However, it is worth mentioning that simulations at higher stress lead to the presence of ratcheting and for that reason, they were not considered in this study. The stress control condition introduces an asymmetry in the hysteresis curves as all the hysteresis curves exhibit a non-zero mean stress.

4.2.2 Modeling of notched polycrystalline aggregates

The microstructures generated in this study are also based on the method described in Chapter II, with the statistical data obtained from EBSD analyses. For each material, ten square-domain microstructures are generated. The size of the domain is set to include the stress concentration area due to the presence of the elliptic defect (about three times the minor axis length). However, due to the significant difference in average grain size,

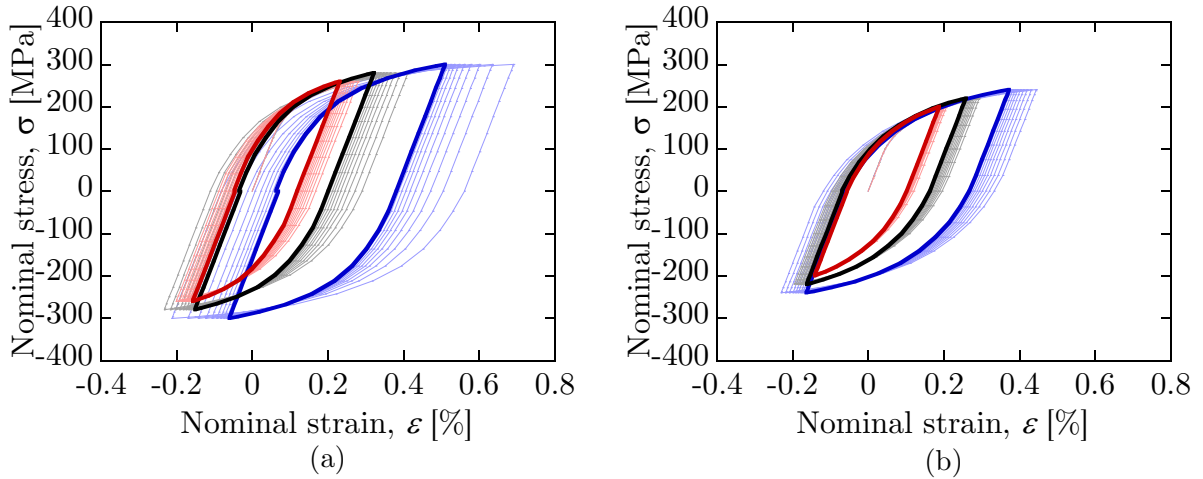


Figure IV.17 – Macroscopic stress-strain curves of the global model for (a) the α -iron and (b) the FP steel.

the dimensions of the domains are different to include the same number of grains. It is $400 \times 400 \mu\text{m}$ and $200 \times 200 \mu\text{m}$ for α -iron and FP steel respectively. The number of grains is ranging between 110 to 140 for α -iron and 100 to 120 for FP steel. The microstructures are reconstructed in Abaqus through custom-made python scripts. An elliptic notch is then made in each model. The models are meshed with four-node plane strain elements (CPE4) with an average size of $4 \mu\text{m}$ for α -iron and $2 \mu\text{m}$ for FP steel. The meshes are refined in the vicinity of the notch. An example of the meshed microstructures is shown in Fig. IV.18. Approximately 23,000 and 12,000 elements are used in each model for α -iron and FP steel. Grains near the ellipse have about 1000 elements while on the edge of the domain it is about 600 elements for the largest grains. These values are higher than those of Diard et al. [82] who suggested in the case of 3-D model an average of 350 integration points to correctly capture the average mechanical response of the grain.

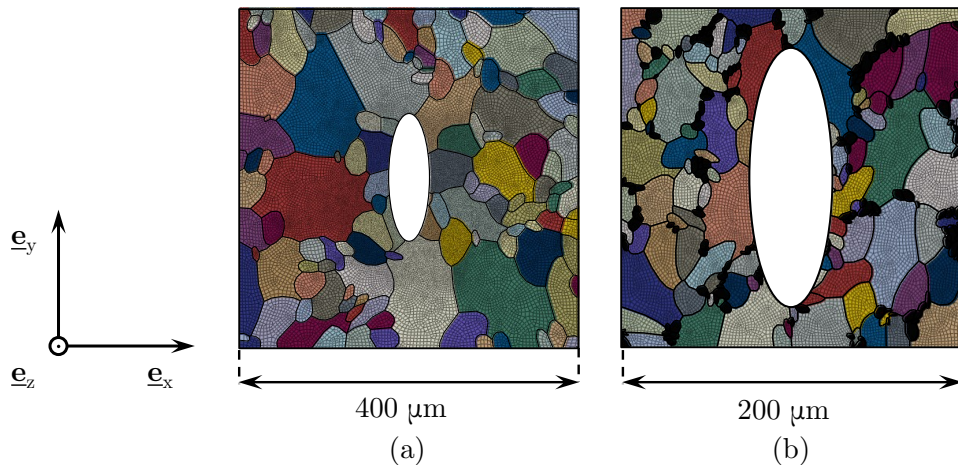


Figure IV.18 – Geometry of the notched polycrystalline aggregates of (a) α -iron and (b) FP steel. Pearlite grains appear in black.

4.2.3 Introduction of a crack

The introduction of a crack in the microstructure can be achieved according to various methods (seam crack, XFEM, degraded stiffness) as described in Chapter I. In this

study, cracks are modeled based on the seam crack method. The methodology for the introduction of a crack is summarized in Fig. IV.19 and explained below:

1. **Definition of a crack path.**
2. **Meshing:** the mesh follows the path with duplicate overlapping nodes on the path. Each node within a pair is allowed to move independently from one another.
3. **Definition of the master surface.**
4. **Definition of the slave nodes:** particular attention should be made to not include the node at the crack tip since there is no duplicate node. Indeed a node cannot be master and slave at the same time.
5. **Definition of the surface interaction:** as the fatigue simulations are under negative stress ratio, a "hard contact" interaction is introduced to prevent the two free surfaces from overlapping. No friction is considered in this study.

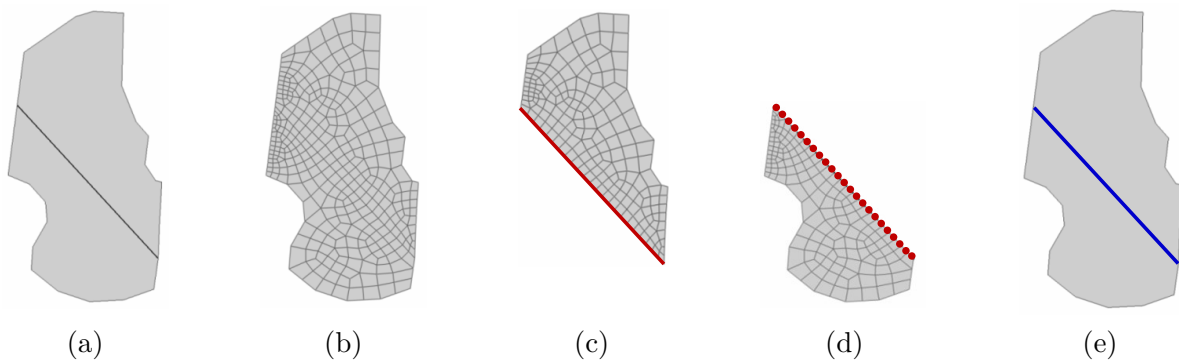


Figure IV.19 – Procedure for the introduction of a seam crack with non-overlapping faces.

As it is expected that the presence of the crack will raise the stress in its vicinity, the mesh of the neighbor grains are refined. The same loading conditions as for the uncracked microstructures are applied. However, in a significant number of simulations, a converged solution was not always found and different mesh qualities were tested until convergence was achieved.

4.3 Results and discussion

This section is divided into two parts: the analysis of crack initiation from the simulation of uncracked microstructures and the analysis of crack propagation from the results of the cracked microstructures.

4.3.1 Analysis of crack initiation

Local mechanical responses

The analysis first focuses on the mechanical response in the polycrystals. The von Mises stress fields at the tensile stress of the last cycle are illustrated in Fig. IV.20 and IV.21 for the isotropic models and three microstructure models. In the case of FP steel, the stress field in the pearlite grains was not plotted due to a much higher stress than in the ferrite grains which is attributable to the higher yield strength and elastic modulus of the pearlite phase compared to the ferrite phase. It can be observed in both cases that the anisotropy of the elastic behavior due to the cubic elasticity generates both inter and intra-granular heterogeneous stress field which is often higher than for an isotropic medium. The notch generally raises the stress in its vicinity. However, the maximum values of the von Mises stress are not always found in grains directly in contact with the notch. The crystal orientation still has a significant effect on the stress and strain localization even in presence of a notch. Besides the presence of pearlite in FP steels tends to induce higher stress in surrounding ferrite grains. In the absence of a notch, it is therefore very likely that crack mainly initiates in grains directly in contact with pearlite. A recent study of Guerchais *et al.* [72] on the effect of defect size and shape on the high-cycle fatigue behavior revealed different von Mises stress fields. In their study, the defect size is much larger than the grain size such that the effect of the crystal orientation is reduced in the vicinity of the notch leading to a stress field very similar to that of an isotropic medium. A last remark concerns the effect of the boundary conditions imposed by the submodeling technique. From the observation of the von Mises stress fields, no significant constant increase of the stress is found in the grains in contact with the edge of the domain. Compared with the simulations in the previous section where the conditions were directly applied on the edge of the model, it seems that the submodeling technique allows reducing such an edge effect.

The distributions of the stress concentration factor $K_t = \sigma_{yy}/\Sigma_{max}$ along an horizontal path starting from the center of the notch ($y = 0$) are represented for all the results in Fig. IV.22. The profile of the stress concentration factor in the case of an isotropic linear elastic medium is also plotted on each graph. From these graphs, it can be noted that K_t strongly oscillates and does not monotonically decrease. However, in the case of α -iron, K_t tends to decrease in average when getting away from the notch. It seems that past 100 μm , the effect of the notch is negligible and the disparity is mainly due to the crystal orientation. It can be observed that the highest stress concentration is not always found in the grains directly in contact with the elliptic notch. In the case of FP steel, such a decrease is not clearly found since the size of the domain is smaller than that of α -iron. Besides, several peaks over a K_t of 2 are observed. They correspond to pearlite grains which mainly behave elastically at these stress conditions. These observations highlight the fact that a damage tolerant approach based on the computation of the stress concentration factor in a notched region may underestimate the actual stress condition and therefore lead to a not conservative enough prediction especially when the notch size and grain size are close.

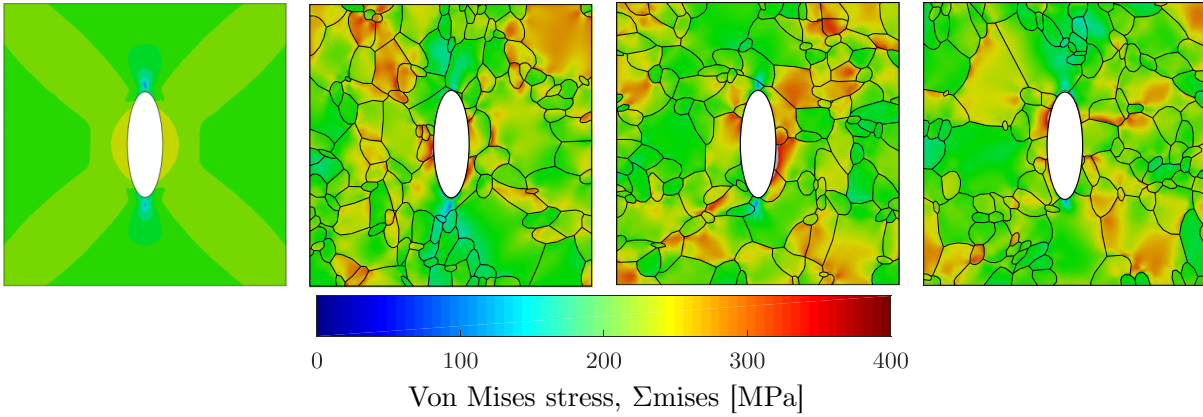


Figure IV.20 – Von Mises stress fields at the peak tensile stress of the last cycle for the global isotropic model and three different α -iron microstructures subjected to a stress amplitude of 260 MPa.

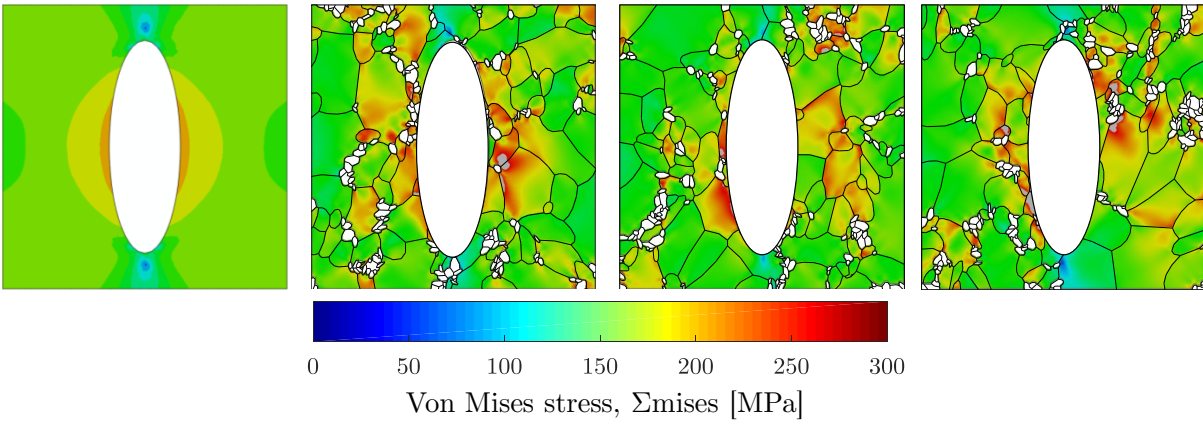


Figure IV.21 – Von Mises stress fields at the peak tensile stress of the last cycle for the global isotropic model and three different FP steel microstructures subjected to a stress amplitude of 200 MPa.

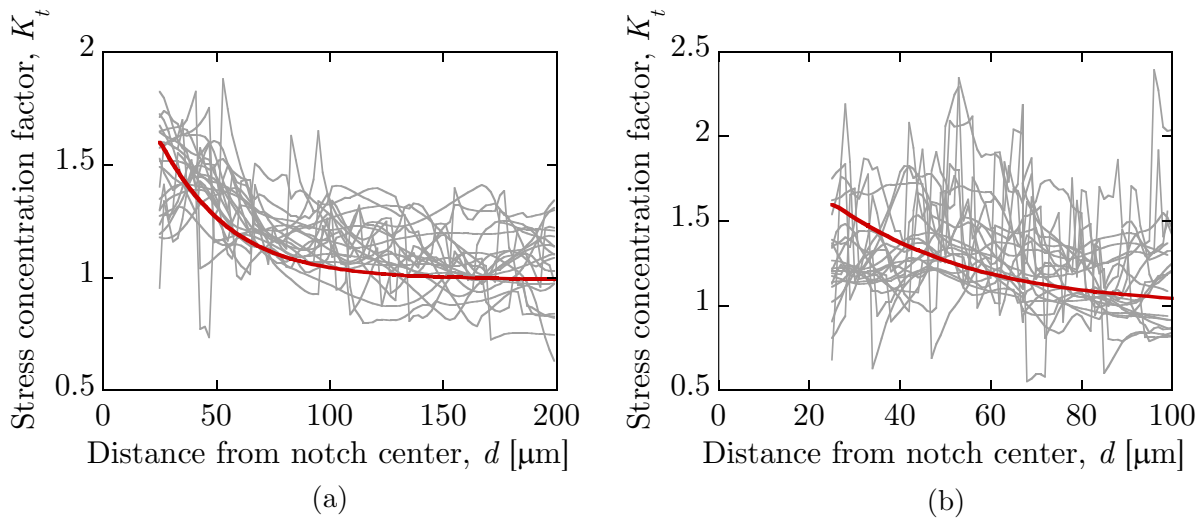


Figure IV.22 – Distribution of the stress concentration factor K_t along the line $y = 0$ for all the simulations of (a) α -iron and (b) FP steel.

Analysis of the slip activity and crack initiation sites

In order to evaluate the FIP defined in Eq. IV.2, the relevant mechanical field to be considered is the local plastic strain γ^α on each individual slip system. As the presence of the notch induces a multiaxial stress condition, the usage of the effective Schmid factor is less relevant. The maximum plastic strain amplitude fields for the last cycle over the 12 available slip systems are reported in Fig. IV.23 and IV.24 for eight α -iron and FP steel microstructures subjected to a stress amplitude of 260 and 200 MPa respectively. It is computed at each integration point and gives a direct indication of the intensity and location of maximum plastic activity. It can be observed that the plastic activity is highly heterogeneous, with both inter and intra-granular heterogeneities noticeable. While the first one is mainly due to the lattice orientation compared with the macroscopic applied stress, the latter one can be attributed to grains interaction generating stress gradients due to local misorientations also referred as local micro-texture. Overall the plastic strain is slightly higher in the vicinity of the ellipse. However, this increase seems to be confined to the first surrounding grains. When compared to the von Mises stress fields one can notice that the location of the highest local plastic strain amplitude does not always correspond to location of the highest von Mises stress. However, the total accumulated plastic strain over all the slip systems fits relatively well with the von Mises stress field. This observation highlights a significant difference in the mechanical response from grain to grain. Indeed, in grains where the maximum plastic strain amplitude is high, it is found that the number of active slip systems is relatively low (1 or 2). On the other hand, grains with high von Mises stress generally tend to exhibit a higher number of activated slip systems and a better distribution of the plastic strain among these slip systems. Experimentally, it is observed that the number of active slip systems is often less or equal to 2 which corresponds to the primary and secondary slip systems.

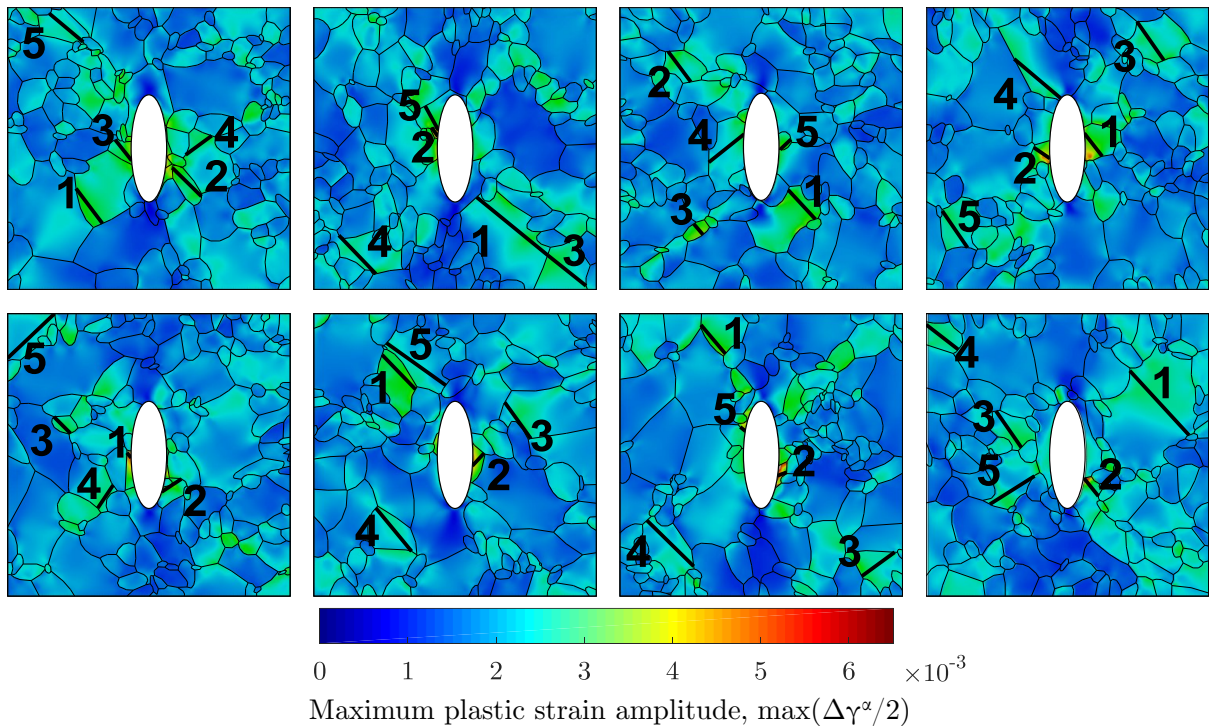


Figure IV.23 – Maximum plastic strain amplitude $\max_\alpha(\Delta\gamma^\alpha/2)$ accumulated in the last cycle among the 12 available slip systems for eight α -iron microstructures.

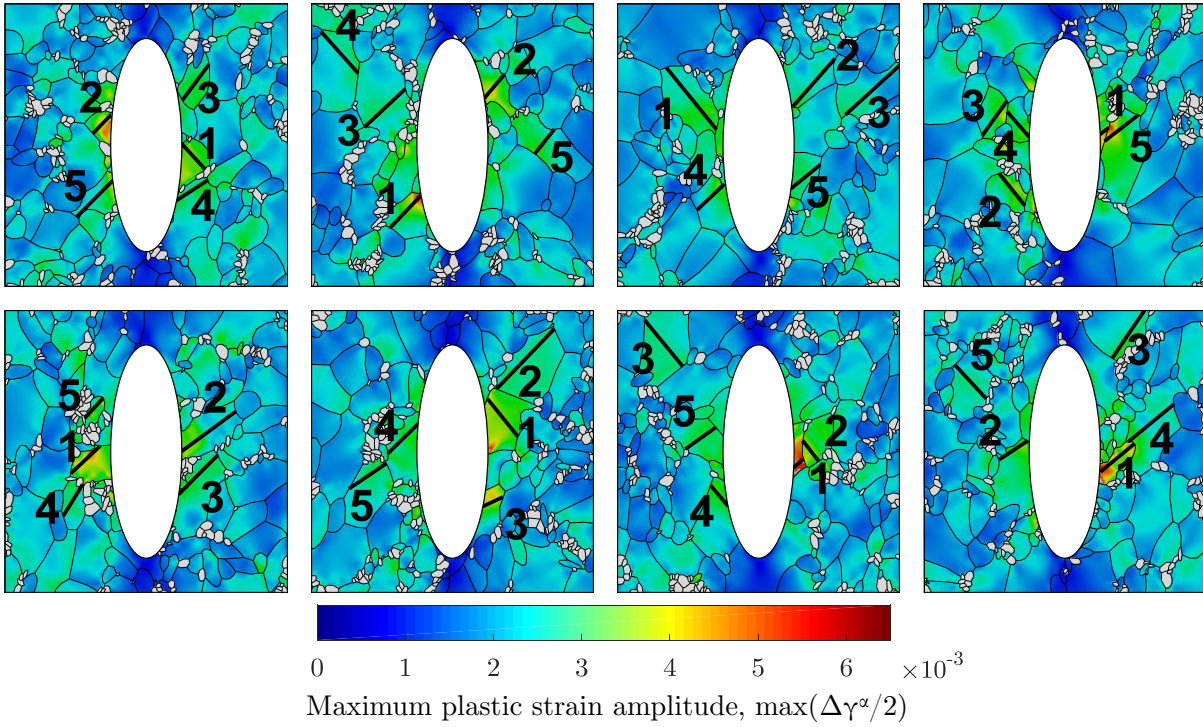


Figure IV.24 – Maximum plastic strain amplitude $\max_\alpha(\Delta\gamma^\alpha/2)$ accumulated in the last cycle among the 12 available slip systems for eight FP steel microstructures.

The positions and orders of the five PCPs having the highest FIPs for each microstructure are also reported in Fig. IV.23 and IV.24. The use of a path average in the evaluation of the FIP instead of a local value on integration points or a grain averaged value allows capturing the local slip heterogeneity present in each grain, particularly noticeable in some large grains. The PCPs mainly find their origins close to or on triple points of grain boundaries as they correspond to zones of local stress concentration due to the orientation and strain incompatibility arising from the three adjacent grains. Within a grain, the maximum FIP does not generally associate with the longest possible slip band, especially in largest grains of α -iron where the plastic strain is highly heterogeneous. In fact, the grain shape seems to play a significant role, as found in the previous section, as in the case of elongated grains, if the slip plane is perpendicular to the grain major axis, the PCP will be relatively shorter and consequently have the lower FIP. It is also noticed that the predicted PCPs are often close to the notch and mostly oriented 45° from the loading direction. When comparing the crack initiation sites of the two materials, it is observed that the highest FIPs are always in contact with the notch for FP steel while it is not the case in several α -iron microstructures. Indeed, the size of the ellipse is close to the average grain size of α -iron so that a limited number of grains are observed in its surrounding. Accordingly, if the neighboring grains are unfavorably oriented, crack initiation around the notch might be delayed. In the case of FP steel, the notch is surrounded by several grains on each side which increases the possibility of crack initiation in its vicinity. This conclusion is very consistent with the experimental observations made in the previous chapter where in a significant number of cases, crack was not found to initiate in the notch for microstructures where the average grain size was of the same order than the notch size. In this regard, the position and size of the ellipse relative to the microstructure seem to play a major role in the FIP value. Also when compared with experimental cracks, it is noted that a crack may initiate anywhere on the edge of the notch and not

only at the position of highest stress concentration factor. The position and order of the FIPs seem also to not be affected by the change in stress amplitude.

Quantitative analysis of the FIPs

Fig. IV.25 illustrates the Schmid factor in the standard triangle for the $\{110\}\langle\bar{1}11\rangle$ slip system. The crystal orientation of all the grains of the ten microstructures are plotted for the two materials. Besides for each microstructure, the crystal orientation of the five grains having the highest FIP are highlighted. While orientations are widely scattered in the standard triangle, maximum FIPs are preferentially found in high Schmid factor region but do not always correspond to the highest FIP in a given microstructure. It can be observed that the FP steel microstructures have several grains whose $[111]$ direction is parallel to the loading direction while it is not the case for α -iron.

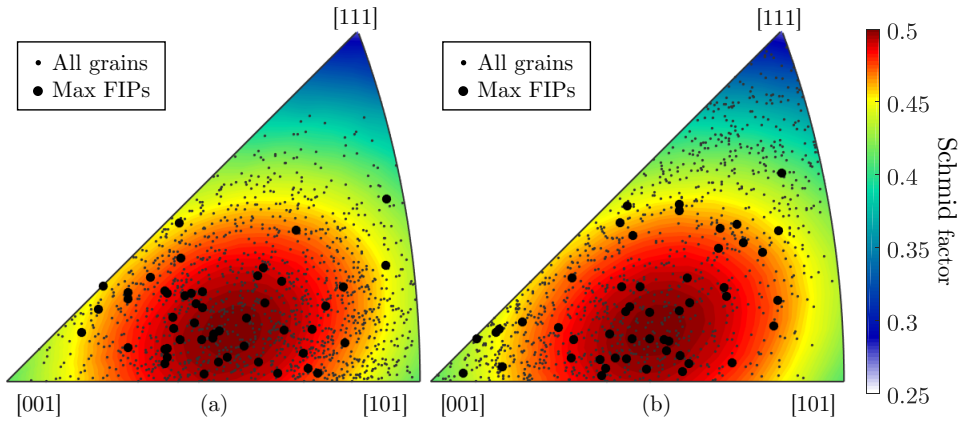


Figure IV.25 – Inverse pole figure from the loading axis (y -direction) including surfaces with similar Schmid factor for (a) α -iron and (b) FP steel. Filled circles represent the crystal orientation of the five highest FIPs per microstructure.

A more quantitative view is provided in Fig. IV.26 which depicts the cumulative probability of the Schmid factor for all the grains and for the five grains with the highest FIP per microstructure. The highest FIPs mainly belong to the Schmid factor domains $[0.42, 0.5]$. This domain is smaller than that found experimentally in stainless steels subjected to low-cycle fatigue conditions, where cracks were mainly found in Schmid factor region ranging from 0.4 to 0.5 [55, 157]. While stainless steel microstructure is a FCC austenite phase, the Schmid factor distribution on the standard triangle is similar in both cases, assuming only the $\{110\}\langle\bar{1}11\rangle$ slip system for the BCC lattice. In fact, including the additional $\{112\}\langle 11\bar{1}\rangle$ and $\{123\}\langle 11\bar{1}\rangle$ slip systems in the simulations may bring different results as regions of low Schmid factor for the $\{110\}\langle\bar{1}11\rangle$ slip system have a higher Schmid factor for the two other slip systems. However, it would require the knowledge of hardening parameters for the systems and would significantly extend the computational time due to the increase in the internal state variables (ISV) number.

Fig. IV.27 shows the FIP of all the realizations against the orientation of the PCP. The maximum FIP in each microstructure is also indicated. Logically, the highest FIPs are found on crack paths oriented in the orientation domain of $[40^\circ, 50^\circ]$ relative to the loading direction. The FIP also tends to decrease when the PCP direction deviates from this domain as the Schmid factor decreases.

The distribution of the FIPs against the plastic strain amplitude are displayed in

Fig. IV.28 for the stress amplitude of 260 MPa and 200 MPa for α -iron and FP steel, respectively. The relation defined in Eq. IV.2 is represented for different lengths d : 120, 60, 45, 30, 15 and 8 μm . Highest FIPs are mostly found in grains having PCP longer than the average grain size, i.e. between 60 to 120 μm for α -iron and 30 to 60 μm for FP steel, despite not always having the highest plastic strain amplitude. By directly accounting for the length of the PCP into the evaluation of the FIP a competition is introduced between the two variables of the FIP. Among two grains or slip lines having the same plastic strain amplitude, the one with longer PCP should have higher FIP based on the Tanaka-Mura model as it will accumulate more plastic strain on its slip band every cycle. This observation emphasizes the fact that accurate representation of grain size distribution is crucial to reliably predict crack initiation. Additionally, a crack belonging to a large grain will reach a larger size before being blocked at a grain boundary and therefore be more likely to propagate and become the major crack. At this point, it is worth mentioning that the crystal plasticity formulation used in this study does not account for grain size effect such as the Hall-Petch law. A CP model accounting for such effect would support even more this observation as larger grains would tend to be “softer” than the smaller one.

Fig. IV.29 presents the cumulative distributions of the FIP for the different stress conditions for all the realizations. The grey line represents the data for individual microstructures while the colored ones are for all the data combined. Due to the scattering on several orders of magnitude, the distributions are shown on a log-scale which gives a better representation of the tails of the distributions. It is observed that the distributions scatter on about three and five orders of magnitude for α -iron and FP steel respectively. The shape of the distribution does not seem to change with the macroscopic stress amplitude. The increase in stress amplitude logically tends to shift the CDF in higher FIP values. Interestingly, the CDFs of α -iron are relatively symmetric while a wide lower tail below 20% of the CDF is noticeable. Table IV.6 summarizes the statistical data of the distributions. Since the distributions have different mean values, the coefficient of variation (CV) defined as the ratio of the standard deviation with the mean provides a normalized comparative indicator to assess the scattering of the data than the standard deviation. It is noted that the CV is higher for FP steel which confirms the highest dispersion of the average behavior of FP polycrystals. The CV also increases with the increase in stress amplitude. To quantify the asymmetry of the distributions, we also reported the skewness of the distributions. The skewness b_1 of a sample of n values x is given by [158]:

$$b_1 = \frac{\frac{1}{n} \sum_{i=1}^n (x_i - \bar{x})^3}{\left[\frac{1}{n-1} \sum_{i=1}^n (x_i - \bar{x})^2\right]^{3/2}} \quad (\text{IV.25})$$

where \bar{x} is the sample mean. It is observed that the skewness is always positive and higher for FP steel. Interestingly, the skewness of the distributions increases with the stress amplitude. This observation, combined with the fact that the CV also increases shows that the increase in the stress amplitude mainly affects the grains where the FIP is already high. In other words, the plastic deformation accumulates more easily on already favorable grains or clusters and does not spread more evenly with a higher applied stress. Finally in order to explain the higher scattering observed in FP steel, we can refer to the IPF in Fig. IV.25 or the Schmid factor distributions in Fig. IV.26. It is observed that a significant number of grains in FP steel have their [111] direction parallel to the loading direction and therefore have a much lower Schmid factor. Consequently, it can be expected that the behavior of a FP microstructure is more heterogeneous than for α -iron.

4. SIMULATIONS OF STAGE I FATIGUE CRACKS IN NOTCHED POLYCRYSTALLINE AGGREGATES

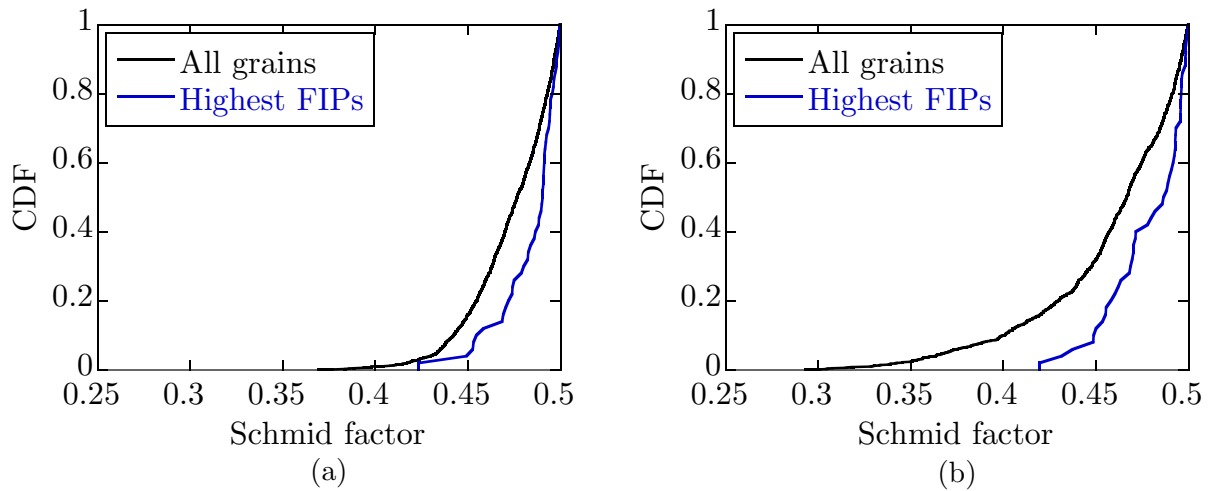


Figure IV.26 – Cumulative probability of the Schmid factor of all the grains in the microstructures and of the five highest FIPs per microstructure for (a) α -iron and (b) FP steel.

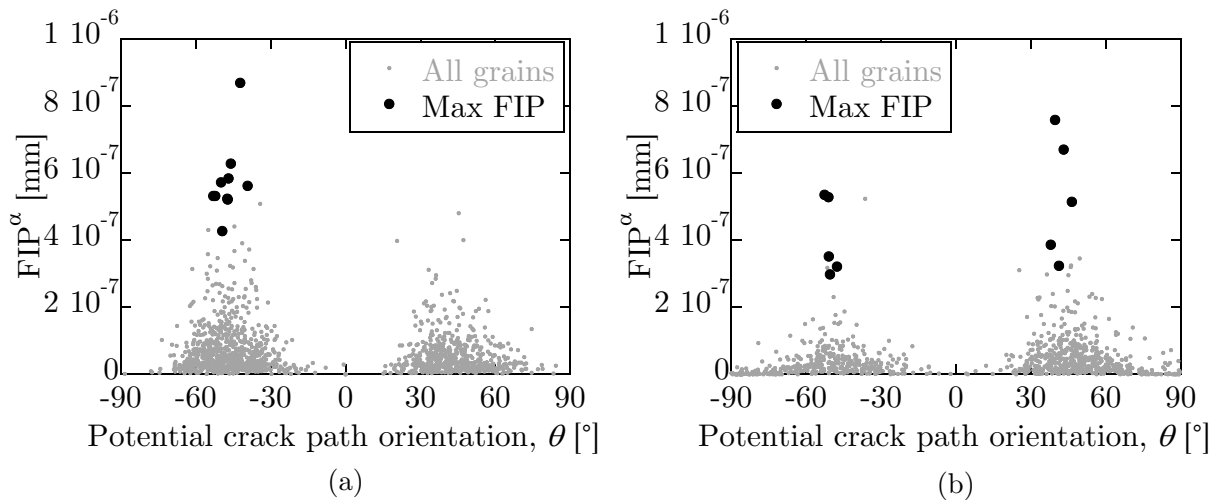


Figure IV.27 – Distribution of the maximum FIP per grain for all the microstructures against the orientation of the potential crack path for (a) α -iron and (b) FP steel.

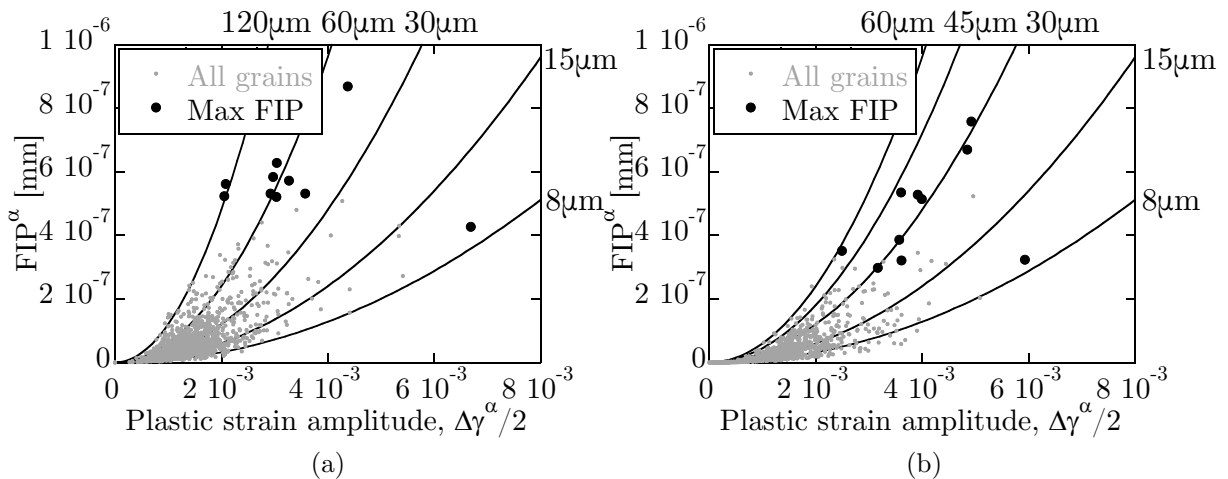


Figure IV.28 – Distribution of the maximum FIP per grain for all the microstructures against the orientation of the potential crack path for (a) α -iron and (b) FP steel.

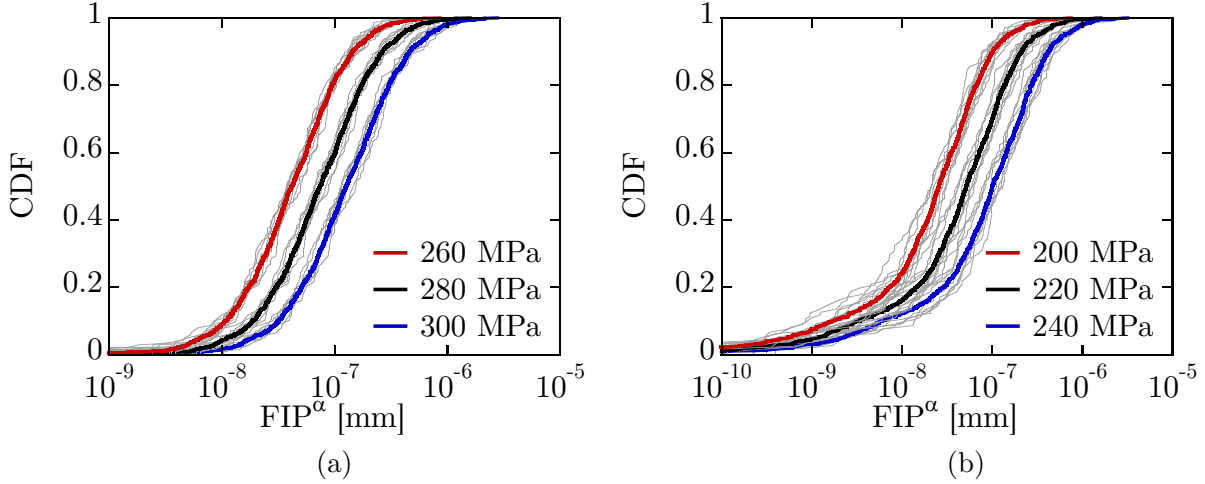


Figure IV.29 – Cumulative distribution of the maximum FIP per grain for all the microstructures for (a) α -iron and (b) FP steel.

Table IV.6 – Statistical data of the FIP distribution for the two materials and the different stress conditions.

	α -iron			FP steel		
Σ_{amp} [MPa]	260	280	300	200	220	240
Min [mm]	1.83e-14	4.89e-14	1.01e-13	2.32e-14	1.77e-13	1.32e-12
Max [mm]	8.69e-7	1.61e-6	2.81e-6	7.58e-7	1.62e-6	3.22e-6
Mean [mm]	6.77e-8	1.23e-7	2.13e-7	4.67e-8	8.64e-8	1.90e-7
STD [mm]	7.97e-8	1.50e-7	2.62e-7	6.84e-8	1.43e-7	2.83e-7
CV	1.18	1.21	1.23	1.46	1.49	1.49
Skewness	3.48	3.56	3.61	4.43	4.53	4.57

Analysis of crack initiation around the notch

The study finally focuses on the extreme value of the inverse FIP for each individual realization as an indicator of the number of cycles for crack initiation. From the results of the previous chapter, it was found that for these two materials under $R=-1$ stress ratio, all the micro-cracks leading to final failure directly appeared in the vicinity of the defect. However, it does not mean that the first crack to nucleate originates from the notch. It was indeed observed that several micro-cracks formed far from the notch but did not propagate. Consequently, it is decided to evaluate the extreme inverse FIP in the grains in direct contact with the notch. For each realization, the highest FIP on each side of the notch is extracted and reported in Fig. IV.30 (a) for the two materials and the different stress amplitudes. The mean values as well as one standard deviation scattering are represented in Fig. IV.30 (b). The statistical data of the extreme inverse FIPs are reported in Table IV.7.

First, it is observed that for similar mean values there is a difference of about 60-70 MPa between the two materials. It has to be compared with the experimental results in the previous chapter where a difference of 90 to 100 MPa could be observed for similar crack initiation lives. Considering the fact that no further calibrations except for the CP parameters were performed and that very few experimental data were obtained for each stress amplitude, these results are in relative good agreement. It is also noted that as the stress amplitude increases the extreme value distribution of the inverse FIP shifts to the left towards shorter fatigue lives. However, the sensitivity of the mean value against the stress amplitude seems to be constant. Indeed, analyzing microstructure by microstructure, one can note that the effect of the stress amplitude is always the same as the slope of the $S - FIP^{-1}$ curves is similar for each microstructure. This may be attributed to the boundary conditions which are invariant from one model to another. The slope of the $S - FIP^{-1}$ curve is also directly related to the square exponent in Eq. IV.2 which, combined with the fact that the hardening parameters of the CP model are identical, explains why the two materials exhibit similar trends. In fact, it was pointed out by Chan [35] that it may range from 1 to 2 depending on the strain-localization process and therefore on the stacking fault energy.

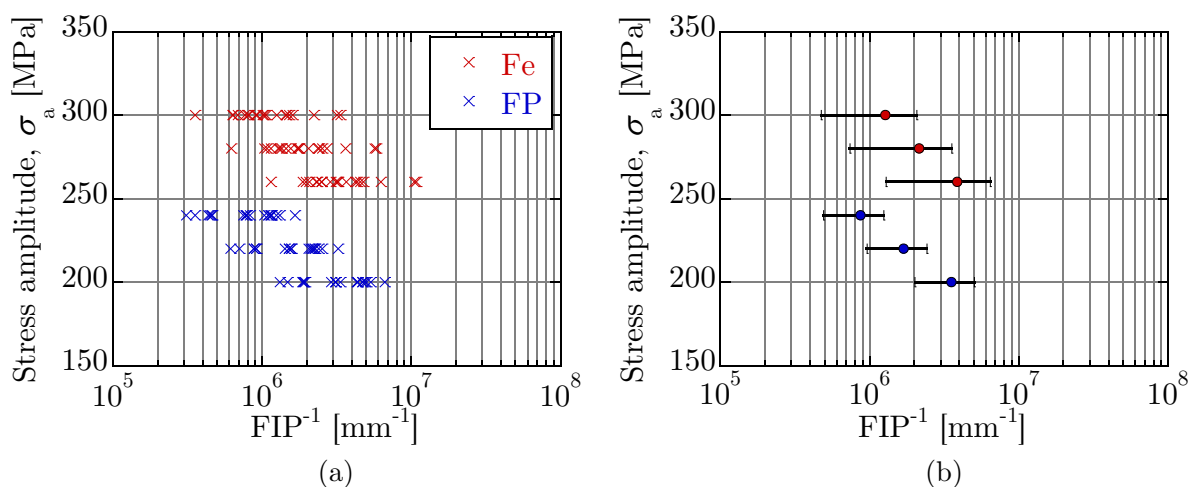


Figure IV.30 – (a) Distribution of the inverse extreme FIP for the two materials and different stress amplitudes. (b) Mean and standard deviation of these distributions.

Analyzing the dispersion, it is observed that the data scatter on about one order of

magnitude for α -iron while it is slightly lower for FP steel and does not seem to vary with the applied stress. The absence of sensitivity is logical since the extreme FIPs are found in the same location independently of the loading condition and since the CP parameters are always identical. Interestingly, this trend is contrary to the global behavior of the aggregates analyzed previously where it was found that the scattering was lower for α -iron. However, the reason behind this observation is different and may be attributed to the difference in grain size distribution. Indeed, considering Fig. IV.23 and IV.24, it was observed that fewer grains were in direct contact with the notch in the case of α -iron. Thus, the lower variability of the microstructure in the vicinity of the notch will therefore contribute to an increase in the dispersion of these FIPs.

Estimation of the Tanaka-Mura parameter

In this part, an estimation of the Tanaka-Mura parameter A defined in Eq. IV.1 is attempted.

The extreme inverse FIPs are first fitted to the generalized extreme value (GEV) distribution described in Chapter I using the maximum likelihood method and the software Matlab. The definition of the GEV is recalled here:

$$F(x|\mu, \sigma, \xi) = \begin{cases} e^{-(1+\xi(\frac{x-\mu}{\sigma}))^{-\frac{1}{\xi}}} & \text{if } \xi \neq 0, \forall x/\frac{x-\mu}{\sigma} > 0 \\ e^{-e^{-\frac{x-\mu}{\sigma}}} & \text{if } \xi = 0. \end{cases} \quad (\text{IV.26})$$

with μ , σ and ξ the location, scale and shape parameters, respectively. In opposition to Przybyla *et al.* [12–14, 159–161] who fitted the extreme values to the Gumbel distribution, assuming a shape parameter of zero, the extreme values are fitted without any constraint on the shape parameter. The parameters of the distribution as well as the coefficient of determination R^2 for the different materials and loading conditions are reported in Table IV.7. The CDF of these distributions are represented in Fig. IV.31 with the data from the simulations. The CDF are represented using a $\ln(\ln(1/F)^{-1})$ scale as when the GEV corresponds to the Gumbel distribution ($x_i = 0$), the CDF is a straight line. It is observed that the data are fitted with a relatively high confidence ($R^2 > 0.98$ and 0.95) suggesting that the GEV can be estimated with about 20 data points.

The shape parameters of the different distributions all differ from 0 suggesting that the Gumbel distribution is not necessarily the best choice of distribution. It can be observed that the shape parameter is always positive for α -iron and negative for FP steel. A physical explanation behind this difference is relatively complicated to give as these parameters are only the result of an optimization of likelihood. In fact, it seems more relevant to describe the shape parameters in term of confidence intervals. The 95% confidence interval (CI) of the shape parameters are also reported in Table IV.7. It is noticed that the confidence interval of ξ always contains 0 suggesting that a Gumbel type distribution may be a suitable candidate in each case. However, in both materials, the confidence interval shifts towards the negative domain with the increase of the stress amplitude meaning that in the case of FP steel, the distribution moves away from the Gumbel distribution.

4. SIMULATIONS OF STAGE I FATIGUE CRACKS IN NOTCHED POLYCRYSTALLINE AGGREGATES

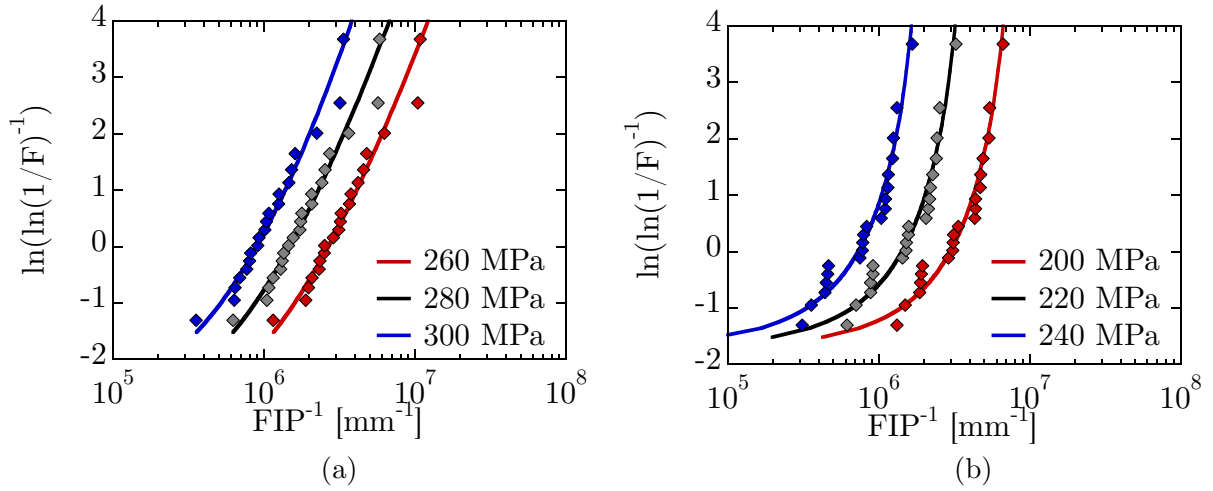


Figure IV.31 – Cumulative distribution of the maximum FIP per grain for all the microstructures for (a) α -iron and (b) FP steel.

Table IV.7 – Statistical data of the extreme inverse FIP and fitted parameters of the generalized extreme value distribution for the two materials and the different stress conditions.

	α -iron			FP steel		
Σ_{amp} [MPa]	260	280	300	200	220	240
Min [mm^{-1}]	1.15e6	6.22e5	3.56e5	1.32e6	6.17e5	3.11e5
Max [mm^{-1}]	1.08e7	5.83e6	3.35e6	6.65e6	3.24e6	1.67e6
Mean [mm^{-1}]	3.92e6	2.17e6	1.29e6	3.52e6	1.69e6	8.67e5
STD [mm^{-1}]	2.59e6	1.41e6	8.02e5	1.50e6	7.21e5	3.74e5
CV	0.662	0.652	0.623	0.425	0.427	0.432
ξ	0.300	0.291	0.252	-0.225	-0.224	-0.233
95% CI (lower)	-0.0532	-0.0633]	-0.0942	-0.646	-0.601	-0.605
95% CI (upper)	0.6526	0.645	0.599	0.196	0.1528	0.138
σ	1.24e6	6.99e5	4.26e5	1.40e6	6.76e5	3.52e5
μ	2.67e6	1.48e6	6.86e5	2.98e6	1.43e6	7.32e5
R^2	0.988	0.988	0.987	0.954	0.950	0.953

To evaluate the parameter A , we then define the following likelihood $L(A)$:

$$L(A) = f_A(N_1, \dots, N_p; A) = \prod_{i=1}^p f\left(\frac{N_i}{A} \mid \mu_i, \sigma_i, \xi_i\right) \quad (\text{IV.27})$$

where N_1, \dots, N_p are the experimentally measured crack initiation lives and μ_i, σ_i, ξ_i are the parameters of the GEV distribution f estimated numerically from the inverse FIPs at the stress amplitude $\Sigma_{amp}(N_i)$. Finally, we seek to find the value A that maximizes the likelihood as a simple optimization problem.

Since the simulations were not performed at all the stress amplitudes considered experimentally, the inverse FIPs for the missing stress amplitudes are first extrapolated based on the individual fitting of each inverse FIP to a power law (Fig. IV.32(a)). This assumption is relatively valid in uniaxial loading since we have shown that the location of crack initiation was the same at each stress amplitude and the inverse FIP varies smoothly. The purpose here is to simply use these additional data in order to obtain a better estimation of the parameter A .

Fig. IV.32(a) shows the normalized likelihood defined in Eq. IV.27 for the two materials data. Here it is assumed that the parameter A is dependent on the material. The maximum likelihood is found for a value of 0.144 and 0.037 mm.cycle for α -iron and FP steel respectively. It is worth noting that the likelihoods do not overlap significantly, suggesting that even though initiation occurs in ferrite grains in both case, a common Tanaka-Mura parameter for the two materials is relatively unlikely. Finally, Fig. IV.32(b) depicts the experimental and fitted crack initiation lives for the two materials. The difference in the estimated Tanaka-Mura parameter is directly related to the parameters of the constitutive models estimated in Chapter III. Indeed, the cyclic stress response of FP steel revealed almost no variation while significant softening was observed in α -iron. In this regard, the assumption made considering only a low hardening phase may be more suitable for FP steel than α -iron. Accordingly, the simulations may overestimate the actual plastic strain in the case of α -iron and therefore also overestimate the Tanaka-Mura parameter.

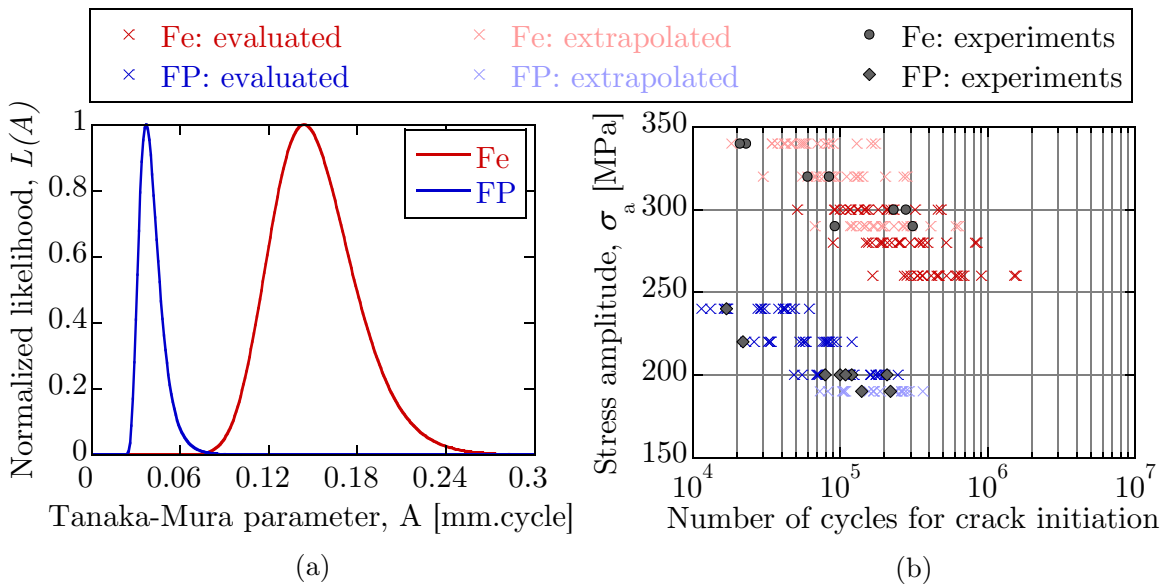


Figure IV.32 – (a) Likelihoods defined in Eq. IV.27 based on the experimental data of the two materials. (b) Experimental and fitted crack initiation lives for the two materials.

4.3.2 Analysis of crack propagation

In this section the results from the simulations of cracked microstructures are analyzed. Cracks were introduced on each side of the notch on the potential crack paths with the highest FIP. In the case of the FP steel, if the crack was in contact with a pearlite grain, it was extended to the nearest ferrite-ferrite grain boundary, assuming that the crack cannot propagate through the pearlite grains.

Analysis of slip activity

In order to compare the simulation results with those obtained in the previous section, the maximum plastic strain amplitude fields among the 12 available slip systems are again computed and reported in Fig. IV.33 and IV.34 for the same microstructures than in Fig. IV.23 and IV.24 and the same stress amplitudes. This way a comparison of a crack introduction effect can be carried out. The cracks are highlighted in black lines.

As expected, the introduction of a notch directly affects the strain distribution in its vicinity. Regions over and below the crack are completely relaxed from any stress and therefore do not develop any plastic deformation. On the other hand, regions near and ahead of the crack tips exhibit a significant increase in the plastic strain. It is observed that the shape of the plastic strain near the crack tip is not similar to that of a crack in an isotropic medium suggesting that the anisotropy introduced by the cubic crystal lattice and the orientation of the grains still has an influence. In most cases, the plastic strain is higher in the grain in contact with the crack tip but it is not a general conclusion. Indeed, observing the microstructure 4 in Fig. IV.33, one can notice that in the case of the right crack, the plastic strain in the grain in contact with the crack tip is unchanged compared to Fig. IV.23. In fact, the strain remained confined in the cracked grain which suggests in this case that the crack may be reflected at the grain boundary. Far from the cracks, the plastic activity shows the same intensity than in the case of the uncracked microstructure. The crack only affects the stress and strain distribution in its close neighboring which suggests that the proposed approach to reload a cracked microstructure with the initial internal state variables is relatively correct. However, it should be emphasized that the 2D simulation assumes a crack through the thickness, which most likely generates higher stresses ahead of the crack tip than for 3D simulations where only the first grain in the thickness is cracked. Finally, one can observe that in some cases, the plastic activity is higher in some grains not in direct contact with the crack suggesting that independent crack nucleation may occur. Two separate cases may be observed. In the first case, grains with high plastic strain already had such a strain in the simulations without crack. In the second case, the crack tip is located near a very small grain, and the second neighbor is actually affected by its presence (for instance the microstructure 6 in Fig. IV.34).

The locations and directions of the predicted paths for crack propagation are also represented in each microstructure by a straight red line. It is worth reminding that crack propagation is assumed to be transgranular. As can be seen, in most cases, the crack deflects from the initial direction. Obviously, it is directly attributable to the difference in crystal orientation between the two grains. It is also observed that the path does not always match the path of highest plastic strain amplitude since the trace of the slip plane is not parallel to such path. A more quantitative analysis of the influence of the cracks is given in the next section.

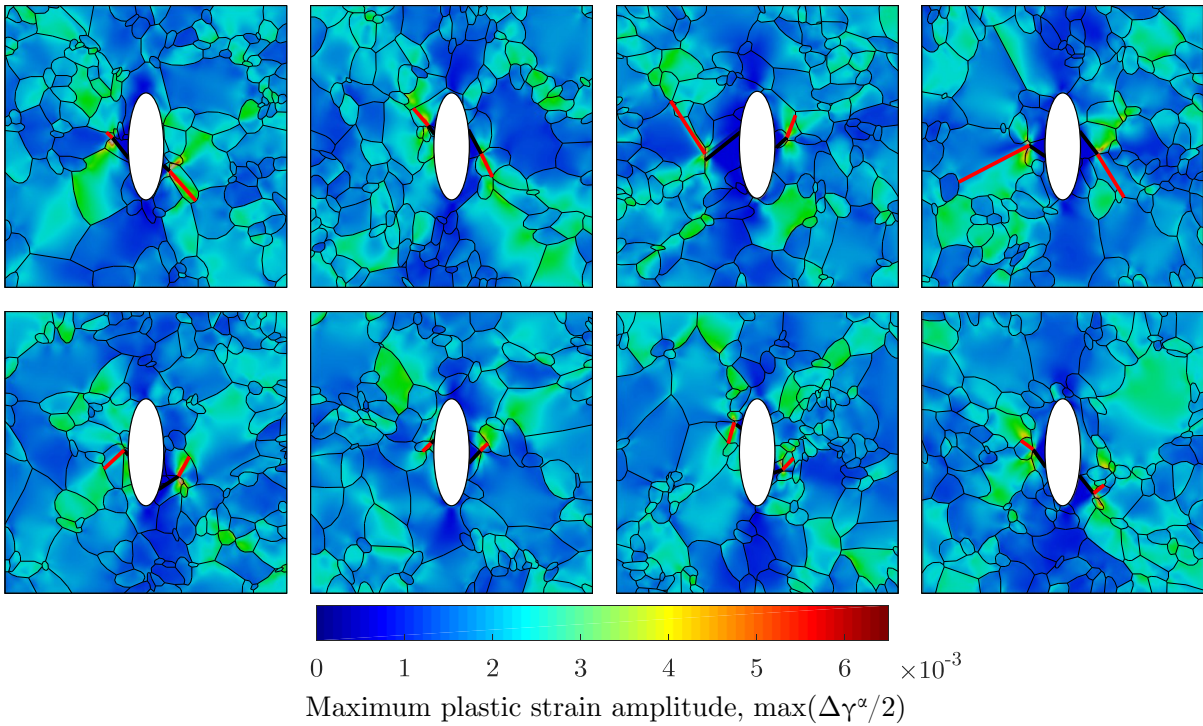


Figure IV.33 – Maximum plastic strain amplitude $\max_\alpha(\Delta\gamma^\alpha/2)$ accumulated in the last cycle among the 12 available slip systems for eight α -iron microstructures including cracks.

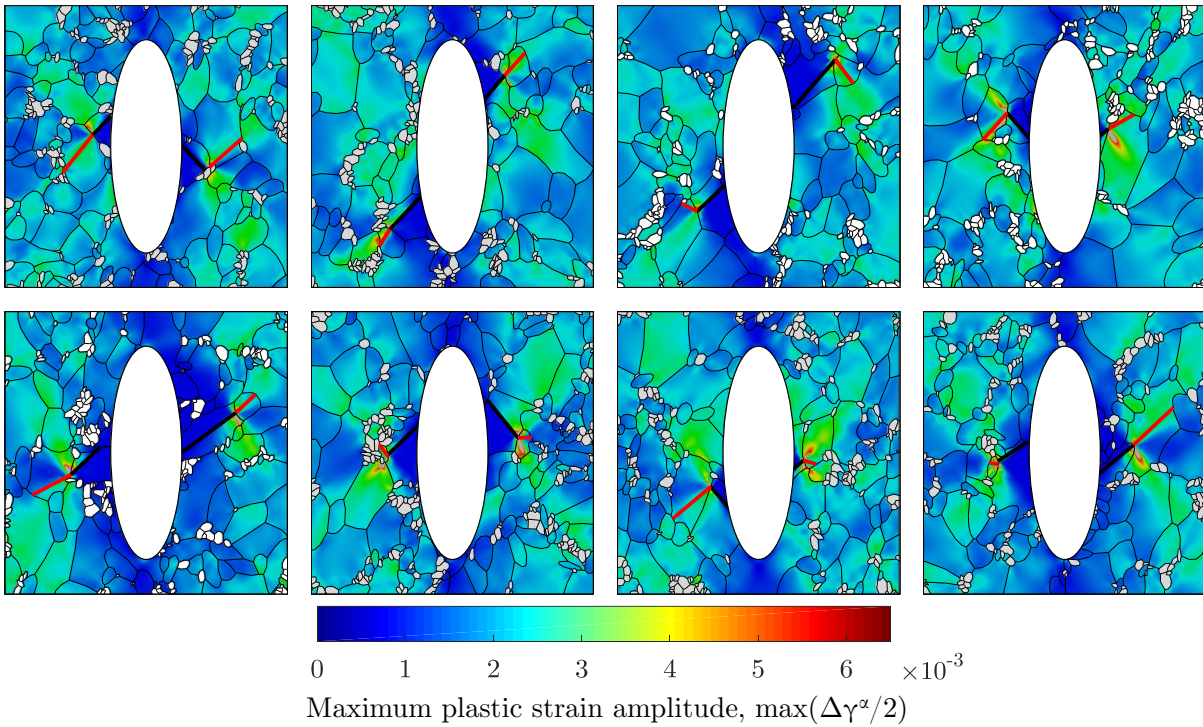


Figure IV.34 – Maximum plastic strain amplitude $\max_\alpha(\Delta\gamma^\alpha/2)$ accumulated in the last cycle among the 12 available slip systems for eight FP steel microstructures including cracks.

Evaluation of the grain boundary resistance

The study now focuses on the blocking character of the grain boundary. Since the lowest grain boundary resistance is almost always associated with the lowest twist angle, we particularly focus on this parameter. Fig. IV.35 shows the cumulative probability of the twist angles for the two materials and three different cases: all the slip systems in the grains in contact with the crack tip, the slip systems having the highest FIPs and the slip systems with the lowest resistance. In the same way, Fig. IV.36 represents the cumulative probability of the grain boundary resistance for the two materials and same three cases.

At first, it is noted that the twist angle is uniformly distributed in both materials. About 90% of the slip systems having the lowest resistance have a twist angle below 20°. Nonetheless, when considering the slip systems with the highest FIPs (blue lines), it does not always correspond to the slip system with the lowest twist angle and therefore the lowest grain boundary resistance. In fact, about 40% of the highest FIPs belongs to the slip planes with the lowest resistance. It is also observed that about 90% of the highest FIPs exhibit a twist angle below 40°. The jump in the cumulative distribution of the resistance is directly related to the equation of the resistance based on a Weibull distribution.

To explain the fact that a crack is predicted to propagate on a slip system which does not have the lowest resistance, it is interesting to look at the plastic strain accumulated on the crack path for the lowest resistance and for the one with the highest FIP. Fig. IV.37 shows the frequency distribution of the plastic strain amplitude, $\frac{\Delta\gamma^p}{2}$ for the three cases mentioned previously for α -iron and FP steel loaded at 260 and 200 MPa, respectively. It is noticed that the plastic strain ahead of the crack tip is still highly heterogeneous and mainly concentrated in few slip systems as the distribution of the plastic strain on all the available slip systems scatters on four orders of magnitude. Comparing the plastic strain distribution of the PCP with the highest FIP and with the lowest resistance, it is observed that for about 40% of the cases, the most active slip system matches the one with the lowest resistance. In the remaining 60%, the amplitude of the plastic strain is about 1 order of magnitude lower than for the highest FIP. Since the FIP defined in Eq. IV.18 involves the square of the plastic strain amplitude, a difference of two orders of magnitude may be observed. Compared with a difference of a factor 2 or 3 between the lowest and second lowest resistance, this shows that the plastic strain is still the main factor controlling the propagation path. This observation emphasizes the fact that the introduction of an explicit crack is crucial to correctly predict the propagation path. Finally, comparing the two materials with each other, no significant difference is found for the three studied parameters.

These observations need to be confronted to experimental results. Unfortunately, the literature is very scarce for this type of experiments and only FCC aluminum alloys data are available. In their work, Wen and Zhai [150, 152] measured the twist and tilt angle cracks in aluminum alloys and compared it to the slip plane having the lowest twist angle. They showed that in most cases, the cracks propagate on the slip plane with the lowest twist angle. However, in several cases, where two twist angles were close while the tilt angles were significantly different, the crack did not propagate on the lowest twist angle slip plane. This observation emphasized the fact that the tilt angle should contribute to the grain boundary resistance as proposed by Musinski [116]. Interestingly, the highest twist angle for a crack to propagate was found to be 47.3° which is very close to the one found in our simulations. Proudhon [153] enriched these results by also conducting

similar experiments on aluminum alloys. He concluded that a crack does not always propagate on the slip system with the lowest twist angle but sometimes on the second lowest twist angle among the four available slip planes in FCC lattice. By comparing the Schmid factors, he showed that the crack mainly propagates on the slip system with a high Schmid factor. Thus, he proposed to use a parameter based on the ratio of the Schmid factor with the twist angle to predict the crack propagation direction. One limitation of these studies concern the geometry of the grain boundary. Since only EBSD of the surface were available, it was assumed (as in our study) that the normal of the grain boundary belonged to the EBSD plane or in other words that the grain boundary was perpendicular to the specimen surface. This assumption is relatively valid in the case of rolled materials but might be wrong in a more random microstructure.

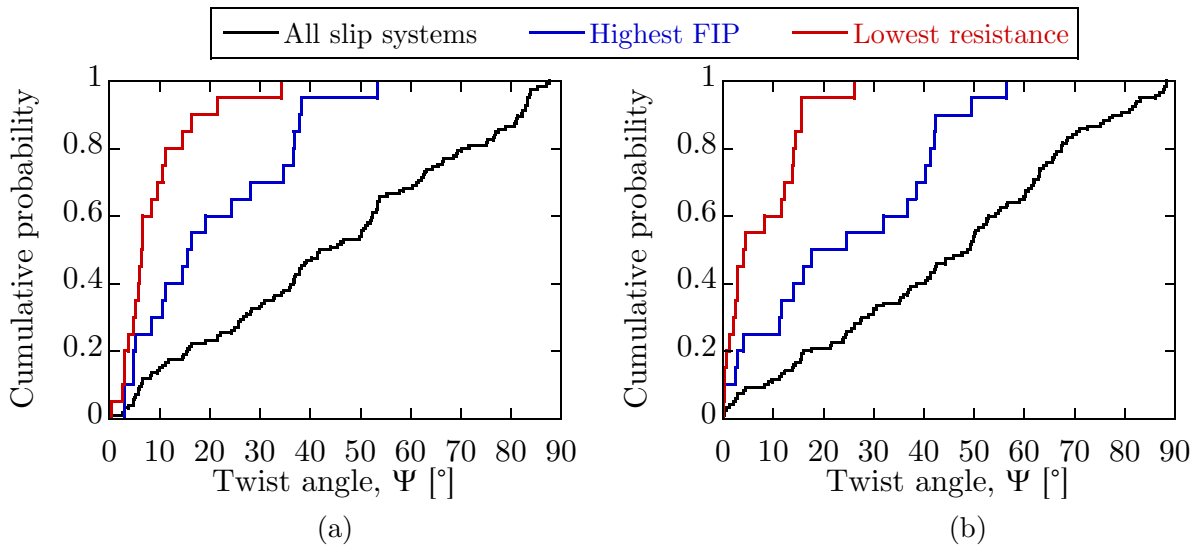


Figure IV.35 – Cumulative probability of the twist angle for all the slip systems, the highest FIP and the lowest resistance slip planes for (a) α -iron and (b) FP steel.

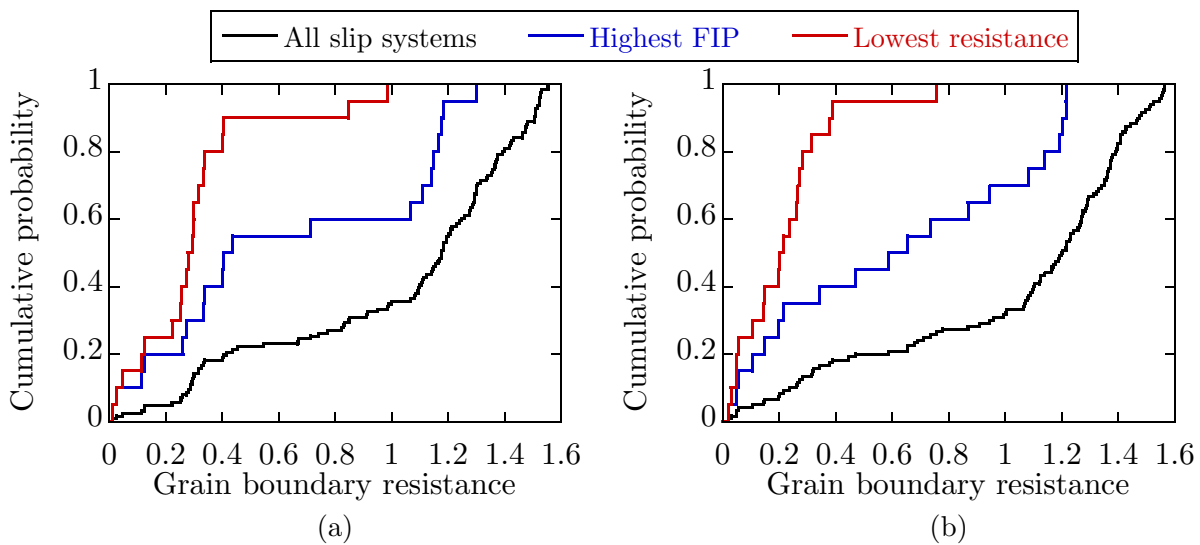


Figure IV.36 – Cumulative probability of the grain boundary resistance for all the slip systems, the highest FIP and the lowest resistance slip planes for (a) α -iron and (b) FP steel.

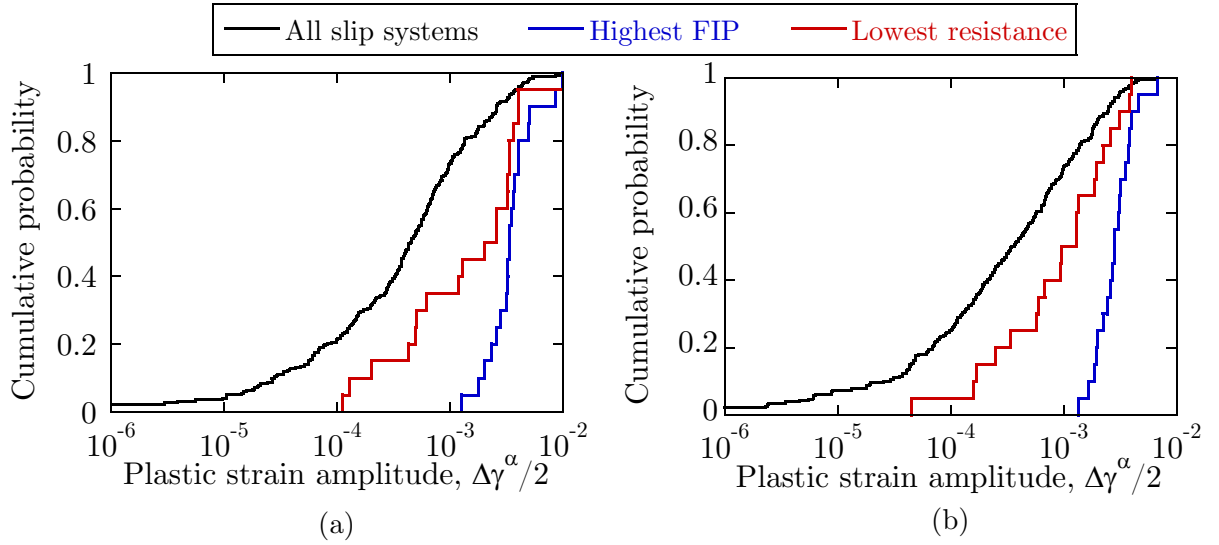


Figure IV.37 – Cumulative probability of the plastic strain amplitude $\frac{\Delta\gamma^\alpha}{2}$ for all the slip systems, the highest FIP and the lowest resistance slip planes for (a) α -iron and (b) FP steel.

Comparison of the inverse FIP for nucleation and blocking lives

In this part, the explicit value of the inverse FIP defined in Eq. IV.18 is discussed as a direct indication of the blocking time at the grain boundary. The value of the inverse FIP is compared with those from the previous section with uncracked microstructure. The sum of the inverse FIP for the nucleation and blocking time at the first grain boundary is also calculated. The crack growth rate will be evaluated in the next section. It is worth reminding that the sum corresponds to a sum within the same microstructure meaning that a crack may have a long initiation life and a short blocking time and vice versa.

Fig. IV.38 depicts the cumulative probabilities of the inverse FIPs for α -iron and FP steel subjected to a stress amplitude of 260 and 200 MPa, respectively. It can be observed that the blocking time scatters on about 3 and 2 orders of magnitude for the two materials. In about 50% of the case for α -iron and 30% for the FP steel, the blocking time at the grain boundary is much lower than the initiation life meaning that the crack easily crosses the grain boundary. In the remaining cases, the values have similar orders of magnitude. When summing the two inverse FIPs, the distribution are naturally shifted to higher values. The dispersion seems to increase in FP steel.

Table IV.8 summarizes the statistical data for the two materials and the different loading conditions. The data for the initiation life from the previous section are also reported for convenience. Looking at the coefficient of variation, it is observed that the retardation time shows a higher scattering than the initiation life. When summed with the initiation life, the scattering is reduced but still higher than the initiation alone. However, this observation is incomplete if we do not consider the propagation within the first grain.

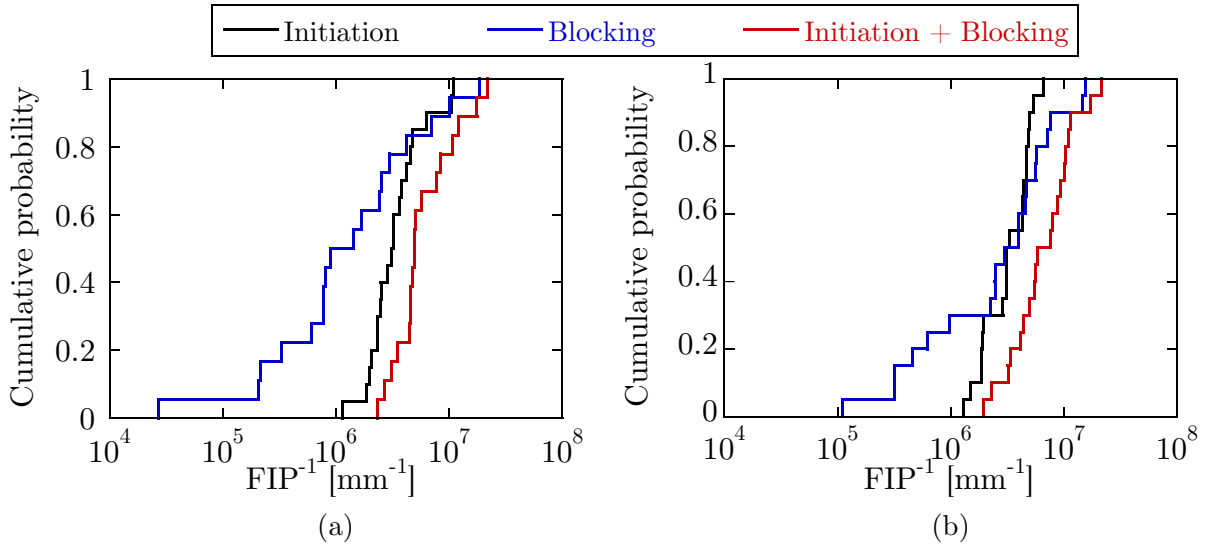


Figure IV.38 – Cumulative probability of the inverse FIP for (a) α -iron and (b) FP steel.

Table IV.8 – Statistical data of the extreme inverse FIP for crack initiation, retardation and the sum of both for the two materials and the different stress conditions.

		α -iron			FP steel		
	Σ_{amp} [MPa]	260	280	300	200	220	240
Initiation	Min [mm ⁻¹]	1.15e6	6.22e5	3.56e5	1.32e6	6.17e5	3.11e5
	Max [mm ⁻¹]	1.08e7	5.83e6	3.35e6	6.65e6	3.24e6	1.67e6
	Mean [mm ⁻¹]	3.92e6	2.17e6	1.29e6	3.52e6	1.69e6	8.67e5
	STD [mm ⁻¹]	2.59e6	1.41e6	8.02e5	1.50e6	7.21e5	3.74e5
	CV	0.662	0.652	0.623	0.425	0.427	0.432
Retardation	Min [mm ⁻¹]	2.72e4	1.56e4	1.23e4	1.12e5	5.12e4	2.78e4
	Max [mm ⁻¹]	1.87e7	1.10e7	7.14e6	1.55e7	1.02e7	6.01e6
	Mean [mm ⁻¹]	3.35e6	1.71e6	1.26e6	4.35e6	2.31e6	1.41e6
	STD [mm ⁻¹]	4.81e6	2.68e6	1.72e6	4.35e6	2.56e6	1.60e6
	CV	1.43	1.56	1.37	1.00	1.11	1.13
Sum	Min [mm ⁻¹]	2.35e6	1.30e6	7.79e5	1.96e6	9.86e5	5.06e5
	Max [mm ⁻¹]	2.19e7	1.27e7	8.21e6	2.13e7	1.11e7	6.47e6
	Mean [mm ⁻¹]	7.27e6	3.88e6	2.54e6	7.87e6	4.00e6	2.28e6
	STD [mm ⁻¹]	5.21e6	2.96e6	1.91e6	4.97e6	2.70e6	1.70e6
	CV	0.716	0.762	0.751	0.631	0.675	0.744

Evaluation of crack growth through the first two grains

In this section, we attempt to calculate the crack growth rate in the first two encountered grains based on Eq. IV.11. The crack growth rate model is recalled here:

$$\frac{da}{dN} = B(\Delta\gamma^\alpha)^n (d - a)^{1-\beta} a^\beta \quad (\text{IV.28})$$

Three parameters need to be calibrated: B , n and β . As described in the first section, the parameter β controls the shape of the crack growth rate and therefore the shape of the crack length against the number of cycles. The longest propagation time is found for $\beta = 0$ or $\beta = 1$ while the shortest propagation is for $\beta = 0.5$ where the growth rate is symmetric around $a = d/2$. In this study the parameter is set to 0.6. The parameter n gives the sensitivity to the strain rate and is often equal to 1. Finally the parameter B is set so that most of the crack growth rates are between 10^{-7} and 10^{-6} mm/cycle, $B = 1.0 \times 10^{-2}$. Here again, the purpose is not to get a precise prediction of the crack growth rate but rather to estimate the contribution of the crack propagation in the first few grains on the fatigue life and its variability.

Fig. IV.40 and IV.41 shows the crack growth rate against the crack length of the microstructure shown in Fig. IV.33 and IV.34 for α -iron and FP steel under a stress amplitude of 300 and 200 MPa, respectively. The long crack growth model used in the previous chapter is also reported on each graph. The crack length corresponds to the horizontal extension of the crack added with half the ellipse minor axis. Varying the stress amplitude naturally shifts the growth rate vertically but does not change the shape of the curves since cracks are predicted to propagate on the same path independently on the load level. The following observations are therefore general.

Two types of scattering may be observed on these graphs. The vertical scattering translates a difference in crack growth rate and is mainly related to the amplitude of the plastic strain on the slip path ahead of the crack tip. The horizontal scattering translates a variability in the microstructure as the crack may initiate in a large grain to then propagate in a small grain, and vice versa. From the length reached by the cracks after having encountered two grains, it seems that in average, two to four grains are needed to reach the long crack growth regime which is in agreement with the number of oscillations observed experimentally. It is observed that past the first grain boundary, the driving force for a crack to propagate may increase, be similar or may even be much lower than for the first grain. These results are consistent with the results obtained by Castelluccio and McDowell [112] who showed that the Fatemi-Socie FIP to quantify the driving force for crack propagation tends to be lower in the second grain than in the grain where the crack originally nucleated. Comparing the two materials with each other, it seems that for the stress amplitudes of 300 and 200 MPa the cracks propagate at a relatively similar rate. This suggest that for these conditions, the two materials should exhibit relatively close fatigue life. These ascertainment are independent of the parameter used which emphasizes the idea that the simulation of cracked microstructures can also be used as a comparative tool.

Fig. IV.39 shows the fatigue lives for the two materials after the crack has propagated through two grains. Table IV.9 summarizes the statistical data of these results. Overall, the fatigue lives at 300 and 200 MPa for α -iron and FP steel respectively are in relatively good agreement with experimental results. Analyzing the coefficient of variations of the fatigue lives in the end of the simulations with that for crack initiation in Table IV.7,

it is observed that the scattering tends to increase for the two materials. From the results in Table IV.8 this variation in scattering is directly attributable to the retardation at the first grain boundary. For high stress amplitudes, the fatigue lives for FP steels are overestimated meaning that the model is not conservative enough. Experimentally, for these stress conditions, crack propagation is not controlled by the growth of a single crack but by the growth and coalescence of several cracks which greatly reduces the total fatigue life of the specimens. It emphasizes a limitation in the critical plane approach as it seems to be limited to HCF regime. Indeed, for LCF conditions, several slip systems may be activated within a grain and demonstrate equivalent plastic strain amplitude. However, the different models assume an independent contribution of each individual slip system towards the initiation and propagation of micro-cracks. Also, in this study, crack propagation was only assumed to be transgranular and intergranular crack propagation was not considered. However, steels often exhibit both types of propagation. Perhaps, instead of being blocked at a grain boundary a crack may propagate faster in the grain boundary if the resistance is lower on this path. In this regard, introducing a parameter to comparatively quantify the competitive mechanisms between transgranular and intergranular crack propagation would certainly improve the results. However, theoretical or empirical models for intergranular crack propagation are currently lacking compared to the transgranular ones.

Table IV.9 – Statistical data for the fatigue lives after a propagation across two grains.

		α -iron			FP steel		
	Σ_{amp} [MPa]	260	280	300	200	220	240
MSC	Min [mm^{-1}]	4.05e5	2.38e5	1.5e5	1.57e5	9.5e4	6.04e4
	Max [mm^{-1}]	3.27e6	1.92e6	1.25e6	9.58e5	5.06e5	3.17e5
	Mean [mm^{-1}]	1.14e6	6.30e5	4.21e5	3.89e5	2.17e5	1.36e5
	STD [mm^{-1}]	7.65e5	4.38e5	2.84e5	2.05e5	1.14e5	7.53e4
	CV	0.671	0.696	0.675	0.528	0.525	0.555

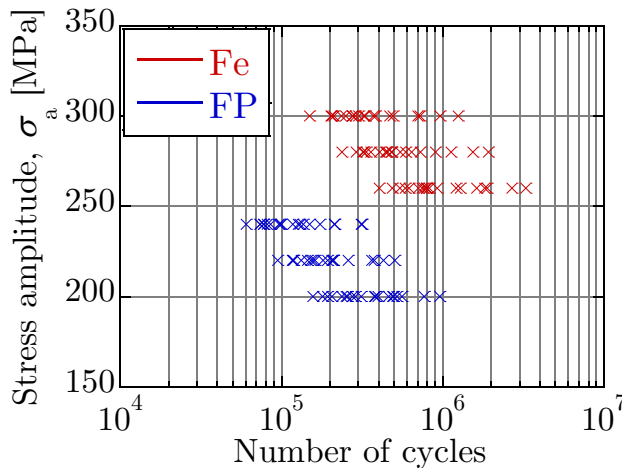


Figure IV.39 – Fatigue lives after a propagation across two grains.

4. SIMULATIONS OF STAGE I FATIGUE CRACKS IN NOTCHED POLYCRYSTALLINE AGGREGATES

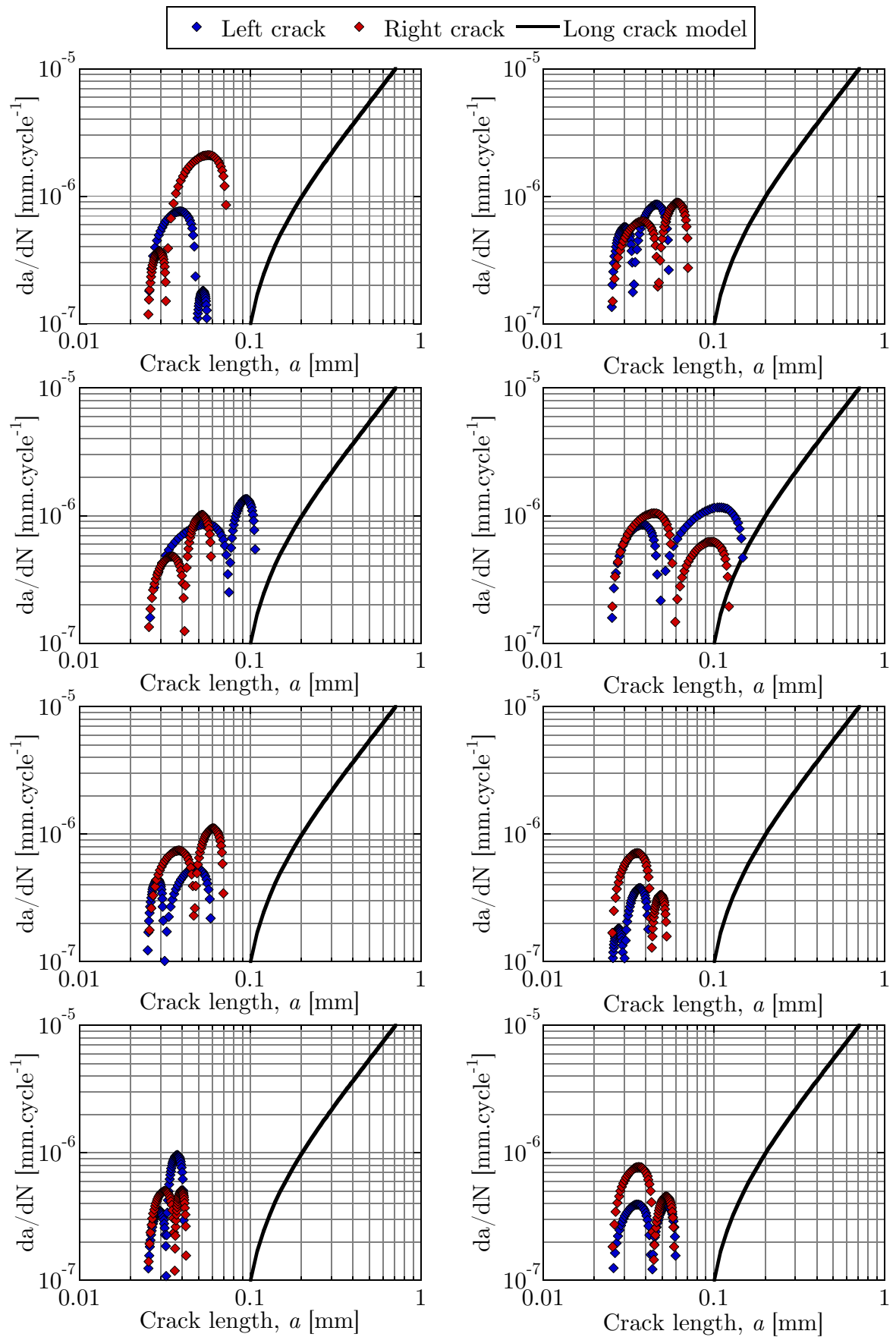


Figure IV.40 – Fatigue crack growth rates against the crack length for the eight α -iron microstructures in Fig. IV.33 subjected to a stress amplitude of 300MPa.

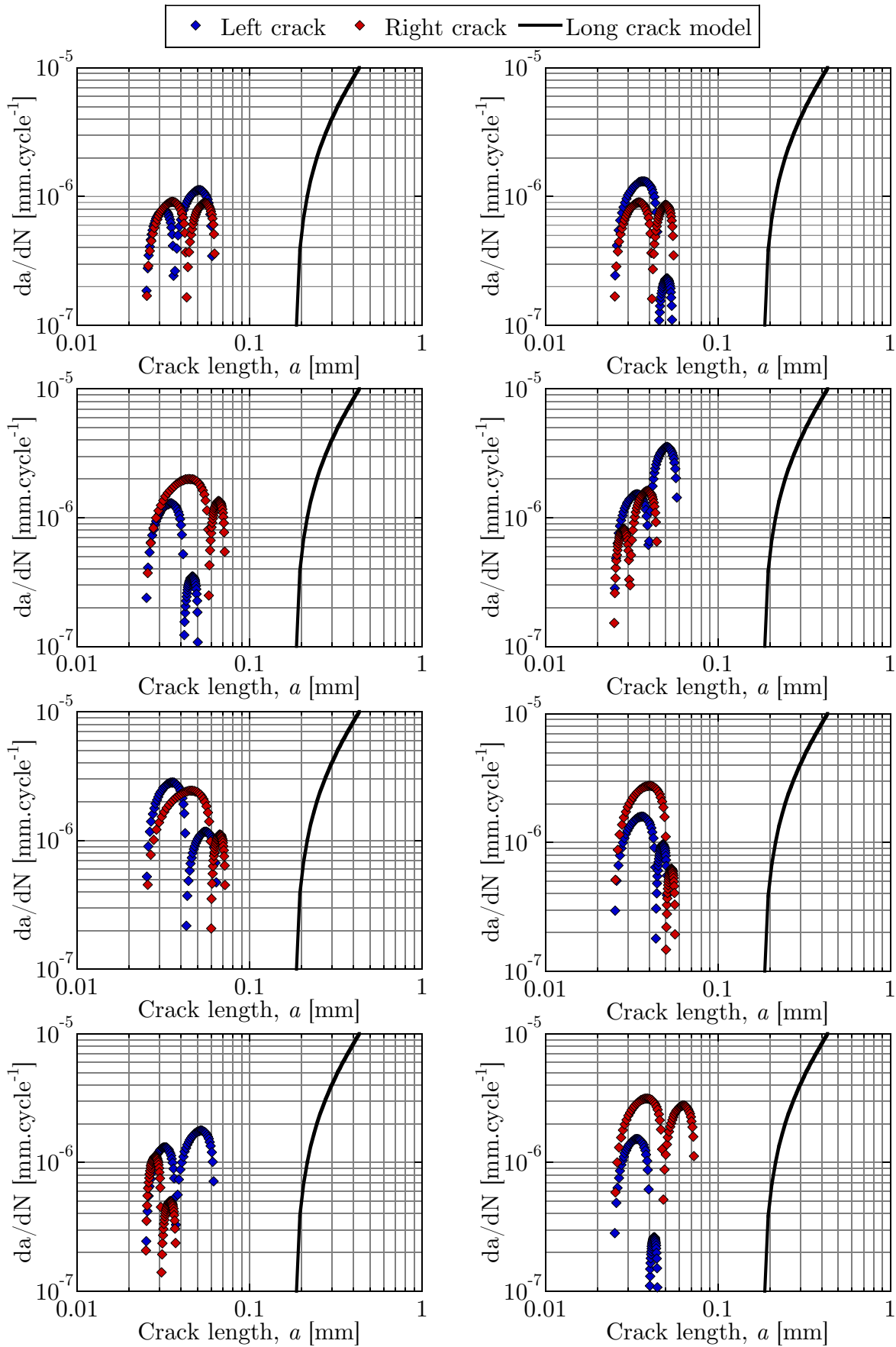


Figure IV.41 – Fatigue crack growth rates against the crack length for the eight FP steel microstructures in Fig. IV.34 subjected to a stress amplitude of 200MPa.

4.4 Conclusions

This section was dedicated to the simulations of notched microstructures meant to reproduce the geometry and loading conditions of the experiments conducted in the previous chapter for α -iron and FP steel. Two types of simulations were performed in order to evaluate the influence of the microstructure on the propagation of microstructurally short cracks: uncracked and cracked microstructures. The following concluding remarks may be drawn from the simulations of uncracked microstructures:

- In presence of a notch, the mechanical response of a polycrystal is still strongly affected by microstructural features as regions far from the notch may exhibit similar or even higher deformations than the grains in direct contact with the notch.
- The critical plane FIP based on the Tanaka-Mura model was evaluated for the two materials at different stress amplitudes. Overall the prediction made based on the inverse FIP are in good agreement with experimental results. Such FIP may be used as a comparative tool for the estimation of the fatigue performances and a quantification of the scattering related to the variability of the microstructure.
- A method was proposed to estimate the Tanaka-Mura parameter based on the fitting of the numerical data to GEV distribution and the application of the maximum likelihood method.

The following concluding remarks may be drawn from the simulations of cracked microstructures:

- The introduction of micro-cracks in the microstructure seems to only affect the grains in direct contact with the cracks as the plastic strain far from them showed similar amplitude than in uncracked microstructures. It was observed that the intensity of the plastic strain ahead of the crack front is sometimes lower than in some other grains suggesting that the microstructure still has a significant influence even in presence of crack. This also suggests that in some cases propagation may be governed by the nucleation and coalescence of several cracks rather than the propagation of a single crack.
- The FIP for the crack retardation at the grain boundary mainly predicted a propagation on a slip system with relatively low twist angle and high plastic strain. However, the slip system did not always correspond to the lowest twist angle highlighting the necessity to explicitly model cracks in order to consider the stress redistribution ahead of the crack tip.
- A comparison between the inverse FIP for nucleation and blocking time was proposed. It was shown that the number of cycles to overcome the first grain boundary may be of same order of magnitude or even higher than for the nucleation of the initial crack.
- Short crack growth rates were evaluated for cracks up to two grains. The growth rate in the second grain was found to vary significantly from microstructure to microstructure.
- Fatigue lives in the end of the simulations were qualitatively compared with experimental results. Prediction at high stress amplitudes are relatively not conservatives which highlights a limitation in the critical plane models applied here.

5 Investigation of the strain localization in martensitic microstructure under fatigue conditions

5.1 Introduction

From the microstructural characterization in the second chapter, it was observed that all the materials subjected to the first thermal treatment were nearly 100% martensitic steels. EBSD analyses revealed extremely large prior austenite grains and relatively well defined packets and blocks that could be quantified by the ellipse fitting procedure. High-cycle fatigue experiments showed clear crystallographic facets suggesting that the microstructure also has an significant role in martensitic steel.

In literature, martensitic polycrystals are often modeled with a single scale of heterogeneity, either prior grain austenite or packets [162] and relatively few studies focused on the influence of the lower scales of heterogeneity [163], especially on fatigue crack initiation. Accordingly, the last study focuses on lath martensitic steels and more specifically on the morphological and crystallographic effect of packets and blocks within prior austenite grains on fatigue crack initiation.

5.2 Description of the numerical models

The modeling of martensitic steels follows the multi-scale procedure developed in the second chapter. Two types of geometrical models are considered in this study: microstructures considering only prior austenite grain and packet boundaries and identical microstructures with additional block boundaries included. For ease of describing the results, microstructures considering only packets are referred as P and those considering both packets and blocks are referred as B . The models consist in $1500 \times 1500 \mu\text{m}$ square domains. The prior austenite grain size follows the one of the B14-10 steels studied in the second chapter. In average, each domain is composed of 15 prior austenite grains. Each grain is then decomposed into domains representing packets with about 7-10 packets for the largest grains and 2-3 for the smallest. Since the phenomenological crystal plasticity model does not consider any size effect, the size of the blocks naturally does not have any influence on the plastic strain. Therefore, to avoid unnecessary mesh refinement, blocks are arbitrarily described as ellipses with a major axis of $100 \mu\text{m}$ and a minor axis of 10 to $15 \mu\text{m}$. The direction of the blocks is set to be parallel to the $[10\bar{1}]_\gamma$ or $[01\bar{1}]_\gamma$ direction knowing the crystal orientation of the prior austenite grain. In average, each model is composed of about 50 packets and 700 blocks. In the models without blocks, the orientations of the packets are randomly selected among the 6 variants of one of the 4 possible habit planes while for the blocks, all the variants of a given habit plane are represented within a packet. Fig. IV.42(a) and IV.42(b) show an example of martensitic microstructure without and with block boundaries. 10 unique microstructures were generated with and without block boundaries.

The microstructures are then reconstructed in the FE software with custom-made python scripts and meshed with four-node plane strain elements (CPE4) having an average element size of $10 \mu\text{m}$. Fig. IV.42(c) and IV.42(d) depict the mesh of the reconstructed microstructures without and with block boundaries. An average of 30,000 elements is used in each model. Between one to five elements are used to mesh the width of each block. Due to strong sharpness of the block boundaries, about 4% of the elements are distorted

5. INVESTIGATION OF THE STRAIN LOCALIZATION IN MARTENSITIC MICROSTRUCTURE UNDER FATIGUE CONDITIONS

in B microstructures. The parameters of the CP model calibrated for the B14-10 steel are used in this study.

The models are loaded in fully reversed tension-compression in the y -direction with a stress amplitude of 300MPa for 10 cycles. It is modeled by imposing a displacement $U = 0$ to the lower or left edge of the aggregate and a cyclic macroscopic stress $\Sigma(t) = \Sigma_{amp} \sin(0.4\pi t)$ to the upper. To prevent rigid body motion, the displacement of the bottom left corner is also constrained. The results are analyzed using the last loading cycle of the simulations.

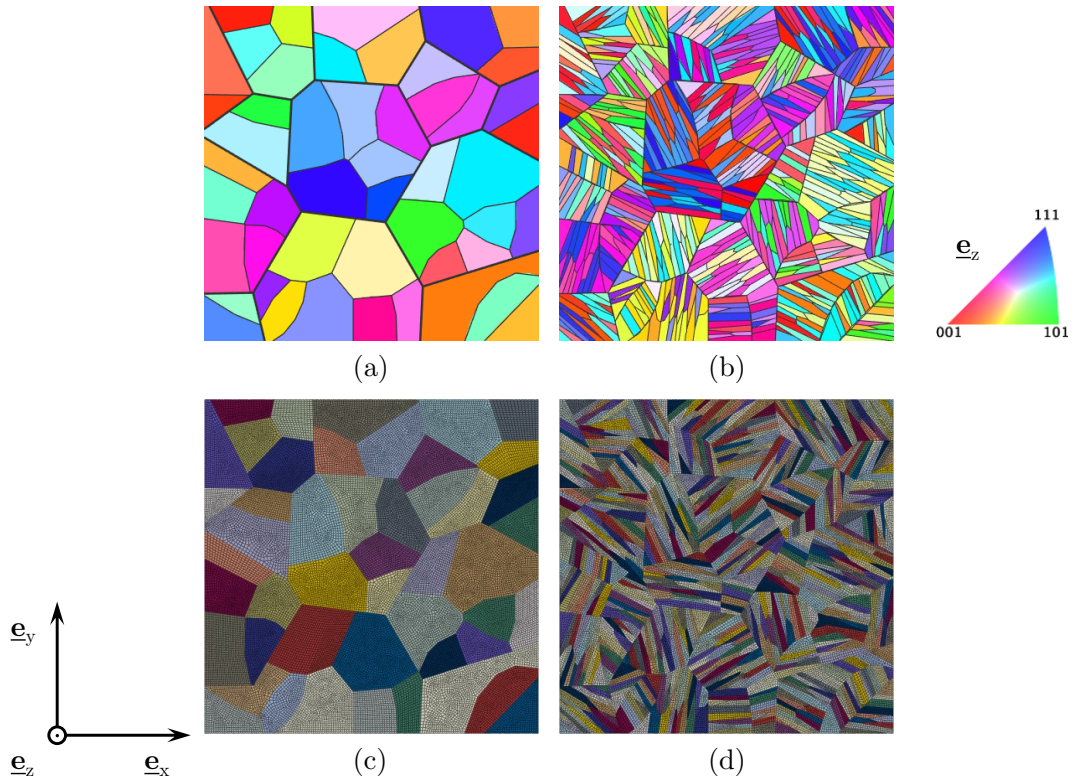


Figure IV.42 – Martensitic microstructure considering (a) prior austenite and packet boundaries, (b) prior austenite, packet and block boundaries.

5.3 Results and discussion

5.3.1 Comparison of the strain partitioning

The study focuses first on the comparison of the plastic strain distribution when considering or not the block boundaries. Fig. IV.43 and IV.44 display the maximum plastic strain amplitude distribution among the twelve available slip systems for eight different microstructures with and without block boundaries. The scale is bounded to 2.5×10^{-4} to ease the observation of the intragranular heterogeneity of the plastic strain. Parts appearing in gray exhibit a plastic strain over the upper bound of the scale. It is worth reminding that the absolute value of the plastic strain is most certainly overestimated especially when modeling blocks since the CP model lacks of size effect. The main purpose here is to assess how modeling hypotheses affect the strain distribution and therefore the value of a given criterion.

The plastic strain distribution reveals a significant heterogeneity from microstructure to microstructure, within packets of a same grain and finally between blocks of a same packet. It is noted on the one hand that when a packet exhibits a high plastic activity in P models, blocks sharing the same crystal orientation will also have a high plastic activity emphasizing here again the importance of the crystal orientation. On the other hand, blocks of packets with low plastic strain in P may still show a relatively high plastic activity. Indeed, P microstructures are equivalent to modeling a single large block per packet which will therefore correspond to one of 6 possible variants of the same habit plane. If the selected variant is poorly oriented, then no plastic flow may occur in this packet as the five remaining variants are not present. Since the 6 variants are represented in B microstructures, it is more likely to have at least one of them active.

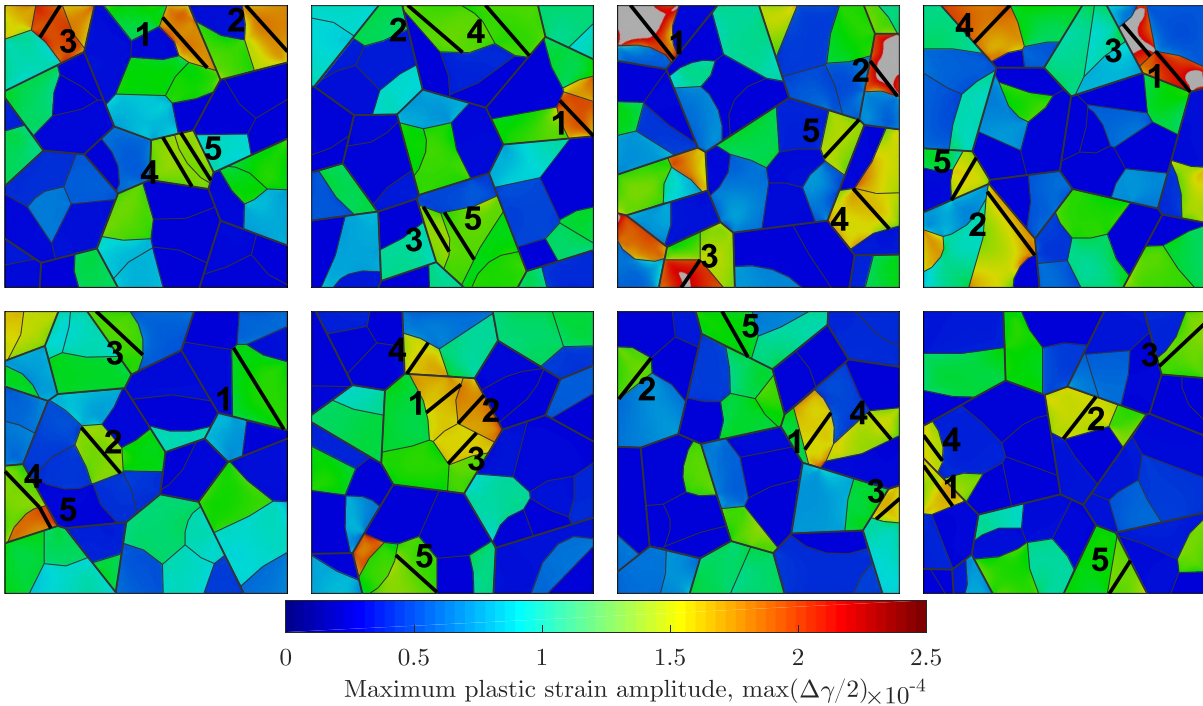


Figure IV.43 – Maximum plastic strain amplitude $\max_{\alpha}(\Delta\gamma^{\alpha}/2)$ accumulated in the last cycle among the 12 available slip systems for eight P microstructures.

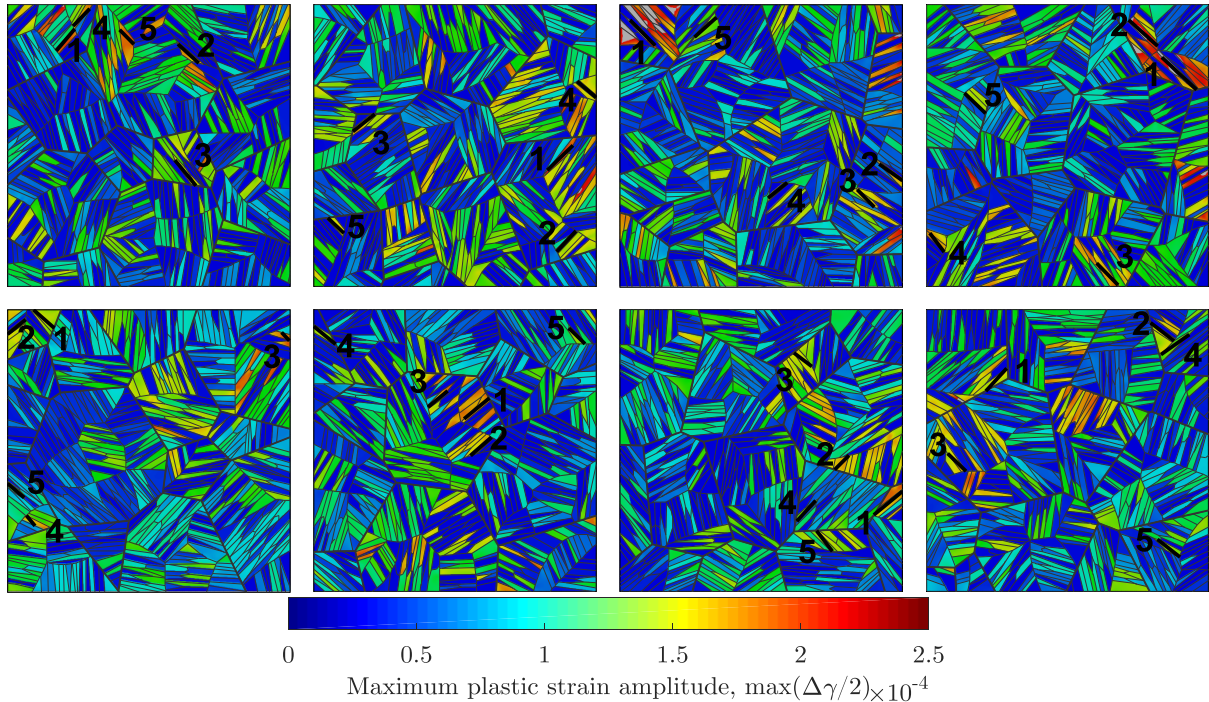


Figure IV.44 – Maximum plastic strain amplitude $\max_{\alpha}(\Delta\gamma^{\alpha}/2)$ accumulated in the last cycle among the 12 available slip systems for eight B microstructures.

5.3.2 Influence of the Schmid factor

To further investigate the effect of crystal orientation on plastic deformation, the Schmid factor maps of the eight B microstructures in Fig. IV.44 are represented in Fig. IV.45. They were produced by calculating the maximum Schmid factor among the 12 available slip systems in a custom-made Matlab script. As can be seen, blocks with high plastic activity tend to show a high Schmid factor and conversely. This shows that the Schmid law is relatively well applicable for martensitic steels, at least for two-dimensional models under uniaxial loading. Slight discrepancies may be observed in blocks near the upper and lower edge of the domain most likely due to the boundary conditions. The crystal orientation within martensite packets seems therefore to play a major role in the strain localization.

This conclusion emphasizes a major limitation in modeling only packets boundaries as it may overestimate the actual plastic strain if the variant selected corresponds to the one with the highest Schmid factor, or on the opposite, may underestimate it if the selected variants have a low Schmid factor. It seems indeed that at least one or two variants per packet show a significant plastic activity so that strain distribution appears better distributed in B microstructures.

5.3.3 Location of crack initiation

The procedure to evaluate the location of crack initiation based on the critical plane application of the Tanaka-Mura model was also used here. Since in the FE software no difference exists in the definition of grain, packet or block domain, the procedure evaluates the FIP in each block independently as if they were single grains. Therefore, it is possible and actually very likely that several blocks within the same packet have the highest FIP. Accordingly, it was decided to consider only the highest FIP per packet to simplify the

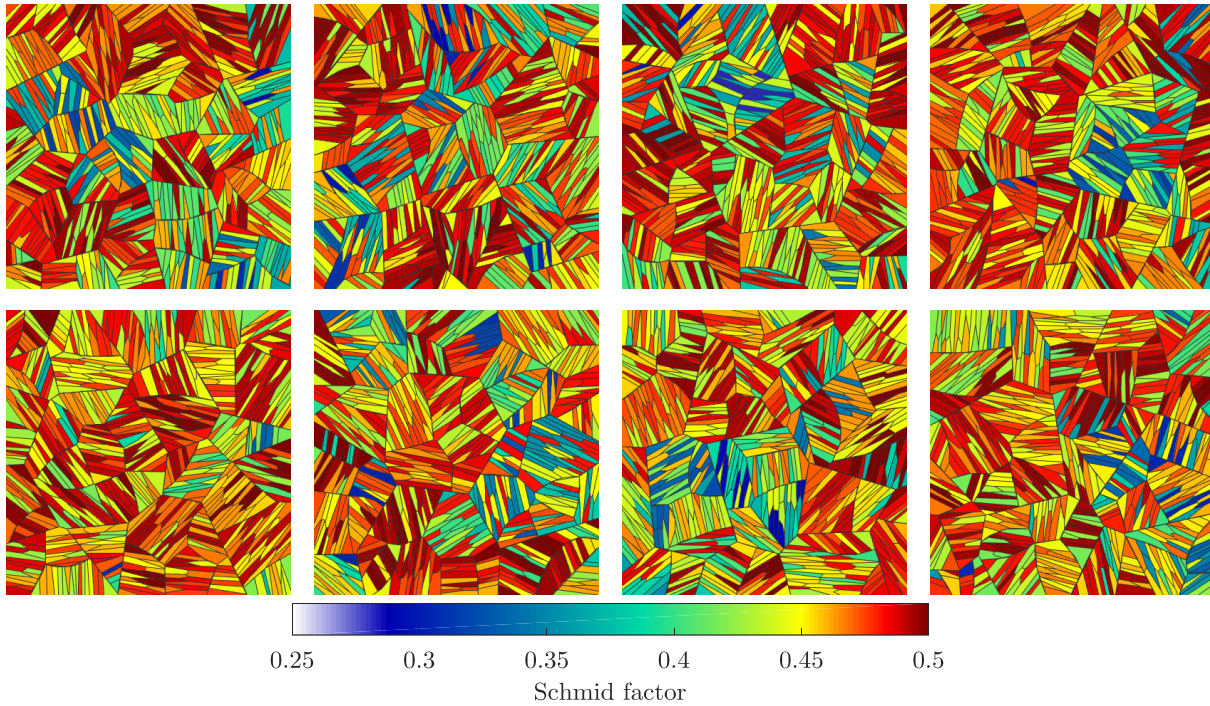


Figure IV.45 – Schmid factor map for the eight B microstructures represented in Fig. IV.44.

comparison with P microstructures.

The location of the five potential crack paths having the highest Tanaka-Mura FIP are displayed in Fig. IV.43 and IV.44 for the different microstructures. Similar observations than the one in the two previous sections can be made from the location and direction of the PCPs in P microstructures. The interesting point here is to observe the differences in location and orientation between P and B models. Two different cases may be observed. On the one hand, the position and orientation can be very close between the two models when the active slip system is the one having its slip plane trace parallel to the block direction (for instance in microstructures 3 and 4 for the highest FIP). On the other hand, P models will always predict crack initiation in the largest and most activated packets such as in microstructure 6. However, in this case the block direction and slip plane trace do not match leading to a different predicted location for crack initiation even if the plastic strain in these blocks is very high.

By not considering the block boundaries in P microstructures, the PCPs are just limited by the packet boundaries. Therefore, the relationship between the variant morphologies and orientations, inherent to lath martensite is lost. This highlights a second limitation in not considering block boundaries in martensitic microstructures. It is worth saying that the critical plane FIP only predicts transgranular (or in this case trans-block) crack initiation. However, as emphasized by Tanaka and Mura [33], several parallel slip bands may pile up dislocations on the same grain boundary leading to intergranular crack initiation. This behavior is not currently accounted in the developed procedure. Nonetheless, in both cases the crack is predicted to be parallel to block boundaries.

5.3.4 Quantitative evaluation of the Tanaka-Mura FIP

Fig. IV.46 depicts the cumulative probability of the Tanaka-Mura FIP for the two models. The highest FIP per packet is considered in each case. Fine lines represent

individual aggregates and bold lines represent all the data combined. Between 40 to 50% of packets in P models are basically inactive as their FIPs are several order of magnitude below the minimum FIP in B microstructures.

The shape of the upper tails is nonetheless very similar which is to be expected since the location of predicted crack initiation are identical when block and slip plane trace are parallel. The extreme values are slightly lower for B microstructures mainly due to the fact that blocks do not always extend trough all the packet length.

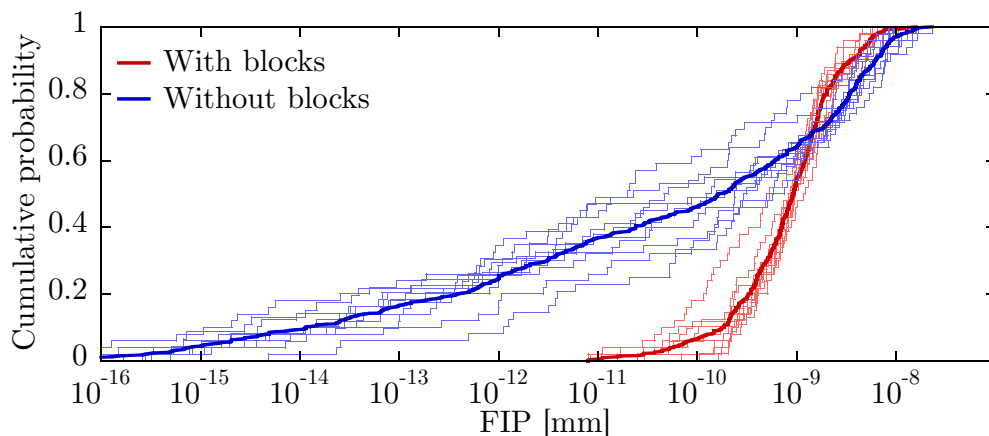


Figure IV.46 – Cumulative probability of the Tanaka-Mura FIP for the two models.

5.4 Conclusions

The role of different scales of heterogeneity in the fatigue crack initiation of martensitic steel was investigated through a comparative study considering or not block boundaries. The results indicate that block morphology and orientation relationship significantly affects the strain distribution and the predicted location of crack initiation. In this regard, the effective critical size in low-carbon steels seems to be the lath long direction. The application of the Tanaka-Mura model mainly predicts cracks initiation along the lath direction.

However, the application of a size-independent crystal plasticity model most likely overestimate the plastic flow within blocks. Finally it is worth mentioning that despite explicitly considering blocks and packets, boundaries may be of different nature in term of strength or ease of slip transfer which is also not accounted in the CP framework.

Conclusions and Recommendations

Conclusions

The work presented in this dissertation focused on the fatigue behavior in low-carbon steels from a microstructure-sensitive point of view using the crystal plasticity finite element method.

A literature review on the fatigue problem in metallic single crystals and polycrystals was presented in the first chapter. The various sources of scattering in high-cycle fatigue as well as its statistical treatment, especially using the extreme value theory, were first discussed. The review continued by describing the mechanisms and existing models related to the formation and early propagation of fatigue cracks. The models are mainly based on the local mechanical fields at the grain scale (plastic strain, shear stress), microstructural and crystallographic attributes (grain size, twist and tilt angles). In this regard, the recent trend for the application of these models is based on microstructural mechanics through the explicit modeling of polycrystalline aggregates and the evaluation of mesoscopic fields using finite element method coupled with crystal plasticity models for the elasto-plastic behavior at the crystal level. The evaluation of a fatigue criterion, often referred as fatigue indicator parameter (FIP) is mainly based on a critical plane approach in which the criterion is assessed on discrete crystallographic planes. The current limitations regarding the modeling of synthetic aggregates, crystal plasticity models and methods for the evaluation of FIPs were finally raised.

The second chapter focused on the characterization and modeling of the materials studied in this work from a microstructural aspect. The chemical and metallurgical characteristics of the low-carbon steels were first presented. The microstructural attributes of the three steels numerically studied in the last chapter were then extensively investigated by EBSD analyses. It was shown that polycrystals with a single scale of heterogeneity could be well characterized using an ellipse fitting process. However, EBSD measurement of multi-scale materials such as martensitic steels requires initial data processing in order to separate and accurately quantify the different scales of heterogeneity. Several procedures were then developed to generate synthetic polycrystalline aggregates based on elliptic seeds and a novel anisotropic tessellation that takes into account the shape and orientation of the grains. A framework was also presented to generate martensitic microstructures based on sequential multi-scale tessellations. The reproduction of the crystallographic texture followed existing algorithms. The developed methods were finally validated by comparing experimental and synthetic EBSD images. It was shown that the anisotropic tessellation is capable of reproducing grain boundaries with a relatively high confidence.

The mechanical behavior of the different steels under cyclic conditions has been experimentally investigated in the third chapter. At first, low-cycle fatigue experiments were conducted at constant applied strain amplitudes and fully reversed uniaxial tension-compression conditions. The cyclic stress response of most of the materials revealed three phases commonly reported in literature: cyclic hardening for ten to hundred cycles, soft-

ning up to half-life and a stabilization of the cyclic stress-strain curve until the final failure. The effect of the thermal treatment pattern was analyzed by studying the strain-life behavior and comparing the fracture surfaces. It was found out that the first treatment pattern, leading to a significant increase in the grain size, reduces the cyclic ductility of the steels.

Numerical procedures based on homogenization and scale transition theories were then applied to calibrate the parameters of phenomenological crystal plastic and isotropic J_2 -plasticity models by inverse analysis on stabilized stress-strain hysteresis curves. A three-dimensional RVE constituted of 300 grains was modeled using Voronoi tessellation and cycled with the same conditions as in experiments and considering Periodic Boundary Conditions (PBC). As expected for similar parameters, the Taylor-Lin model overestimates the behavior of the materials as it represents the upper-bound of the average mechanical response.

The experimental study followed with load-controlled high-cycle fatigue experiments under fully reversed ($R=-1$) and positive stress ratio ($R=0.1$). The experiments were conducted on specimens including an elliptical notch in order to measure the crack initiation lives and short crack growth rates of the different steels without significantly affecting both the fatigue strength and fatigue limit. A procedure was developed to record the specimen surface at regular interval. In most specimens, crack initiated from the notch on a random angular position and not always at the location of highest stress concentration factor. The numbers of cycles for crack initiation were recorded and did not reveal any clear trend when decreasing the stress amplitude or compared with the number of cycles to failure. Overall, crack initiation was randomly scattered between 20 to 60% of the total fatigue life of the specimen. The crack length was then measured against the number of cycle and the crack growth rate was computed based on a standard polynomial reduction method in order to reduce the measurement errors. The crack growth rate was then represented against the crack length and confronted to a typical long crack growth model based on the computation of the stress intensity factor of a semi-circular crack. In most specimens, an oscillatory behavior of the crack growth rate was observed, most particularly for large notch specimens where the average grain size was about several hundreds of microns. In small notch specimens, after two to three oscillations the crack growth rate followed that of long cracks, which was confirmed by the investigation of the fracture surface revealing striations at about three grain size length from the notch. These observations were different for large notch specimens where the crack growth rate was still heavily fluctuating close to the final failure. This was also confirmed by the observation of the fracture surface.

The last chapter was dedicated to numerical simulations of polycrystalline aggregates under fatigue conditions. At first, fatigue criteria for crack initiation, propagation and retardation and methods for their evaluation were presented. To assess the predictive capabilities of the different criteria, three distinct numerical studies were conducted.

The first study concerned the evaluation of the possible influence of grain morphology and cold rolling texture on fatigue crack initiation. It was found that describing a microstructure only in term of average grain size was insufficient as the grain size distribution can significantly affect the scattering in crack initiation lives. Accordingly, accurately reproducing a certain grain size distribution appeared to be necessary to reliably assess the scattering in fatigue life. Also, the morphology of the grains as well as the cold rolling texture tend to increase the crack initiation lives and decrease its variability. Finally, the twist and tilt angles at the tips of the predicted cracks were evaluated. It was found that

while cold rolling texture provides a better resistance against crack initiation, the low disorientation between neighbor grains induces a lower resistance to crack propagation compared with a random texture.

The second study was a comparative study aimed to reproduce the fatigue experiments conducted in the third chapter for two materials with close properties: α -iron and FP steel. Simulations of notched microstructures were conducted for different stress amplitudes. The prediction of crack initiation lives based on the Tanaka-Mura model showed a relative good agreement for ranking the fatigue performances between the two materials compared with experiments. However, the estimation of the Tanaka-Mura parameter based on extreme value theory and the maximum likelihood method revealed that the parameter was unlikely to be the same for the two materials even though they were both constituted of ferrite phase. Simulations of cracked microstructures showed that the presence of short cracks only affects the grains in their direct vicinity. Crack propagation across the first grain boundary was predicted to occur on a slip system with high plastic strain and low twist angle. However, it was observed that it does not always correspond to the slip system with the lowest twist angle, revealing the importance on considering the stress redistribution due to the presence of a crack. The scattering of the fatigue lives past the first two grains appeared to also increase compared with the scattering of the initiation lives.

The last study aimed to evaluate the influence of modeling hypotheses when simulating martensitic steels. Two types of microstructures with and without block boundaries were considered. While the intensity of the plastic strain was relatively similar in both cases due to the lack of size effects in the phenomenological model, the distribution of the plastic strain could be significantly different when considering the six possible variants within a packet. It was finally noticed that the location of crack initiation could vary between the two models since the critical plane approach using potential crack paths directly accounts for the relationship between variant morphologies and orientations.

The framework of the microstructure-sensitive procedure for the comparative evaluation of the fatigue performances is depicted in Fig. V.1. The framework is carried out in three main steps combining experimental data and numerical methods:

1. **Microstructure characterization and modeling.** The key microstructural attributes are quantified whether from EBSD observation or the reconstruction of 3D microstructures based on serial-sectioning or DCT technique. Robust numerical procedures are then applied to instantiate multiple synthetic aggregates based on these data.
2. **Mechanical characterization and CP calibration.** Strain-controlled cyclic experiments are first conducted for specific loading conditions (strain rate, ratio...) to quantify the mechanical response of the materials. Inverse analyses are then performed using scale transition or homogenization models to calibrate the CP model.
3. **Fatigue experiments and CPFEM simulations.** Fatigue simulations are conducted on sets of polycrystalline aggregates and relevant FIPs are evaluated and compared to quantify the effect of certain microstructural or mechanical parameters on the fatigue response. In this step, FIPs can be fitted to experimental data of fatigue crack initiation or propagation to be further used to predict the fatigue life of the materials for other loading conditions, microstructure distribution...

Such procedure can be used to evaluate the influence of microstructural attributes on fatigue performances/variability by simulating completely synthetic aggregates (cf. Chapter IV Section 3), different existing materials with similar phases (cf. Chapter IV Section 4), or even the same material but with different loading conditions.

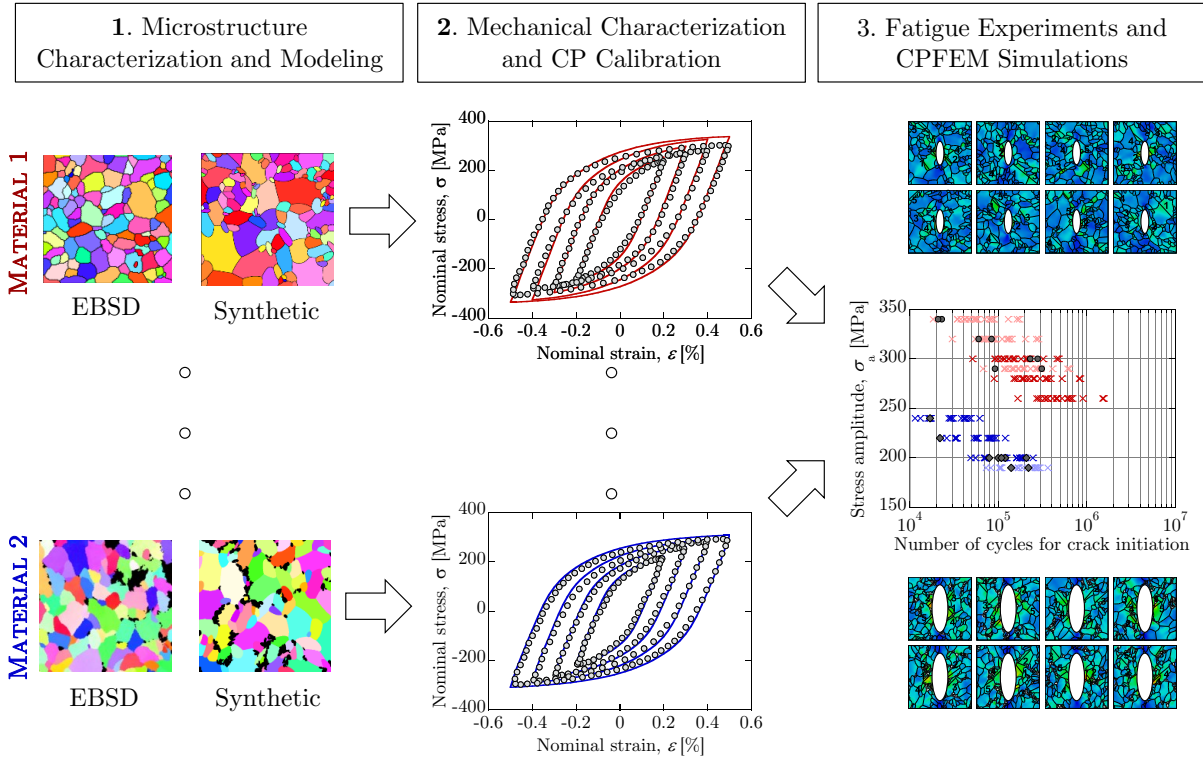


Figure V.1 – Scheme of the microstructure-sensitive procedure for the evaluation of the fatigue responses for different materials.

Recommendations for Future Work

An experimental-computational framework was presented for the quantification of the fatigue response of metallic polycrystalline aggregates from a microstructure-sensitive point of view. Several recommendations for future work can be suggested based on specific limitations regarding each chapter of this thesis:

- Characterization and modeling of three-dimensional polycrystalline aggregates.** The simulations conducted in this work were only two-dimensional (with the exception of the calibration procedure). Microstructures and fatigue cracks are inherently three-dimensional and simulating 3D aggregates should provide additional information such as the competitive mechanisms between crystallographic crack initiation at the surface and subsurface crack initiations from defects/inclusions. The developed tessellation framework can easily be transposed to 3D with the exception of the grain boundary reconstruction which will need further development and the likely usage of CAD softwares and robust procedures [81]. In this regard, experimental database of three-dimensional microstructures could be built based on the reconstruction of EBSD sections or using DCT technique.

- **Development of constitutive models and integration scheme suitable for the simulations under cyclic conditions for a large number of cycles.** The CP model used in this work only considers the mesoscopic critical resolved shear stress and back-stress as internal state variables. The use of size-dependent CP model using dislocation densities as state variables should provide better estimation of the strain distribution inside a grain. However, the continuum mechanics approach of CPFEM simulations does not permit to reproduce the mechanisms of appearance and localization of strain in dislocation structures during cyclic loading, nor do they predict the amount of reversibility arising from the motion of dislocations leading to a roughening of the surface. In this regard, discrete dislocation dynamics could be of great interest if coupled with larger scale models for a realistic representation of grains and boundary conditions. Also, constitutive model can be developed based on a composite partitioning of stress or strain for instance between persistent slip band and matrix. Finally, CPFEM simulations are computationally expensive and can only be performed for few cycles. Specific integration schemes can be developed to accelerate these simulations for fatigue problems such as the dual-time-scale approach proposed by Manchiraju *et al.* [117].
- **Development of optimization schemes for the calibration of crystal plasticity parameters .** The simulations require a crystal plasticity model calibrated with experimental results. The procedure to fit the parameters is currently based on a trial and error extremely time consuming. To circumvent the need to extensively use 3D RVE, a scale transition approach based on the Taylor-Lin model was first used. Overall the differences between the two methods were not so significant, therefore a derivative-free optimization routine can be developed to estimate those parameters automatically and rapidly.
- **Fined calibration of models for crack initiation and propagation.** In Chapter IV, a method was presented for the estimation of the Tanaka-Mura parameter based on the fitting of the FIP to probability distributions and the maximization of a likelihood using experimentally evaluated crack initiation lives. A better approach to calibrate the models can be to monitor the surface or the volume by EBSD or DCT techniques during fatigue experiments, numerically reproduce the microstructure and loading conditions and fit the parameters by a one-on-one comparison. In this regard, database of EBSD taken during fatigue experiments to follow the evolution of microstructures with the number of cycles can be of great interest to calibrate the parameters or even propose new criteria.
- **Development of optimization schemes for the design of materials with improved performances against fatigue.** The fatigue criterion based on the Tanaka-Mura model has shown to be sensitive to crystallographic and microstructural attributes. Even though the absolute values may be incorrect, it can be used as an objective function in an optimization routine to tailor a microstructure against fatigue crack initiation. However, one should not forget that a microstructure optimized against crack initiation may not be an optimum for crack propagation as shown in the case of cold-rolled microstructure. A cluster criterion based on the evaluation of mechanical quantities through several grains may be the correct approach to account for both initiation and propagation mechanisms.

Bibliography

- [1] G.B. Olson. Computational Design of Hierarchically Structured Materials. *Science*, 277(August):1237–1242, 1997.
- [2] Hael Mughrabi. Specific features and mechanisms of fatigue in the ultrahigh-cycle regime. *International Journal of Fatigue*, 28(11):1501–1508, 2006.
- [3] C. Bathias. There is no infinite fatigue life in metallic materials. *Fatigue and Fracture of Engineering Materials and Structures*, 22(7):559–565, 1999.
- [4] M Klesnil and P Lukáš. *Fatigue of metallic materials*. Elsevier, 1992.
- [5] I. Marines, X. Bin, and C. Bathias. An understanding of very high cycle fatigue of metals. *International Journal of Fatigue*, 25(9-11):1101–1107, 2003.
- [6] S. K. Jha, M. J. Caton, and J. M. Larsen. A new paradigm of fatigue variability behavior and implications for life prediction. *Materials Science and Engineering A*, 468-470(SPEC. ISS.):23–32, 2007.
- [7] Y. Murakami and T. Endo. Effects of small defects on fatigue strength of metals. *International Journal of Fatigue*, 2(1):23–30, 1980.
- [8] Y Murakami and M Endo. Effects of defects, inclusions and inhomogeneities on fatigue strength. *International Journal of Fatigue*, 16:163–182, 1994.
- [9] Yukitaka Murakami. *Metal Fatigue: Effects of Small Defects and Nonmetallic Inclusions*. Elsevier Science Ltd, 2002.
- [10] Anne Le Pécheur. Fatigue thermique d’ un acier inoxydable austénitique : influence de l’état de surface par une approche multi-échelles. 2008.
- [11] Yan Li, Veronique Aubin, Colette Rey, and Philippe Bompard. Polycrystalline numerical simulation of variable amplitude loading effects on cyclic plasticity and microcrack initiation in austenitic steel 304L. *International Journal of Fatigue*, 42: 71–81, 2012.
- [12] Craig P. Przybyla and David L. McDowell. Microstructure-sensitive extreme value probabilities for high cycle fatigue of Ni-base superalloy IN100. *International Journal of Plasticity*, 26(3):372–394, 2010.
- [13] Craig P. Przybyla and David L. McDowell. Simulated microstructure-sensitive extreme value probabilities for high cycle fatigue of duplex Ti-6Al-4V. *International Journal of Plasticity*, 27(12):1871–1895, 2011.
- [14] C. P. Przybyla and D. L. McDowell. Microstructure-sensitive extreme-value probabilities of high-cycle fatigue for surface vs. subsurface crack formation in duplex Ti-6Al-4V. *Acta Materialia*, 60(1):293–305, 2012.
- [15] A. F. Jenkinson. The frequency distribution of the annual maximum (or minimum) values of meteorological elements. *Quarterly Journal of the Royal Meteorological Society*, 81(348):158–171, 1955.
- [16] H Mughrabi. The Cyclic Hardening and Saturation Behaviour of Copper Single Crystals. *Materials Science and Engineering A*, 33(9):207–223, 1978.

-
- [17] Z. S. Basinski, A. S. Korbel, and S. J. Basinski. The temperature dependence of the saturation stress and dislocation substructure in fatigued copper single crystals. *Acta Metallurgica*, 28(2):191–207, 1980.
- [18] R. Wang, Haël Mughrabi, S. McGovern, and M. Rapp. Fatigue of Copper Single Crystals in Vacuum and in Air I: Persistent Slip Bands and Dislocation Microstructures R. *Materials Science and Engineering*, 65:219–233, 1984.
- [19] Zhirui Wang, Bo Gong, and Zhongguang Wang. Cyclic deformation behavior and dislocation structures of [001] copper single crystals-II. Characteristics of dislocation structures. *Acta Materialia*, 45(4):1379–1391, 1997.
- [20] Hael Mughrabi. Cyclic slip irreversibilities and the evolution of fatigue damage. *Metallurgical and Materials Transactions B: Process Metallurgy and Materials Processing Science*, 40(4):431–453, 2009.
- [21] P Lukáš and M Klesnil. Cyclic stress-strain response and fatigue life of metals in low amplitude region. *Materials Science and Engineering*, 11(6):345–356, 1973.
- [22] C.E Feltner and C Laird. Cyclic stress-strain response of F.C.C. metals and alloys-I Phenomenological experiments. *Acta Metallurgica*, 15(1):1621–1632, 1967.
- [23] C.E Feltner and C Laird. Cyclic stress-strain response of F.C.C. metals and alloys-II Dislocation structures and mechanisms. *Acta Metallurgica*, 15:1633–1653, 1967.
- [24] S. Suresh. *Fatigue of Materials*. Cambridge University Press, 2nd edition, 1998.
- [25] K J Miller. The behavior of short fatigue cracks and their initiation Part II-A general summary. *Fatigue & Fracture of Engineering Materials & Structures*, 10(2): 93–113, 1987.
- [26] Z. S. Basinski, R. Pascual, and S. J. Basinski. Low amplitude fatigue of copper single crystals-I. The role of the surface in fatigue failure. *Acta Metallurgica*, 31: 591–602, 1982.
- [27] Ma Bao-Tong and C. Laird. Overview of fatigue behavior in copper single crystals-I. Surface morphology and stage I crack initiation sites for tests at constant strain amplitude. *Acta Metallurgica*, 37(2):325–336, 1989.
- [28] B. T. Ma and C. Laird. Overview of fatigue behavior in copper single-crystals. 2 Population, size distribution and growth kinetics of stage {I} cracks for tests at constant strain amplitude. *Acta Metallurgica*, 37(2):337–348, 1989.
- [29] H. L. Huang, N. J. Ho, and W. B. Lin. The study of dislocation structures at fatigue crack tips in polycrystalline copper under various crack propagation rates at stage II: Crack propagation. *Materials Science and Engineering A*, 279(1-2): 261–265, 2000.
- [30] Z. F. Zhang and Z. G. Wang. Comparison of fatigue cracking possibility along large- and low-angle grain boundaries. *Materials Science and Engineering A*, 284 (1-2):285–291, 2000.
- [31] Z. F. Zhang and Z. G. Wang. Dependence of intergranular fatigue cracking on the interactions of persistent slip bands with grain boundaries. *Acta Materialia*, 51(2): 347–364, 2003.
- [32] M. Anglada, B. Etemad, J. A. Planell, and F. Guiu. Stress asymmetry and shape

- changes in cyclically deformed Mo single crystals. *Scripta metallurgica*, 14(12):1319–1322, 1980.
- [33] K Tanaka and T Mura. A Dislocation Model for Fatigue Crack Initiation. *Journal of Applied Mechanics*, 48:97–103, 1981.
- [34] K. Tanaka and T. Mura. A micromechanical theory of fatigue crack initiation from notches. *Mechanics of Materials*, 1(1):63–73, 1982.
- [35] Kwai S Chan. A Microstructure-Based Fatigue-Crack-Initiation Model. *Metallurgical and Materials Transactions A: Physical Metallurgy and Materials Science*, 34 (January):43–58, 2003.
- [36] M. Risbet, X. Feaugas, C. Guillemer-Neel, and M. Clavel. Use of atomic force microscopy to quantify slip irreversibility in a nickel-base superalloy. *Scripta Materialia*, 49(6):533–538, 2003.
- [37] H.S. Ho, M. Risbet, and X. Feaugas. On the unified view of the contribution of plastic strain to cyclic crack initiation: Impact of the progressive transformation of shear bands to persistent slip bands. *Acta Materialia*, 85:155–167, 2015.
- [38] S. Pearson. Initiation of fatigue cracks in commercial aluminium alloys and the subsequent propagation of very short cracks. *Engineering Fracture Mechanics*, 7(2), 1975.
- [39] J. Lankford. The effect of environment on the growth of small fatigue cracks. *Fatigue of Engineering Materials and Structures*, 6(1):15–31, 1983.
- [40] J. Lankford. the Influence of Microstructure on the Growth of Small Fatigue Cracks. *Fatigue & Fracture of Engineering Materials and Structures*, 8(2):161–175, 1985.
- [41] S. Suresh and R. O. Ritchie. Propagation of short fatigue cracks. *International Metals Reviews*, 29(1):445–475, 1984.
- [42] P D Hobson. The formulation of a crack growth equation for short cracks. *Fatigue of Engineering Materials and Structures*, 5(4):323 – 327, 1982.
- [43] K. Tanaka, Y. Akiniwa, Y. Nakai, and R. P. Wei. Modelling of small fatigue crack growth interacting with grain boundary. *Engineering Fracture Mechanics*, 24(6):803–819, 1986.
- [44] C. Blochwitz, J. Brechbühl, and W. Tirschler. Analysis of activated slip systems in fatigue nickel polycrystals using the EBSD-technique in the scanning electron microscope. *Materials Science and Engineering: A*, 210(1-2):42–47, 1996.
- [45] C Blochwitz, R Richter, W Tirschler, and K Obrtlik. The effect of local textures on microcrack fatigued f . c . c . metals propagation in. *Materials Science*, 236:563–566, 1997.
- [46] David M. Saylor, Bassem S. El Dasher, Anthony D. Rollett, and Gregory S. Rohrer. Distribution of grain boundaries in aluminum as a function of five macroscopic parameters. *Acta Materialia*, 52(12):3649–3655, 2004.
- [47] T. Zhai, A. J. Wilkinson, and J. W. Martin. A crystallographic mechanism for fatigue crack propagation through grain boundaries. *Acta Materialia*, 48(20):4917–4927, 2000.
- [48] W. L. Morris, M. R. James, and O. Buck. Growth rate models for short surface cracks in AI 2219-T851. *Metallurgical Transactions A*, 12(January):57–64, 1981.

-
- [49] H. Kitagawa and S. Takahashi. Applicability of fracture mechanics to very small cracks or the cracks in the early stage. *ICM-2*, pages 627–631, 1976.
- [50] M.W. Brown. Interfaces between short, long, and non-propagating cracks. In *The Behaviour of Short Fatigue Cracks*, pages 423–439. 1986.
- [51] ELBER W. Fatigue Crack Closure Under Cyclic Tension. *Engineering Fracture Mechanics*, 2(1):37–45, 1970.
- [52] G. Cailletaud, S. Forest, D. Jeulin, F. Feyel, I. Galliet, V. Mounoury, and S. Quilici. Some elements of microstructural mechanics. *Computational Materials Science*, 27(3):351–374, 2003.
- [53] R. Hill. Elastic properties of reinforced solids: Some theoretical principles. *Journal of the Mechanics and Physics of Solids*, 11(5):357–372, 1963.
- [54] A. Musienko, A. Tatschl, K. Schmidegg, O. Kolednik, R. Pippan, and G. Cailletaud. Three-dimensional finite element simulation of a polycrystalline copper specimen. *Acta Materialia*, 55(12):4121–4136, 2007.
- [55] L. Signor, P. Villechaise, T. Ghidossi, E. Lacoste, M. Gueguen, and S. Courtin. Influence of local crystallographic configuration on microcrack initiation in fatigued 316LN stainless steel: Experiments and crystal plasticity finite elements simulations. *Materials Science and Engineering A*, 649:239–249, 2016.
- [56] Michael Groeber, Somnath Ghosh, Michael D. Uchic, and Dennis M. Dimiduk. A framework for automated analysis and simulation of 3D polycrystalline microstructures. Part 1: Statistical characterization. *Acta Materialia*, 56(6):1257–1273, 2008.
- [57] Michael Groeber A. and Michael Jackson A. DREAM.3D: A Digital Representation Environment for the Analysis of Microstructure in 3D. *Integrating Materials and Manufacturing Innovation*, 3(1):5, 2014.
- [58] William D. Musinski and David L. McDowell. Microstructure-sensitive probabilistic modeling of HCF crack initiation and early crack growth in Ni-base superalloy IN100 notched components. *International Journal of Fatigue*, 37:41–53, 2012.
- [59] Y. Guilhem, S. Basseville, F. Curtit, J-M. Stéphan, and G. Cailletaud. Investigation of the effect of grain clusters on fatigue crack initiation in polycrystals. *International Journal of Fatigue*, 32(11):1748–1763, 2010.
- [60] Maxime Sauzay and Thomas Jourdan. Polycrystalline microstructure, cubic elasticity, and nucleation of high-cycle fatigue cracks. *International Journal of Fracture*, 141(3-4):431–446, 2006.
- [61] S. Osterstock, C. Robertson, M. Sauzay, V. Aubin, and S. Degallaix. Stage I surface crack formation in thermal fatigue: A predictive multi-scale approach. *Materials Science and Engineering A*, 528(1):379–390, 2010.
- [62] Atsuyuki Okabe, Barry Boots, Kokichi Sugihara, and Sung Nok Chiu. *Spatial Tessellations: Concepts and Applications of Voronoi Diagrams*. John Wiley & Sons, Chichester, second edi edition, 2000. ISBN 0471934305.
- [63] G. Bertolino, N. Bilger, and J. Crépin. Modeling microstructures and microstructural effects on macroscopic and intragranular mechanical behavior. *Computational Materials Science*, 40(3):408–416, 2007.

- [64] K. Kusuura T. Hoshide. Life Prediction By Simulation of Crack Growth in Notched Components With Different Microstructures and Under Multiaxial Fatigue. pages 201–213, 1998.
- [65] Toshihiko Hoshide. Procedia Engineering Life prediction based on biaxial fatigue crack growth simulated in different microstructures modeled by using Voronoi-polygons. *Procedia Engineering*, 2(1):111–120, 2010.
- [66] R. Quey, P. R. Dawson, and F. Barbe. Large-scale 3D random polycrystals for the finite element method: Generation, meshing and remeshing. *Computer Methods in Applied Mechanics and Engineering*, 200(17-20):1729–1745, 2011.
- [67] Yoann Guilhem, Stéphanie Basseville, François Curtit, Jean Michel Stéphan, and Georges Cailletaud. Numerical investigations of the free surface effect in three-dimensional polycrystalline aggregates. *Computational Materials Science*, 70:150–162, 2013.
- [68] R. Guerchais, N. Saintier, F. Morel, and C. Robert. Micromechanical investigation of the influence of defects in high cycle fatigue. *International Journal of Fatigue*, 67:159–172, 2014.
- [69] R. Guerchais, C. Robert, F. Morel, and N. Saintier. Micromechanical study of the loading path effect in high cycle fatigue. *International Journal of Fatigue*, 59:64–75, 2014.
- [70] R. Guerchais, F. Morel, N. Saintier, and C. Robert. Influence of the microstructure and voids on the high-cycle fatigue strength of 316L stainless steel under multiaxial loading. *Fatigue & Fracture of Engineering Materials & Structures*, 38(9):1087–1104, 2015.
- [71] R. Guerchais, G. Scalet, A. Constantinescu, and F. Auricchio. Micromechanical modeling for the probabilistic failure prediction of stents in high-cycle fatigue. *International Journal of Fatigue*, 87:405–417, 2016.
- [72] R. Guerchais, F. Morel, and N. Saintier. Effect of defect size and shape on the high-cycle fatigue behavior. *International Journal of Fatigue*, 2016.
- [73] Lu Wang, Zheng Wang, and Jie Zhao. Life prediction by ferrite-pearlite microstructural simulation of short fatigue cracks at high temperature. *International Journal of Fatigue*, 80:349–356, 2015.
- [74] Susmit Kumar and Stewart K. Kurtz. Properties of a two-dimensional Poisson-Voronoi tessellation: A Monte-Carlo study. *Materials Characterization*, 31(1):55–68, 1993.
- [75] M Tanemura. Statistical distributions of Poisson Voronoi cells in two and three dimensions. *Forma*, (18):221–247, 2003.
- [76] P. Zhang, D. Balint, and J. Lin. Controlled Poisson Voronoi tessellation for virtual grain structure generation: a statistical evaluation. *Philosophical Magazine*, 91 (February 2015):4555–4573, 2011.
- [77] Michael Groeber, Somnath Ghosh, Michael D. Uchic, and Dennis M. Dimiduk. A framework for automated analysis and simulation of 3D polycrystalline microstructures. Part 2: Synthetic structure generation. *Acta Materialia*, 56(6):1274–1287, 2008.

-
- [78] B. Regener, C. Krempaszky, E. Werner, and M. Stockinger. Modelling the micro-morphology of heat treated Ti6Al4V forgings by means of spatial tessellations feasible for FEM analyses of microscale residual stresses. *Computational Materials Science*, 52(1):77–81, 2012.
- [79] N. Vajragupta, P. Wechsuanmanee, J. Lian, M. Sharaf, S. Münstermann, a. Ma, a. Hartmaier, and W. Bleck. The modeling scheme to evaluate the influence of microstructure features on microcrack formation of DP-steel: The artificial microstructure model and its application to predict the strain hardening behavior. *Computational Materials Science*, 94:198–213, 2014.
- [80] M. Sharaf, P. Kucharczyk, N. Vajragupta, S. Münstermann, a. Hartmaier, and W. Bleck. Modeling the microstructure influence on fatigue life variability in structural steels. *Computational Materials Science*, 94:258–272, 2014.
- [81] S. Ghosh, Y. Bhandari, and M. Groeber. CAD-based reconstruction of 3D polycrystalline alloy microstructures from FIB generated serial sections. *CAD Computer Aided Design*, 40(3):293–310, 2008.
- [82] O. Diard, S. Leclercq, G. Rousselier, and G. Cailletaud. Evaluation of finite element based analysis of 3D multicrystalline aggregates plasticity Application to crystal plasticity model identification and the study of stress and strain fields near grain boundaries. *International Journal of Plasticity*, 21(4):691–722, 2005.
- [83] F. Roters, P. Eisenlohr, C. Kords, D. D. Tjahjanto, M. Diehl, and D. Raabe. DAMASK: The Düsseldorf advanced material simulation kit for studying crystal plasticity using an fe based or a spectral numerical solver. *Procedia IUTAM*, 3:3–10, 2012.
- [84] P. Shanthraj, P. Eisenlohr, M. Diehl, and F. Roters. Numerically robust spectral methods for crystal plasticity simulations of heterogeneous materials. *International Journal of Plasticity*, 66:31–45, 2014.
- [85] E. H. Lee and D. T. Liu. Finite-Strain Elastic-Plastic Theory with Application to Plane-Wave Analysis. *Journal of Applied Physics*, 38(1):19, 1967.
- [86] J.R. Rice. Inelastic constitutive relations for solids: An internal-variable theory and its application to metal plasticity. *Journal of the Mechanics and Physics of Solids*, 19(6):433–455, 1971.
- [87] F. Roters, P. Eisenlohr, L. Hantcherli, D. D. Tjahjanto, T. R. Bieler, and D. Raabe. Overview of constitutive laws, kinematics, homogenization and multiscale methods in crystal plasticity finite-element modeling: Theory, experiments, applications. *Acta Materialia*, 58(4):1152–1211, 2010.
- [88] C. Déprés, M. Fivel, and L. Tabourot. A dislocation-based model for low-amplitude fatigue behaviour of face-centred cubic single crystals. *Scripta Materialia*, 58(12):1086–1089, 2008.
- [89] J.W. Hutchinson. Bounds and self-consistent estimates for creep of polycrystalline materials. *Proceedings of Royal Society of London A*, 348:101–127, 1976.
- [90] D. Peirce, R.J. Asaro, and A. Needleman. An analysis of nonuniform and localized deformation in ductile single crystals. *Acta Metallurgica*, 30(6):1087–1119, 1982.
- [91] D. Peirce, R. J. Asaro, and A. Needleman. Material rate dependence and localized deformation in crystalline solids. *Acta Metallurgica*, 31(12):1951–1976, 1983.

- [92] C.A. Bronkhorst, S.R. Kalidindi, and L. Anand. Polycrystalline plasticity and the evolution of crystallographic texture in FCC metals. *Phil. Trans. R. Soc. Lond. A*, 341:443–477, 1992.
- [93] Ladislav Kubin, The French, and Ladislav Kubin. IUTAM Symposium on Mesoscopic Dynamics of Fracture Process and Materials Strength. *IUTAM Symposium*, (January 2004):59–68, 2004.
- [94] L. S. Tóth, a. Molinari, and N. Zouhal. Cyclic plasticity phenomena as predicted by polycrystal plasticity. *Mechanics of Materials*, 32(2):99–113, 2000.
- [95] C O Frederick and P J Armstrong. A mathematical representation of the multiaxial Bauschinger effect. *Materials at High Temperatures*, 24(1):1–26, 1966.
- [96] DS Simulia. Abaqus Keywords Reference Manual (6.12), 2012.
- [97] D. L. McDowell and F. P E Dunne. Microstructure-sensitive computational modeling of fatigue crack formation. *International Journal of Fatigue*, 32(9):1521–1542, 2010.
- [98] E. Orowan. Theory of the fatigue of metals. *Proceedings of the Royal Society of London A*, 171(944):79–106, 1939.
- [99] K Dang Van. Sur la résistance à la fatigue des métaux. *Sciences et Techniques de l’armement*, 47:641–722, 1973.
- [100] A Fatemi and D F Socie. Critical Plane Approach To Multiaxial Fatigue Damage Including Out-of-Phase Loading. *Fatigue and Fracture of Engineering Materials and Structures*, 11(3):149–165, 1988.
- [101] A Brucknerfoit and X Huang. Numerical simulation of micro-crack initiation of martensitic steel under fatigue loading. *International Journal of Fatigue*, 28(9):963–971, sep 2006.
- [102] J. Kramberger, N. Jezernik, P. Göncz, and S. Glodež. Extension of the Tanaka-Mura model for fatigue crack initiation in thermally cut martensitic steels. *Engineering Fracture Mechanics*, 77(11):2040–2050, jul 2010.
- [103] Srečko Glodež, Marko Šori, and Janez Kramberger. Prediction of micro-crack initiation in high strength steels using Weibull distribution. *Engineering Fracture Mechanics*, 108:263–274, aug 2013.
- [104] Fabien Briffod, Takayuki Shiraiwa, and Manabu Enoki. Fatigue Crack Initiation Simulation in Pure Iron Polycrystalline Aggregate. *Materials Transactions*, 57(10):1–6, 2016.
- [105] V. P. Bennett and David L. McDowell. Polycrystal orientation distribution effects on microslip in high cycle fatigue. *International Journal of Fatigue*, 25(1):27–39, 2003.
- [106] T Belytschko and T Black. Elastic Crack Growth in Finite Elements With Minimal Remeshing. *Int. J. Numer. Meth. Engng*, 45(July 1998):601–620, 1999.
- [107] Ted Belytschko, Robert Gracie, and Giulio Ventura. A review of extended/generalized finite element methods for material modeling. *Modelling and Simulation in Materials Science and Engineering*, 17(4):043001, 2009.

-
- [108] J. Li, H. Proudhon, a. Roos, V. Chiaruttini, and S. Forest. Crystal plasticity finite element simulation of crack growth in single crystals. *Computational Materials Science*, 94:191–197, 2014.
- [109] H. Proudhon, J. Li, F. Wang, a. Roos, V. Chiaruttini, and S. Forest. 3D simulation of short fatigue crack propagation by finite element crystal plasticity and remeshing. *International Journal of Fatigue*, 82:1–9, 2015.
- [110] Jia Li. *Numerical simulation of fatigue crack propagation in real polycrystals imaged by X ray tomography*. PhD thesis, Ecole Nationale Supérieure des Mines de Paris, 2015.
- [111] Gustavo M. Castelluccio and David L. McDowell. Assessment of small fatigue crack growth driving forces in single crystals with and without slip bands. *International Journal of Fracture*, 176(1):49–64, 2012.
- [112] Gustavo M. Castelluccio and David L. McDowell. A mesoscale approach for growth of 3D microstructurally small fatigue cracks in polycrystals. *International Journal of Damage Mechanics*, 23(6):791–818, 2014.
- [113] Gustavo M. Castelluccio and David L. McDowell. Microstructure-sensitive small fatigue crack growth assessment: Effect of strain ratio, multiaxial strain state, and geometric discontinuities. *International Journal of Fatigue*, 82:521–529, 2015.
- [114] William D. Musinski and David L. McDowell. Simulating the effect of grain boundaries on microstructurally small fatigue crack growth from a focused ion beam notch through a three-dimensional array of grains. *Acta Materialia*, 112:20–39, 2016.
- [115] T. Zhai, X. P. Jiang, J. X. Li, M. D. Garratt, and G. H. Bray. The grain boundary geometry for optimum resistance to growth of short fatigue cracks in high strength Al-alloys. *International Journal of Fatigue*, 27(10-12):1202–1209, 2005.
- [116] William D Musinski. *Modeling The Effects Of Shot-Peened Residual Stresses And Inclusions On Microstructure-Sensitive Fatigue Of Ni-Base Superalloy Components*. PhD thesis, Georgia Institute of Technology, 2014.
- [117] S Manchiraju, M Asai, and S Ghosh. A dual-time-scale finite element model for simulating cyclic deformation of polycrystalline alloys. *The Journal of Strain Analysis for Engineering Design*, 42(4):183–200, 2007.
- [118] F. Bachmann, Ralf Hielscher, and Helmut Schaeben. Texture Analysis with MTEX - Free and Open Source Software Toolbox. *Solid State Phenomena*, 160:63–68, 2010.
- [119] S. Morito, X. Huang, T. Furuhashi, T. Maki, and N. Hansen. The morphology and crystallography of lath martensite in alloy steels. *Acta Materialia*, 54(19):1789–1799, 2006.
- [120] Hiromoto Kitahara, Rintaro Ueji, Nobuhiro Tsuji, and Yoritoshi Minamino. Crystallographic features of lath martensite in low-carbon steel. *Acta Materialia*, 54(5):1279–1288, 2006.
- [121] S. Morito, Y. Adachi, and T. Ohba. Morphology and Crystallography of Sub-Blocks in Ultra-Low Carbon Lath Martensite Steel. *Materials Transactions*, 50(8):1919–1923, 2009.
- [122] Gilles Tarjus, Pierre Schaaf, and Julian Talbot. Random sequential addition: A distribution function approach. *Journal of Statistical Physics*, 63(1-2):167–202, 1991.

- [123] Zhigang Fan, Yugong Wu, Xuanhe Zhao, and Yuzhu Lu. Simulation of polycrystalline structure with Voronoi diagram in Laguerre geometry based on random closed packing of spheres. *Computational Materials Science*, 29(3):301–308, 2004.
- [124] W Q Huang, Y Li, H Akeb, and C M Li. Greedy algorithms for packing unequal circles into a rectangular container. *Journal of the Operational Research Society*, 56(5):539–548, 2005.
- [125] G. Delette. Polycrystalline models of anisotropic sintered magnets: Influence of grain alignment on mechanical properties and residual stresses. *Journal of Magnetism and Magnetic Materials*, 389:10–20, 2015.
- [126] L. St-Pierre, E. Héripré, M. Dexet, J. Crépin, G. Bertolino, and N. Bilger. 3D simulations of microstructure and comparison with experimental microstructure coming from O.I.M analysis. *International Journal of Plasticity*, 24(9):1516–1532, 2008.
- [127] Franz Aurenhammer. Voronoi diagrams - A survey of a fundamental data structure. *ACM Computing Surveys*, 23(3):345–405, 1991.
- [128] Lan Mu. Polygon Characterization With the Multiplicatively Weighted Voronoi Diagram. *The Professional Geographer*, 56(February 2014):37–41, 2004.
- [129] F. Aurenhammer and H. Edelsbrunner. An optimal algorithm for constructing the weighted voronoi diagram in the plane. *Pattern Recognition*, 17(2):251–257, 1984.
- [130] Yoann Guilhem. *Etude numérique des champs mécaniques locaux dans les agrégats polycristallins d’acier 316L sous chargement de fatigue*. PhD thesis, Ecole nationale supérieure des mines de Paris, 2011.
- [131] H.-J. Bunge. *Texture Analysis in Materials Science*. Elsevier, 1982. ISBN 9780408106429.
- [132] László S. Tóth and Paul Van Houtte. Discretization Techniques for Orientation Distribution Functions. *Textures and Microstructures*, 19(4):229–244, 1992.
- [133] Philip Eisenlohr and Franz Roters. Selecting a set of discrete orientations for accurate texture reconstruction. *Computational Materials Science*, 42(4):670–678, 2008.
- [134] Maxime A. Melchior and Laurent Delannay. A texture discretization technique adapted to polycrystalline aggregates with non-uniform grain size. *Computational Materials Science*, 37(4):557–564, 2006.
- [135] V. Tari, A. D. Rollett, and H. Beladi. Back calculation of parent austenite orientation using a clustering approach. *Journal of Applied Crystallography*, 46(1):210–215, 2013.
- [136] E. Voce. The relationship between stress and strain for homogeneous deformations. *Journal of the Institute of Metals*, 74:537–562, 1948.
- [137] G. Laschet, P. Fayek, T. Henke, H. Quade, and U. Prahl. Derivation of anisotropic flow curves of ferrite-pearlite pipeline steel via a two-level homogenisation scheme. *Materials Science and Engineering A*, 566:143–156, 2013.
- [138] S. Allain and O. Bouaziz. Microstructure based modeling for the mechanical behavior of ferrite-pearlite steels suitable to capture isotropic and kinematic hardening. *Materials Science and Engineering: A*, 496(1-2):329–336, 2008.

-
- [139] P. C. Chakraborti and M. K. Mitra. Room temperature low cycle fatigue behaviour of two high strength lamellar duplex ferrite-martensite (DFM) steels. *International Journal of Fatigue*, 27(5):511–518, 2005.
- [140] Surajit Kumar, Nicole Stanford, and Timothy Hilditch. Materials Science & Engineering A Effect of martensite volume fraction on low cycle fatigue behaviour of dual phase steels : Experimental and microstructural investigation. *Materials Science & Engineering A*, 638:296–304, 2015.
- [141] Surajit Kumar Paul, Nicole Stanford, and Timothy Hilditch. Effect of martensite morphology on low cycle fatigue behaviour of dual phase steels: Experimental and microstructural investigation. *Materials Science and Engineering: A*, 644:53–60, 2015.
- [142] Surajit Kumar Paul, Nicole Stanford, Adam Taylor, and Timothy Hilditch. The effect of low cycle fatigue, ratcheting and mean stress relaxation on stress–strain response and microstructural development in a dual phase steel. *International Journal of Fatigue*, 80:341–348, 2015.
- [143] C C Tasan, M Diehl, D Yan, C Zambaldi, P Shanthraj, F Roters, and D Raabe. Integrated experimental - numerical analysis of stress and strain partitioning in multi-phase alloys. *Acta Materialia*, 81:1–19, 2014.
- [144] Sudook A. Kim and Ward L. Johnson. Elastic constants and internal friction of martensitic steel, ferritic-pearlitic steel, and alpha-iron. *Materials Science and Engineering A*, 452-453:633–639, 2007.
- [145] E. Héripré, M. Dexet, J. Crépin, L. Gélébart, A. Roos, M. Bornert, and D. Caldemaison. Coupling between experimental measurements and polycrystal finite element calculations for micromechanical study of metallic materials. *International Journal of Plasticity*, 23(9):1512–1539, 2007.
- [146] P. Lorenzino and A. Navarro. Grain size effects on notch sensitivity. *International Journal of Fatigue*, 70:205–215, 2015.
- [147] M Isida, H Noguchi, and T Yoshida. Tension and bending of finite thickness plates with a semi-elliptical surface crack. *International Journal of Fracture*, 26:157–188, 1984.
- [148] Jan Kohout. A new function describing fatigue crack growth curves. *International Journal of fatigue*, 21(8):813–821, 1999.
- [149] K. Hussain, E. R. De los Rios, and A. Navarro. A two-stage micromechanics model for short fatigue cracks. *Engineering Fracture Mechanics*, 44(3):425–436, 1993.
- [150] Wei Wen and Tongguang Zhai. Three-dimensional effects of microstructures on short fatigue crack growth in an Al-Li 8090 alloy. *Philosophical Magazine*, 91(27):3557–3577, 2011.
- [151] Wei Wen and Tongguang Zhai. Quantification of resistance of grain boundaries to short-fatigue crack growth in three dimensions in high-strength al alloys. *Metallurgical and Materials Transactions A: Physical Metallurgy and Materials Science*, 43(8):2743–2752, 2012.
- [152] Wei Wen. *A Three-Dimensional Quantitative Understanding of Short Fatigue Crack Growth in High Strength Aluminum Alloys*. PhD thesis, University of Kentucky, 2013.

- [153] Henry Proudhon. *Identification des mécanismes de fissuration dans un alliage d'aluminium sollicité en fretting et en fatigue*. PhD thesis, Ecole Centrale de Lyon, 2005.
- [154] Gustavo M. Castelluccio and David L. McDowell. Mesoscale modeling of microstructurally small fatigue cracks in metallic polycrystals. *Materials Science and Engineering A*, 598:34–55, 2014.
- [155] M. Hölscher, D. Raabe, and K. Lücke. Rolling and Recrystallization Textures of BCC Steels. *Steel Research International*, 14(100):585–596, 1991.
- [156] Dassault Systèmes Simulia Corporation. ABAQUS V6.14, Standard User's Manual, 2014.
- [157] P. Mu, V. Aubin, I. Alvarez-Armas, and a. Armas. Influence of the crystalline orientations on microcrack initiation in low-cycle fatigue. *Materials Science and Engineering A*, 573:45–53, 2013.
- [158] D. N. Joanes and C. A. Gill. Comparing Measures of Sample Skewness and Kurtosis. *Journal of the Royal Statistical Society*, 47(1):183–189, 1998.
- [159] Craig P. Przybyla, Rajesh Prasannavenkatesan, Nima Salajegheh, and David L. McDowell. Microstructure-sensitive modeling of high cycle fatigue. *International Journal of Fatigue*, 32(3):512–525, 2010.
- [160] Craig P Przybyla. Microstructure-Sensitive Extreme Value Probabilities of Fatigue in Advanced Engineering Alloys. (August), 2010.
- [161] Craig P. Przybyla, William D. Musinski, Gustavo M. Castelluccio, and David L. McDowell. Microstructure-sensitive HCF and VHCF simulations. *International Journal of Fatigue*, 57:9–27, 2013.
- [162] Martin Diehl, Pratheek Shanthraj, Philip Eisenlohr, and Franz Roters. Neighborhood influences on stress and strain partitioning in dual-phase microstructures: An investigation on synthetic polycrystals with a robust spectral-based numerical method. *Meccanica*, 51(2):429–441, 2015.
- [163] Pratheek Shanthraj. *Microstructural Modeling of Failure Modes in Martensitic Steels*. PhD thesis, North Carolina State University, 2011.

